**The Dissertation Committee for Chicheng Xu Certifies that this is the approved version of the following dissertation:**

# Reservoir Description with Well-Log-Based and Core-Calibrated Petrophysical Rock Classification

**Committee:**

Carlos Torres-Verdín, Supervisor

Ekwere J. Peters

Sanjay Srinivasan

Jon E. Olson

Ronald J. Steel

# Reservoir Description with Well-Log-Based and Core-Calibrated Petrophysical Rock Classification

**by**

**Chicheng Xu, B.S.; Ph. M.**

**Dissertation**

Presented to the Faculty of the Graduate School of

The University of Texas at Austin

in Partial Fulfillment

of the Requirements

for the Degree of

**Doctor of Philosophy**

**The University of Texas at Austin**

**August, 2013**

# Dedication

To my dear wife, Yingying Cao, for her unconditional love and support.

To my two lovely sons, for the joy they brought me in overcoming the hard times.

To my beloved parents, for continuously encouraging me to explore new areas.

To my supportive parents-in-law, for their deep love and care of my family.

## Acknowledgements

First and foremost I would like to express my sincere gratitude to my supervisor, Dr. Carlos Torres-Verdín, for his patient and insightful guidance through my Ph.D. study. The work presented in this dissertation would not have been possible without his continuous encouragement and unreserved knowledge sharing. Particularly, his tenets on integrating multiple disciplines and multiple physics for petrophysical data interpretation ensured that my research work was on the right track. I also want to thank the other members of my dissertation committee, Dr. Ekwere J. Peters, Dr. Sanjay Srinivasan, Dr. Jon E. Olson, and Dr. Ronald J. Steel, for their meticulous dissertation review and helpful technical comments. In particular, Dr. Peters' *Advanced Petrophysics* lecture notes (now also published books) enlightened my thoughts in several research projects.

I would like to thank the faculty of the Petroleum & Geosystems Engineering department at The University of Texas at Austin for teaching me courses. Special gratitude goes to staff members Reynaldo Casanova, Frankie Hart, and Cheryl Kruzie for their help with document preparation and to Roger Terzian for his support with IT. I am greatly indebted to my current and former group workers, who have developed a reliable and versatile petrophysical framework equipped with fast log simulations that tremendously accelerated my research. My sincere gratitude goes to Ben Voss, Paul Linden, Gongli Wang, Jun Ma, Pawel Matuszyk, David Pardo-Zubiaur, Guodong Jin, Alberto Mendoza, Qinshan Yang, Jesús Mauricio Salazar, Renzo Angeles, Robert Mallan, David Wolf, Zoya Heidari, Rohollah Abdollah Pour, and Olabode Ijasan.

Along the journey of my Ph.D. study, I received a lot of kind support from the following friends, and I truly enjoyed their friendship: Jorge Sanchez, Shan Huang, Vahid Shabro, Wei Li, Hamid Hadibeik, Amir Frooqnia, Abhishek Bansal, Rebecca Gao,

Andrew Popielski, Philippe Marouby, Haryanto Adiguna, Elton Ferreria, Essi Kwabi, Hyungjoo Lee, Shaina Kelly, Paul Sayar, Siddharth Mishra, Edwin Ortega, Oyinkansola Ajayi, Tatyana Torskaya, Dipo Olukitibi, Kanay Jerath, Jordan Mimoun, Ankur Gandhi, Malek Lemkecher, Amir Reza-Rahmani, and Ali Moinfar. In addition, I would like to thank my Chinese classmates for accompanying me during my Ph.D. study. A special note of gratitude goes to Bo Gao, Yao Peng, Tie Sun, Qing Tao, Li Ji, Tiantian Zhang, Peila Chen, Wei Yu, and Kaimin Yue for their help in my study and life.

I am also grateful to many geoscientists in the Bureau of Economic Geology, Jackson School of Geosciences, the Kansas Geological Survey, and the oil and gas industry. Technical discussions with Mr. Jerry Lucia, Dr. Charlie Kerans, Dr. Hongliu Zeng, Dr. Ronald Steel, Dr. John Doveton, Mr. David Spain, Dr. Shujie Liu, and Mr. Jeffry Hamman were particularly helpful in developing the ideas in my dissertation. I also benefited from thought-provoking discussions with these visiting scholars in our consortium group, Dr. Guangzhi Liao, Dr. Jie Gao, Dr. Maojin Tan, and Dr. Ruijia Wang.

I would like to thank BP America Inc. for supporting my three summer intern projects on characterizing different reservoir types, including coalbed methane, deepwater turbidite, and deepwater carbonate, which greatly improved my rock typing skills and consolidated my understanding of reservoir characterization. I appreciate the project opportunities provided by the Unconventional Gas Flagship Team, the Kaskida Reservoir Team, and the Integrated Subsurface Description and Modeling Team. A note of special gratitude goes to the following people for their guidance and support during my internships: David Spain, Richard Volz, Chris Morton, German Merletti, Tobi Odumosu, Cherie Lee, Yuanlin Jiang, Oluwagbenga Alabi, Ramsey Fisher, Ivan Pinzon, Elnara Mammadova, Echezona Uzoh, Jennifer Nelson, Gillian Apps, Mick Casey, Bo Lu, Jeffry

Hamman, Hilary Rose, Michael Webster, Glen Gettemy, Shenghui Li, Chris Cade, Walter Guidroz, Vivek Chitale, Maryam Mousavi, Steve Dorobek, Michael Rabinovich, and many others.

I want to express my sincere gratitude to the following groups for traveling fund support for my attendance at conferences: BP America Inc. and Chevron Corporation (SPWLA 2011 Topical Conference and SPWLA 2013 Annual Symposium), SPE Dallas Chapter (AAPG 2012 Annual Convention & Exhibition and SPWLA 2013 Annual Symposium), and UT's Graduate School (SEG 2012 Annual Meeting). In addition, I also want to thank ExxonMobil for providing SEG Student Education Program (SEP) support during my trip to the SEG 2012 annual meeting.

The work reported in this paper was funded by The University of Texas at Austin's Research Consortium on Formation Evaluation, jointly sponsored by Afren, Anadarko, Apache, Aramco, Baker-Hughes, BG, BHP Billiton, BP, Chevron, China Oilfield Services, LTD., ConocoPhillips, ENI, ExxonMobil, Halliburton, Hess, Maersk, Marathon Oil Corporation, Mexican Institute for Petroleum, Nexen, ONGC, OXY, Petrobras, PTTEP, Repsol, RWE, Schlumberger, Shell, Statoil, Total, Weatherford, Wintershall and Woodside Petroleum Limited.

# Reservoir Description with Well-Log-Based and Core-Calibrated Petrophysical Rock Classification

Chicheng Xu, Ph.D.

The University of Texas at Austin, 2013

Supervisor: Carlos Torres-Verdín

Rock type is a key concept in modern reservoir characterization that straddles multiple scales and bridges multiple disciplines. Reservoir rock classification (or simply rock typing) has been recognized as one of the most effective description tools to facilitate large-scale reservoir modeling and simulation. This dissertation aims to integrate core data and well logs to enhance reservoir description by classifying reservoir rocks in a geologically and petrophysically consistent manner. The main objective is to develop scientific approaches for utilizing multi-physics rock data at different time and length scales to describe reservoir rock-fluid systems. Emphasis is placed on transferring physical understanding of rock types from limited ground-truthing core data to abundant well logs using fast log simulations in a multi-layered earth model.

Bimodal log-normal pore-size distribution functions derived from mercury injection capillary pressure (MICP) data are first introduced to characterize complex pore systems in carbonate and tight-gas sandstone reservoirs. Six pore-system attributes are interpreted and integrated to define petrophysical orthogonality or dissimilarity between two pore systems of bimodal log-normal distributions. A simple three-dimensional (3D) cubic pore network model constrained by nuclear magnetic resonance (NMR) and MICP

data is developed to quantify fluid distributions and phase connectivity for predicting saturation-dependent relative permeability during two-phase drainage.

There is rich petrophysical information in spatial fluid distributions resulting from vertical fluid flow on a geologic time scale and radial mud-filtrate invasion on a drilling time scale. Log attributes elicited by such fluid distributions are captured to quantify dynamic reservoir petrophysical properties and define reservoir flow capacity. A new rock classification workflow that reconciles reservoir saturation-height behavior and mud-filtrate for more accurate dynamic reservoir modeling is developed and verified in both clastic and carbonate fields.

Rock types vary and mix at the sub-foot scale in heterogeneous reservoirs due to depositional control or diagenetic overprints. Conventional well logs are limited in their ability to probe the details of each individual bed or rock type as seen from outcrops or cores. A bottom-up Bayesian rock typing method is developed to efficiently test multiple working hypotheses against well logs to quantify uncertainty of rock types and their associated petrophysical properties in thinly bedded reservoirs. Concomitantly, a top-down reservoir description workflow is implemented to characterize intermixed or hybrid rock classes from flow-unit scale (or seismic scale) down to the pore scale based on a multi-scale orthogonal rock class decomposition approach.

Correlations between petrophysical rock types and geological facies in reservoirs originating from deltaic and turbidite depositional systems are investigated in detail. Emphasis is placed on the cause-and-effect relationship between pore geometry and rock geological attributes such as grain size and bed thickness. Well log responses to those geological attributes and associated pore geometries are subjected to numerical log simulations. Sensitivity of various physical logs to petrophysical orthogonality between

rock classes is investigated to identify the most diagnostic log attributes for log-based rock typing.

Field cases of different reservoir types from various geological settings are used to verify the application of petrophysical rock classification to assist reservoir characterization, including facies interpretation, permeability prediction, saturation-height analysis, dynamic petrophysical modeling, uncertainty quantification, petrophysical upscaling, and production forecasting.

# Table of Contents

# List of Tables

# List of Figures

# Chapter 1: Introduction

The main thrust of this dissertation is to integrate core data and well logs to improve reservoir description by developing new rock classification methods honoring scientific rules of geology, petrophysics, and physics. Three important questions are raised and answered in this dissertation based on field applications of different reservoir types from various geological settings. The first question is: how can petrophysical rock classification improve reservoir description? The second question is: why should core and log data be integrated to enhance the accuracy of rock classification? The third question is: what is the essence of rock classification: a geological hypothesis, a petrophysical interpretation, a physical model, or a mathematical description?

## 1.1 BACKGROUND

Rock classification (or simply rock typing) is an emerging reservoir description tool that elicits broad research interests in the oil and gas industry. It has become increasingly important in modern reservoir characterization to invoke close integration of multi-discipline, multi-physics, and multi-scale subsurface data, including pore imaging, core measurements, well logs, seismic amplitude data, well testing, and production surveillance (Gunter et al., 1997a). Interestingly, the definition of rock type still remains ambiguous and sometimes arguable in many situations as it depends on the specific description purposes to be achieved by geoscientists and engineers working in different disciplines. Geologists consider rock types as depositional facies or lithofacies which emphasize the genesis of rock formations to enable 3D stratigraphic reservoir modeling (Fisher, 1982; Van Wagoner et al., 1990; Kerans and Tinker, 1999; Muto et al., 2007; Slatt, 2007). Petrophysicists define rock types based on pore geometry that relates all static and dynamic petrophysical properties (Archie, 1950 and 1952). Reservoir and

production engineers group rock types as flow units that are stratigraphically continuous intervals of similar geologic and petrophysical features to upscale reservoir grids for efficient fluid-flow simulation (Gunter et al., 1997b). Therefore, developing new rock classification schemes and workflows that serve multiple characterization purposes from different disciplines remains a challenging but important task. Noteworthy is that reservoir characterization teams are working toward a common objective: to construct a valid reservoir model populated with accurate petrophysical properties for reserves estimation and production forecasting (Lucia, 1999). This dissertation firmly adheres to the latter tenet in researching new petrophysical rock classification methods to enable quantitative connections to the geological framework for practical reservoir characterization applications.

In geological literature, there are several existing schemes for sedimentary rock classification. Two classic schemes are the Wentworth scale of particle sizes in clastic sedimentary rocks (Wentworth, 1922) and Dunham's scheme of mud-grain composition in carbonate sedimentary rocks (Dunham, 1962). The classification of clastic sedimentary rocks is further complicated by the clay type and distribution (Neasham, 1977). Lucia modified Dunham's carbonate classification and introduced rock fabric number to quantify rock pore-scale properties (Lucia, 1995).

In petrophysical study, rock classification based on routine and special core measurements was studied extensively by many workers. Pittman introduced the Winland $R_{35}$[1] method derived from Spindle field sandstone core samples (Pittman, 1992). Amaefule et al. (1993) initialized the concept of hydraulic flow unit based on the Hagen–Poiseuille flow equation and used the flow zone indicator (FZI) to characterize several

[1] Pore throat radius at 35% non-wetting phase saturation.

heterogeneous reservoirs. Other methods based on mercury injection capillary pressure (MICP), pore-throat size distribution, and thin sections are also frequently used (Lucia, 1995; Clerke et al., 2008). For rock classification on a larger scale, Gunter et al. (1997b) utilized the Stratigraphic Modified Lorenz Plot for characterizing reservoir flow units.

However, the rock types established from core measurements need to be propagated to the uncored zones or wells in the reservoir through integration with well log data. Or in some cases where core data are unavailable, the rock classification needs to be based solely on well logs. Geologists and petrophysicists have been working on this topic for decades. Geologists use well log data to define lithologic columns, model depositional facies, and study high-resolution stratigraphy (Serra and Sulpice, 1975; Van Wagoner et al., 1990; Serra and Serra, 2003). For example, the shapes of gamma ray and spontaneous potential logs are typically used to correlate with grain size changes to define fining-upward or coarsening-upward sequences (Pirson, 1983). Serra initialized the electro-facies concept to study geological sequences based on well logs. Petrophysicists use well log data to infer petrophysical information such as volumetric concentration of clay, porosity, and water saturation, which provide a basis for petrophysical rock classification. Generally, a rock type that has less clay content, larger porosity, and smaller irreducible water saturation tends to be of better reservoir quality in terms of storage/flow capacity. Based on this principle, some rock quality indices were calculated from well logs, such as bulk volume of water (Buckles, 1965). Some authors use neural network techniques to establish a non-linear relation between core measurements and various log responses to propagate rock types from the core data domain to the log data domain (Kharrat et al., 2009). However, those methods neglect the adverse effects of shoulder beds and mud-filtration invasion on well logs, which are the two main challenges to be addressed here.

## 1.2 PROBLEM STATEMENT

The awareness of the importance of rock classification in reservoir description prompted this dissertation research. G.E. Archie (1950) defined petrophysical rock type based on the associated pore-size distribution, which acts as the hub linking the rock's static and dynamic petrophysical properties (Fig. 1.1). In the same paper, Archie mentioned the possibility of using various types of well logs to probe the pore-size distribution and identify petrophysical rock types. In most cases, core data cover a very limited segment of the reservoir. Integration of core and well logs is therefore necessary to extrapolate geological and petrophysical attributes from cored depth intervals to remaining wells and into the reservoir. However, currently used core-based and log-based rock typing methods still face a series of technical challenges that need to be addressed before gaining wider acceptance in integrated reservoir description. This section briefly summarizes current challenges in core-based rock typing, log-based rock typing, and correlating petrophysical rock types with geological facies.

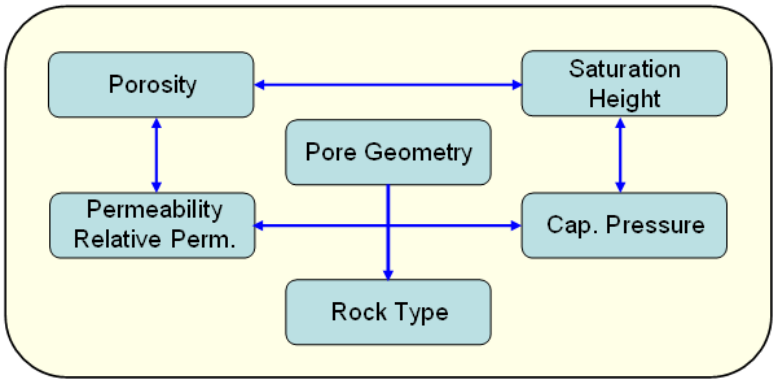


**Figure 1.1:** Archie's original definition of rock type and its central role in relating all petrophysical properties (modified from Archie, 1950).

### 1.2.1 Core-Based Rock Typing

Rock classification should first close the petrophysics loop anchored on pore geometry before invoking a specific geological framework (Fig. 1.1; Archie, 1950). Therefore, the focus of this dissertation was first placed on pore-scale and core-scale petrophysical rock description. Existing core-based petrophysical rock typing methods tend to rely on only one major pore-system attribute to classify rocks (Leverett, 1941; Pittman, 1992; Amaefule et al., 1993). Although these methods have been proved sufficient in many conventional reservoirs where one major attribute properly represents the entire pore network system, they become inadequate to describe the effects of complex pore systems that originated from significant diagenetic overprints such as those commonly encountered in carbonate and tight-gas sandstone reservoirs. Pore geometry is described with many attributes, including pore volume, pore-body size, pore-throat size, pore connectivity, pore-size uniformity, and pore morphology. Figure 1.2 shows an example of poor ranking of petrophysical rock types in the porosity-permeability data domain based only on MICP-derived Winland $R_{35}$ in the Cotton Valley tight gas field. The samples in the dashed circle are misclassified as the best rock type (RT-A) because they fall on the same $R_{35}$ trend line as RT-A. However, those two samples have much lower porosity and permeability compared to the other RT-A rocks.

New methods for describing complex pore systems are therefore necessary for reliable petrophysical modeling and rock typing. The problem is exacerbated when fluid saturation and distribution during multi-phase flow are taken into account. Hence, it is also imperative to study fluid distribution as a consequence of different pore geometries.

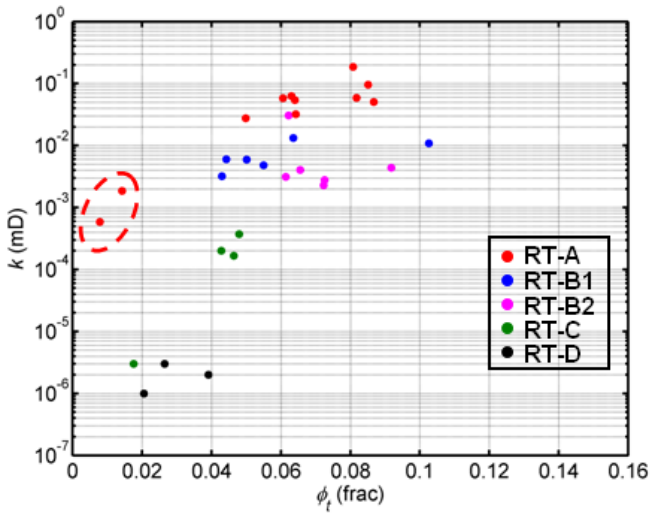


**Figure 1.2:** Example of poor petrophysical ranking in the porosity ($\phi_t$) and permeability ($k$) data domain. Five rock types (A, B1, B2, C, and D) are identified and classified by using MICP-derived $R_{35}$ as the only classification criterion.

### 1.2.2 Log-Based Rock Typing

Rock classification based on core data is relatively simple because petrophysical properties are rigorously measured under the same protocol. However, rock classification using downhole well logs is more challenging and is subject to great uncertainty. Four technical problems arise immediately when moving from core data to well logs for rock typing, namely data quality, indirect measurements, variable reservoir conditions, and scale discrepancy. The compounded technical problem was defined by Archie (1950) as the "geometrical problem" in the logging industry. The following are further elaborations on these problems, illustrated by specific synthetic or field examples.

#### *1.2.1.1 Data Quality Consideration*

Data quality of well logs is typically compromised by operational problems and downhole environments, including stick-and-slip effect, depth shift, borehole rugosity, mud-filtrate invasion, etc. (Theys, 1999). Figure 1.3 shows an example of a depth shift problem encountered in a log run where resistivity logs mismatch nuclear logs in their

bed boundaries. This is a common issue for general log analysis, as well as for log-based rock typing. The depth shift problem can be effectively remedied by meticulous depth matching procedures.

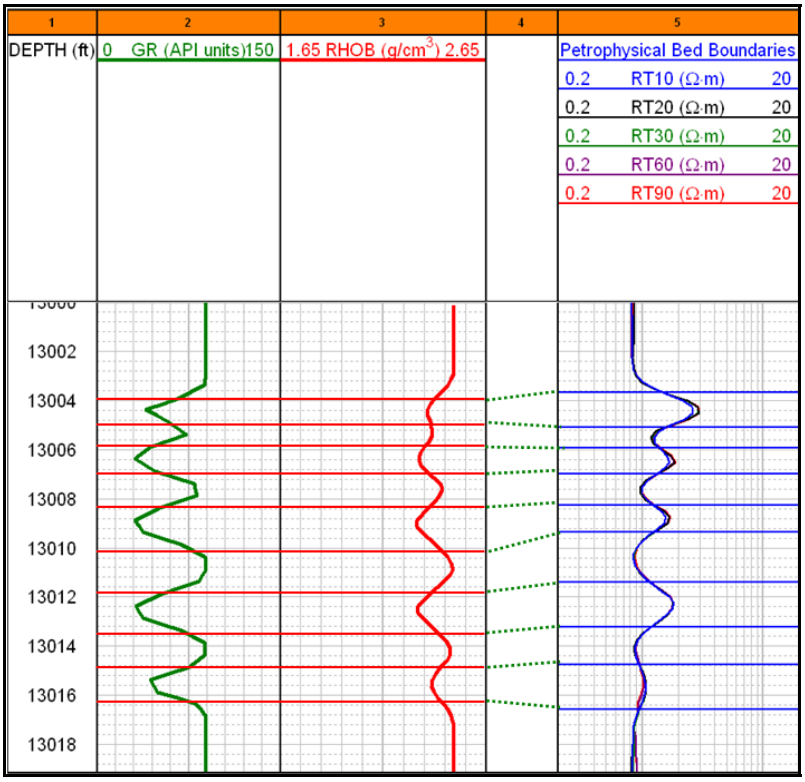


**Figure 1.3:** Example of depth shift between nuclear logs and resistivity logs due to stick-and-slip effect. Track 1: depth; Track 2: gamma ray log; Track 3: bulk density log; Track 4: bed boundary correlation; Track 5: resistivity logs.

Another problem is deep mud-filtrate invasion that alters the near borehole fluid distribution, which significantly modifies the rock properties measured by various logs (Gandhi et al., 2010). Figure 1.4 shows an example of deep mud-filtrate invasion where even the deep-reading resistivity logs become non-representative of the original formation resistivity (Track 7). Rock typing based on those non-representative logs will

certainly increase the error and petrophysical uncertainty that will cascade into reservoir modeling.

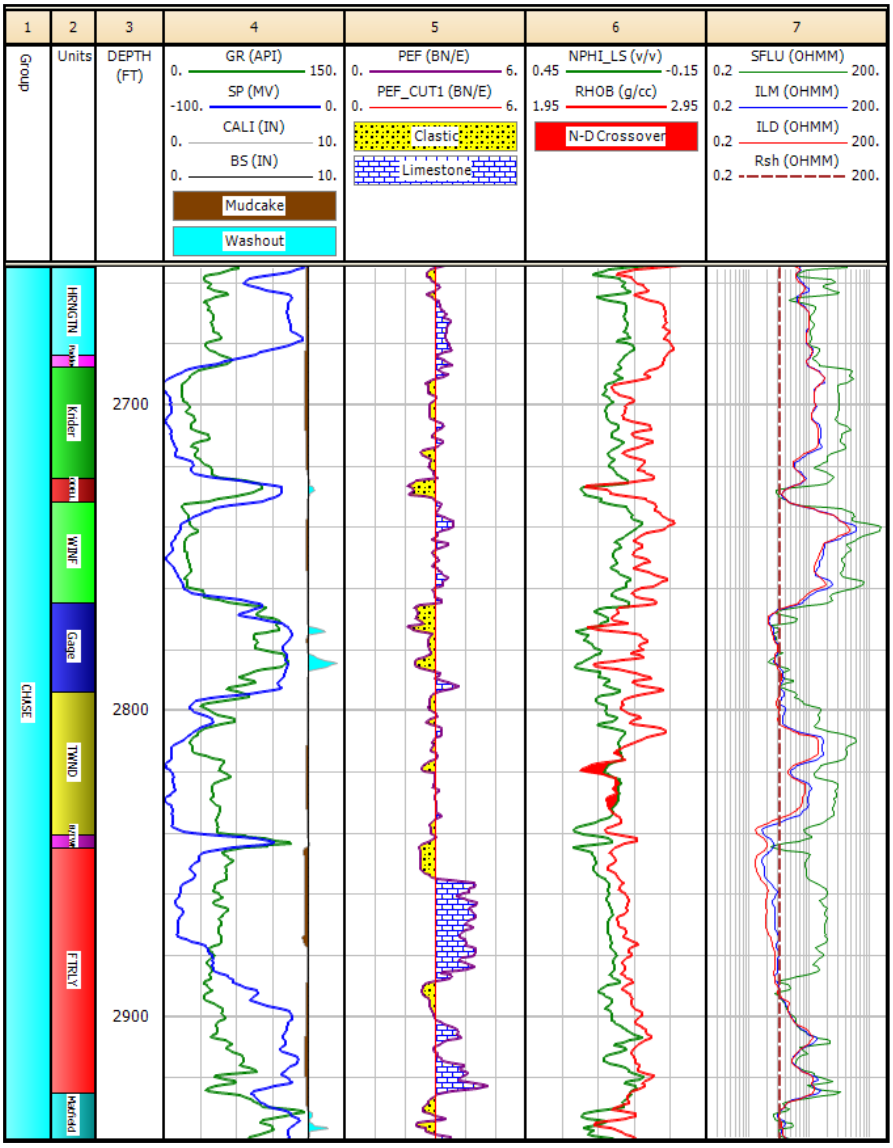


**Figure 1.4:** Example of non-representative neutron porosity, bulk density, and resistivity logs due to deep mud-filtrate invasion. Track 1: chase group; Track 2: units; Track 3: depth; Track 4: gamma ray and spontaneous potential logs; Track 5: photo-electric factor log; Track 6: neutron porosity and bulk density logs; Track 7: resistivity logs.

#### *1.2.1.2 Indirect Measurements Problem*

The indirectness problem lies in using physical measurements to infer petrophysical properties and geological attributes. In fact, most well logs are more sensitive to grains, bedding structure, and pore-filling fluids than to pore geometry (texture) itself. Table 1.1 summarizes the sensitivity of various well logs to petrophysical properties and geological attributes of rocks. Noteworthy is that the logs sensitive to pore geometry are also significantly influenced by fluid content, such as resistivity and NMR.

**Table 1.1:** Sensitivity of well logs to petrophysical properties and geological attributes of rocks (modified from Serra and Abbott, 1980).

| | Composition | Texture | Structure | Fluid |
|---|---|---|---|---|
| Gamma Ray | **High** | Low | Low | Low |
| PE Factor | **High** | Low | Low | Low |
| Neutron Porosity | Medium | Medium | Low | **High** |
| Bulk Density | Medium | Medium | Low | **High** |
| Electrical Resistivity | Low | Medium | **High** | **High** |
| Acoustic Slowness | **High** | Medium | Medium | **High** |
| NMR | Medium | **High** | Low | **High** |

#### *1.2.1.3 Variable Reservoir Conditions Problem*

The variable reservoir conditions problem refers to the change of reservoir pressure, temperature, capillary pressure (as in a capillary transition zone), and fluid content along the vertical reservoir column that may give rise to different log responses even for the same rock properties. Figure 1.5 shows such a field example from the North

Sea, UK. From top to bottom, the main reservoir fluid changes from gas to oil and then to water. The fluid change gives rise to different responses of bulk density and neutron porosity even with the same rock type (i.e., rock of similar range of porosity and permeability) (Track 3). Further, the entire oil zone undergoes a typical capillary transition as it approaches the base aquifer. Water saturation gradually increases toward the oil-water contact, which gives rise to different resistivity responses even for the same petrophysical rock type (Track 4).

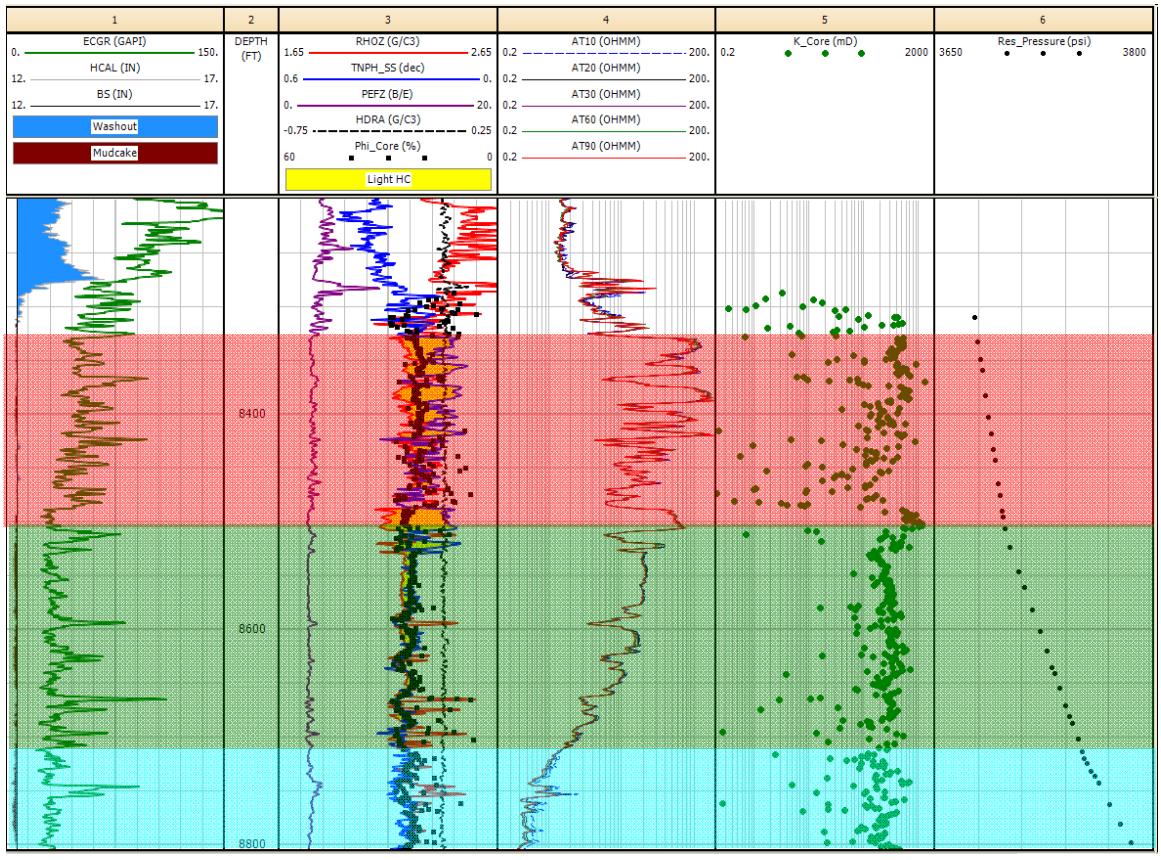


**Figure 1.5:** Example of capillary transition zone and fluid content variations from top to bottom. Red shadow: gas zone; Green shadow: oil zone; Cyan shadow: water zone. Track 1: gamma ray; Track 2: depth; Track 3: neutron porosity, bulk density, and photo-electric factor; Track 4: resistivity logs; Track 5: core permeability; Track 6: reservoir pressure.

### *1.2.1.4 Scale Discrepancy Problem*

Scale discrepancy here needs to be understood from two perspectives. First, core measurements are usually performed at the inch scale, whereas most well logs exhibit foot-scale resolution (Fig. 1.6). This difference will normally cause log-derived rock types not to match core-derived rock types. Second, multiple-physics well logs have different volumes of investigation, which introduces large uncertainty in petrophysical estimation of thinly bedded or laminated formations (Fig. 1.6).

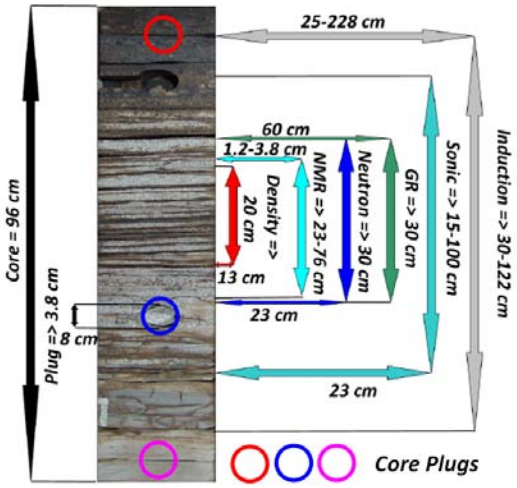


**Figure 1.6:** Scale discrepancy between core plugs and various well logs (modified from Diniz-Ferreira and Torres-Verdín, 2012).

### *1.2.1.5 Fallacies of Rock Classification Using Apparent Electrofacies*

The above-mentioned problems are general for all log-based petrophysical or geological studies, including log-based rock classification. Conventional rock typing methods that use supervised or unsupervised clustering/machine learning techniques on apparent electrofacies (Serra and Abbott, 1980) would fail to deliver reliable petrophysical rock types without addressing the problems listed above. The old belief that *same rock types have similar log responses* does not necessarily hold true in those

challenging cases. Several synthetic and field examples are used to further illustrate the potential fallacies of rock classification that apparent electrofacies may encounter.

**Fallacy No. 1: Mud-filtrate invasion has only minor effects on log-based rock classification.**

Numerous field cases have indicated that mud-filtrate invasion has great impact on shallow-reading and fluid-sensitive logs, such as neutron porosity, bulk density, resistivity, and NMR logs (Salazar, 2004; Gandhi et al., 2010). The adverse effects of mud-filtrate invasion on various logs are most detectable in gas reservoirs drilled with water-base mud (WBM) due to highly contrasting fluid density (water vs. gas), salinity contrast between mud filtrate and connate water, high mobility of gas phase, and water-wet feature of rocks. Consequently, fast and deep invasion takes place in WBM-drilled gas reservoirs. Figure 1.7 shows a synthetic case of typical log responses simulated in a WBM-drilled gas reservoir at both pre-invasion and post-invasion conditions. Mud-filtrate invasion significantly changes the neutron porosity, bulk density, and resistivity logs after deep mud filtrate invasion. As a result, some diagnostic log attributes for rock typing, such as neutron-density crossover and deep resistivity amplitude, become less distinct and less separable than at pre-invasion conditions (Figure 1.8). If the same classification algorithm is applied to the post-invasion well logs, less satisfactory results will be achieved due to the inherently large uncertainties associated with logging measurements. To achieve better rock classification results, some additional invasion-induced attributes need to be included to separate different rock types, such as radial resistivity profiles.

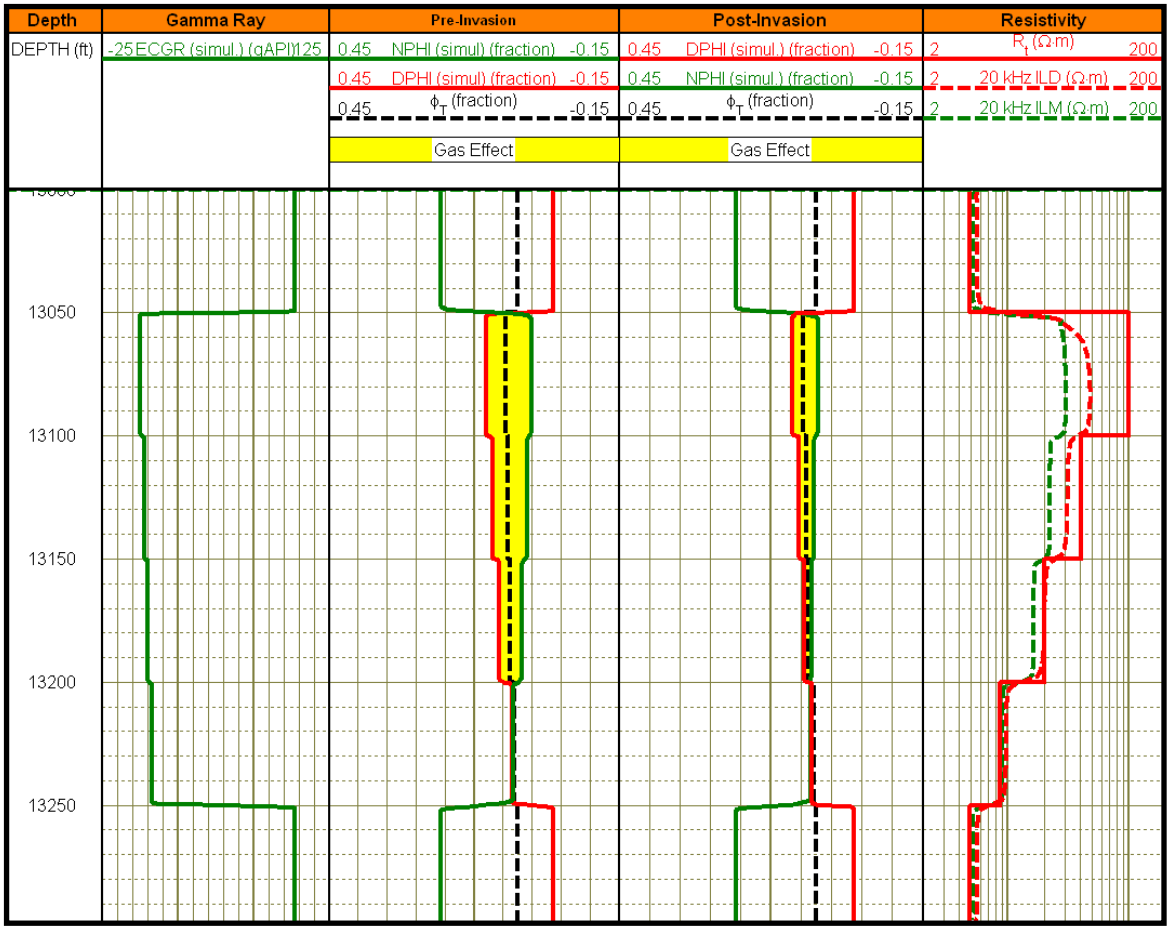


**Figure 1.7:** Synthetic case of mud-filtrate invasion impacting neutron porosity, density porosity, and resistivity logs. Track 1: depth; Track 2: gamma ray; Track 3: neutron porosity and bulk density before invasion; Track 4: neutron porosity and bulk density after invasion; Track 5: resistivity logs.

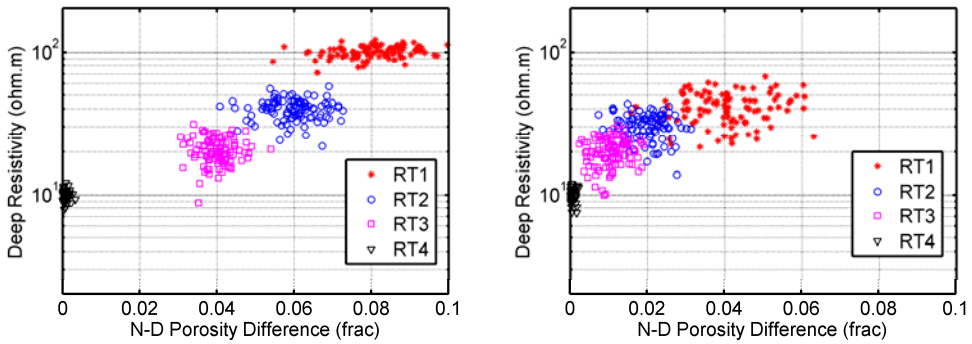


**Figure 1.8:** Clusters of different rock types before invasion (left panel) and after invasion (right panel) presented in a crossplot of deep resistivity and neutron-density porosity difference. RT1-4 indicates four different rock types.

**Fallacy No. 2: Rock classification with well logs without correction of fluid effects.**

It is common to have different fluid types across a hydraulically connected reservoir. When fluid content changes from gas to oil or water, neutron porosity and bulk density logs change significantly. When the fluid changes from hydrocarbon to water, resistivity logs change accordingly. In capillary transition zones, the gradual change of resistivity logs due to water saturation change versus height also impacts rock classification. The North Sea field case shown in Fig. 1.5 is a good example. Using the same field example, we first classified rock types from abundant core samples and found that major rock types derived from core data remained the same across different fluid zones. Rock types were also determined from gamma-ray, neutron porosity, and bulk density logs by applying the *k*-means clustering method (Press et al., 2007). Well-log-derived rock types showed significant difference in the gas zone and oil zone. We then included resistivity logs in addition to previously used logs to derive rock types by applying the *k*-means clustering method. It was found that log-derived rock types in the water zone were different from those defined in the oil/gas zones.

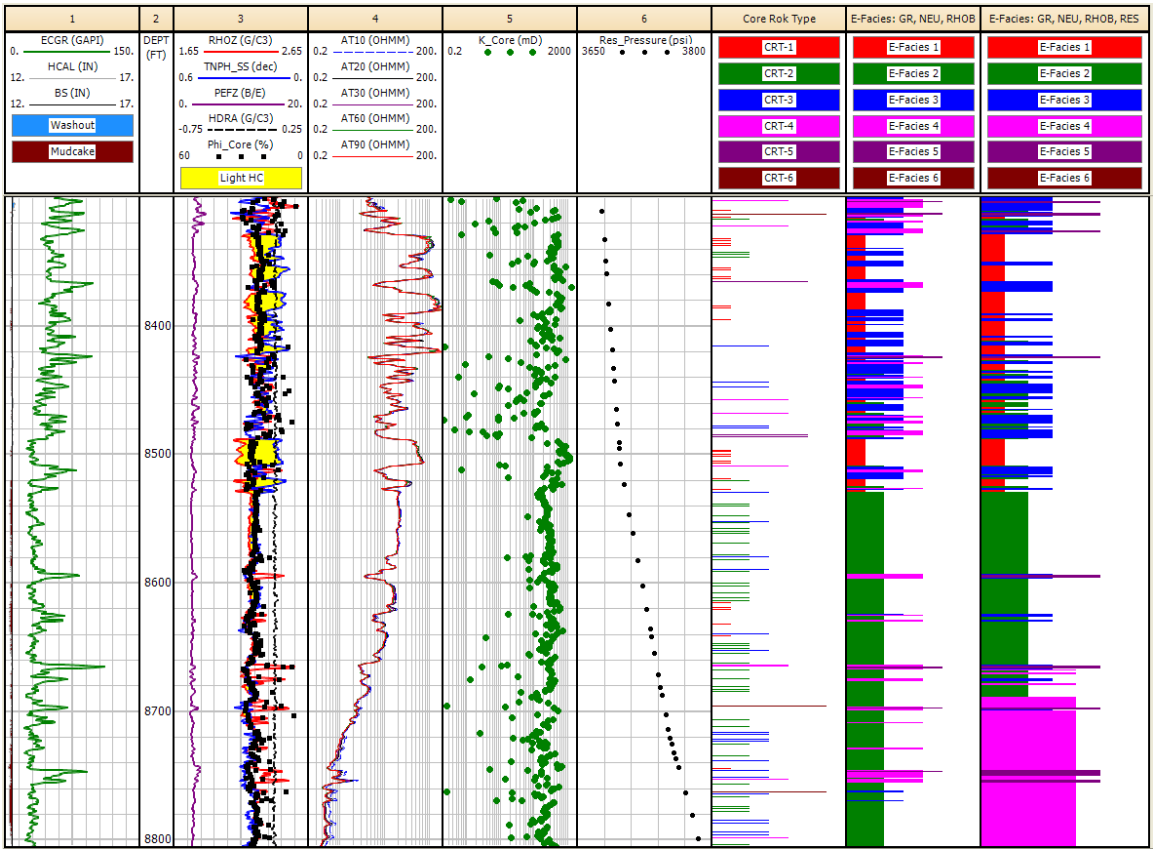


**Figure 1.9:** Example of fluid effects on log-based rock classification. Track 1: Gamma ray; Track 2: Depth; Track 3: PEF, neutron, and bulk density, core porosity; Track 4: Resistivity; Track 5: Core permeability; Track 6: Reservoir pressure; Track 7: Core-derived RQI rock types; Track 8: Electrofacies from clustering gamma ray, neutron, and density logs; Track 9: Electrofacies from clustering gamma ray, neutron, density, and resistivity logs.

**Fallacy No. 3: Supervised learning with core in thinly bedded or laminated zones.**

Another common approach used for rock typing is to use core data to calibrate or supervise log responses using various machine-learning algorithms. The assumption is that rock physical properties measured at the core and log scales are the same. This approach ignores the scale discrepancy between core data and well logs, thereby leading to misclassifications in thinly bedded or laminated zones. Figure 1.10 shows an example of a laminated turbidite field from the Gulf of Mexico. Core samples highlighted in the

red oval were plugged from thin sands in between shales, but they cannot be recognized from well logs due to the effects of shoulder beds. Core-supervised learning fails to identify those rock types in this case.

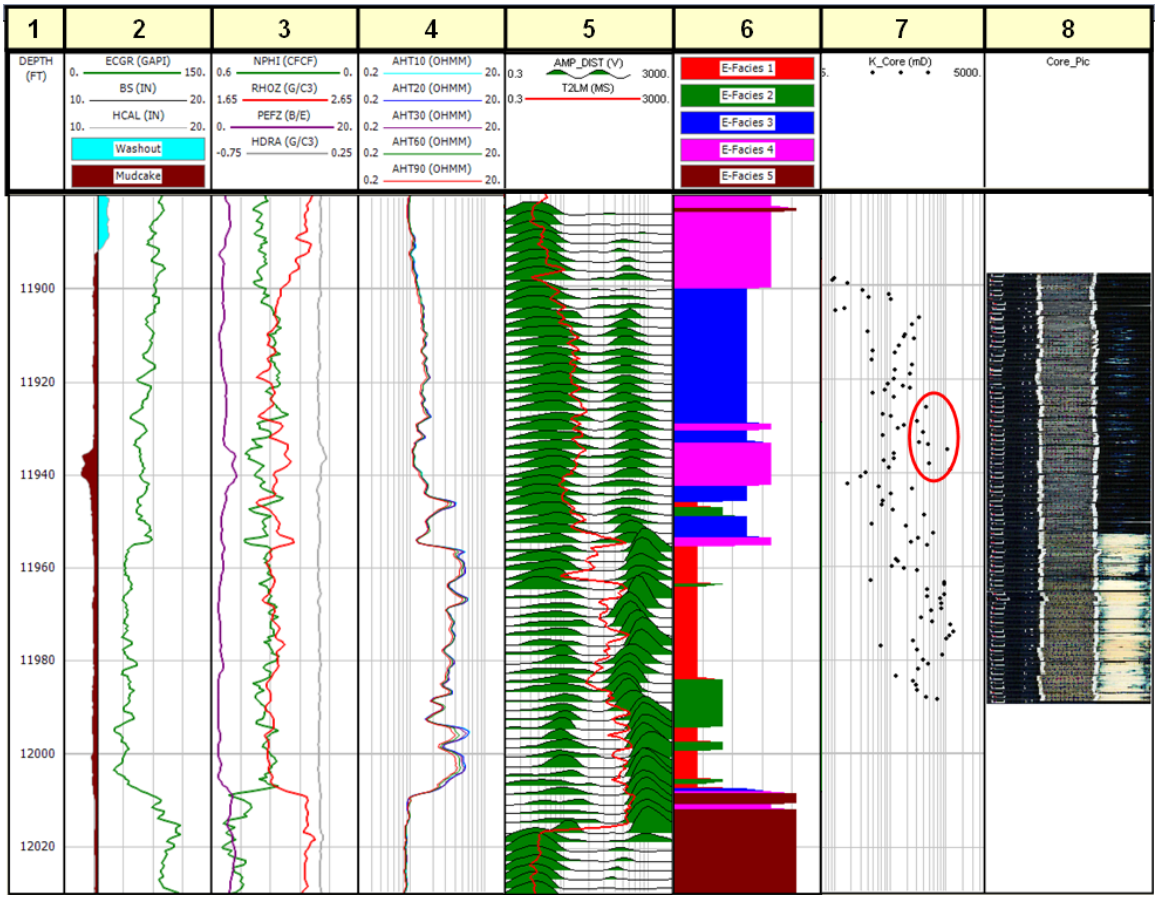


**Figure 1.10:** Example of core-supervised learning for rock typing in laminated sand-shale formations. Track 1: Depth; Track 2: Gamma ray; Track 3: PEF, neutron, and bulk density; Track 4: Resistivity; Track 5: NMR; Track 6: E-facies from gamma ray, neutron, density, resistivity, and NMR logs supervised by core data; Track 7: Core permeability; Track 8: Core images.

### 1.2.3 Correlating Petrophysical Rock Types with Geological Facies

The ultimate goal of rock classification is to associate petrophysical rock types with geological framework and reconcile with seismic facies so as to propagate rock-type

associated petrophysical properties into the reservoir model. The mission is impossible without understanding the cause-and-effect relationship between pore geometry and geological attributes of rocks such as grain size and bed thickness. Hence, it is necessary to investigate the sensitivities of well logs to those geological attributes and the associated pore geometries in the presence of different fluid saturation conditions resulting from either hydrocarbon migration or mud-filtrate invasion.

## 1.3 RESEARCH OBJECTIVES

This dissertation aims to integrate core data and well logs to enhance reservoir description by classifying reservoir rocks in a geologically and petrophysically consistent manner. The main objective is to investigate scientific approaches of utilizing rock data at different time and length scales to describe reservoir rock-fluid systems consistently. Well-log-based and core-calibrated petrophysical rock typing methods or workflows that circumvent the above-mentioned technical problems are the main deliverables. An important test is to transfer physical understanding of rock types from core data to well logs. The following is an itemized list of research objectives:

i. To develop new quantitative methods that derive analytical pore-size distribution functions from MICP data to characterize complex pore systems.

ii. To integrate multiple pore system attributes from (i) to define petrophysical dissimilarity between pore systems that improves petrophysical ranking of rock types.

iii. To understand the effect of pore geometry on the microscopic fluid distribution during two-phase fluid displacement and develop new methods to model relative permeability from MICP and NMR data.

iv. To probe the hidden petrophysical information from macroscopic fluid distributions in the vertical direction (due to migration on a geologic time scale) and the radial direction (due to mud-filtrate invasion on a drilling time scale) to quantify dynamic reservoir petrophysical properties and define reservoir flow capacity.

v. To develop a bottom-up Bayesian rock typing method based on an aggregation approach to efficiently test multiple working hypotheses against well logs to quantify uncertainty of rock types and their associated petrophysical properties.

vi. To develop a top-down rock typing workflow to characterize intermixed reservoir rock types from the flow unit or seismic scale all the way down to the pore scale based on rock class decomposition techniques.

vii. To investigate the correlations between petrophysical rock types and geological facies in typical siliciclastic reservoirs (deltaic or turbidite) for assisting stratigraphic reservoir modeling.

## 1.4 METHOD AND APPROACH OVERVIEW

Torres-Verdín (2012) proposed an integrated approach to achieve high-resolution reservoir description by closely integrating geology, petrophysics, and physics based on core data and well logs (Fig. 1.11).

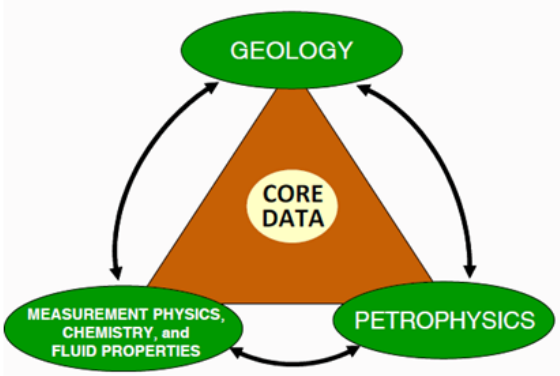


**Figure 1.11:** Torres-Verdín's (2012) reservoir description approach integrating geology, petrophysics, and physics based on log measurements and core-calibration.

This dissertation firmly adheres to Torres-Verdín's approach and employs diverse scientific and engineering methods from multiple disciplines including:

- Philosophy,
- Geology,
- Petrophysics,
- Physics,
- Mathematics, and
- Computer Science.

**Philosophy:** Philosophy is the guidance for thinking that leads this dissertation research. First of all, the rule of simplicity (or Occam's razor) is followed in selecting methods from multiple choices. Simple approaches are always used to test hypotheses and simple models are preferred to demonstrate the physics involved. Secondly, a "Yin-Yang" binary perspective is frequently adopted to describe the rock-fluid system. Binary pairs in this dissertation include: grains versus pores, big versus small pore (or throat) size modes, wetting versus non-wetting phases, etc. Thirdly, thinking across time and

space has been proved to be helpful in interpreting subsurface data regarding migration, production, and drilling in both vertical and horizontal directions. Last but not least, the difference between causation and correlation is emphasized when linking geology, petrophysics, and physics measurements.

**Geology:** Geology is the basis for petrophysical interpretation of core and log data because rocks are products of a series of depositional and diagenetic processes (Torres-Verdín, 2012). When interpreting well logs, earth scientists should pay particular attention to the sensitivity of logs to geological attributes such as grain size, bed thickness, and their variations in both vertical and horizontal directions. In addition, hydrocarbon migration provides direct petrophysical evidences for reservoir quality analysis.

**Petrophysics:** On the petrophysics side, this dissertation is firmly anchored on Archie's pore-size distribution for petrophysical rock classification (Fig. 1.1). The dissertation also resorts to many classic concepts, models, and tools developed by generations of scientists and engineers. An incomplete list includes the capillary tube model (Childs and Collis-George, 1950), Purcell's permeability model (1949), Leverett's *J*-function (1941), and Corey-Burdine's relative permeability model (Burdine, 1953). Pore network modeling is utilized to study fluid distribution at the microscopic level. Macroscopic fluid saturation and distribution in subsurface reservoirs are considered as petrophysical consequences of vertical hydrocarbon migration and radial mud-filtrate invasion, which give rise to different well log responses that can be decoded for rock classification.

**Physics:** Fast numerical log simulations are indispensible tools for testing hypotheses against well logs acquired in the field. Hou et al. (2006) and Wang et al. (2009) built accurate resistivity log simulators in 2D and 3D anisotropic, inhomogeneous

media over a wide range of frequencies. Mendoza et al. (2007) developed fast numerical algorithms that use spatial flux-scattering functions (FSF) obtained from the Monte Carlo method to simulate nuclear logs within seconds. Pour et al. (2011) implemented the mud-filtrate invasion simulators based on an equation-of-state formulation. This dissertation integrates all the above-mentioned simulation techniques to interpret well logs for different rock types.

**Mathematics:** The mathematical methods used in this dissertation include inversion techniques (Aster et al., 2005) and multi-variate analysis such as classification and clustering algorithms (Bishop et al., 1975; Press et al., 2007).

**Computer Science:** Computer programs are implemented in this dissertation for realizing all numerical algorithms. The Matlab[2] package is used for programming and visualizing plots. In addition, the software package UTAPWeLS[3] provides an efficient tool for analyzing logging tool responses across different rock types (Voss et al., 2009).

## 1.5 DISSERTATION OUTLINE

This dissertation consists of nine chapters including the present introductory chapter and a final conclusion and summary chapter. The main body of this dissertation research is divided into three parts.

The first part, chapters 2, 3, and 4, discusses petrophysical rock description based on core- and pore-level perspectives. Chapter 2 introduces a bimodal log-normal density function to model pore-size distributions from MICP data analytically. Correlations between the estimated Gaussian attributes and various petrophysical properties are investigated for petrophysical modeling and rock typing. Chapter 3 integrates all the Gaussian parameters defined in Chapter 2 to quantify petrophysical dissimilarity or

[2] Trademark of the Mathworks

[3] The University of Texas at Austin's Petrophysics and Well Log Simulator

orthogonality between pore systems. We develop a new method that consistently identifies and ranks rock classes in various petrophysical data domains, including porosity-permeability trend, pore-size distribution, MICP, and core NMR $T_2$ spectra. Chapter 4 investigates fluid distribution and phase connectivity in rock pore system by constructing a pore network model constrained by NMR and MICP data. The microscopic understanding of fluid distribution provides important aids to subsurface log interpretation in reservoirs that straddle capillary transition zones and are subject to mud-filtrate invasion.

The second part, chapters 5 and 6, probes the underlying petrophysical information from fluid flow in vertical migration at a geologic time scale and radial mud-filtrate invasion at a drilling time scale. Relevant log attributes are captured to quantify dynamic reservoir petrophysical properties and define reservoir flow capacity. Chapter 5 describes the implication of reservoir capillary transition on saturation-height relations for different hydraulic rock types. A new log attribute considering both water saturation and reservoir column height is proposed to be included in hydraulic rock typing. The method finds important applications in deepwater turbidite oil reservoirs from the Gulf of Mexico and the North Sea. Chapter 6 examines the hidden information in mud-filtrate invasion behavior for more accurate rock classification. A new concept, referred to as invasion facies, is advanced to link static and dynamic petrophysical rock properties for rock typing. The application of this new method in a carbonate field significantly enhances permeability prediction when compared to conventional methods.

The third part is composed of chapters 7 and 8, which introduces integrative petrophysical workflows based on rock classification in thinly bedded and heterogeneous reservoirs. Chapter 7 documents a bottom-up reservoir characterization workflow utilizing fast numerical log simulation techniques and a Bayesian hypothesis testing

approach to quantify uncertainty of rock types and the associated petrophysical properties. The method improves the correlation between core-measured and log-predicted permeability by 16% when compared to conventional methods. Chapter 8 introduces a top-down reservoir characterization workflow based on multi-scale orthogonal rock class decomposition. It is particularly useful in describing heterogeneous reservoirs where different rock types intermix at the sub-foot scale. The new method successfully predicts cumulative flow profiles of a tight-gas sandstone reservoir.

Chapter 9 summarizes the technical achievements and concludes the learnings about rock typing stemming from this dissertation research. Additionally, recommendations regarding future research possibilities on rock typing are given in this final chapter.

Table 1.2 lists the topic, field, data, and the main applications for each main-body chapter.

**Table 1.2** Summary of the topic, field, data, and the main applications for each main-body chapter.

| Chapter | Topic | Field | Data | Applications |
|---|---|---|---|---|
| **2** | Mathematical description of complex pore systems | Hugoton Carbonate Gas Field, Kansas | Core porosity, permeability, MICP, relative permeability | Rock typing and relative permeability modeling |
| **3** | Petrophysical orthogonality | Cotton Valley Tight-Gas Sand, East Texas | Core porosity, permeability, MICP, core NMR | Petrophysical ranking and relative permeability modeling |
| **4** | Pore network modeling of fluid distribution | Cotton Valley Tight-Gas Sand, East Texas | Core porosity, permeability, MICP, core NMR | Fluid distribution analysis and relative permeability modeling |
| **5** | Saturation-height and invasion consistent hydraulic rock typing | Deepwater Turbidite Oil Fields, Gulf of Mexico and North Sea | Core porosity, permeability, MICP, grain size, triple-combo well logs, reservoir pressure | Permeability prediction, saturation-height analysis, reservoir quality analysis and facies interpretation |
| **6** | Invasion facies analysis | Hugoton Carbonate Gas Field, Kansas | Core porosity, permeability, MICP, relative permeability, and triple-combo well logs | Permeability prediction and dynamic petrophysical modeling |
| **7** | Bayesian rock typing | Deepwater Deltaic Gas Field, Trinidad | Core porosity, permeability, grain size, MICP, triple-combo well logs | Permeability prediction, uncertainty quantification, and facies interpretation |
| **8** | Multi-scale orthogonal rock class decomposition | Bossier Tight Gas Sand, East Texas | Core porosity, permeability, MICP, core NMR, triple-combo well logs, NMR log | Petrophysical upscaling and production forecasting |

## 1.6 LIST OF PUBLICATIONS

Below is a list of journal and conference papers that have been published or submitted for review as a result of my dissertation research.

### 1.6.1 Refereed Journal Publications

Xu, C., Torres-Verdín, C., 2013. Pore system characterization and petrophysical rock classification using a bimodal Gaussian density function. Mathematical Geosciences, 45(6): 753-771 (DOI: 10.1007/s11004-013-9473-2).

Xu, C., and Torres-Verdín, C., 2013. Petrophysical rock classification in the Cotton Valley tight gas sand reservoir with a clustering pore-system orthogonality matrix. SEG Interpretation Journal (under review).

Xu, C., and Torres-Verdín, C., 2013. Quantifying fluid distribution and phase connectivity with a simple 3D cubic pore network model constrained by NMR and MICP. Computers & Geosciences (accepted).

Xu, C., Torres-Verdín, C., and Gao, S., 2013. Interpretation of hydraulic rock types with resistivity logs in Tertiary deepwater turbidite reservoirs: pore-scale modeling verified with field observations in the Gulf of Mexico, U.S. SEG Interpretation Journal (accepted).

Xu, C., and Torres-Verdín, C., 2013. Rock-type based analysis of hydration water effect on capillary pressure in shaly sand formations: a case study in a deltaic gas reservoir, offshore Trinidad. Journal of Petroleum Science and Engineering (under review).

Xu, C., Heidari, Z., Torres-Verdín, C., 2013. Rock classification connecting static and dynamic petrophysical properties with core measurements and conventional logs: a case study of a mixed clastic-carbonate reservoir in the Anadarko Basin. SPE Reservoir Evaluation and Engineering (under review).

Xu, C., and Torres-Verdín, C., 2013. Water saturation – irreducible or not: the key to reliable hydraulic rock typing in reservoirs straddling multiple capillary windows. SPE Reservoir Evaluation and Engineering (under review).

Xu, C., Torres-Verdín, C., and Steel, R.J., 2013. Geological attributes from well logs: relating rock types to depositional facies in deepwater turbidite reservoirs. SPE Reservoir Evaluation and Engineering (under review).

### 1.6.2 Refereed Conference Proceedings

Xu, C., Torres-Verdín, C., and Steel, R.J., 2012. Facies interpretation based on quantitative analysis of grain size and bed thickness from well logs in deepwater

turbidite reservoirs. AAPG Annual Convention and Exhibition, Long Beach, California, April 22 - 25.

Xu, C., and Torres-Verdín, C., 2012. Saturation-height and invasion consistent hydraulic rock typing using multi-well conventional logs. Paper KK presented at SPWLA 53rd Annual Logging Symposium, Cartagena, Colombia, June 16-20.

Xu, C., Heidari, Z., and Torres-Verdín, C., 2012. Rock classification in carbonate reservoirs based on static and dynamic petrophysical properties estimated from conventional well logs. Paper 159991 presented at SPE Annual Technical Conference and Exhibition, San Antonio, Texas, October 5-9.

Xu, C., Torres-Verdín, C., Ma, J., and Li, W., 2012. Fluid substitution analysis to correct borehole geophysical measurements acquired in gas-bearing formations invaded by oil-base mud. 83rd SEG Annual Meeting, Las Vegas, Nevada, Nov 4-9.

Xu, C., and Torres-Verdín, C., 2013. Multi-scale orthogonal rock class decomposition: top-down reservoir characterization integrating logs and core in tight gas sands. Paper FF presented at SPWLA 54th Annual Logging Symposium, New Orleans, Louisiana, June 22-26.

Xu, C., Yang, Q., and Torres-Verdín, C., 2013. Bayesian hypothesis testing: using fast well-log forward modeling to validate petrophysical rock typing and to quantify uncertainty in deepwater reservoirs. Paper FFFF presented at 2013 54th SPWLA Annual Symposium, New Orleans, Louisiana, June 22-26.

Xu, C., Torres-Verdín, C., Yang, Q., and Diniz-Ferreira, E., 2013. Water saturation – irreducible or not: the key to reliable hydraulic rock typing in reservoirs straddling multiple capillary windows. Paper 166082 presented at SPE Annual Technical Conference and Exhibition, New Orleans, Louisiana, September 30-October 2.

Xu, C., Torres-Verdín, C., and Steel, R.J., 2013. Geological attributes from well logs: relating rock types to depositional facies in deepwater turbidite reservoirs. Paper 166178 presented at SPE Annual Technical Conference and Exhibition, New Orleans, Louisiana, September 30-October 2.

Xu, C., and Torres-Verdín, C., 2013. Core-based petrophysical rock classification by quantifying pore-system orthogonality with a bimodal Gaussian density function. Paper SCA2013-079 presented at International Symposium of Society of Core Analysts. Napa Valley, California, September 16 – 19.

Xu, C., Torres-Verdín, C., and Gao, S., 2013. Electrical vs. hydraulic rock types in clastic reservoirs: pore-scale understanding verified with field observations in the Gulf of Mexico, U.S. 84th SEG Annual Meeting, Houston, Texas, September 22-27.

# Chapter 2: Pore-System Characterization and Petrophysical Rock Classification Using a Bimodal Gaussian Density Function

This chapter introduces a bimodal Gaussian density function to characterize pore-size distributions in terms of incremental pore volume fraction versus logarithmic pore-throat radius. An inverse problem is formulated and solved to reconstruct MICP curves by enforcing a bimodal Gaussian pore-size distribution. The bimodal Gaussian model generates six petrophysically interpretable attributes that provide a quantitative basis for petrophysical modeling and rock typing. Correlations between these attributes and their associated petrophysical properties are investigated to verify interpretations. Petrophysical modeling based on the bimodal Gaussian pore-size distribution with sufficient core data calibration predicts static and dynamic petrophysical properties that are in agreement with laboratory core measurements. The quantitative pore-system description underlies a new petrophysical rock typing method that combines all relevant pore-system attributes. Verification of the method was performed with field data from two key wells in the Hugoton carbonate gas field, Kansas.

## 2.1 INTRODUCTION

Pore-size distribution relates all petrophysical properties, which is the central theme in petrophysical characterization of reservoir rocks (Archie, 1950 and 1952). Different forms of pore-size distribution from various data sources have been documented and compared in the existing technical literature (Basan et al., 1997). In this chapter, pore-size distribution refers to incremental pore volume fraction versus logarithmic pore-throat radius (denoted as $\log R$), which can be derived from MICP curves (Peters, 2012). Several types of density functions have been used to model pore-size distributions or related petrophysical measurements analytically. The first type of

density function is that of Thomeer (1960), who invoked hyperbolic functions to fit MICP curves. This procedure implicitly makes use of the derivative of Thomeer's hyperbolas (referred to as Thomeer's derivative) as the pore-size distribution function. Several authors (Clerke, 2009; Gao et al., 2011) reported the use of multiple Thomeer's hyperbolas to characterize complex carbonate rock pore systems. The use of Thomeer's parameters for saturation-height modeling, upscaling, and rock typing have been reported elsewhere (Thomeer, 1960; Clerke et al., 2008; Buiting, 2011). In addition, Hidajat et al. (2004) used a trimodal Weibull distribution to fit nuclear magnetic resonance (NMR) $T_2$ spectra, which is closely correlated to the pore-body size distribution when the rock is fully water saturated. Similarly, Genty et al. (2007) fitted NMR $T_2$ spectra using up to three Gaussian components. In fact, Gaussian (or log-normal) density functions have been routinely used for modeling pore-size and grain-size distributions in the open technical literature (Spencer, 1963; Nimmo, 2004). The parameters associated with a Gaussian density function relate directly and intuitively to pore-system attributes. However, only a relatively small body of work has been documented on the interpretation and petrophysical meaning of these Gaussian attributes and on their use for petrophysical modeling and rock classification.

In this chapter, an inverse problem is formulated to fit MICP curves based on a bimodal Gaussian pore-size distribution model. A set of six attributes included with each bimodal Gaussian density function is estimated and interpreted for petrophysical meaning and subsequently used in petrophysical modeling to predict rock petrophysical properties. Results from fitting MICP data from two key wells in the Hugoton carbonate gas field confirm that bimodal Gaussian density functions are appropriate to describe complex pore systems. A new petrophysical rock typing method that combines all Gaussian attributes is introduced after fitting MICP data, which provides better ranking of rock

types and shows petrophysical consistency among all static and dynamic properties. The main advantage of this new rock typing method is that it simultaneously considers pore volume, major pore throat radius, and pore-throat size uniformity as input attributes for petrophysical classification, whereas existing core-based petrophysical rock typing methods tend to rely solely on hydraulic radius to rank reservoir rocks.

## 2.2 PORE-SYSTEM CHARACTERIZATION WITH A BIMODAL GAUSSIAN DENSITY FUNCTION

Pore-throat size is empirically characterized on a logarithmic scale due to its large variability across several orders of magnitude. Therefore, all Gaussian density functions in this dissertation treat the distribution of pore-throat size on a logarithmic scale (i.e., log-normal distribution).

### 2.2.1 Bimodal Gaussian Pore-Size Distribution

A bimodal Gaussian density function is expressed as

$$p(\log R; w_1, \log \mu_1, \log \sigma_1; w_2, \log \mu_2, \log \sigma_2) = w_1 \frac{1}{\sqrt{2\pi}\log \sigma_1} e^{-\frac{(\log R - \log \mu_1)^2}{2(\log \sigma_1)^2}} + w_2 \frac{1}{\sqrt{2\pi}\log \sigma_2} e^{-\frac{(\log R - \log \mu_2)^2}{2(\log \sigma_2)^2}}, \quad (2.1)$$

where $R$ is pore-throat radius in $\mu$m, $w_1$ and $w_2$ are weighting coefficients for each Gaussian mode, $\log\mu_1$ and $\log\mu_2$ are the mean values of logarithmic pore-throat radius, and $\log\sigma_1$ and $\log\sigma_2$ are the corresponding standard deviations of logarithmic pore-throat radius. The following constraints apply to the Gaussian attributes included in Eq. (2.1):

$$w_1 + w_2 = 1.0, \text{ and } 0 < w_{1,\,2} < 1.0. \quad (2.2)$$

The corresponding cumulative distribution function (CDF) is given by

$$P(\log R; w_1, \log \mu_1, \log \sigma_1; w_2, \log \mu_2, \log \sigma_2) =$$
$$\frac{w_1}{2}[1 + erf(\frac{\log R - \log \mu_1}{\sqrt{2(\log \sigma_1)^2}})] + \frac{w_2}{2}[1 + erf(\frac{\log R - \log \mu_2}{\sqrt{2(\log \sigma_2)^2}})], \quad (2.3)$$

where *erf* function is the Gaussian error function, given by

$$erf(z) = \frac{2}{\sqrt{\pi}} \int_0^z e^{-t^2} dt \,. \quad (2.4)$$

Figure 2.1 shows a typical bimodal Gaussian density function and its corresponding CDF. Overlapping of two independent Gaussian modes of pore-size distribution is commonly observed with experimental data.

### 2.2.2 Petrophysical Interpretation of Gaussian Attributes and CDF

As emphasized by Eq. (2.1), a bimodal Gaussian density function includes six attributes to describe a pore-size distribution. Each attribute has petrophysical implications interpreted as follows:

$w_1$: fraction of pore volume connected by large pore-throat sizes where most residual non-wetting phase preferentially resides during imbibition (Handy and Datta, 1966; Mohanty and Salter, 1982). Flow capacity or permeability of reservoir rocks is dominantly controlled by this fraction of pore volume and the associated pore-throat radius ($\mu_1$).

$w_2$: fraction of pore volume connected by small pore-throat sizes where most irreducible wetting-phase preferentially resides during drainage; therefore, its contribution to fluid flow is marginal.

$\log\mu_1$ and $\log\mu_2$: mean values of large and small logarithmic pore-throat radius modes, respectively; larger values indicate larger fluid-flow conduits

as well as higher hydraulic conductivity; $\mu_1$ is correlated with hydraulic radius.

$\log\sigma_1$ and $\log\sigma_2$: standard deviation of large and small pore-throat radius modes, which represents the uniformity of "capillary tube sizes" (Childs and Collis-George, 1950); a larger value indicates lower sorting of tube sizes and higher tortuosity of the pore network, thereby lower permeability given the same mean value of pore-throat radius and pore volume.

CDF: capillary pressure in the "bundle-of-capillary-tubes" model, according to Laplace's equation, is given by

$$P_c = \frac{2\Gamma|\cos\theta|}{R}, \tag{2.5}$$

where $R$ is pore-throat radius, $\Gamma$ is interfacial tension, and $\theta$ is contact angle. For the CDF shown in Fig. 2.1, pore-throat radius on the x-axis can be transformed to capillary pressure using Eq. (2.5), whereas the y-axis is equivalent to wetting-phase saturation. Therefore, the CDF can be interpreted as a standard drainage capillary pressure curve.

## 2.3 Derivation of the Bimodal Gaussian Pore-Size Distribution from MICP Data

Two methods are used to estimate a bimodal Gaussian pore-size distribution from MICP data. The first (or differentiation) method derives a pore-size distribution by differentiating $S_w$ (wetting-phase saturation) with respect to log$R$ from MICP data and then decomposes the distribution into two Gaussian components using a Gaussian

mixture model algorithm (Press et al., 2007). The second (or inversion) method solves an inverse problem to estimate a bimodal Gaussian pore-size distribution by minimizing the quadratic residual between the modeled $S_w$ and the measured $S_w$ at all lab-used capillary pressure points (see Appendix A for details of the formulation). In practice, it is often difficult to obtain a smooth pore-size distribution from the differentiation method due to both limited number of measurement points and noisy data. Therefore, the inversion method is preferred in this dissertation to provide stable and smooth results. Figures 2.2 and 2.3 show the workflows of the differentiation and inversion methods, respectively. Figures 2.4 and 2.5 compare results obtained when applying the two methods to an example of MICP data from the Hugoton gas field.

## 2.4 FIELD CASE: HUGOTON GAS FIELD, KANSAS

The Hugoton field in Kansas is one of the largest conventional gas fields in North America. It has cumulatively produced more than 23 trillion cubic feet of gas during the past 70 years (Olson et al., 1997). Gas production originates mainly from the Lower Permian Chase and Council Grove Groups. The reservoir is divided into 13 stratigraphic intervals that have complex lithofacies spreading from continental and marine siltstones to sandstones, mudstone to grainstone limestones, fine- to medium-crystalline dolomites, and phylloid algal bafflestones (Dubois et al., 2006). Consequently, existing rock pore systems are extremely complex due to both depositional control and diagenetic overprints.

Routine core porosity and permeability measurements were acquired from more than 200 core samples (Fig. 2.6) in two key wells (API No. 15-189-20657 and 15-055-21045). In addition, MICP curves measured from 33 core samples were available for this study (Fig. 2.7a), among which 13 core samples included measured primary drainage

relative permeability curves (Fig. 2.7b). Core data exhibit large variability in all petrophysical properties, which renders the petrophysical modeling and rock typing work very difficult (Dubois et al., 2006). Pore-size distributions are first modeled with bimodal Gaussian density functions for all core-measured MICP curves. The correlation between petrophysical properties (permeability, irreducible water saturation, and relative permeability end points) and the Gaussian attributes set is then studied to verify the petrophysical interpretation. Based on these Gaussian attributes, a new petrophysical rock typing method is proposed to classify complex carbonate rocks for reservoir characterization studies.

### 2.4.1 Pore-Size Distribution Modeling

The inversion method was applied to derive bimodal Gaussian pore-size distributions from 33 MICP curves. Appendix B summarizes the corresponding results. Histograms of the six Gaussian attributes (Fig. 2.8) indicate that rocks exhibit wide variability in all petrophysical properties. It is observed that the standard deviation of the large pore-throat size mode is much smaller than those of the small pore-throat size mode, thereby suggesting that most rocks in this study have a narrowly distributed dominant pore-throat radius.

### 2.4.2 Absolute Permeability Prediction (*k*)

Absolute permeability is mainly controlled by the large pore-throat size mode. Figure 2.9 shows the correlations between permeability and attributes of the large pore-throat size mode. Positive correlation with permeability is observed for the pore volume (Fig. 2.9a) and the mean pore-throat size (Fig. 2.9b), whereas correlation between permeability and standard deviation is negative (Fig. 2.9c). The highest correlation is observed between permeability and mean value of large pore-throat size mode, with the

correlation coefficient (0.93) being much higher than between total porosity and permeability (0.77, as in Fig. 2.6), thereby suggesting reliability for predicting permeability once $\mu_1$ is known.

### 2.4.3 Irreducible Water Saturation ($S_{wirr}$) and Critical Water Saturation ($S_{wcrit}$)

In a water-wet rock, water preferentially resides in pores connected by the smallest pore throats during migration or drainage. Consequently, irreducible and critical water saturations are chiefly conditioned by the small pore-throat size mode. Below, we define irreducible and critical water saturations and study their correlations with Gaussian attributes separately.

**Irreducible water saturation from capillary pressure:** Water saturation that cannot be forced out of the pore system at a given threshold capillary pressure during drainage ($10^3$ psi in this study). This value is normally used to calculate total hydrocarbon volume in static reservoir modeling. Under such a definition, irreducible water has a high correlation with the mean value of the small pore-throat size mode (Fig. 2.10, $R^2 = -0.88$).

**Critical water saturation from relative permeability:** Water saturation (Marschall et al., 1995) at which the corresponding water phase relative permeability is below a threshold value ($10^{-4}$ frac in this study). The latter value is normally larger than irreducible water saturation derived from MICP. It is used to calculate water production in dynamic reservoir modeling. Under this definition, critical water saturation approximates the pore volume fraction associated with the small pore-throat size mode (Fig. 2.11, $R^2 = 0.613$).

### 2.4.4 Gas Relative Permeability End Point ($k_{rg}$ at $S_{wirr}$)

In a water-wet rock, gas is the non-wetting phase that preferentially resides in pores connected by large pore throats, whereas irreducible water remains in the smallest

pores. Consequently, permeability to gas is mainly controlled by the large pore throats. Figure 2.12 shows the correlation between gas relative permeability at critical water saturation and the mean value of large pore-throat size mode ($\mu_1$). The correlation coefficient is 0.715, which ensures a good prediction of the end point value of gas relative permeability in this particular reservoir when $\mu_1$ is known.

### 2.4.5 Residual Gas Saturation ($S_{gr}$) and End Point Water Relative Permeability ($k_{rw}$ at $S_{gr}$)

Because imbibition capillary pressure and relative permeability were not measured, residual gas saturation is unavailable in this study. Only some theoretical discussions are included to explain the possible relation between Gaussian attributes and residual gas saturation. In a water-wet rock, gas is the non-wetting phase that first invades pores connected by large pore throats during migration or drainage. Consequently, residual gas saturation is mainly determined by the attributes of the large pore-throat size mode when an imbibition cycle begins. Rocks of larger pore-throat radius (larger $\mu_1$) tend to exhibit less gas saturation trapped in the pore system. Given the same mean value of pore-throat radius, rocks of more uniform pore-size distribution (smaller $\sigma_1$) tend to exhibit less trapped gas (Mohanty and Salter, 1982). However, it is difficult to establish an analytical function between residual gas saturation and Gaussian attributes. An empirical model may be reliable with sufficient core calibration.

### 2.4.6 Model Drainage Relative Permeability from MICP Curve

With all previous correlations established, one can derive primary drainage relative permeability curves from the bimodal Gaussian pore-size distribution using Corey-Burdine's model (Burdine, 1953; Huang et al., 1997). Critical water saturation ($S_{wcrit}$) is calculated from its correlation with parameter $w_2$ (Fig. 2.11), whereas the end

point of gas relative permeability is predicted by its correlation with parameter $\mu_1$ (Fig. 2.12). The end point of water relative permeability is set to 1.0 and residual gas saturation ($S_{gr}$) is set to 0 in a primary drainage process. Burdine's wetting phase relative permeability is given by

$$k_{rw} = (S_w^*)^2 \frac{\int_0^{S_w^*} \frac{1}{(P_c)^2} dS_w^*}{\int_0^1 \frac{1}{(P_c)^2} dS_w^*} = (S_w^*)^2 \frac{\int_0^{S_w^*} R^2 dS_w^*}{\int_0^1 R^2 dS_w^*}, \tag{2.6}$$

and non-wetting phase relative permeability by

$$k_{rnw} = (1 - S_w^*)^2 \frac{\int_{S_w^*}^1 \frac{1}{(P_c)^2} dS_w^*}{\int_0^1 \frac{1}{(P_c)^2} dS_w^*} = (1 - S_w^*)^2 \frac{\int_{S_w^*}^1 R^2 dS_w^*}{\int_0^1 R^2 dS_w^*}, \tag{2.7}$$

where $P_c$ is capillary pressure and $R$ is the corresponding pore-throat radius as in Eq. (2.5); $S_w^*$ is normalized water saturation, defined as

$$S_w^* = \frac{S_w - S_{wirr}}{1 - S_{wirr} - S_{gr}}. \tag{2.8}$$

Based on MICP-derived bimodal Gaussian pore-size distribution, primary drainage relative permeability curves modeled with Burdine's equations agree well with core data (Fig. 2.13).

### 2.4.7 Petrophysical Rock Typing

The above Gaussian attributes contain rich petrophysical information, whereby they become suitable for petrophysical rock classification. Multi-dimensional *k*-means clustering analysis (Press et al., 2007) was performed on the six Gaussian attributes and classified the 33 samples into four rock types. Figure 2.14a shows that rock types rank well in the porosity and permeability crossplot, with their MICP data also consistently classified by rock type (Fig. 2.14b). With the same rock type information, the 13 primary

drainage relative permeability curves are plotted in Fig. 2.15. For rock types I, II, and III, reservoir quality decreases as rock type number increases. Accordingly, critical water saturation increases and, on average, the end point value of gas relative permeability decreases. Rock type IV is mostly non-reservoir rock that acts as baffle or seal in a reservoir. The only relative permeability curve available for this rock type (Fig. 2.15d) is from a special trimodal-pore-sized rock, which has a similar large pore-throat size mode as rock type II and a similar small pore-throat size mode as rock type IV. Consequently, this rock sample exhibits some flow capacity, but it lacks significant initial gas saturation under reservoir capillary pressure conditions. Because of the above results, we did not construct a separate rock type for this particular sample, but still classified it as rock type IV.

## 2.5 CONCLUSIONS

Bimodal Gaussian density function is a useful analytical tool to describe complex pore systems. Gaussian attributes included in this model have interpretable petrophysical meaning, which can be quantitatively used for petrophysical modeling and rock typing. Verification studies in the Hugoton gas field yielded the following petrophysical interpretations:

1) Absolute permeability is mainly controlled by the large pore-throat size mode. It is positively correlated with mean pore-throat radius and the associated pore volume while negatively correlated with standard deviation.
2) Irreducible or critical water saturation is mainly controlled by the small pore-throat size mode. Both are correlated with the mean value of small pore-throat size mode and the associated pore volume fraction.

3) The end point value for gas relative permeability at critical water saturation is mainly controlled by the large pore-throat size mode, especially the mean value.

Moderate to high correlations were observed between Gaussian attributes and various petrophysical properties. Therefore, it is possible to model several static and dynamic petrophysical properties (irreducible and critical water saturation, absolute permeability, drainage relative permeability) based on a bimodal Gaussian density function. Given sufficient core calibration, pore systems in reservoir rocks can be fully characterized by a set of six Gaussian attributes that predict consistent petrophysical properties for subsequent reservoir characterization studies. Petrophysical rock typing based on Gaussian attributes provides reliable ranking of reservoir quality and simplifies reservoir modeling by enforcing a consistent petrophysical description based on pore geometry. However, the classification method proposed in this chapter still considers the six Gaussian attributes as individual input. More advanced classification methods that integrate all six Gaussian attributes to define petrophysical dissimilarity are necessary for future implementation.

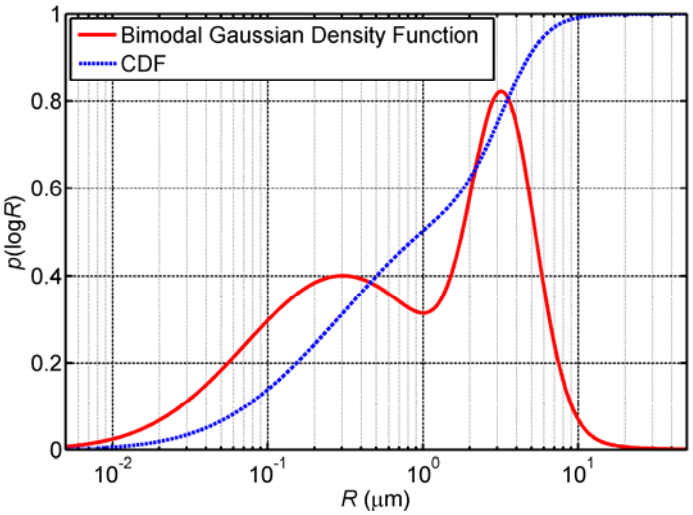


**Figure 2.1:** Example of a bimodal Gaussian density function and corresponding CDF.

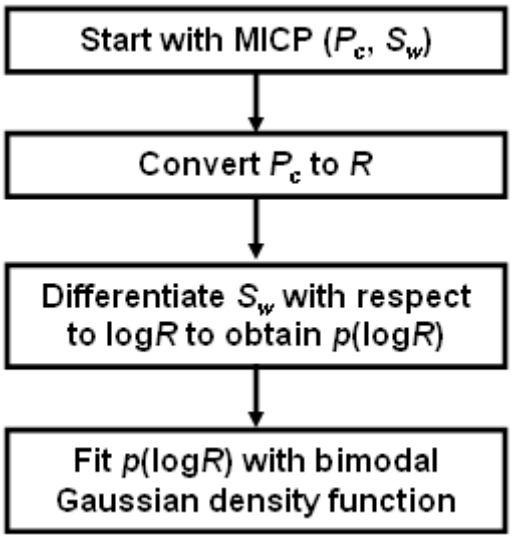


**Figure 2.2:** Workflow used to derive a bimodal Gaussian pore-size distribution by differentiating $S_w$ with respect to log$R$ and then fitting the results with a Gaussian mixture model (Press et al., 2007).

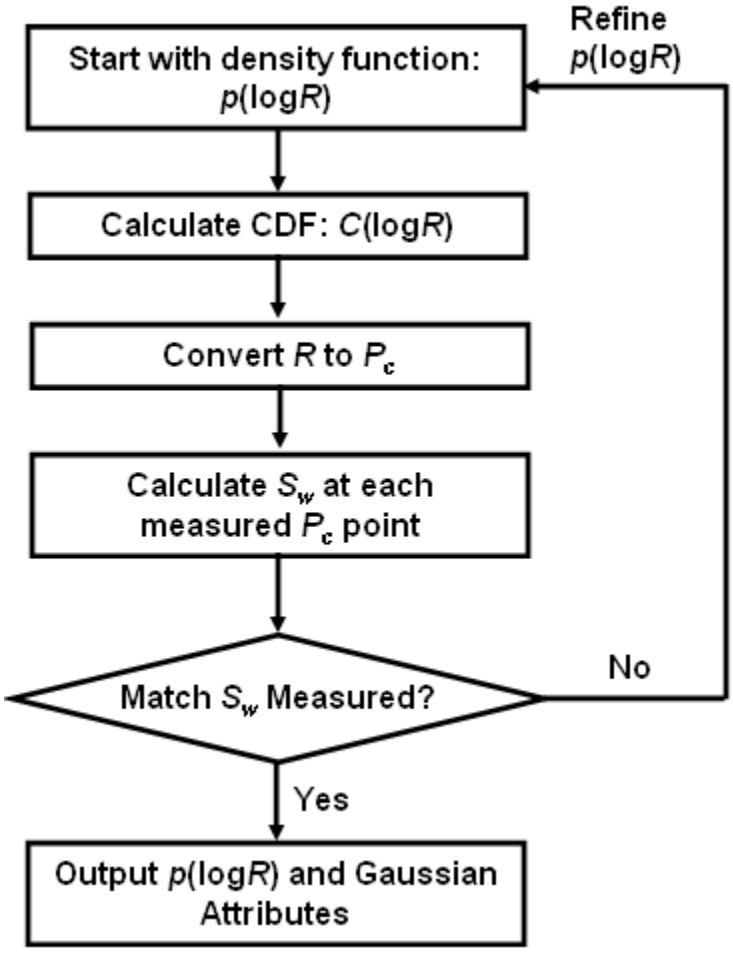


**Figure 2.3:** Workflow used to derive a bimodal Gaussian pore-size distribution by iteratively matching MICP data using inversion.

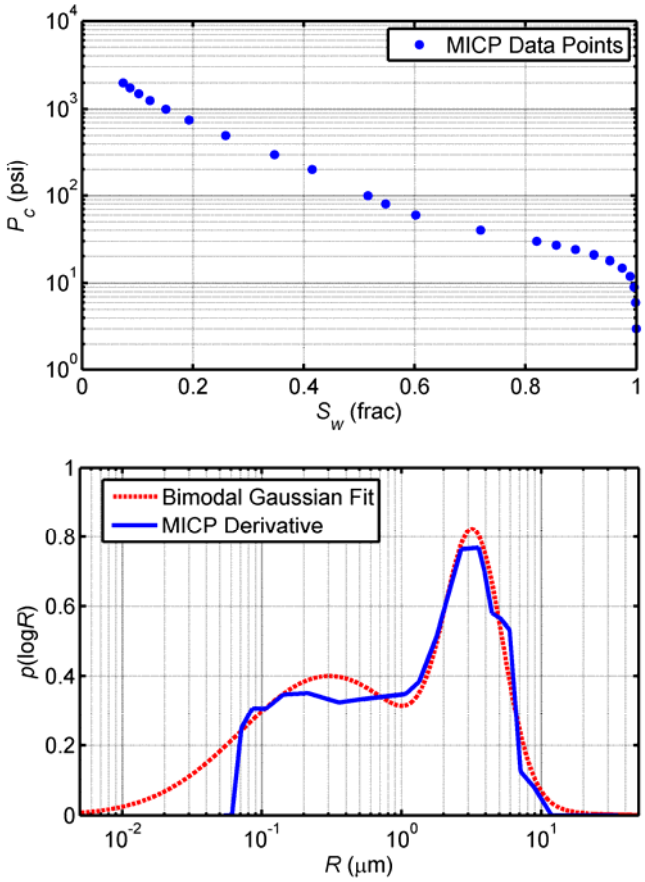


**Figure 2.4:** Example of derivation of a bimodal Gaussian pore-size distribution from MICP data using the differentiation method. Differentiation of experimental data is commonly noisy (Peters, 2012).

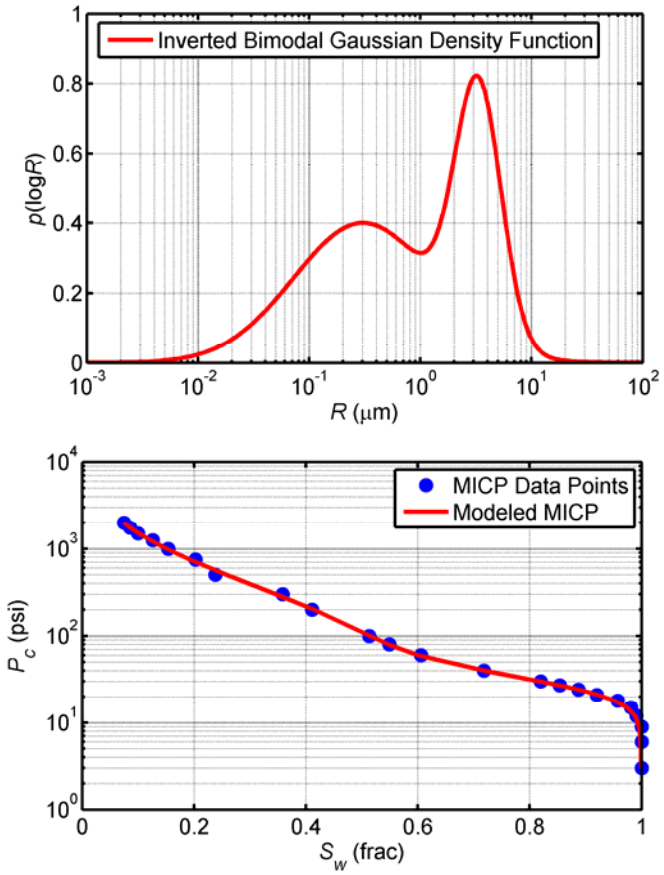


**Figure 2.5:** Example of the derivation of a bimodal Gaussian pore-size distribution from MICP using the inversion method (Appendix A).

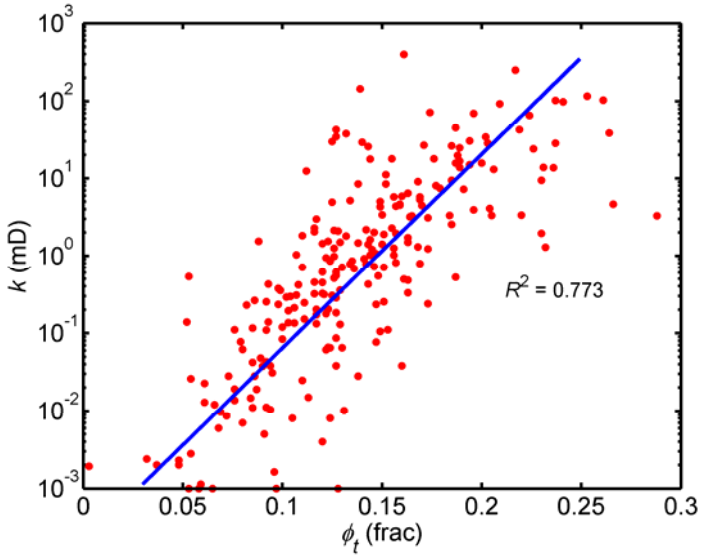


**Figure 2.6:** Crossplot of total porosity and permeability. Large uncertainty is associated with permeability modeling based on porosity-permeability correlation.

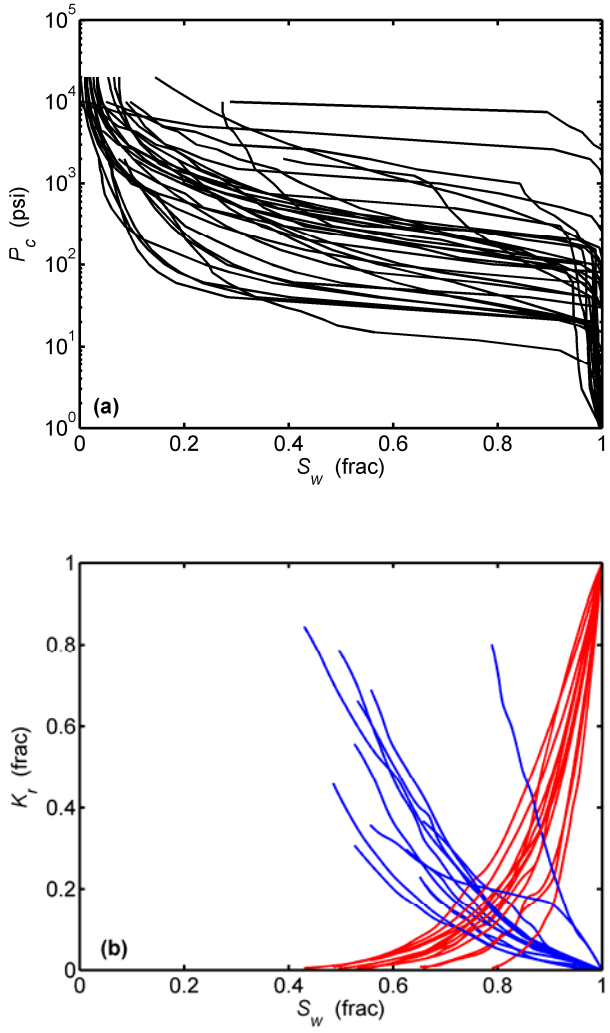


**Figure 2.7:** **(a)** Unclassified MICP capillary pressure curves from 33 core samples, and **(b)** primary drainage relative permeability ($S_{gr} = 0$) curves from 13 core samples acquired in the Hugoton gas field.

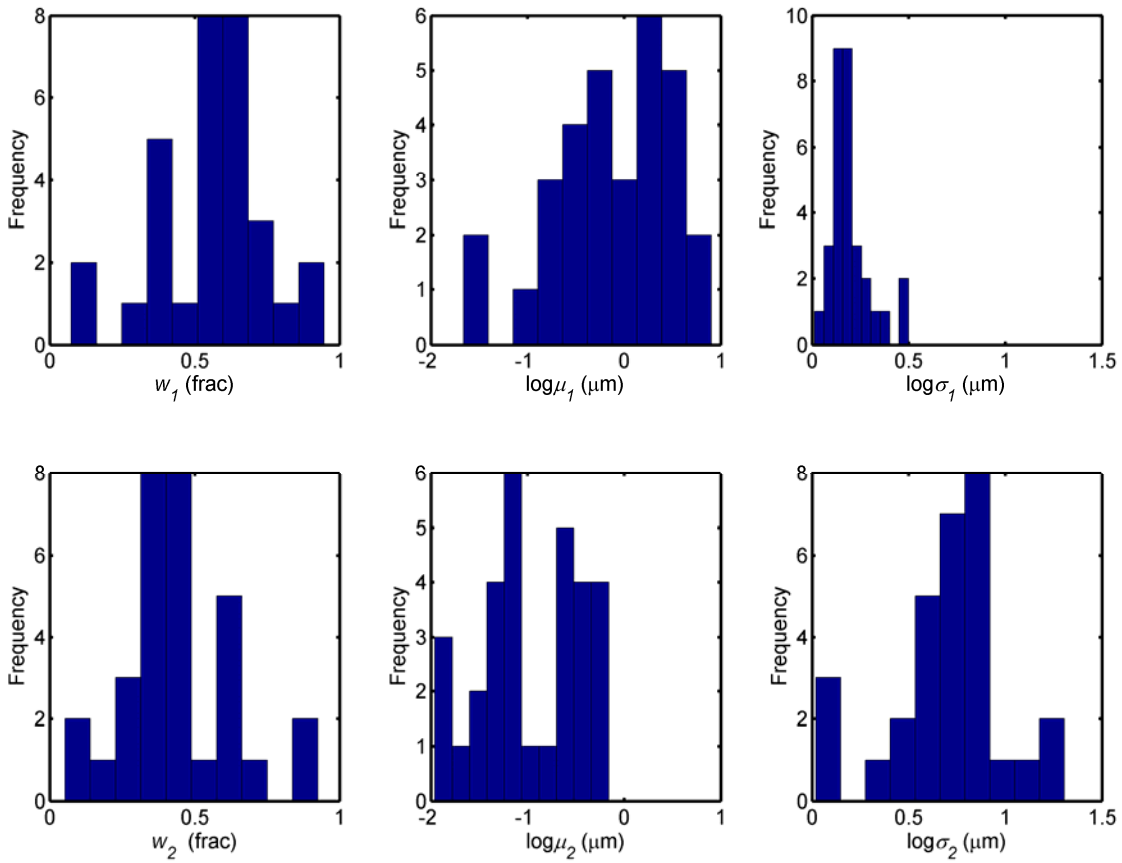


**Figure 2.8:** Histograms of all Gaussian attributes. Upper and lower panels show the histograms for large and small pore-throat size modes, respectively.

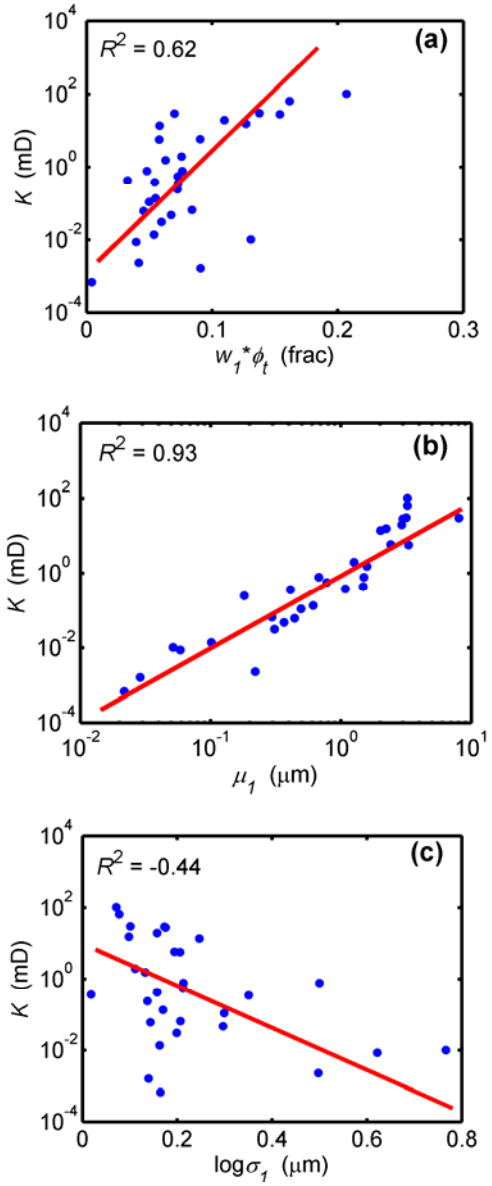


**Figure 2.9:** Correlation between permeability and Gaussian attributes for the large pore-throat size mode: **(a)** pore volume, **(b)** mean value, and **(c)** standard deviation.

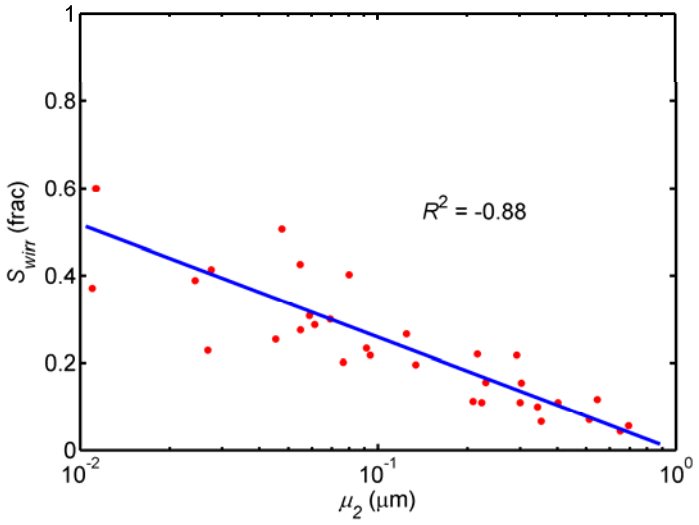


**Figure 2.10:** Correlation between irreducible water saturation (derived from MICP with cutoff $P_c$ = 1000 psi) and mean value of the small pore-throat size mode.

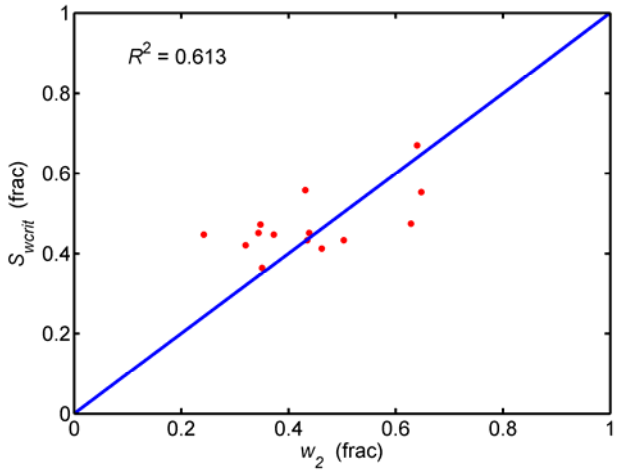


**Figure 2.11:** Correlation between critical water saturation derived from relative permeability and pore volume fraction of the small pore-throat size mode. The blue line identifies the $y = x$ line.

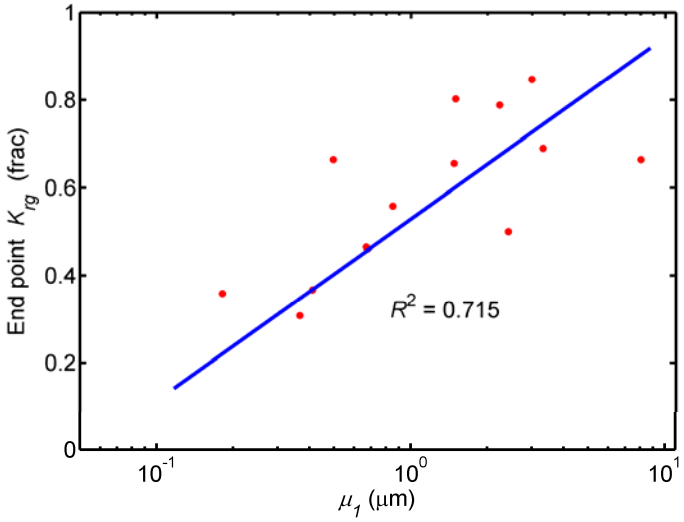


**Figure 2.12:** Correlation between the end point value of gas relative permeability at critical water saturation and mean value of the large pore-throat size mode.

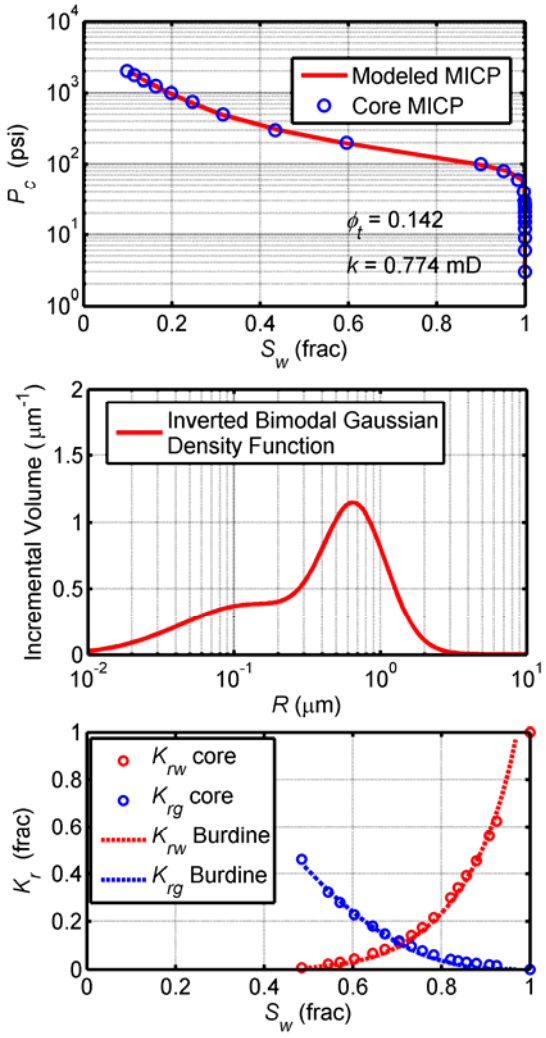


**Figure 2.13:** Modeled primary drainage capillary pressure curves from the bimodal Gaussian pore-size distribution data using Corey-Burdine's model. The end point of water relative permeability is set to 1.0 and residual gas saturation ($S_{gr}$) is set to 0.

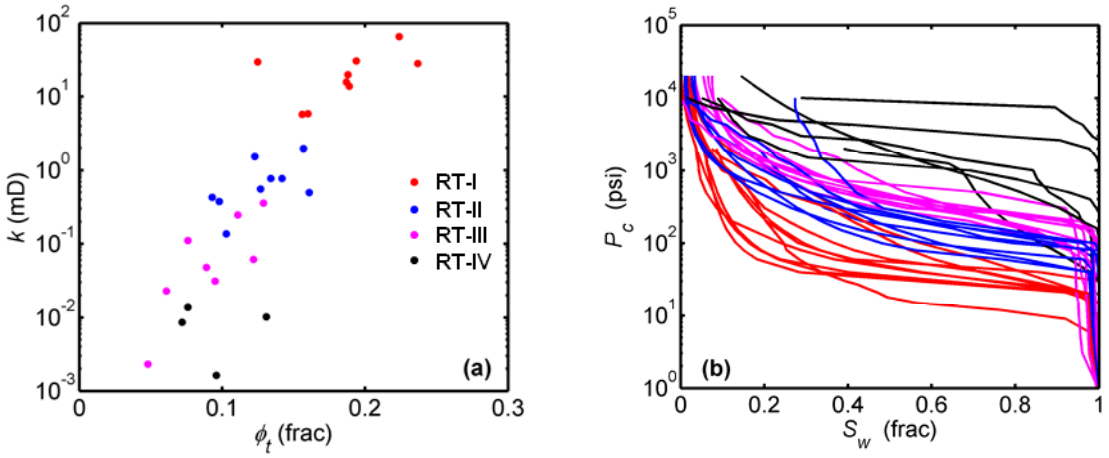


**Figure 2.14: (a)** Porosity-permeability crossplot ranked with rock types, and **(b)** MICP data ranked with rock types.

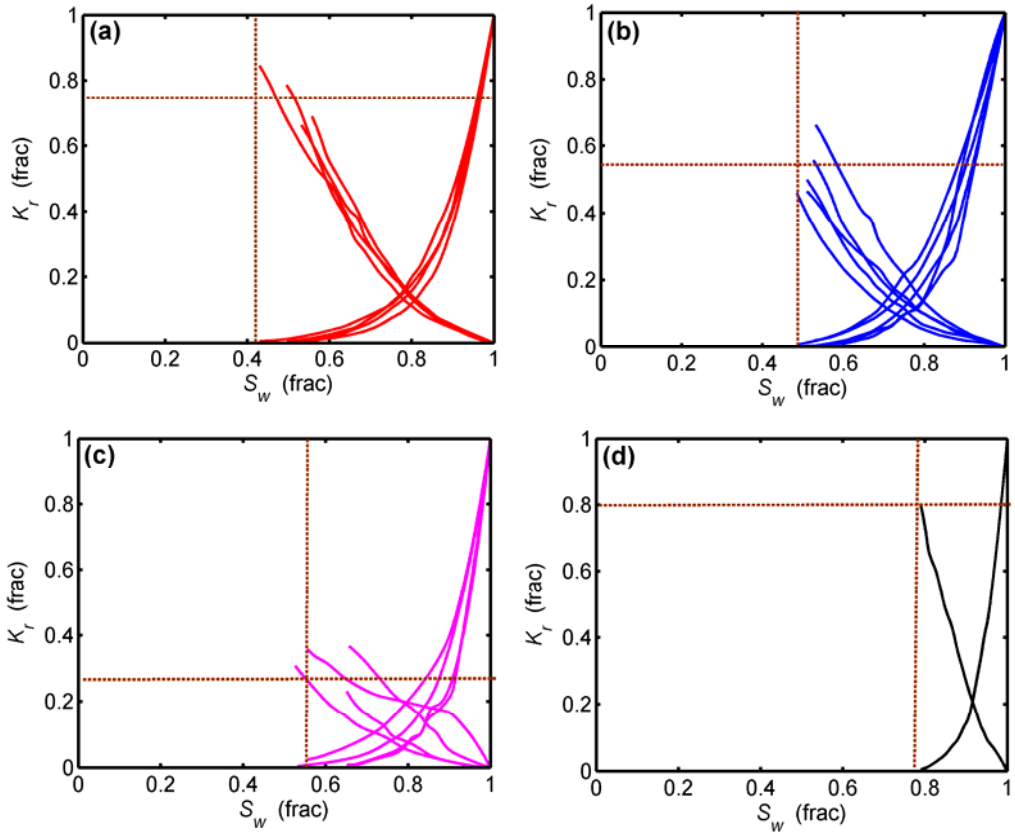


**Figure 2.15:** Primary drainage relative permeability ($S_{gr} = 0$) curves grouped according to rock type: **(a)** rock type I, **(b)** rock type II, **(c)** rock type III, and **(d)** rock type IV.

# Chapter 3: Petrophysical Rock Classification in the Cotton Valley Tight-Gas Sand Reservoir with a Clustering Pore-System Orthogonality Matrix

Tight-gas sandstones exhibit large variability in all petrophysical properties due to complex pore topology resulting from diagenesis. Conventional methods that rely solely on hydraulic radius to classify and rank reservoir rocks are inadequate to capture such degree of variability. This chapter continues with the bimodal Gaussian density function introduced in Chapter 2 to quantify complex pore systems in terms of pore volume, major pore-throat radius, and pore-throat size uniformity. We define petrophysical dissimilarity (referred to as orthogonality) between two different pore systems using the "bundle of capillary tubes" model and subsequently classify rocks by clustering an orthogonality matrix constructed with all available MICP data. The new method consistently identifies and ranks rock classes in various petrophysical data domains, including porosity-permeability trends, pore-size distribution, MICP, and core NMR $T_2$ spectra. Relative permeability curves for tight rocks, which are difficult to measure in the laboratory, are quantified with Corey-Burdine's model using the bimodal Gaussian pore-size distribution and are validated with core data. The new rock typing method is verified using field data acquired in the Cotton Valley tight-gas sand reservoir located in the East Texas Basin.

## 3.1 INTRODUCTION

G.E. Archie (1950) defined petrophysical rock type based on the associated pore-size distribution, which acts as the hub linking the rock's static and dynamic petrophysical properties. Numerous core-based rock typing methods were advanced during the past decades, including Leverett's reservoir quality index (RQI) (Leverett, 1941), Winland $R_{35}$ (Pittman, 1992), and flow zone indicator (FZI) (Amaefule et al.,

1993). However, these methods tend to use only one major pore system attribute – hydraulic radius – to classify rocks. Even though such procedures have proven reliable and practical in many conventional reservoirs where one major petrophysical attribute satisfactorily describes the entire pore system, they become inadequate to quantify complex pore systems originating from diagenetic overprint, such as those of carbonate and tight-gas reservoirs (Lucia, 1995; Rushing et al., 2008). New methods for describing complex pore systems are needed for reliable petrophysical rock typing.

MICP have been widely used in pore system characterization (Purcell, 1949; Peters, 2012). Several authors (Clerke, 2009; Gao et al., 2011) documented work on using multiple Thomeer's hyperbolas (1960) to fit MICP to describe complex carbonate rock pore systems. This procedure implicitly invokes the derivative of Thomeer's hyperbolas (referred to as Thomeer's derivative) as the pore-size distribution function. Chapter 2 of this dissertation introduced a bimodal Gaussian density function to characterize pore-size distributions in terms of incremental pore volume fraction versus logarithmic pore-throat radius, which gives rise to six attributes of interpretable petrophysical meaning. An important remaining piece of work is to define the petrophysical dissimilarity (conceptualized as petrophysical orthogonality in this dissertation) between two pore systems based on all relevant attributes for a petrophysically consistent rock classification.

This chapter continues with bimodal Gaussian density functions to quantify complex pore systems in terms of pore volume, major pore-throat radius, and pore-throat size uniformity. Six attributes for each density function are estimated and interpreted for petrophysical meaning and subsequently integrated to assess petrophysical orthogonality between two pore systems. A new petrophysical rock typing method is introduced by clustering an orthogonality matrix after fitting MICP data, which provides improved

ranking of rock types compared to existing rock classification methods and enforces petrophysical consistency among all static and dynamic petrophysical properties. We apply the new method to field data acquired in the Cotton Valley tight-gas sand reservoir located in the East Texas Basin.

## 3.2 RESERVOIR QUALITY RANKING IN TIGHT ROCKS: LEVERETT VS. WINLAND $R_{35}$ VS. FZI

Existing core-based petrophysical rock typing methods tend to rely solely on hydraulic radius to rank reservoir rocks. Among these methods, only Winland $R_{35}$ is a direct derivative from MICP data. When MICP data are not available, all rock-typing methods adopt similar mathematical formulae to quantify reservoir quality in terms of porosity and permeability. While such procedures are reliable and practical for conventional reservoirs where the same rock type exhibits narrow variability in porosity, they can lead to misclassifications in cases of low-porosity and low-permeability rocks. Figure 3.1 shows three porosity-permeability trends (or rock types) identified by Leverett's, Winland $R_{35}$, and FZI, respectively. They intersect at the point [0.1 frac, 0.01 mD]; FZI exhibits the steepest trend, which tends to classify a rock of [0.025 frac, 0.0002 mD] as belonging to the same group with a rock of [0.17 frac, 0.5 mD]. However, these two rocks differ from each other significantly in terms of both storage and flow capacity, whereby it is not petrophysically feasible to classify the two rocks into the same group. Geologically, it is very likely that these two rocks have undergone very different depositional and diagenetic processes. Leverett and Winland $R_{35}$ define flatter porosity-permeability trends compared to FZI, but still lack the ability to separate rocks with different storage capacity or effective pore volume.

It is therefore necessary to develop a new rock classification method that integrates pore volume, major pore-throat radius, and pore-throat size uniformity to

enforce petrophysical consistency among all static and dynamic properties, and which better relates to geological facies. This requirement is particularly important for those rocks exhibiting significant pore-scale heterogeneity that leads to poor correlation between pore volume, major pore-throat radius, and pore-throat size uniformity.

## 3.3 PORE-SYSTEM DESCRIPTION

Pore system is complex and can be characterized by many attributes, including pore volume, pore size, pore-throat size, pore connectivity, pore uniformity, and pore morphology. MICP data are sensitive to pore volume, pore-throat size, pore connectivity, and pore-size uniformity. Therefore MICP data become indispensible for core-based petrophysical rock typing.

### 3.3.1 Bimodal Gaussian Density Function

Chapter 2 has introduced a bimodal Gaussian density function expressed as:

$$p(\log R; w_1, \log \mu_1, \log \sigma_1; w_2, \log \mu_2, \log \sigma_2) = w_1 \frac{1}{\sqrt{2\pi}\log \sigma_1} e^{-\frac{(\log R - \log \mu_1)^2}{2(\log \sigma_1)^2}} + w_2 \frac{1}{\sqrt{2\pi}\log \sigma_2} e^{-\frac{(\log R - \log \mu_2)^2}{2(\log \sigma_2)^2}} \quad (3.1)$$

where $R$ is pore-throat radius in $\mu$m, $w_1$ and $w_2$ are weighting coefficients for each Gaussian mode, $\log\mu_1$ and $\log\mu_2$ are the mean values of pore-throat size on a logarithmic scale, and $\log\sigma_1$ and $\log\sigma_2$ are the corresponding standard deviations on a logarithmic scale. The petrophysical interpretation of these attributes is summarized as follows:

**Pore Volume:** $w_1$ and $w_2$ are fractions of pore volume connected by large and small logarithmic pore-throat size modes, respectively; $w_1$ correlates with residual

non-wetting phase saturation during imbibition, while $w_2$ correlates with irreducible wetting-phase saturation during drainage.

**Pore-Throat Radius:** $\log\mu_1$ and $\log\mu_2$ are mean values of large and small logarithmic pore-throat size modes, respectively; larger values indicate better pore connectivity and permeability.

**Pore-Throat Size Uniformity:** $\log\sigma_1$ and $\log\sigma_2$ are standard deviations of large and small logarithmic pore-throat size modes, which describe the uniformity of "capillary tube sizes" (Childs and Collis-George, 1950). A larger value of standard deviation of pore-throat size indicates lower sorting of tube sizes, hence higher tortuosity of the pore network.

Chapter 2 also introduced both differentiation and inversion methods to derive bimodal Gaussian density functions from MICP data. The inversion method is preferred because it generates stable and smooth pore-size distribution functions.

### 3.3.2 Permeability Calculation with "Bundle-of-Capillary-Tubes" Model

For a "bundle-of-capillary-tubes" model that exhibits a pore-size distribution function *f*, absolute permeability can be calculated as (Peters, 2012):

$$k = \frac{\phi}{32\sqrt{\tau}}\left[\frac{\int_0^\infty f(\delta)\delta^4 d\delta}{\int_0^\infty f(\delta)\delta^2 d\delta}\right] = \frac{\phi}{32\sqrt{\tau}}(\overline{R})^2, \tag{3.2}$$

where $\phi$ is porosity, $\overline{R}$ is mean pore-throat radius, and $\tau$ is tortuosity of the capillary tubes which is inversely proportional to the uniformity of capillary-tube sizes (Al-

Tarawneh et al., 2009; Hirasaki, 2009). Equation (3.2) implies the following petrophysical interpretations:

1) Permeability is linearly proportional to porosity (pore volume) given the same mean pore-throat radius and pore-throat size uniformity;
2) Permeability is linearly proportional to the square of mean pore-throat radius (pore connectivity) given the same pore volume and pore-throat size uniformity;
3) Permeability is inversely proportional to the square root of tortuosity (correlated with pore-throat size uniformity) given the same pore volume and major pore-throat radius.

Figure 3.2 further describes reservoir-quality differences between rocks of different pore volume, major pore-throat radius, and pore-throat size uniformity. For rocks with the same major pore-throat radius and pore-throat size uniformity but significantly different pore volume, capillary pressure curves ($P_c$ vs. $S_w$) cannot differentiate their reservoir quality. However, when capillary pressure is plotted against mercury-invaded pore volume, they can be easily differentiated (Fig. 3.2c).

### 3.3.3 Pore-System Orthogonality

To synthesize the interpretations indicated by Eq. (3.2) for quantifying petrophysical dissimilarity between two pore systems, we implement a logarithmic transformation on both sides of Eq. (3.2) to obtain

$$\log k = \log \phi + \log \overline{R}^2 + \log \frac{1}{\sqrt{\tau}} - 1.51, \tag{3.3}$$

where $k$ is permeability, $\phi$ is porosity, $\overline{R}$ is mean pore-throat radius, and $\tau$ is tortuosity. Three components, namely $\log\phi$, $\log\overline{R}^2$, and $\log\frac{1}{\sqrt{\tau}}$, fully characterize the pore system in the data space of $\log k$. In analogy with analytical geometry, we define petrophysical orthogonality as the $L_1$ norm between two rock samples of properties: ($\phi_1$, $\overline{R}_1$, $\tau_1$) and ($\phi_2$, $\overline{R}_2$, $\tau_2$). After substituting tortuosity $\tau$ with the pore-size uniformity parameter, the formula is expressed as

$$\begin{aligned} ORT_{1,2} &= [\log\phi_1 - \log\phi_2] + [\log(\overline{R}_1^2) - \log(\overline{R}_2^2)] + [\log(\frac{1}{\sqrt{\sigma_1}}) - \log(\frac{1}{\sqrt{\sigma_2}})] \\ &= \log(\frac{\phi_1}{\phi_2}) + 2\log(\frac{\overline{R}_1}{\overline{R}_2}) - 0.5\log(\frac{\sigma_1}{\sigma_2}), \end{aligned} \tag{3.4}$$

where $ORT_{1,2}$ stands for orthogonality between two single-mode Gaussian pore-size distributions. A positive value indicates better reservoir quality, whereas a negative value indicates poorer reservoir quality in terms of flow capacity. Under this definition, orthogonality has the following properties:

(i) the orthogonality between two identical pore systems (if they do exist) is zero;

(ii) $$ORT_{1,3} = ORT_{1,2} + ORT_{2,3}, \tag{3.5}$$

where subscripts 1, 2, and 3 represents three pore systems.

Rocks commonly exhibit bimodal Gaussian pore-size distributions in reservoirs with significant diagenesis, such as carbonates and tight-gas sandstones. Therefore, the definition of orthogonality needs to be extended to a bimodal case. A simple way to achieve this is to define orthogonality between large and small pore-size modes separately (Fig. 3.3). Orthogonality between large pore-size modes differentiates permeability or flow capacity while orthogonality between small pore-size modes differentiates non-movable wetting phase saturation. Pore-system orthogonality provides

a metric for quantifying the petrophysical dissimilarity between two rocks, thereby becoming an important attribute for classifying petrophysical rock types.

## 3.4 FIELD CASE: COTTON VALLEY TIGHT-GAS SANDSTONE, EAST TEXAS BASIN

The Cotton Valley formation is a tight-gas play located in Northeast Texas and Northwest Louisiana. Upper Jurassic/Lower Cretaceous Cotton Valley tight-gas sandstones have significantly contributed to U.S. gas production during the past decades. The formation is spatially heterogeneous due to complex depositional controls and diagenetic overprints (Liu et al., 2011), consisting mainly of tightly cemented, very fine- to fine-grained sandstone interbedded with mudstone, siltstone, and carbonate (Spain et al., 2011). Depositional facies are interpreted as stacked shoreface/barrier bar deposits, tidal channel, tidal delta, and inner shelf and back-barrier deposits (Wescott, 1984; Spain et al., 2011). The reservoir has an average porosity lower than 10% and permeability in the micro-darcy range.

To enable high-resolution reservoir description, comprehensive core samples and associated laboratory measurements were acquired from a key-study well – TW George 8H (Liu et al., 2011; Spain et al., 2012). Routine core porosity and permeability measurements were performed on more than 200 core plugs. In addition, both high-pressure MICP (0 – 60, 000 psi) and NMR measurements were conducted on thirty preserved core plugs covering a range of depositional facies from a continuous full-diameter whole core.

Core data show large variability in all petrophysical properties, which renders petrophysical modeling and rock typing very difficult. In our study, we first model pore-size distributions with bimodal Gaussian density functions for all core-measured MICP curves and then assess petrophysical orthogonality between each core sample pair. A new

petrophysical rock typing method is proposed to classify these complex tight gas sands by clustering the orthogonality matrices to simplify reservoir description. Rock typing results are then used to rank other petrophysical properties, including porosity-permeability trends, pore-size distribution, MICP, and core NMR $T_2$ spectra.

### 3.4.1 Pore-Size Distribution Modeling

The inversion method introduced in Chapter 2 (Appendix A) was applied to estimate bimodal Gaussian pore-size distributions from 30 MICP curves. Histograms of the six Gaussian attributes (Fig. 3.4) indicate that rocks exhibit extreme variability in all petrophysical properties. It is observed that the standard deviation of the logarithmic large pore-throat size mode is much smaller than that of the small pore-throat size mode, thereby suggesting that most rocks in this study have a narrowly distributed dominant pore-throat size.

### 3.4.2 Rock Classification by Clustering Orthogonality Matrices

After fitting all MICP curves, we assess the petrophysical orthogonality between each core sample pair using Eq. (3.4) for both large and small pore-size modes, which are summarized in the form of 30x30 matrices, as shown in Fig. 3.5. Diagonal elements of orthogonality matrices are all zero. Red and blue colors identify large petrophysical orthogonality in positive and negative domains, respectively. For example, samples 17, 18, and 19 exhibit the lowest reservoir quality, whereby a blue color belt is observed in the map (highlighted in the red dashed boxes). The matrix ranks all core samples in terms of reservoir quality and hence becomes suitable for petrophysical rock classification. A dissimilarity matrix clustering technique (Hahsler and Hornik, 2011) is next applied to the orthogonality matrices and classify the 30 core samples into 5 rock types, denoted as A, B1, B2, C, and D with descending reservoir quality.

In the following sections, we use the rock types to rank different petrophysical data, including porosity-permeability trends, pore-size distribution, MICP, and core NMR $T_2$ spectra. Relative permeability curves are described for each reservoir facies using Corey-Burdine's model and based on the associated bimodal Gaussian pore-size distribution.

### 3.4.3 Ranking Porosity-Permeability

We use the classification results obtained from clustering orthogonality matrices to color-code the porosity-permeability crossplot (Fig. 3.6). Distinct porosity-permeability trends emerge for all rock types. Table 3.1 summarizes the statistical distributions of porosity and permeability. For comparison, Fig. 3.7 shows the same porosity-permeability crossplot ranked with rock types classified from MICP-derived Winland $R_{35}$. Two rock samples of extremely low porosity (highlighted with a dashed red circle) are misclassified as the rock type of the best reservoir quality (rock type A). However, these two samples are reliably classified with pore-system orthogonality (highlighted in dashed pink circle in Fig. 3.6). In fact, the two samples have very small pore volume but very large pore-throat size, which may deserve a new rock type in a detailed analysis. In our study, in order to keep the number of rock types manageable, we still classify them as rock type B2 based on overall reservoir quality instead of only invoking hydraulic radius in the classification.

### 3.4.4 Ranking MICP and Pore-Size Distribution

The industry standard, high-pressure (0 - 60, 000 psia) MICP was used to assess pore-throat size and total pore volume of core plugs. We use classification results to color-code both MICP data and the associated pore-size distribution (in terms of incremental pore volume fraction versus logarithmic pore-throat size). Fig. 3.8 shows the

ranked MICP data in the form of $P_c$ vs. $S_w$, where MICP curves of rock type B1 and rock type B2 intermix with each other. However, when MICP data are plotted in the form of $P_c$ vs. invaded pore volume (Fig. 3.9), MICP curves of rock type B1 and rock type B2 separate well. Fig. 3.10 shows MICP-derived pore-size distributions ranked with rock types classified from clustering orthogonality matrices. Rock types A, B1, and B2 all exhibit a major pore-size distribution and a tail of small pore-size distribution; rock type C mostly exhibits a balanced pore-volume fraction between the large and small pore-size mode; rock type D has a unimodal behavior in pore-size distribution.

### 3.4.5 Ranking Core NMR Data

Laboratory NMR experiments were performed on the same 30 core samples (100% water saturated) using a MARAN Ultra Magnetic Resonance Core Analyzer (operating frequency ~ 2 MHz) with multiple inter-echo spacing of 300, 600, and 1200 μs. Transverse relaxation time ($T_2$) distributions were obtained by inverting multi-exponential echo data with 51 preset decay times evenly spaced logarithmically between 0.1 ms and 10,000 ms (Liu et al., 2011). Because diffusion effects on proton relaxation are negligible in water-filled rocks, relaxation times are mainly determined by pore-body size (Winkler et al., 2006). With the assumption that pore-body size is well correlated with pore-throat size, it is possible to derive synthetic capillary pressure curves from NMR $T_2$ spectra (Altunbay et al., 2001). Therefore, rock types derived from MICP data should also rank NMR $T_2$ spectra consistently. Fig. 3.11 shows the core NMR $T_2$ spectra grouped by rock types and Fig. 3.12 shows the crossplot of permeability and NMR $T_2$ logarithmic mean (T2LM) color coded by rock type. Generally, the $T_2$ peak locations shift to left side (lower relaxation times) as rock type number increases (and overall reservoir quality decreases). Table 3.1 summarizes the statistics of NMR T2LM for each rock type.

### 3.4.6 Modeling Primary Drainage Relative Permeability for Rock Types

Laboratory measurements of relative permeability measurements can take significant time when performed on tight-gas sandstone samples. Therefore, it would be useful to model relative permeability curves from MICP data (Byrnes, 2008). Liu et al. (2012) used rock types to guide the prediction of dynamic flow behavior in the Cotton Valley formation. Here we derive primary drainage relative permeability curves from the bimodal Gaussian pore-size distribution using Corey-Burdine's model (Burdine, 1953; Huang et al., 1997). Critical water saturation ($S_{wcrit}$) is calculated from its correlation with parameter $w_2$, whereas the end point of gas relative permeability is predicted by its correlation with parameter $\mu_1$. The end point of water relative permeability is set to 1.0 while residual gas saturation ($S_{gr}$) is set to 0 in a primary drainage process. Table 3.2 lists the gas relative permeability properties of each rock type.

Burdine's wetting phase relative permeability is given by

$$k_{rw} = (S_w^*)^2 \frac{\int_0^{S_w^*} \frac{1}{(P_c)^2} dS_w^*}{\int_0^1 \frac{1}{(P_c)^2} dS_w^*} = (S_w^*)^2 \frac{\int_0^{S_w^*} R^2 dS_w^*}{\int_0^1 R^2 dS_w^*}, \tag{3.6}$$

and non-wetting phase relative permeability by

$$k_{rnw} = (1-S_w^*)^2 \frac{\int_{S_w^*}^1 \frac{1}{(P_c)^2} dS_w^*}{\int_0^1 \frac{1}{(P_c)^2} dS_w^*} = (1-S_w^*)^2 \frac{\int_{S_w^*}^1 R^2 dS_w^*}{\int_0^1 R^2 dS_w^*}, \tag{3.7}$$

where $P_c$ is capillary pressure and $R$ is the corresponding pore-throat radius; $S_w^*$ is normalized water saturation, defined as

$$S_w^* = \frac{S_w - S_{wirr}}{1 - S_{wirr} - S_{gr}}. \tag{3.8}$$

Based on MICP-derived bimodal Gaussian pore-size distribution, primary drainage relative permeability curves for each rock type are calculated with Corey-Burdine's equations (Fig. 3.13). The modeled primary drainage relative permeability curves agree well with core data and show consistency with the data presented in Byrnes' work (2008).

## 3.5 CONCLUSIONS

Conventional core-based rock typing methods dominantly emphasize hydraulic radius and tend to neglect the impact of effective pore volume and pore-size uniformity on overall petrophysical quality. Consequently, they are prone to misclassifications in tight-gas sandstones that exhibit poor correlation between hydraulic radius and other pore-system attributes. We introduced a bimodal Gaussian density function to describe complex pore systems analytically in terms of pore volume, major pore-throat radius, and pore-throat size uniformity. A new concept, referred to as pore-system orthogonality, was introduced to quantify petrophysical dissimilarity between two pore systems, which takes into account all relevant pore-system attributes, including pore volume, major pore-throat radius, and pore-throat size uniformity. Rock classification via clustering orthogonality matrices enables consistent reservoir quality ranking in all petrophysical data domains, including porosity-permeability trends, pore-size distribution, MICP, and core NMR $T_2$ spectra. The analytical bimodal Gaussian pore-size distribution model also lends itself to the prediction of saturation-dependent, primary drainage relative permeability with Corey-Burdine's model. A test of the new method on thirty core samples of Cotton Valley tight-gas sandstones, East Texas, verified its advantage over conventional rock typing methods.

**Table 3.1:** Statistical distributions of porosity, permeability, and NMR T2LM for each rock type.

| Rock Type | Porosity (frac) | Permeability ($10^{-3}$ mD) | T2LM (ms) |
|---|---|---|---|
| **A** | 0.071 ± 0.013 | 70 ± 48 | 29.5 ± 26.6 |
| **B1** | 0.065 ± 0.026 | 9.0 ± 4.0 | 7.16 ± 2.65 |
| **B2** | 0.053 ± 0.027 | 6.0 ± 2.0 | 5.0 ± 1.54 |
| **C** | 0.052 ± 0.014 | 0.76 ± 0.03 | 1.9 ± 0.7 |
| ***D*** | 0.026 ± 0.010 | 0.0025 ± 0.001 | 0.93 ± 0.29 |

**Table 3.2:** Gas relative permeability properties for each reservoir facies in a primary drainage process ($S_{gr} = 0$).

| Rock Type | Average $S_{wcrit}$ | Average End-Point $K_{rg}$ |
|---|---|---|
| **A** | 0.38 | 0.78 |
| **B1** | 0.50 | 0.62 |
| **B2** | 0.43 | 0.51 |
| ***C*** | 0.71 | 0.42 |

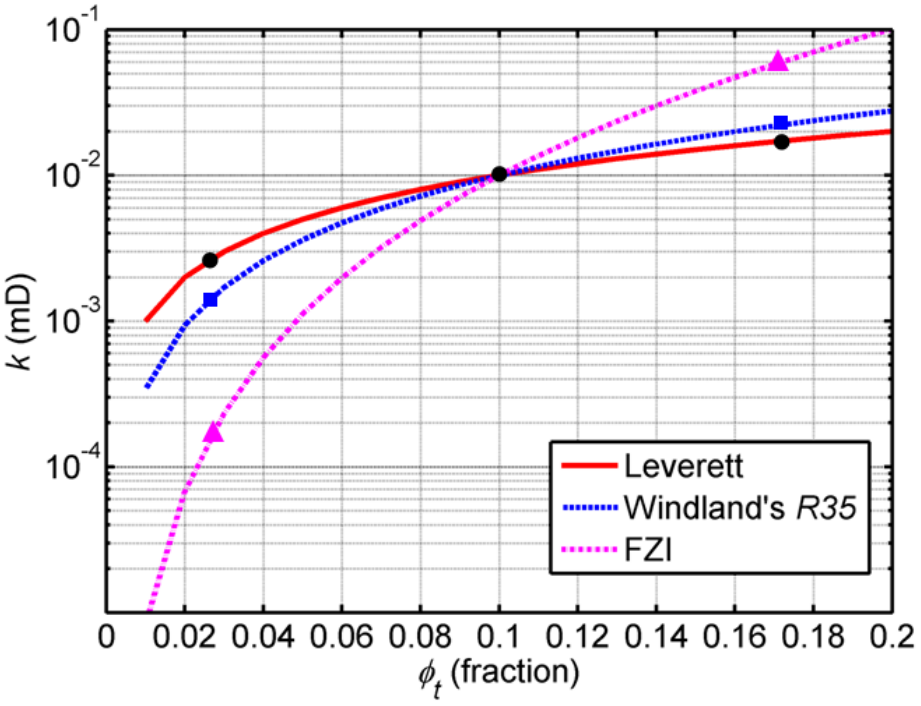


**Figure 3.1:** Illustration of misclassifications of rock types when using three existing core-based petrophysical rock classification methods for low-porosity rocks. Differences in storage capacity or pore volume are overlooked by these methods.

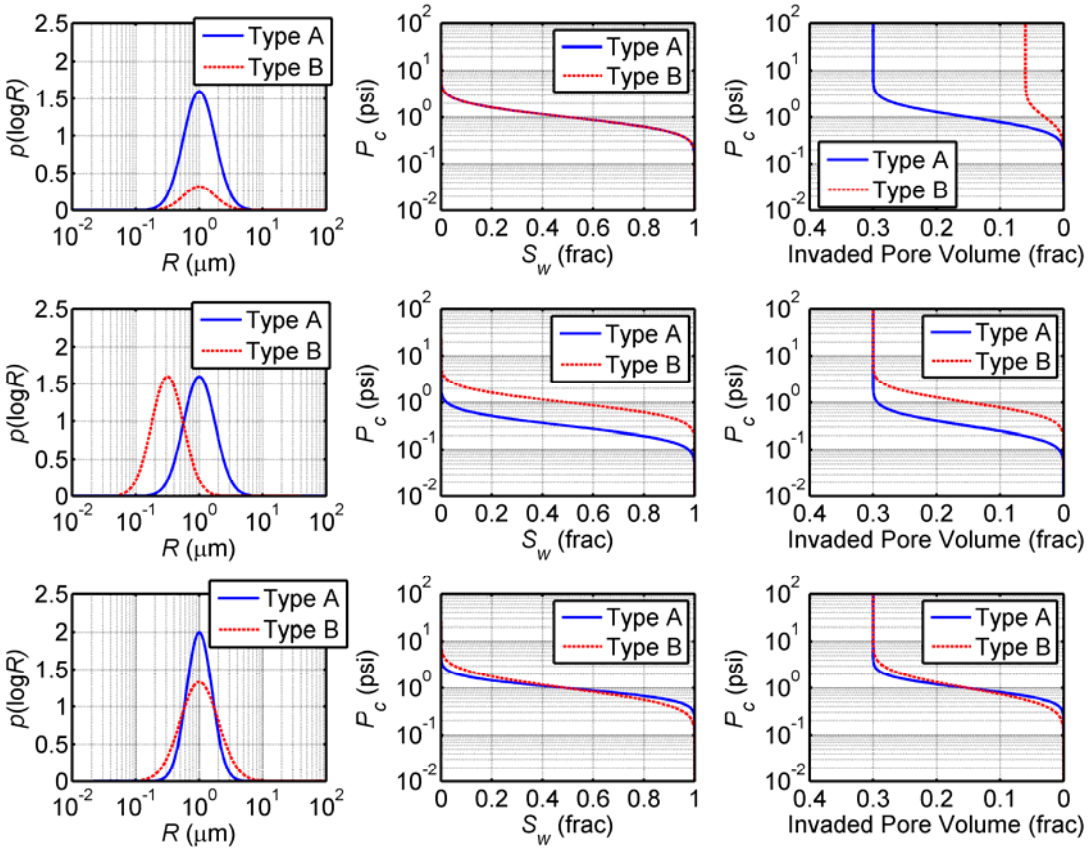


**Figure 3.2:** Comparison of **(a)** pore size distribution, **(b)** MICP $P_c$ - $S_w$ plot, and **(c)** MICP $P_c$ vs. mercury invaded pore volume plot for two rock types of different pore volume (upper panel), major pore-throat radius (center panel), and pore-throat size uniformity (lower panel).

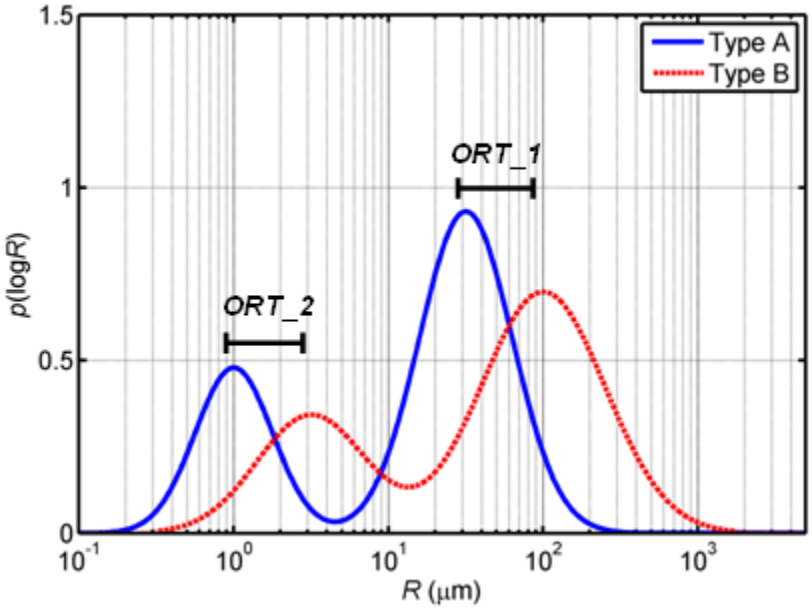


**Figure 3.3:** Orthogonality between two rocks of bimodal Gaussian pore-size distribution functions. ORT_1: orthogonality between the large pore-throat size modes; ORT_2: orthogonality between the small pore-throat size mode.

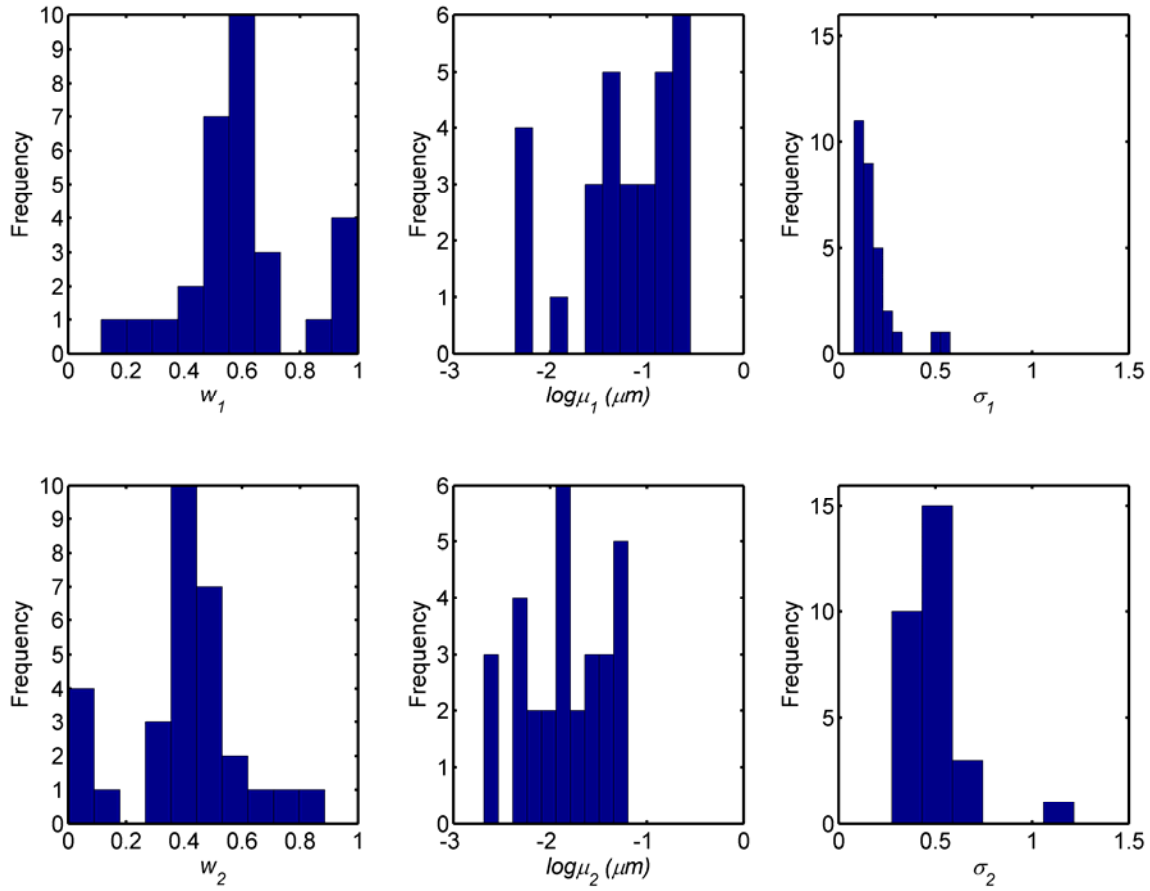


**Figure 3.4:** Histograms of all Gaussian attributes. Upper and lower panels show the histograms for large and small pore-throat size modes, respectively.

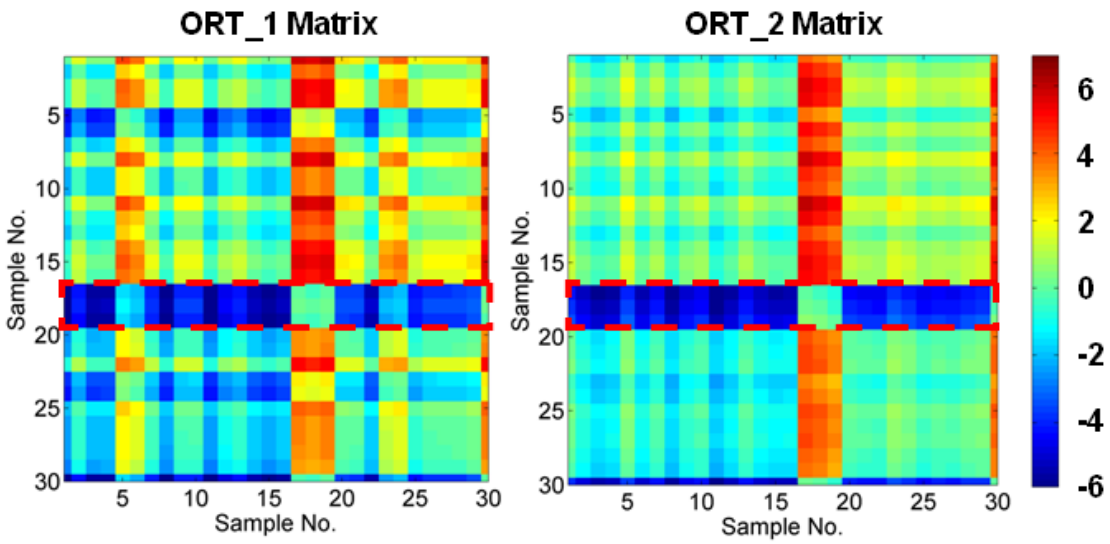


**Figure 3.5:** Color maps describing the orthogonality matrices obtained from 30 MICP curves in the Cotton Valley tight-gas sandstone reservoir. Blue and red indicate low and high orthogonality, respectively.

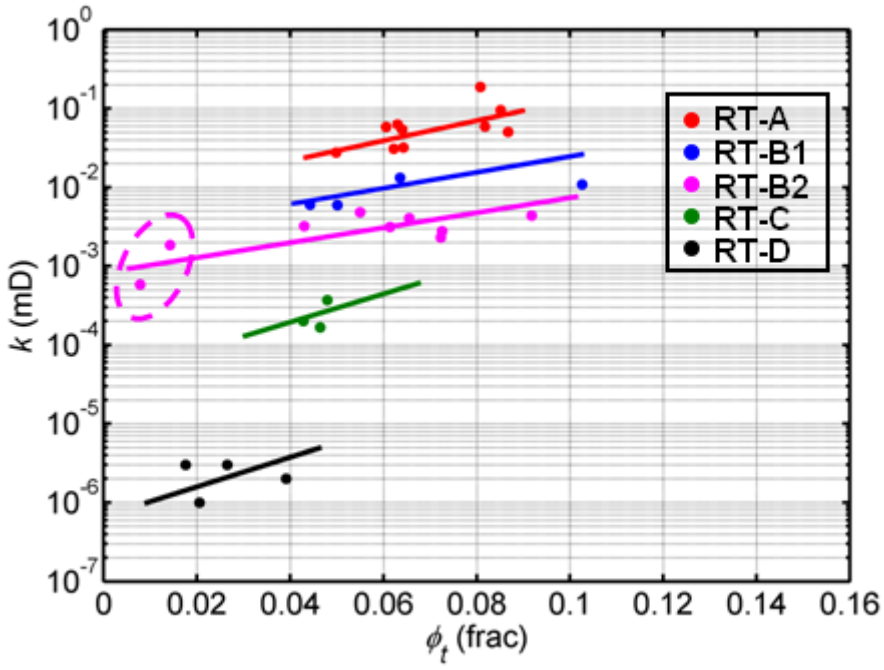


**Figure 3.6:** Porosity-permeability crossplot ranked with rock types detected and classified from the clustering orthogonality matrices.

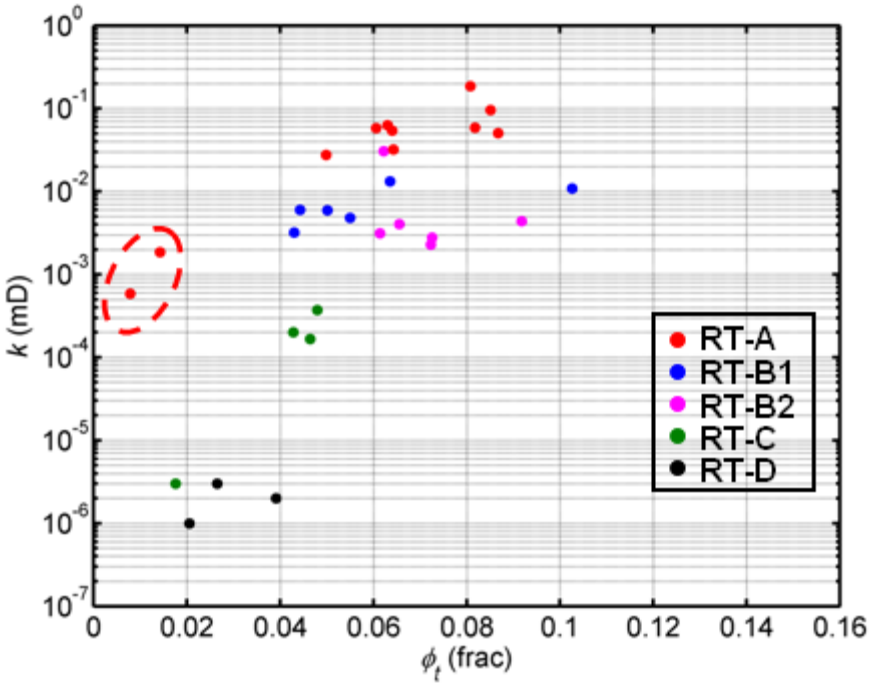


**Figure 3.7:** Porosity-permeability crossplot ranked with rock types classified from MICP-derived Winland $R_{35}$.

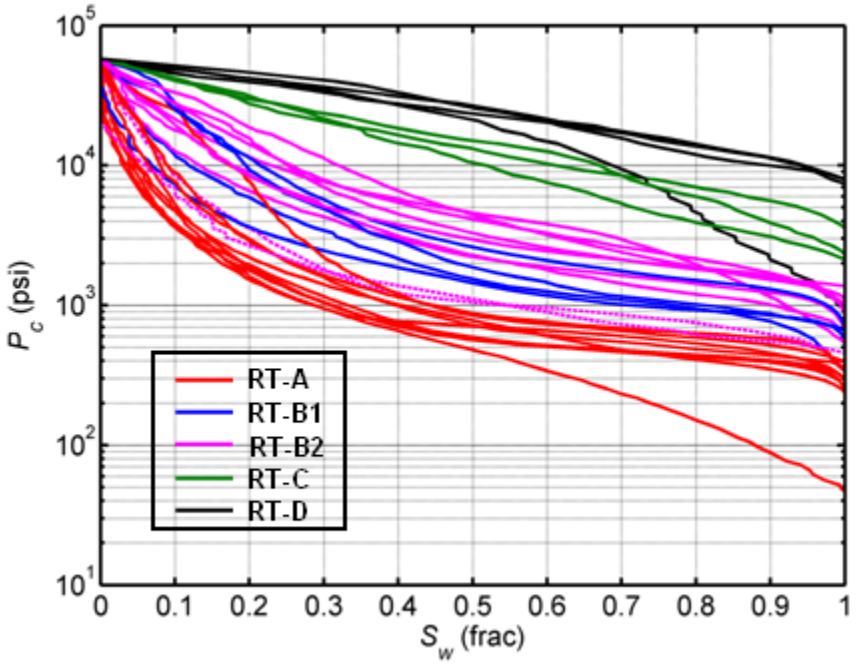


**Figure 3.8:** MICP data in the form of $P_c$ vs. $S_w$ ranked with rock types classified from clustering orthogonality matrices. Dashed lines identify the two peculiar samples circled in Figs. 3.6 and 3.7.

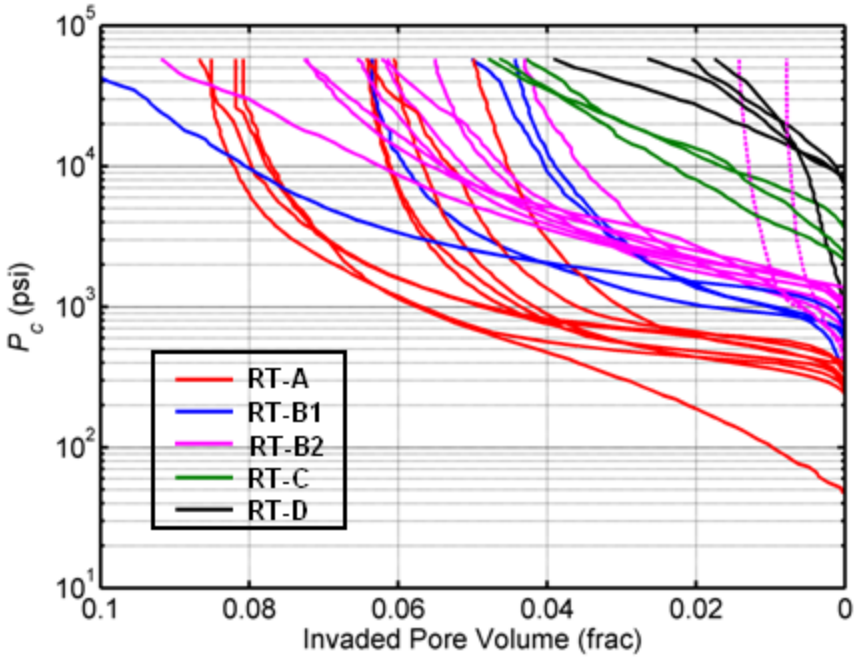


**Figure 3.9:** MICP data (in the form of $P_c$ vs. invaded pore volume) ranked with rock types classified from clustering orthogonality matrices. Dashed lines identify the two peculiar samples circled in Figs. 3.6 and 3.7.

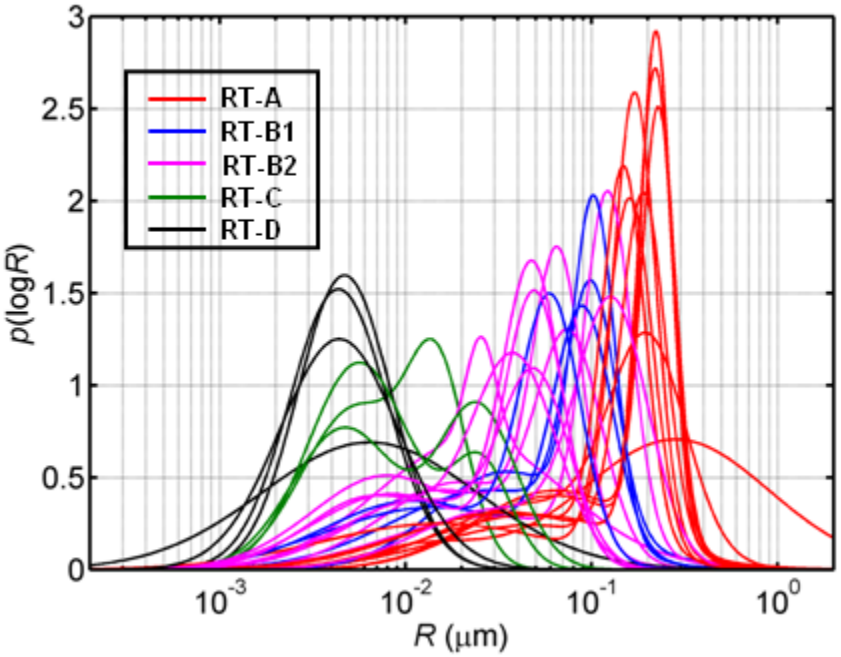


**Figure 3.10:** MICP derived pore-size distributions ranked with rock types classified from clustering orthogonality matrices.

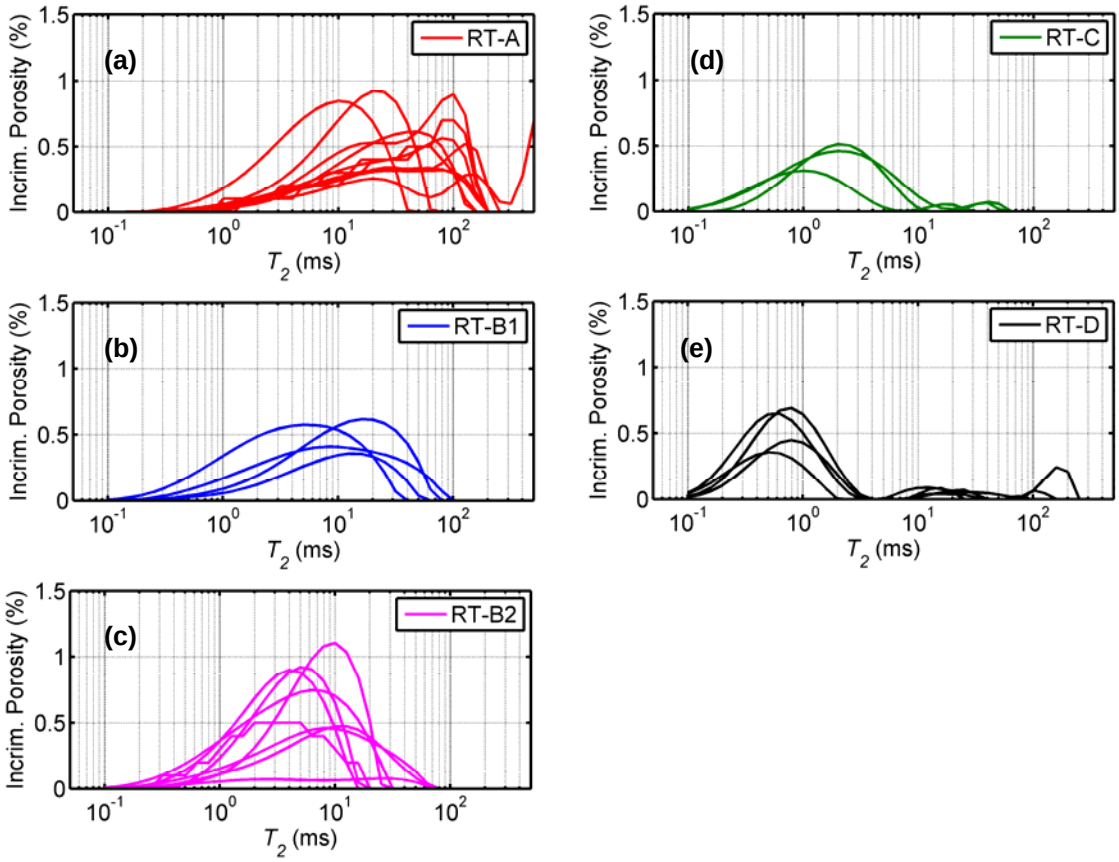


**Figure 3.11:** Core-measured NMR $T_2$ spectra grouped by rock type: **(a)** rock type A, **(b)** rock type B1, **(c)** rock type B2, **(d)** rock type C, and **(e)** rock type D.

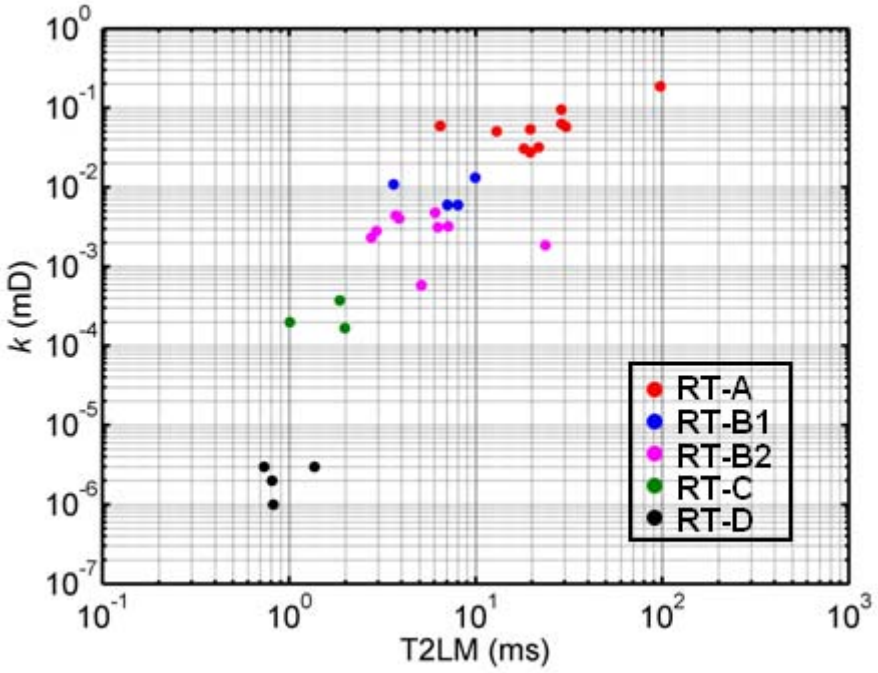


**Figure 3.12:** Crossplot of permeability and T2LM, color coded by rock type.

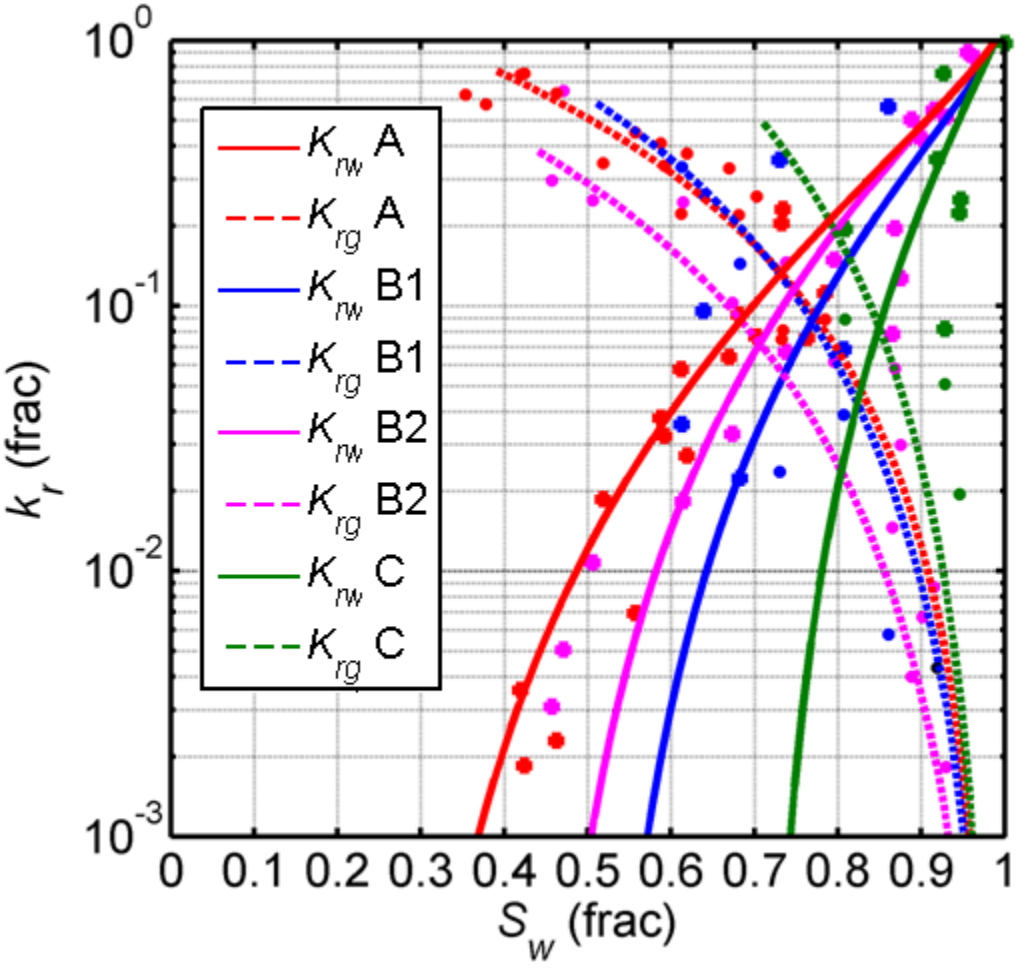


**Figure 3.13:** Primary drainage relative permeability curves ($S_{gr}$ = 0) modeled with Burdine's equations for each rock type. The colored points identify the core-measured relative permeability for each rock type.

# Chapter 4: Quantifying Fluid Distribution and Phase Connectivity with a Simple 3D Cubic Pore Network Model Constrained by NMR and MICP Data

This chapter introduces a computer algorithm to construct 3D cubic pore networks that simultaneously honor NMR and MICP measurements on core samples. The algorithm uses discretized pore-body size distributions from NMR and pore-throat size vs. incremental pore volume fraction information from MICP as initial inputs. Pore-throat radius distribution and body-throat correlation are iteratively refined to match percolation-simulated primary drainage capillary pressure with MICP data. It outputs a pore-throat radius distribution which is not directly measurable with either NMR or MICP. In addition, quasi-static fluid distribution and single-phase connectivity are quantified at each capillary pressure stage. NMR measurements on desaturating core samples are simulated from the quantitative fluid distribution in a gas-displacing-water drainage process and are verified with laboratory measurements. The effective medium theory is invoked to quantify the single-phase connectivity in two-phase flow by simulating percolation in equivalent sub pore networks that consider the remaining fluid phase as solid cementation. Primary drainage relative permeability curves quantified from fluid distribution and phase connectivity show petrophysical consistency after applying a hydrated-water saturation correction. Core measurements of tight-gas sand samples from the Cotton Valley Formation, East Texas, are used to verify the new algorithm.

## 4.1 INTRODUCTION

Understanding of fluid distribution at multiple times and length scales in subsurface reservoirs is critical to reservoir characterization, including migration history

interpretation, reserves estimation, saturation-height analysis, production optimization, and $CO_2$ sequestration modeling (Akbar et al., 1994; Parnell and Schwab, 2003; Benson and Cole, 2008). Microscopic fluid distributions determine various saturation-dependent petrophysical properties such as capillary pressure and relative permeability, which directly govern the hydrocarbon recovery processes (Lake, 1996; Peters, 2012). Additionally, the fluid distribution has significant effects on various geophysical measurements, including electric or dielectric, acoustic, magnetic resonance, and nuclear well logs (Knight and Nolen-Hoeksema, 1990; Knight, 1991; Endres and Knight, 1991; Chen et al., 1994; Garrouch and Sharma, 1995; Freedman and Heaton, 2004). Therefore, it is imperative to study fluid distributions in reservoir rocks by connecting petrophysical principles with the physics of measurements used to probe rocks.

It has been recognized that microscopic fluid distributions in porous media are a consequence of complex physical and chemical processes and depend on many factors such as fluid displacement mechanism, saturation history, flow rate, and wettability (Handy and Datta, 1966; Mohanty, 1981). Many experimental techniques have been advanced to study fluid distributions during multi-phase flow. The use of computer tomography and X-ray microtomography to visualize fluid distribution has been reported by several research groups (Peters and Hardham, 1990; Tomutsa et al., 1990; Kumar et al., 2009; Silin et al., 2010; Youssef et al., 2010). NMR imaging is an alternative approach to characterize fluid distribution during two phase flow (Liaw et al., 1996; Li, 1997; Chen et al., 2004). Recently, numerical pore network modeling techniques have become increasingly popular in quantifying fluid distributions and predicting petrophysical properties (Mohanty and Salter, 1982; Bryant et al., 1993; Oren et al., 1998; Patzek, 2001; Blunt, 2001; Blunt et al., 2002; Jin et al., 2007; Balhoff et al., 2007). Despite their accuracy, most of the above experimental and numerical techniques require

significant effort to render a representative pore-network model, which limits their extensive use to assist real-time petrophysical interpretation.

In this chapter, we introduce an efficient computer algorithm to construct random 3D cubic pore network models constrained by NMR and MICP measurements acquired from core samples. In addition to pore-throat radius distributions, the algorithm outputs quantitative quasi-static distributions of a specific fluid phase. NMR measurements simulated for desaturating core samples are verified with laboratory measurements. Archie's concept of "effective pore size distribution" is invoked to quantify single-phase connectivity by simulating percolation in equivalent sub-networks that consider the remaining fluid phase as solid cementation. This method generates primary drainage relative permeability curves comparable to NMR-derived values on a first-order approximation. Core measurements acquired from tight-gas sandstone samples from Cotton Valley Formation, East Texas, are used in the study to verify the new algorithm.

## 4.2 PORE SYSTEM CHARACTERIZATION WITH MICP AND NMR

NMR and mercury porosimetry are two experimental techniques commonly used to characterize pore systems (Coates et al., 1999; Purcell, 1949; Peters, 2012). Different pore-size information from NMR and MICP was analyzed and compared in detail by Basan et al. (1997). Methods of correlating MICP and NMR data were documented elsewhere (Altunbay et al., 2001; Marschall et al., 1995; Gao et al., 2011). Projects about combining MICP and NMR data to predict permeability have also been documented in the open technical literature (Glover et al., 2006). However, it should be noticed that MICP and NMR measurements are essentially different in their physics, whereby they probe pore systems based on different petrophysical principles.

NMR transverse relaxation time ($T_2$) is mainly sensitive to pore-body size. With the assumption that bulk relaxation and diffusion coupling are negligible in a fully water-saturated water-wetting rock sample measured under a constant magnetic field, $T_2$ is related to pore-body size by (Coates et al., 1999):

$$\frac{1}{T_2} = \rho \frac{S}{V}, \tag{4.1}$$

where $\rho$ is surface relaxivity in μm/s, $S/V$ is surface to volume ratio in $\mu m^{-1}$, which quantifies the pore-body dimension. Table 4.1 lists the surface-to-volume ratio of some simple pore-body geometries. In this chapter, spherical pore geometry is assumed to simulate NMR and mercury injection measurements. The use of alternative pore geometries requires additional testing.

For a spherical pore body of radius $R_b$, $T_2$ is expressed as:

$$T_2 = \frac{R_b}{3\rho}. \tag{4.2}$$

Figure 4.1 shows an example of converting the NMR $T_2$ spectrum into a pore-body size distribution assuming spherical pore geometry via Eq. (4.2) for a tight-gas sandstone sample. The same sample will be subsequently used for testing the pore-network inversion algorithm.

Mercury porosimetry (Webb, 2001) quantifies the pore volume accessible to the invading non-wetting phase at an exerted value of capillary pressure ($P_c$), which relates to pore-throat size through Laplace's equation:

$$P_c = \frac{2\Gamma\left|\cos\theta\right|}{R_{th}}, \tag{4.3}$$

were $R_{th}$ is pore-throat radius in μm, $\Gamma$ is interfacial tension, and $\theta$ is contact angle. Chapter 2 has introduced a bimodal Gaussian density function to characterize the pore system in terms of incremental pore volume fraction versus log-normal pore-throat radius, as follows:

$$p(\log R_{th}; w_1, \log\mu_1, \log\sigma_1; w_2, \log\mu_2, \log\sigma_2) = \\ w_1 \frac{1}{\sqrt{2\pi}\log\sigma_1} e^{-\frac{(\log R_{th}-\log\mu_1)^2}{2(\log\sigma_1)^2}} + w_2 \frac{1}{\sqrt{2\pi}\log\sigma_2} e^{-\frac{(\log R_{th}-\log\mu_2)^2}{2(\log\sigma_2)^2}}, \tag{4.4}$$

where $w_1$ and $w_2$ are weighting coefficients for each Gaussian mode, $\log\mu_1$ and $\log\mu_2$ are the mean values of logarithmic pore-throat radius, and $\log\sigma_1$ and $\log\sigma_2$ are the corresponding standard deviations of logarithmic pore-throat radius. Figure 4.2 shows an example of deriving pore volume fraction vs. pore-throat radius from MICP data acquired on the same sample considered in Fig. 4.1. Noteworthy is that neither NMR nor MICP directly quantifies the pore-throat radius distribution. In this chapter, we aim to quantify the pore-throat radius distribution from pore network modeling.

## 4.3 3D Construction of a Cubic Pore Network Model

A simple 3D cubic pore network model is used to describe a porous rock (Dullien, 1979; Mohanty and Salter, 1982; Diaz et al., 1986; Chang et al., 2000). Figure 4.3 shows a schematic planar view of the network and the node connectivity. Each node (site) represents a spherical pore body that can be occupied by either wetting or non-wetting phase. Each pore body is connected to six neighboring nodes by cylindrical pore throats (bonds). The overall volume fraction of pore bodies adds up to the total porosity

measured from the core sample. Fluid saturation and distribution are simulated by simulating invasion percolation at different values of exerted capillary pressure. Subsequently, the saturation versus capillary pressure is compared to MICP data and the fluid distribution is used to simulate NMR echo decays at different stages of water saturation.

To simplify the pore network modeling while honoring first-order pore-scale petrophysics, the following assumptions and limitations are associated with the network construction and percolation simulation:

1) The flow in pore network model is quasi-static or dominated by capillary forces.
2) The coordination number of each pore body is constant and equal to six.
3) The rock grain surface is water-wet.
4) The volume of pore throats is negligible compared to pore bodies.
5) Complete displacement occurs once a pore body is invaded by non-wetting phase when simulating the mercury injection process (assuming that hydration water has been completely dried out).
6) A portion of irreducible water is assumed to attach to the grain surface when simulating gas displacing water as in NMR desaturation and relative permeability measurements.
7) A specified portion of pore throats is correlated with pore bodies being topologically connected in their geometrical dimensions. The remaining connections between pore throats and pore bodies are random with restriction specified in (8). This assumption is based on the fact that body-throat correlation is significantly altered after diagenesis as in tight sandstones and carbonates. The degree of body-throat correlation needs to

be initialized from the comparison of NMR and MICP data. Its final value should be determined from the inversion process that reproduces MICP from the percolation simulation.

8) The sizes of six pore throats attached to a particular pore body should always be less than the pore-body size.

Assumptions (5) and (6) have a significant impact on flow simulation while limitations (7) and (8) ensure a realistic pore-network model. To simulate the primary drainage capillary pressure curve that is comparable to MICP, the percolation is run through all six inlet faces of a cubic sample (Fig. 4.4). All numerical experiments in this chapter assume a cubic sample of dimension 100 μm x 100 μm x 100 μm. The percolation simulation stops when the exerted capillary pressure exceeds 60,000 psi (air-mercury system).

## 4.4 PORE NETWORK MODEL INVERSION WORKFLOW

Figure 4.5 shows the numerical workflow used to construct the 3D cubic pore network from NMR and MICP data by iteratively matching the percolation-simulated primary drainage capillary pressure to MICP measurements. The algorithm consists of four major steps, namely, initialization, randomization/correlation, percolation, and inversion.

### 4.4.1 Initialization

The total pore volume is calculated from the input sample dimension and its total porosity. A population of pore bodies is generated following the pore-size distribution estimated by discretizing the NMR $T_2$ spectrum inverted from echo decay acquired from 100% water-saturated core samples. The total number of pore throats is calculated from the total number of nodes in the pore network. A population of pore-throat radii is

initialized with the bimodal Gaussian density function derived from MICP data, as indicated by Eq. 4.4.

### 4.4.2 Randomization/Correlation

Pore bodies are then randomly placed at grids of the cubic network while pore throats are placed between pore-body pairs. Numerous studies indicate that pore-body size and pore-throat size are to some extent correlated (Marschall et al., 1995; Altunbay et al., 2001). However, this correlation does not necessarily apply to all pore-body pairs in rocks subjected to significant diagenesis. To realistically reproduce the correlation between pore throat size and pore body size, only a given portion of body-pairs are enforced to manifest the body-throat correlation rule as in previously stated assumptions (Mohanty and Salter, 1982). The correlation rule enforced by the algorithm is that the radius of the pore throat connecting two pore bodies is proportional to the product of two pore-body radii. Noteworthy is that the distribution of pore throat radius will be altered from the initial values in this step. In addition, the throat-body correlation is considered as independent of the pore-throat size distribution.

### 4.4.3 Percolation

Percolation is given its inception from all six inlet faces of the sample. At a given pressure $P_c$, mercury invades the pore network via paths that are connecting pore throats of size:

$$R_{th} > \frac{2\Gamma\left|\cos\theta\right|}{P_c}, \tag{4.5}$$

where $\Gamma$ is interfacial tension, and $\theta$ is contact angle. All pore bodies along the invaded paths are also occupied by mercury. The saturation of mercury can then be estimated by calculating the ratio between the volume of all occupied pore bodies and the total pore

volume. When the exerted pressure increases, more mercury invades the pore network. A capillary pressure versus mercury saturation curve is then obtained by changing pressure from low to high values to compare to MICP data.

### 4.4.4 Inverse Estimation

The simulated MICP curve is compared to the core MICP measurement. An iterative procedure of refining the throat-body correlation is implemented to invert the optimal pore-network that generates MICP simulations matching core MICP. Due to the random features of the pore network, the inverted pore network might not be the unique answer. However, it should be statistically representative of the properties of the pore-network. Noteworthy is that the initialization of the pore-network model using MICP and NMR measurements significantly reduces the time necessary for convergence and mitigates the possibility that the estimation algorithm be trapped in a local minimum.

## 4.5 VERIFICATION WITH TIGHT-GAS SANDSTONE SAMPLES

The core sample used in this study originates from tight-gas sandstones from the Cotton Valley Formation, East Texas Basin (Liu et al., 2011; Spain et al., 2011). Routine core porosity and permeability, high-pressure MICP (0 – 60, 000 psi), and NMR measurements were acquired on this sample. Figures 1 and 2 show the NMR and MICP measurements acquired on this particular sample, respectively. A bimodal lognormal density function as described in Eq. (4.4) was used to model the distribution of pore volume fraction versus logarithmic pore-throat radius from MICP data. Table 4.2 lists the petrophysical properties and the derived Gaussian parameters of the selected core sample. The values of $w_1$ and $w_2$ suggest that the density function is strongly bimodal in its pore-throat size distribution.

### 4.5.1 Pore Network Model Estimation

We applied the numerical workflow to the tight-gas sample to converge to a final pore network after 11 iterations. The cubic pore network has dimensions of 63x63x63 grids and includes 762,048 pore throats. Figure 4.6 compares the measured NMR $T_2$ spectrum to the simulation at a stage of 100% water saturation with surface relaxivity $\rho$ = 10 μm/s. The NMR simulation algorithm is detailed in Appendix D. A good match indicates that the pore-size distribution in the pore network is consistent with the one evidenced from NMR measurements. The slight discrepancy in the small end of the $T_2$ spectrum is due to the ignored pore volume of pore throats as indicated in the assumption (4).

The primary drainage capillary pressure is simulated by running invasion percolation at different values of capillary pressure. To ensure the stability and reliability of the algorithm, we repeat five simulation runs to compare to the MICP data in Fig. 4.7. All five runs give stable and reproducible values of primary drainage capillary pressure despite the randomly constructed pore networks. The estimated pore network is then used as the basis for subsequent petrophysical modeling.

### 4.5.2 Pore-Throat Radius Distribution

Figure 4.8 shows the normalized pore-throat radius distribution estimated from pore network modeling. The distribution is essentially bimodal lognormal with the log-mean pore throat radius of each mode close to values estimated from MICP data. However, the population of small pore throats is much larger than that of large pore throats. The ratio between total number of small throats to that of large throats is about 4:1. Despite the relatively small contribution of the larger pore throat mode, it topologically connects more than 70% of the total pore volume accessible to the non-wetting phase in the pore network.

### 4.5.3 Fluid Distribution vs. Pore-Body Size

The fluid distribution at specific values of water saturation is quantified by simulating percolation at the corresponding value of capillary pressure. Figure 4.9 shows the water and gas distribution, respectively, at three stages of water saturation: 81%, 46%, and 22%. As the sample is desaturated during a gas-displacing-water drainage process, the population of large pore bodies is gradually occupied by gas. The gas phase occupies a wide distribution and there is no simple cutoff on the pore-size distribution to discriminate water and gas phases. This simulation result is consistent with the observations of oil invading Fontainebleau sandstone described by Zhou et al. (2000) in their CT-based pore network modeling research despite the large difference in pore networks between Fontainebleau sandstone and tight-gas sandstone. A possible explanation for such a behavior is that the two different pore network systems still share some common petrophysical mechanisms regarding body-throat connection and rock-fluid interaction.

We divide the pore-bodies into two groups: large ($R_b$ > 0.5 μm) and small ($R_b$ < 0.5 μm) and analyze the gas invasion in each group. Figure 4.10 shows that the gas phase occupies the large pores sooner than the small pores until it occupies almost all large pores. This phenomenon is attributed to the correlation between pore-throat size and pore-body size. Due to the large number of small pore bodies in the network, there are many pore-body pairs composed of two minimum pore-body sizes connected by small pore throats that can only be invaded by the gas phase at very large values of capillary pressure (or equivalently, high water saturation).

### 4.5.4 NMR Desaturation Simulation and Verification

Using the fluid distribution, we simulated NMR echo decay signals by adding the magnetization decay in each single pore. A regularized inversion technique was applied

to the echo decay signal with 5% additive zero-mean Gaussian noise to estimate the $T_2$ spectrum. The core sample was measured with NMR at three different stages of water saturation: fully brine saturated ($S_w$ = 100%), fresh-stage ($S_w$ = 46%), and a desaturated stage ($S_w$ = 81%). It has been shown previously in Fig. 4.6 that the simulated NMR $T_2$ spectrum agrees with laboratory measurements for a fully brine saturated core sample. Figure 4.11 compares the simulated $T_2$ spectrum to experimental data at the remaining two stages of water saturation. The good match indicates that the pore network reliably reproduces fluid distributions at different stages of saturation, whereby it is judged to be petrophysically representative. Again, ignoring pore volume of pore throats resulted in a slight discrepancy at the short end of the $T_2$ spectrum.

### 4.5.5 Relative Permeability Estimation from Fluid Distributions

Relative permeability is a difficult property to measure in tight-gas sandstone. It is therefore important to estimate relative permeability from some easier-to-perform non-destructive measurements such as NMR (Jorand et al., 2011). This can be achieved by comparing the NMR $T_2$ spectrum of a rock sample at different saturation stages. The NMR $T_2$ spectrum has been long used to estimate absolute permeability based on the Coates and SDR equations (Sigal, 2002):

$$k \propto \phi^m T2LM^2 \tag{4.6}$$

where $\phi$ is porosity, the exponent $m$ is set as 2 for wetting phase and 4 for non-wetting phase, and T2LM represents the logarithmic mean of $T_2$. By analogy, we define logarithmic mean of pore-body size as RBLM. Because $T_2$ and pore-body size exhibit a linear relation, the former can be used to estimate permeability as follows:

$$k \propto \phi^m T2LM^2 \propto \phi^m RBLM^2 \quad . \tag{4.7}$$

Relative permeability of a particular fluid phase can be estimated from its spatial distribution in pore bodies by comparison to the total pore-size distribution (Sigal, 2002; Glover et al., 2006; Jorand et al., 2011):

$$k_{rw} = S_w^m [\frac{RBLM(S_w)}{RBLM(S_w = 1)}]^2 \tag{4.8}$$

and

$$k_{rg} = S_g^m [\frac{RBLM(S_g)}{RBLM(S_g = 1)}]^4 \tag{4.9}$$

Table 4.3 lists the equivalent pore volume occupied by water and gas phases, the log-mean pore-size distribution, and the relative permeability of each phase calculated from Eq. (4.8) and (4.9).

### 4.5.6 Relative Permeability Estimation from Fluid Phase Connectivity

Another approach to estimate relative permeability of a single phase is by quantifying phase connectivity. To this end, we invoke the concept of "effective pore-size distribution" by Archie (1950) or effective medium theory (Kirkpatrick, 1971) to simulate the equivalent MICP curve for the sub pore networks occupied by a particular phase at different stages of saturation. When simulating MICP for a particular phase, the remaining phase is considered as immobile as solid. Figure 4.12 shows the simulated MICP for the effective sub networks during two-phase drainage process. The wetting phase preferentially resides in the smallest pores. As the non-wetting phase occupies the larger pores, the major pore-throat size (inversely proportional to capillary pressure) of the sub pore network occupied by wetting phase gradually decreases (Fig. 4.12a). On the

other hand, the major pore-throat size connecting the sub pore network occupied by the non-wetting phase also decreases (Fig. 4.12b), but its increasing saturation compensates the effect of decreasing pore-throat size on the overall relative permeability.

Comisky et al. (2007) compared 13 models used to derive absolute permeability from capillary pressure curves of tight-gas sandstones and found that Purcell's model (1949) ranked highly in this comparison. Therefore, we adopt Purcell's model (1949) to calculate the permeability of a sub pore network, given by:

$$k \propto \phi \int_0^{100} \frac{dS_{hg}}{P_c^2}, \tag{4.10}$$

where $\phi$ is porosity, $S_{hg}$ is mercury saturation measured with MICP, and $P_c$ is capillary pressure. Hydration water is always present at reservoir conditions, but it cannot be quantified with core MICP measurements due to the drying process involved. We applied the following correction proposed by Hill et al. (1979) to MICP curves to calculate the equivalent gas-water capillary pressure at reservoir conditions:

$$S_g^* = S_{hg}(1 - S_{hw}), \tag{4.11}$$

where $S_g$* is equivalent gas saturation at reservoir conditions and $S_{hw}$ is estimated hydration water saturation. In this particular test sample, $S_{hw}$ is set at 15% based on XRD analysis. Figure 4.13 shows the relative permeability values for the gas and water phases, which are consistent with values obtained from the estimated fluid distributions.

## 4.6 DISCUSSION AND LIMITATIONS

Numerous results have been documented about the use of MICP data to constrain pore network models. However, few of them use additional NMR data as constraint. In

our work, constraints from both NMR and MICP data reduce non-uniqueness associated with pore network construction, which ensures its petrophysical reliability for subsequent petrophysical modeling. Another advantage of the Matlab-based pore-network algorithm is its computational efficiency: it only aims at generating a petrophysically representative network that simultaneously honors pore-size distribution and pore connectivity as evidenced by NMR and MICP. The method bypasses the simulation of complex sedimentary and diagenetic processes as is done with advanced pore network simulation (Bryant et al., 1993). In addition, the method does not resort to solving complex flow equations to derive relative permeability. A forward modeling of invasion percolation in a cubic sample of dimension 100 μm x 100 μm x 100 μm or 63x63x63 grids takes less than 40 seconds of CPU time with a desktop PC (3.4 GHz CPU) and Matlab platform, which makes it possible to efficiently estimate the corresponding pore network model.

However, it should be noted that many assumptions are made in this work to simplify the pore network modeling. Consequently, the simplified model could be subject to errors whenever those assumptions are invalid. The pore-body geometries formed by sedimentary grains are not regular, which causes pendular rings of water that are not considered in this work. The coordination number in a highly diagenetic rock is not constant. In fact, the coordination number can be a variable ranging from 1 to 19 (Al-Kharusi and Blunt, 2007). The effect of clay and the associated hydration water needs to be cautiously corrected to derive realistic values of capillary pressure and relative permeability at reservoir conditions. Wettability alteration may occur during oil-water displacement while mixed wettability is often encountered in carbonate rocks. The relative permeability modeling may also be compromised when ignoring the interaction between fluids and considering one fluid phase as solid cementation. In addition, simulation of imbibition has been proven to be a much more challenging task

(Prodanovic and Bryant, 2006), which should be studied in detail in the next phase of this research.

## 4.7 CONCLUSIONS

An efficient pore-network algorithm was developed and successfully verified to enable inverse estimation of petrophysically representative pore networks from NMR and MICP data. The integration of NMR and MICP data significantly reduces the uncertainty of the pore network model. It quantifies the pore-throat radius distribution and the quasi-static fluid distribution during two-phase drainage displacement. It was found that immiscible fluids in rocks exhibit a wide spatial distribution rather than a clear cutoff separation. It is still true that the non-wetting phase preferentially invades large pore bodies first when a partial body-throat correlation exists. The fluid distribution versus pore-body size is used to simulate NMR desaturation experiments which are verified with laboratory measurements. Percolation simulation of the effective sub-pore-networks occupied by a particular fluid phase quantifies its relative permeability at different stages of saturation, which is consistent with values estimated from the pore-body size distribution occupied by this fluid phase. The method was successfully verified with a tight-gas sandstone sample from the Cotton Valley Formation, East Texas.

**Table 4.1:** Surface-to-volume ratio of simple pore-body geometries.

| **Pore Geometry** | ***Surface*** | ***Volume*** | ***Surface/Volume*** |
|---|---|---|---|
| Sphere (radius = $r$) | $4\pi r^2$ | $4\pi r^3 / 3$ | $3 / r$ |
| Cubic (length = $a$) | $6a^2$ | $a^3$ | $6 / a$ |
| Open-ended cylinder (radius = $r$; height = $h$) | $2\pi rh$ | $\pi r^2 h$ | $2 / r$ |

**Table 4.2:** Petrophysical properties of the tight-gas sandstone sample used for pore network modeling algorithm verification.

| $\phi$ **(frac)** | $k$ **(mD)** | $\mu_1$ **(µm)** | $\mu_2$ **(µm)** | $\log\sigma_1$ | $\log\sigma_2$ | $w_1$ | $w_2$ |
|---|---|---|---|---|---|---|---|
| 0.07 | 0.012 | 0.1225 | 0.0289 | 0.127 | 0.540 | 0.606 | 0.394 |

**Table 4.3:** Relative permeability estimated from effective sub pore networks occupied by the water and gas phases at different water saturation stages.

| | **Water Phase** | | **Gas Phase** | |
|---|---|---|---|---|
| | RBLM (μm) | $k_{rw}$ (frac) | RBLM (μm) | $k_{rg}$ (frac) |
| $\boldsymbol{S_w}$ **= 100%** | 0.708 | 1.0 | 0 | 0 |
| $\boldsymbol{S_w}$ **= 81%** | 0.386 | 0.195 | 1.894 | 0.009 |
| $\boldsymbol{S_w}$ **= 46%** | 0.156 | 0.0103 | 1.479 | 0.371 |
| $\boldsymbol{S_w}$ **= 22%** | 0.067 | 0.0004 | 0.965 | 0.688 |
| $\boldsymbol{S_w}$ **= 0%** | 0 | 0 | 0.708 | 1.0 |

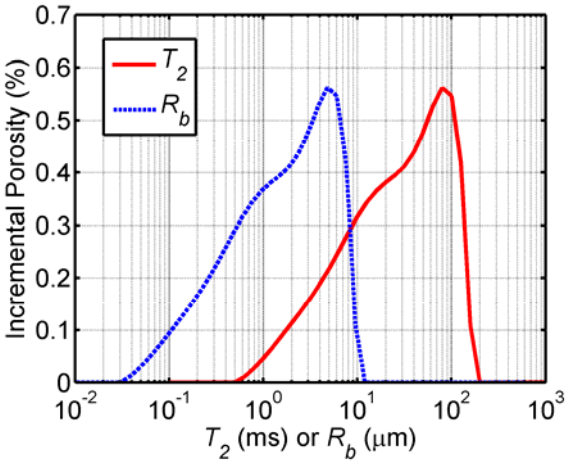


**Figure 4.1:** Example of converting the NMR $T_2$ spectrum into a pore-body size distribution assuming spherical pore bodies and rock surface relaxivity $\rho$ = 10 μm/s.

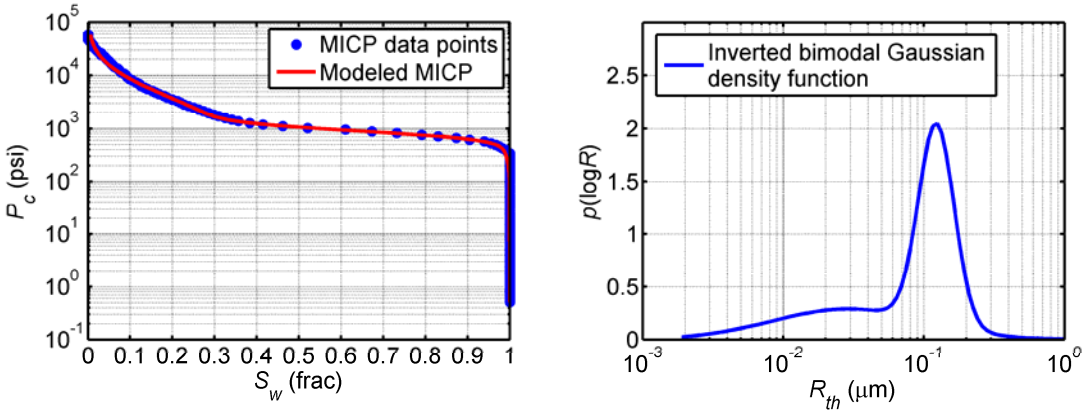


**Figure 4.2:** Example of derivation of a bimodal log-normal pore-size distribution from MICP data using the inversion method (see Chapter 2). The vertical axis of pore-throat size distribution in the right-hand panel describes the pore volume being invaded at a capillary pressure corresponding pore throat radius described in the horizontal axis.

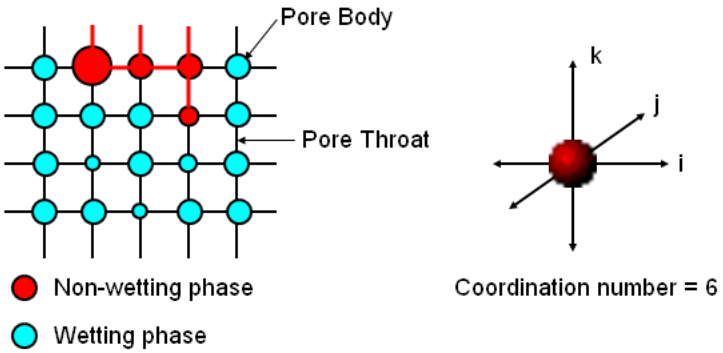


**Figure 4.3:** Schematic planar view of a 3D cubic pore network model (left side) and the corresponding pore body connectivity (right side).

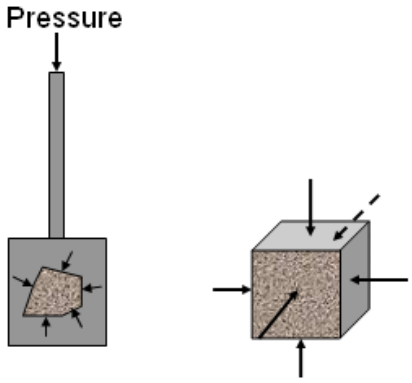


**Figure 4.4:** Invasion percolation from six inlet faces of a cubic sample to emulate the process of pressure-controlled mercury porosimetry (Webb, 2001). Left side: mercury porosimetry; Right side: percolation on a cubic sample.

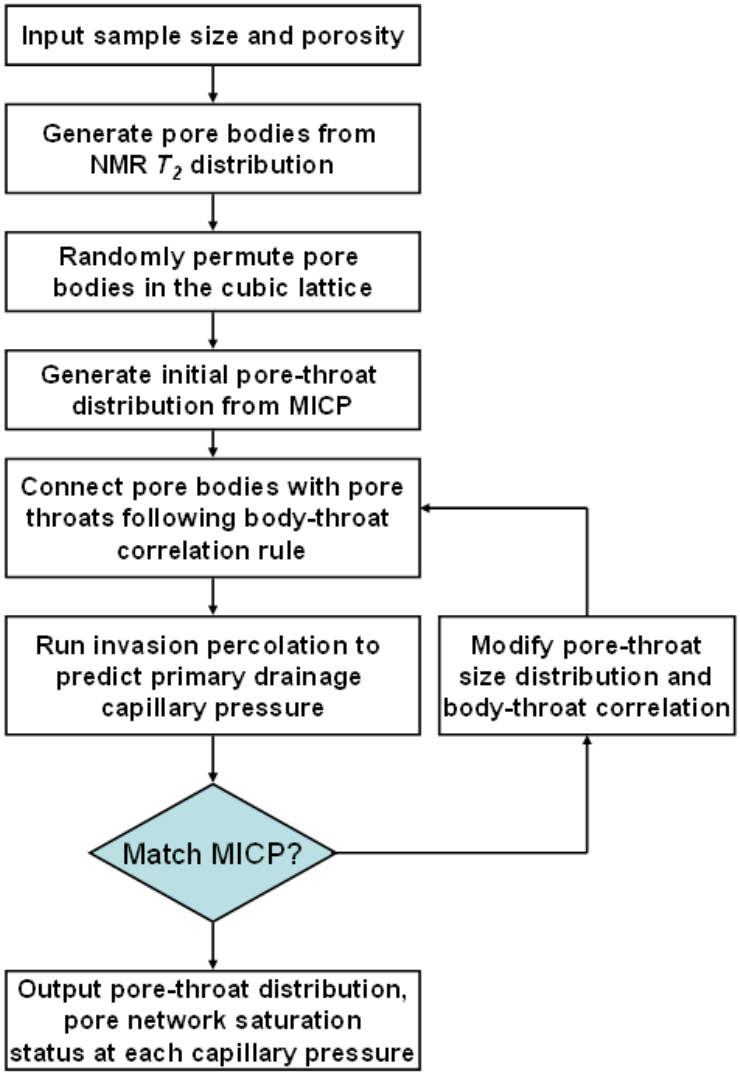


**Figure 4.5:** Workflow used to estimate a representative 3D cubic pore network model constrained by NMR and MICP data.

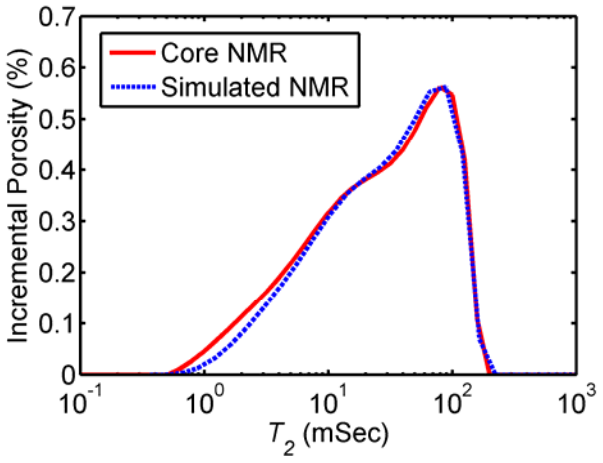


**Figure 4.6:** Comparison of NMR simulation to core NMR measurement at 100% water saturation.

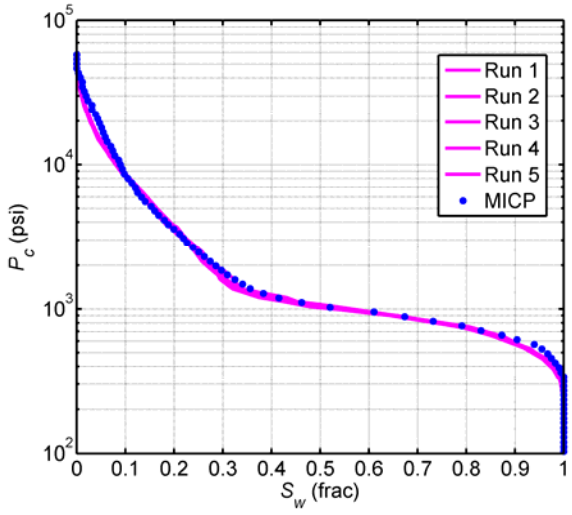


**Figure 4.7:** Comparison of simulations of primary drainage capillary pressure (five runs) to core MICP data.

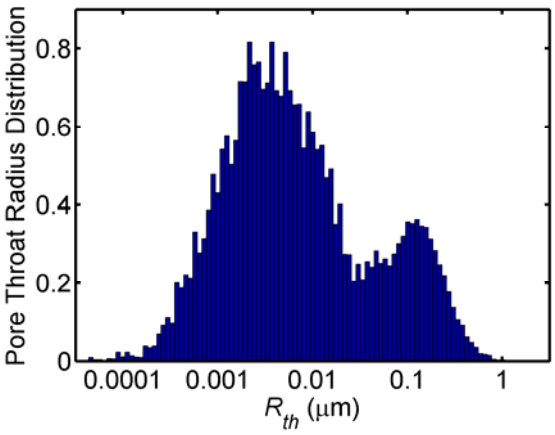


**Figure 4.8:** Normalized pore-throat radius distribution estimated from pore network modeling. The vertical axis represents the frequency of a pore-throat size in this pore network system.

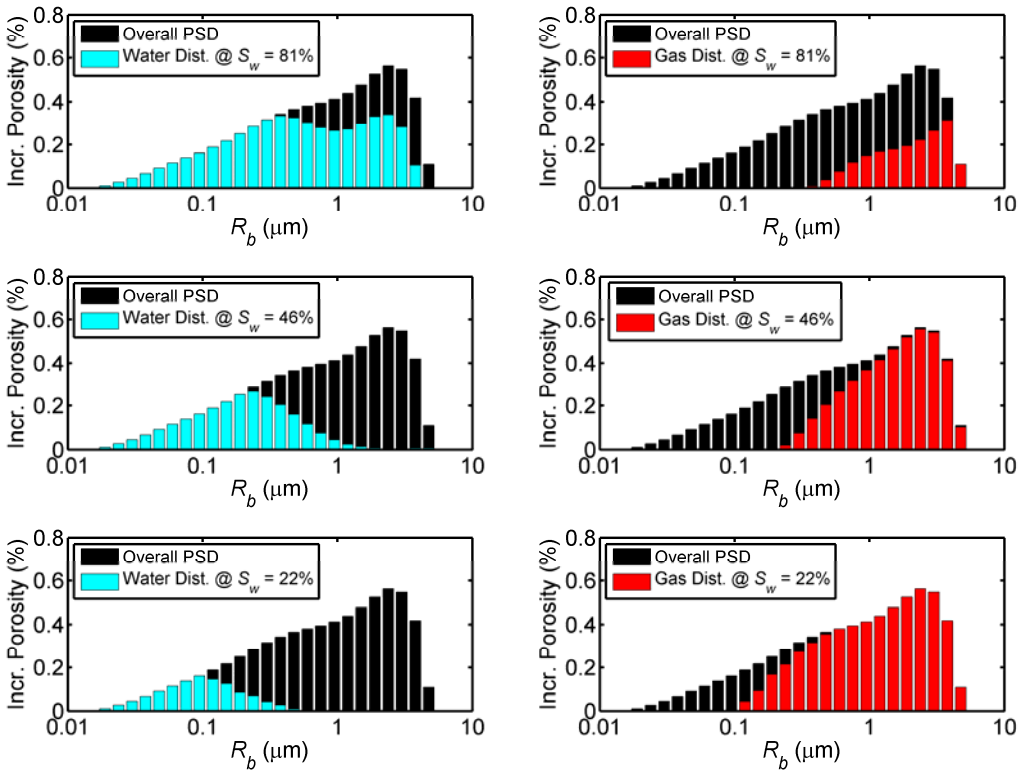


**Figure 4.9:** Fluid distributions within different pore-body sizes at three stages of water saturation. Top row: 81%; Middle row: 46%; Bottom row: 22%.

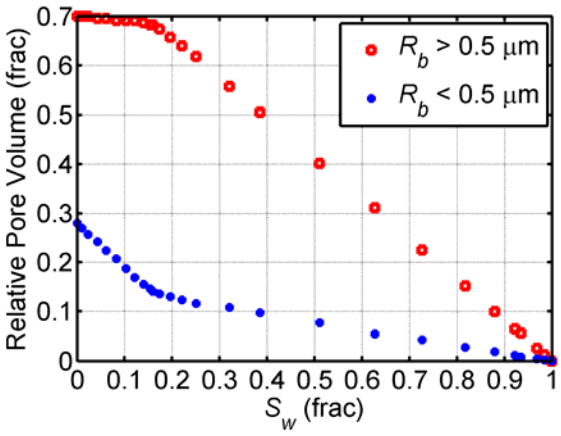


**Figure 4.10:** Pore volume occupied by the invading gas phase at different stages of drainage.

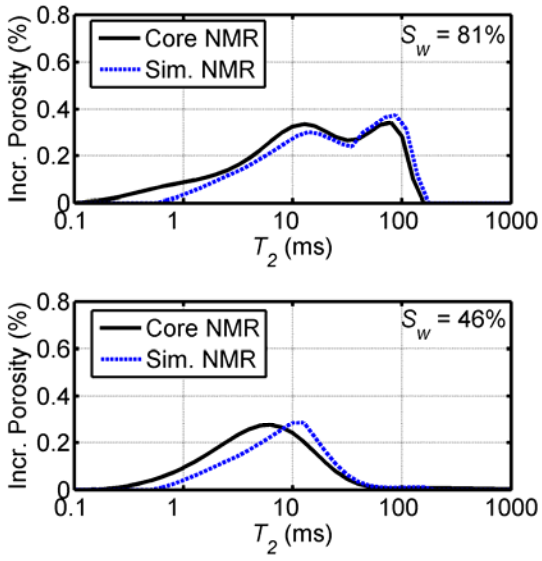


**Figure 4.11:** Comparison of simulated NMR $T_2$ spectra with measured NMR $T_2$ spectra at 81% and 46% water saturation, respectively.

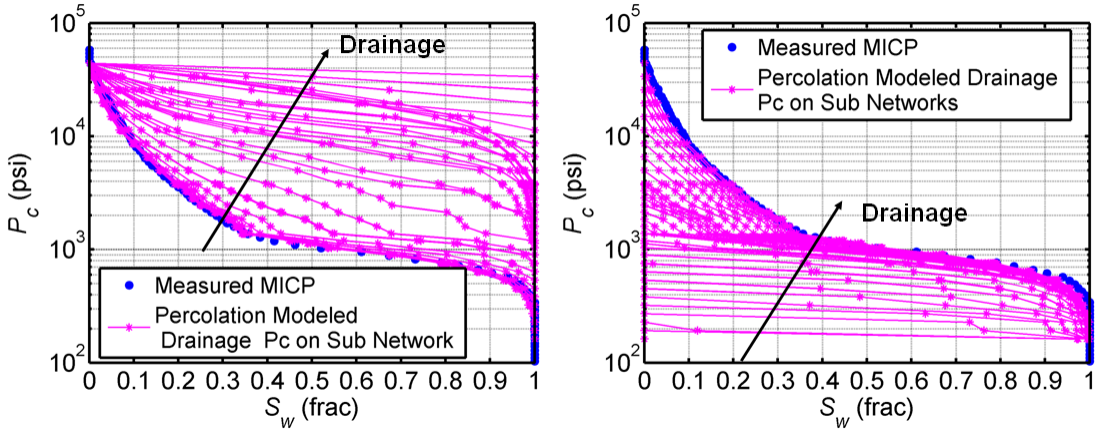


**Figure 4.12:** Simulated primary drainage capillary pressure curves for the effective pore network occupied by wetting (left panel) and non-wetting phase (right panel) during a drainage process.

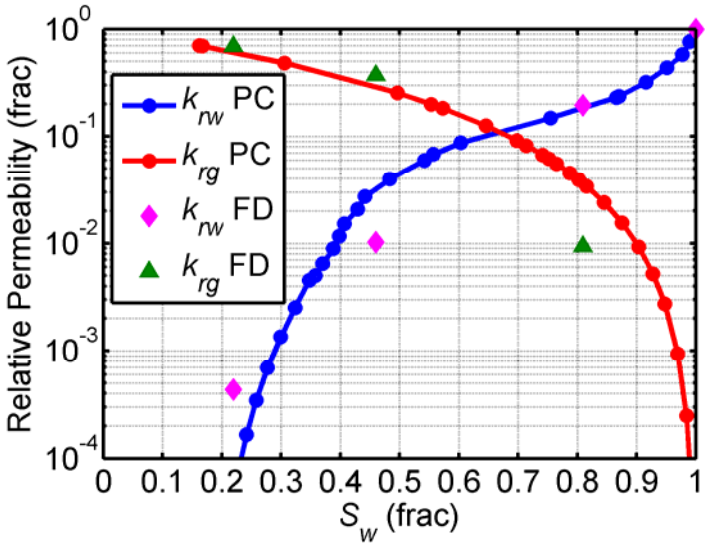


**Figure 4.13:** Water-gas relative permeability estimated from fluid distribution and phase connectivity. FD: Fluid distribution; PC: Phase connectivity.

# Chapter 5: Saturation-Height and Invasion Consistent Hydraulic Rock Typing Using Multi-Well Conventional Logs in Deepwater Turbidite Reservoirs

This chapter extends the understanding of fluid distributions from microscopic scale to macroscopic scales for more accurate rock typing. Hydraulic rock typing is based on pore geometry, which relates to saturation-height modeling at a later stage in reservoir characterization. Additionally, pore geometry affects mud-filtrate invasion under over-balanced drilling conditions. Reliable hydraulic rock typing should simultaneously honor: (1) fluid distributions resulting from hydrocarbon migration in the vertical direction, and (2) mud-filtrate invasion in the radial direction. Such a condition becomes critical when hydraulic rock typing is performed with well logs acquired from multiple wells penetrating the same or different capillary transition zones.

This chapter considers three conventional core-based rock typing methods, namely Leverett's reservoir quality index, Winland $R_{35}$, and Amaefule's flow zone index, to appraise whether rock classifications can be extrapolated from core-data to well-log domains. A new quantitative log attribute is derived from well logs to assist hydraulic rock typing, which integrates in-situ reservoir capillary pressure ($P_c$) and initial water saturation ($S_{wi}$). The assumption is that the reservoir under study underwent hydrocarbon migration wherein vertical fluid distribution is still well represented by the primary-drainage capillary pressure curve. Petrophysical properties that are closely linked to pore geometry are quantified by invoking both Leverett's *J*-function and Thomeer's *G*-factor. The new log attribute is based on standard well-log analysis and only requires conventional well logs for its application. Thus, it can be generally applied to both clastic and carbonate reservoirs in multi-well contexts. It overcomes the limitation of the bulk volume water method, which is only applicable to reservoir zones that are at irreducible

water saturation. Most importantly, it provides good initial estimates to constrain in-situ dynamic rock-fluid properties such as capillary pressure and relative permeability.

The method proceeds with initial estimates of dynamic properties to construct multi-layer petrophysical models with a common stratigraphic framework (CSF) for each rock type, and to simulate the process of mud-filtrate invasion. By honoring all the available well logs with the process of mud-filtrate invasion, pseudo dynamic rock-fluid petrophysical properties (capillary pressure and relative permeability) are calculated for each rock type that are amenable to reservoir modeling and simulation. Synthetic cases constructed from real reservoir analogues are used to test the method with pre-defined rock-type models. Two field cases of turbidite (submarine fan) siliciclastic reservoirs are used to verify the reliability of the new rock-typing method.

## 5.1 INTRODUCTION

G.E. Archie (1950) defined petrophysical rock type based on the associated pore-size distribution, which links the rock's static and dynamic petrophysical properties. Archie also mentioned the possibility of using various types of well logs to probe the pore-size distribution and identify petrophysical rock types. Rock typing is a key element necessary to construct reliable three-dimensional reservoir models. Hydraulic rock typing specifically refers to hydraulic properties of reservoir rocks, including storage and flow capacity, and it provides a basis for many other reservoir characterization efforts such as saturation-height analysis and dynamic reservoir modeling (Rushing et al., 2008). Numerous hydraulic rock typing methods were advanced in the past; some of them use core measurements, such as Leverett's reservoir quality index (RQI) (Leverett, 1941), Winland $R_{35}$ (Pittman, 1992), and flow zone index (FZI) (Amaefule et al., 1993), whereas some others are mainly based on well logs, such as those defined with the concept of

electrofacies (Serra and Abbott, 1980) and bulk volume water (BVW = $\phi_t S_w$, Buckles, 1965). Few authors have discussed the technical challenges remaining to map hydraulic rock types from core to well logs accurately and reliably. Common practice uses core-established rock types and their corresponding well-log responses to identify and classify rock types in a supervised-learning approach. Often, this method is not satisfactory because well-log-defined facies may not be directly related to pore geometry. Indeed, most well logs are more sensitive to mineralogy and pore-filled fluids than to pore geometry. Resistivity logs are possibly the best indicators of rock texture. However, in many deepwater turbidite oil reservoirs, capillary transition effects render resistivity logs difficult to use in rock typing across multiple wells due to fluid saturation changes with height (Fig. 5.1). This chapter introduces a new method to classify rocks based solely on well-log-derived properties; it probes the pore geometry, eliminates the effect of capillary transition on resistivity logs, and reconciles rock classes with core MICP data. Additionally, it extracts important reservoir quality information from the reservoir's saturation-height behavior and has practical applications in reservoir development such as horizontal well steering, facies interpretation, and reservoir connectivity analysis. The method also revisits Archie's rock type definition and enables effective core-log integration.

In the process of reservoir characterization, saturation-height modeling needs to be rock-type based, i.e., different rock types are associated with different saturation-height relations (Lucia, 1999). Core-derived rock types and their capillary pressure properties should be consistent with well-log-derived saturation-height distributions of water. At the same time, under relatively steady drilling conditions, mud-filtrate invasion is dominantly controlled by rock petrophysical properties. The radial invasion profile thus provides important information for hydraulic rock typing. A reliable hydraulic rock

typing scheme must honor both saturation-height variations in the vertical direction and mud-filtrate invasion in the radial direction. Several authors documented cases in which petrophysical properties were inferred from the physics of mud-filtrate invasion (Salazar et al., 2006; Heidari et al., 2011). This chapter extends the concept of mud-filtrate invasion to integrate saturation-height modeling and establish rock-type-based dynamic rock-fluid petrophysical properties.

This study first compares three well-known core-based quantifying methods of hydraulic rock types and concludes that these methods are closely correlated due to their similar mathematical formulae and underlying petrophysical principles (major pore-throat size or hydraulic radius). We then select Leverett's RQI (the simplest among the three methods) and derive its equivalent property from well logs using Leverett's *J*-function to assist rock typing in multiple wells that penetrate the same capillary transition zone. For each identified rock type, we select a thick zone to simulate well logs under mud-filtrate invasion and calibrate the associated dynamic petrophysical properties. The workflow is referred to as "invasion facies" modeling. Final products from rock typing are not only a distribution of rock types along the well trajectory, but also the associated static and dynamic petrophysical properties, which are important for reservoir modeling and simulation. We use the calibrated capillary pressure curves to remodel saturation height based on the diagnosed rock types and compare them to the vertical distribution of resistivity-derived water saturation.

The new method for rock typing is verified with measurements acquired in two field cases of thick turbidite oil reservoirs. In case no. 1, we show how saturation-height and invasion consistent rock typing provides important information for horizontal well placement and steering. In case no. 2, we describe results of the application of the method in multiple wells to assist stratigraphic and sedimentary interpretation.

## 5.2 RQI VS. $R_{35}$ VS. FZI

The three core-derived quantities have been widely used for hydraulic rock typing. Arguments regarding their strengths and weaknesses can be found in numerous publications on a case-by-case basis. Although these quantities originated from different authors using different approaches (empirical vs. experimental vs. analytical), they bear more similarities than differences owing to the common underlying petrophysical property that they intend to quantify - pore-throat size or hydraulic radius. The three quantities are functions of porosity and permeability measured with routine core analysis. Let $\Theta$ stand for any of the above quantities. Their common formulae can be expressed as:

$$\log\Theta = x\log k + y\log\phi + z\,. \tag{5.1}$$

We compared the coefficients *x, y,* and *z* associated with these formulae in Table 5.1 and found that coefficients *x* are all close to 0.5, which has a well-established physical basis: permeability is proportional to the square of pore-throat radius. To emphasize their similarity, we repeat numerical testing of the correlation between these quantities using randomly generated synthetic core porosity-permeability points (Fig. 5.2). Correlations between each pair of quantities on a logarithmic scale are consistently higher than 0.9. This simple exercise indicates that the key to hydraulic rock typing for reservoir characterization does not rest on the selection of the three core-based quantities but on how to map them accurately into the well-log domain.

## 5.3 METHOD AND WORKFLOW

### 5.3.1 Conventional Well-Log Analysis

Core-calibrated conventional well-log analysis is critical to estimate relevant petrophysical properties, such as volumetric concentration of shale ($C_{sh}$), total porosity ($\phi_t$), and connate-water saturation ($S_w$). All these petrophysical properties relate more

directly to hydraulic rock types than to apparent logs. Therefore, it is here suggested that rock typing be based on these petrophysical properties whenever possible.

### 5.3.2 In-situ Reservoir Capillary Pressure

In a hydraulically connected reservoir, in-situ reservoir capillary pressure ($P_c$) is calculated from the difference between true vertical depth (TVD) and the free water level (FWL), which can be derived from pressure measurements, resistivity logs, or core MICP data, namely,

$$P_c = (\Delta\rho)gh = 0.433 \times \Delta\rho \times (FWL - TVD), \tag{5.2}$$

where $\Delta\rho$ is density difference between connate water and hydrocarbon in g/cm$^3$; TVD and FWL are depths in ft.

### 5.3.3 Well-Log-Derived Leverett's RQI

Leverett's RQI can be derived from $P_c$ and initial connate-water saturation ($S_w$) using the empirical *J*-function model (Darling, 2005; Torres-Verdín, 2012)

$$S_w = S_{wirr} + aJ^b \Rightarrow J(S_w) = \left(\frac{S_w - S_{wirr}}{a}\right)^{\frac{1}{b}}, \tag{5.3}$$

together with Leverett's capillary pressure model, given by

$$\sqrt{\frac{k}{\phi}} = \frac{J(S_w)}{P_c} \times \sigma\cos\theta = \left(\frac{S_w - S_{wirr}}{a}\right)^{\frac{1}{b}} \times \frac{\sigma\cos\theta}{P_c}, \tag{5.4}$$

where $S_w$ is initial water saturation, $S_{wirr}$ is irreducible water saturation (which is set to 0.01 lower than the minimum water saturation in the entire reservoir column, Darling, 2005); $a$ and $b$ are constants derived from core-measured capillary pressure curves; $\sigma\cos\theta$ is the product of interfacial tension and contact angle, which is assumed constant in the same reservoir; $P_c$ is in-situ reservoir capillary pressure in psi. Equation (5.4) provides a link between saturation-height and reservoir quality index; it assumes that all reservoir rocks exhibit the same $S_{wirr}$ and constants $a$ and $b$. This assumption is not always true, but it does provide a first-pass quantification of reservoir quality based on a

well-log-derived saturation-height relationship, and it remains reliable in many field cases.

### 5.3.4 Leverett's *J* vs. Thomeer's *G*

An alternative parameter to quantify pore geometry from well-log-derived saturation-height relation is Thomeer's *G* factor. Thomeer (1960) proposed a model to define mercury/air capillary pressure curves given by

$$\frac{S_b}{S_{b\infty}} = e^{-G/\log(P_c/P_e)}, \tag{5.5}$$

where $S_b$ is mercury saturation at capillary pressure $P_c$; $S_{b\infty}$ is mercury saturation at infinite capillary pressure; $G$ is pore geometrical factor reflecting the distribution of pore throats and their associated pore volume; $P_e$ is the extrapolated displacement or entry pressure. Again, due to their similar mathematical expressions, Leverett's $J$ and Thomeer's $G$ factors are highly correlated to each other. Numerical testing using randomly generated saturation-height points consistently gives rise to correlation coefficients higher than 0.9 (Fig. 5.3). For simplicity, we consistently use Leverett's $J$ function and RQI to quantify rock types in this chapter.

### 5.3.5 Rock Classification and Validation

For each field case, we first perform core-based hydraulic rock typing with Leverett's RQI. We then consider the well-log-data domain to classify rock types via cluster analysis on several relevant petrophysical attributes, including volumetric concentration of shale, total porosity, water saturation in the irreducible zone, and well-log-derived RQI (as in Eq. 5.4) in the capillary transition zone. Because both core- and well-log-based rock typing include the same quantity - RQI, the correlation between core-defined and well-log-derived rock types is significantly enhanced. Rock classification results can be validated by predicting permeability based on the well-log-

derived rock types and compared to core measurements. In both cases, we show that a reliably-defined rock type distribution can improve permeability estimation.

### 5.3.6 Calibration of Dynamic Petrophysical Properties from Invasion Simulation - Invasion Facies Modeling

After rock typing, we calculate the porosity-permeability trend, the saturation-height relation, and capillary pressure curves for each rock type. We proceed to calibrate capillary pressure and relative permeability for each rock type by simulating the process of mud-filtrate invasion at reservoir conditions. This simulation involves rock petrophysical properties such as porosity, permeability, capillary pressure, and relative permeability. It also considers drilling engineering parameters such as mud type, invasion duration, and overbalance pressure. Fluid properties such as density, viscosity, salt concentration, and temperature are also taken into consideration. With stable drilling conditions and constant fluid properties, rock petrophysical properties determine the radial distributions of water saturation, which are used to calculate radial distributions of physical properties such as electrical resistivity, density, and migration length, to numerically simulate the corresponding apparent resistivity, density, and neutron logs (Gandhi et al., 2010). By matching all available well logs after mud-filtrate invasion, we obtain a set of estimated rock-fluid dynamic petrophysical properties, including both capillary pressure and relative permeability. We adopt Voss et al.'s (2009) procedure to iteratively estimate petrophysical properties using UTAPWeLS. The measured well logs must be corrected for borehole environmental effects to be compared to numerical simulations. Brooks-Corey's parametric equations are adopted to describe saturation-dependent capillary pressure and relative permeability (Corey, 1994; Peters, 2012), namely

$$P_c = P_c^0 \sqrt{\frac{\phi_t}{k}} (1 - S_N)^{e_p}, \tag{5.6}$$

where $P_c$ is capillary pressure in psi, $P_c^0$ is a constant coefficient in psi.darcy$^{1/2}$, $\phi_t$ is total porosity, $k$ is permeability in Darcy, $e_p$ is pore-size distribution exponent, and $S_N$ is normalized wetting-phase saturation, given by

$$S_N = \frac{S_w - S_{wr}}{1 - S_{wr} - S_{nwr}}, \tag{5.7}$$

where $S_w$ is wetting-phase saturation, $S_{wr}$ is residual wetting-phase saturation, and $S_{nwr}$ is non-wetting phase residual saturation. Wetting and non-wetting saturation-dependent relative permeabilities, $k_{rw}$ and $k_{rnw}$, respectively, are given by

$$k_{rw} = k_{rw}^0 S_N^{e_w} \tag{5.8}$$

and

$$k_{rnw} = k_{rnw}^0 (1 - S_N)^{e_{nw}} \tag{5.9}$$

Note that $S_{nwr}$ must be set to zero in a primary drainage capillary pressure curve while it is non-zero in an imbibition capillary pressure curve (Fig. 5.4).

### 5.3.7 Saturation-Height Modeling with Brooks-Corey's Drainage Capillary Pressure Model

After calibrating each rock type's capillary pressure with invasion simulation, we perform saturation-height modeling on a rock-type basis. In a water-wet reservoir, saturation height modeling is performed by combining Eqs. (5.2), (5.6), and (5.7), i.e.

$$S_w(H) = S_{wirr} + (1 - S_{wirr})[1 - (\alpha H)^{1/e_p}] \tag{5.10}$$

and

$$\alpha = \frac{0.433 \Delta\rho}{P_c^0} \sqrt{\frac{k}{\phi}} \tag{5.11}$$

where $S_{wirr}$ is irreducible water saturation and $e_p$ is pore-size distribution exponent; $H$ is height above the FWL in ft, $\alpha$ is a scale coefficient that depends on rock type and density

difference between water and hydrocarbon. It is necessary to estimate $S_{wirr}$, $\alpha$, and $e_p$ for each rock type under a specific reservoir context to achieve satisfactory saturation-height modeling in formations without well penetration.

## 5.4 SYNTHETIC CASE

A synthetic reservoir model is constructed to gain understanding on how capillary transition affects rock typing via conventional methods such as E-facies and Buckle's number. The reservoir model is an ideal cyclic turbidite sequence with a total thickness of 300 ft. Three hydraulic rock types of different grain sizes (therefore different pore-throat radii) are stacked to form fining-upward sequences (grain-size: RT4 > RT3 > RT2). Bed thickness is uniformly set to 3 ft to minimize thin-bed effects on well logs. Sequences are separated by pure-shale barriers. The reservoir has irreducible water saturation at the top and water saturation gradually increases toward the FWL at the bottom. Figure 5.5 shows the numerically simulated well logs (Tracks 1 - 4), conventional well-log analysis results (Tracks 5 - 6), and rock-typing results obtained with different methods (Tracks 7 - 11). Lithofacies (Track 7) can differentiate sand from shale, but cannot distinguish sands of different grain sizes because all sands are essentially clay free. E-facies from all logs and BVW (Tracks 8 and 9) are significantly biased when moving downward toward the FWL due to fluid effects. We observe that reservoir quality is overestimated in the upper zone while it is underestimated in the lower zone. Rock types diagnosed with the new method (Track 10) yield approximately the same vertical distribution as in the pre-defined (original) model (Track 11). This synthetic case indicates that variations of water saturation due to capillary transition and their effects on well logs must be corrected to enable reliable rock classification across the entire reservoir. Otherwise, resistivity logs, the most texture-sensitive logs among all conventional logs, cannot be included in the

process of rock typing. Consequently, there is great uncertainty associated with rock typing when it is only based on nuclear logs due to their relatively low sensitivity to rock texture.

## 5.5 FIELD CASE NO. 1: DEEPWATER CENTRAL NORTH SEA

### 5.5.1 Reservoir Background

The first field example is a sandstone dome structure of Paleocene age that is located in the Central North Sea (Martin et al., 2005; Salazar et al., 2007). Near-continuous sandstone bodies were formed by overlapping submarine fans during the early Paleocene. Lithology in the preserved Paleocene strata mainly consists of siliciclastic sediments with minor presence of coal, tuff, volcaniclastic rocks, marls, and reworked carbonate sediments (Ahmadi et al., 2003). The reservoir has a typical vertically segregated fluid distribution with a gas cap (gas-oil-ratio = 871 scf/bbl) of average thickness of 192 ft and an oil column (gravity = $40^{o}$ API) of average thickness of 184 ft supported by an active aquifer zone (BP, 2003).

The formation under analysis (B1/B2 sands) is predominantly composed of non-calcareous, blocky and sandy high-density gravity-flow deposits interbedded with gray mudstones. Reservoir units within the formation consist of alternations of sandstones of different grain sizes: fine- to medium-grained, or even coarse-grained. Total porosity ranges from 18 to 28 p.u., and horizontal permeability varies from 10 md in low-quality zones to more than 1,000 md in high-quality intervals.

Hydraulic connectivity in the reservoir section under analysis is confirmed by reservoir pressure measurements. The vertical reservoir fluid distribution agrees well with the saturation derived from the core-measured primary drainage capillary pressure

curve. It is observed that the entire reservoir section under analysis (B1/B2 sands) is in a capillary transition zone with free water.

Well logs from three wells are available for rock typing. The three wells were drilled with OBM. Well No. 1 (key well) is a vertical well penetrating the FWL and wells nos. 2 and 3 are horizontal wells drilled 80 - 100 ft above the FWL.

### 5.5.2 Core-Based Rock Typing and Interpretation

Hydraulic rock types are first established from routine core porosity-permeability measurements (Fig. 5.6). Six hydraulic rock types are identified from the histogram of RQI. Table 5.2 describes the statistics of petrophysical properties for each rock type. We observe that rock types 1- 4 have a largely overlapping porosity range, which indicates that these rock types have similar grain-sorting. However, their average horizontal permeability exhibits a ratio around 2 - 2.5, which indicates that their average pore-throat radius ratio is approximately 1.5 (i.e., $1.5^2 = 2.25$). Because young sediments have not undergone significant diagenesis, the controlling factor for permeability variations is mean grain size. By inspecting the sand grain-size scale, mean grain size of these four rock types is interpreted (from fine to coarse) as lower fine (LF), upper fine (UF), low medium (LM), and upper medium (UM). In rock types 5 and 6, clay cementation plays an important role in reducing permeability. They are mostly composed of very fine (VF) and silty (ST) grains. There are several core samples with permeability higher than 1000 md which are found to contain lower coarse-grained sandstones (LC or RT0). Due to their relatively small population, it is difficult to separate them as one rock class via cluster analysis. The interpreted grain size information greatly contributes to the diagnosis of sedimentary facies in this reservoir.

### 5.5.3 Well-Log-Based Saturation-Height, Rock Typing, and Permeability Estimation

We perform core-calibrated, conventional well-log analysis in the key well (no. 1) to calculate volumetric concentration of shale, total porosity, and water saturation (Fig. 5.7, Tracks 5 - 6). From reservoir pressure measurements, we identify fluid types and their contacts as well as the FWL. Well-log-derived saturation-height and core-measured capillary pressure agree well (Fig. 5.8). From saturation-height, we derive Leverett's RQI using Eq. (5.4) with constants $a$ = 0.33, $b$ = -0.62, and $S_{wirr}$ = 0.04. We then classify rocks based on a combination of several petrophysical attributes, including volumetric concentration of shale, total porosity, and log-derived RQI in the capillary transition zone. Figure 5.7 shows the results of rock classification (Track 7) and the permeability estimated from rock types (Track 8). Estimated permeability agrees well with core-measured permeability (with Klinkenberg correction).

### 5.5.4 Invasion Facies Modeling

After calculating the well-log-based saturation-height relation, we obtain an average capillary pressure curve for each rock type by curve-fitting with the same rock type. Core calibration is preferred but not required here. We select thick zones of rock types 1 to 3 at different height to simulate the radial invasion profile under observed drilling and reservoir conditions to further calibrate capillary pressure and relative permeability curves. In this case, the top formation is saturated with light condensate with almost no free water. When invaded by OBM, the formation should not exhibit radial variations of water saturation in theory. However, we still observe a small separation between apparent resistivity logs with different depths of investigation, which has two possible explanations: The first explanation is that when overbalance pressure is very high (1,400 psi in this case), it can still displace a small amount of capillary-bound water deeper into the reservoir at this height above FWL (Fig. 5.8). The second explanation is

that surfactants in OBM mud filtrate alter rock wettability, which subsequently generates more free water (La Vigne et al., 1997; Salazar et al., 2007; Pour et al., 2011). In both cases, capillary pressure and relative permeability play important roles in determining how this relatively small volume of free water is distributed in the invaded zone regardless of mechanistic origin. Therefore, it is possible to calibrate rock dynamic petrophysical properties by honoring the effects of mud-filtrate invasion on various well logs.

Assuming that the rock is preferentially water-wet, OBM invasion becomes a drainage process. We numerically simulate gamma-ray, bulk density, and array-induction apparent resistivity logs in this example. Neutron and PEF logs are excluded due to environmental correction problems. Table 5.3 lists the simulation parameters and Figs. 5.9 – 5.10 show the radial invasion profiles and numerical well-log simulation for rock types 1 to 3 after 2 days of OBM invasion. It is observed that the best rock type gives rise to the highest resistivity due to the lowest connate water saturation. Table 5.4 and Fig. 5.11 summarize the final capillary pressure and relative permeability curves for the selected rock types. These properties simultaneously honor routine core measurements, the well-log-derived saturation-height relation, and mud-filtrate invasion. Therefore, they are suitable for upscaling in reservoir simulation grids. One key advantage of invasion-calibrated dynamic petrophysical properties is that these properties have been calculated at reservoir conditions.

### 5.5.5 Saturation-Height Modeling After Invasion Simulation

Using the capillary pressure curves calibrated from invasion simulation, we derive saturation-height relations for rock types 1 to 3 (Table 5.5). Saturation-height curves for each rock type are plotted together with the resistivity-derived water saturation (Fig. 5.7,

track 6), indicating a good agreement. We fit 16 core MICP measurements with Brooks-Corey's model and found that the parameters included in Brooks-Corey's function were closely correlated to Leverett's reservoir quality index. Better rock quality indicates higher $P_c^0$ and $e_p$ together with lower $S_{wirr}$ and $P_e$ (Fig. 5.12). These values are also comparable to those calibrated with invasion simulation.

### 5.5.6 Rock Typing and Horizontal Well Steering

After reconciling rock types with their saturation-height relations in the key well, we examine the remaining two horizontal wells (nos. 2 and 3) drilled in the same formation to study lateral variability of reservoir quality. We perform conventional well-log analysis in well no. 2 and find that water saturation in sandstones is approximately 30% with a height above FWL of 100 ft. From the projection of the well-log-derived saturation-height data shown in Fig. 5.8 (red dots), we observe that major rock types in this horizontal section are RRT4 and RRT5 with an average porosity of 12 p.u. and permeability ranging from 1 to 10 md. Decreasing reservoir quality indicates that well no. 2 was drilled toward the levee or distal fan facies and that the well productivity is relatively low (Fig. 5.13).

In well no. 3, predominant washouts render neutron and density logs useless. The only reliable logs are GR and deep resistivity. With an assumed constant porosity of 22 p.u., water saturation calculated with Archie's equation is approximately 20% with a height above FWL of 80 ft. From the projection of well-log-derived saturation-height data shown in Fig. 5.8 (blue dots), we observe that the major rock type is RRT2 with permeability ranging from 100 to 300 md. Reservoir quality remains the same as that of the key well, thereby indicating that the well was drilled along the channel axis or fan

lobe and that well productivity is much better than that of well no. 2 (Fig. 5.13), which is cross-validated by core data available from these two wells.

This example confirms that saturation-height-based rock typing in horizontal wells can reveal lateral reservoir-quality changes and provide critical real-time information for guiding the placement and steering of horizontal wells.

## 5.6 FIELD CASE NO. 2: DEEPWATER GULF OF MEXICO

### 5.6.1 Reservoir Background

The second field example is a Miocene turbidite oil field located in the deepwater Gulf of Mexico (Contreras et al., 2006). The depositional system is interpreted as a submarine fan complex developed in a mini-basin with stacked progradational lobes. Reservoirs primarily consist of sandy turbidite facies interbedded with muddy debris-flow facies. Reservoir rocks are mainly unconsolidated sandstones with very fine to fine- to medium-size grains. Thin-bed zones are present but are not addressed here. In this study, we evaluate only the two hydraulically connected, hydrocarbon-bearing sand units: M40 and M50 in three wells. These sands are buried at depths between 12,000 and 13,000 ft TVD and are dipping toward the West (Fig. 5.14). Core measurements indicate that the massive and planar stratified sands have porosities up to 35%, as well as 100 – 2000 md of nominal permeability. Well logs from three wells are used for rock typing. Well no. 1 was drilled with OBM and penetrated a capillary transition zone and the FWL. Well nos. 2 and 3 were drilled with WBM where the M40-50 sands are located more than 500 ft above FWL (Fig. 5.14).

### 5.6.2 Core-Based Rock Typing and Interpretation

Hydraulic rock types are first established using routine core porosity-permeability measurements. Six hydraulic rock types were identified from the histogram distribution of RQI (Fig. 5.15). Table 5.6 summarizes the statistics of petrophysical properties for each rock type. Similar to field case no. 1, we observe that rock types 1 - 3 exhibit a largely overlapping porosity range. Again, their average horizontal permeability exhibits a ratio around 2 - 2.5, which indicates that their average pore-throat radius ratio is close to 1.5. Laser grain size measurements for rock types confirmed that the controlling factor for permeability was mean grain size. Reservoir quality decreases with decreasing grain size.

### 5.6.3 Well-Log-Based Saturation-Height, Rock Typing, and Permeability Estimation

We perform core-calibrated, conventional well-log analysis in the three wells to calculate volumetric concentration of shale, total porosity, and water saturation. Normalization of gamma-ray logs is not performed in this study because we assume that the gamma-ray log self-normalizes in each well when transforming gamma-ray logs to volumetric concentration of shale. From reservoir pressure measurements, we identify the fluid type, their contacts, and the FWL. Well-log-derived saturation-height and core-measured capillary pressure agree well (Fig. 5.16). From saturation-height results, we derive Leverett's RQI using Eq. (5.4) with constants $a$ = 0.63, $b$ = -0.68, and $S_{wirr}$ = 0.05. Subsequently, we classify rocks based on a combination of several petrophysical attributes including volumetric concentration of shale, total porosity, water saturation in the irreducible depth zone, and log-derived RQI in the capillary transition zone. Figure 5.17 shows results obtained from rock classification (Track 7), as well as the permeability estimated from the rock types (Track 8). Estimated permeability agrees well with permeability (with Klinkenberg correction under stress) measured from whole core in the

key well. In well no. 3, rock types agree well with the permeability measured from sidewall core samples. Rock typing results obtained from the three wells are displayed together to assist in stratigraphic and sedimentary interpretations (Fig. 5.18).

### 5.6.4 Invasion Facies Modeling

We select thick zones of rock types 1 to 3 at irreducible water saturation to simulate invasion with WBM, which is an imbibition process in water-wet rocks. Rock types 1 and 2 are selected from well no. 2 and rock type 3 is selected from well no. 3. Both wells lack whole core samples and special core analysis. It is therefore important to extrapolate our understanding of rock types from the key well to uncored wells. We use gamma-ray, bulk density, neutron porosity, and AIT apparent resistivity logs for simulation. The PEF log is excluded due to presence of barite in the drilling mud. From well logs acquired across each rock type, we observe that they exhibit essentially the same nuclear responses, which confirms one previous conclusion, namely that apparent resistivity logs are irreplaceable for hydraulic rock typing.

Table 5.7 summarizes the simulation parameters. We iteratively match numerically simulated and measured well logs by adjusting the capillary pressure and relative permeability curves. Figure 5.19 shows the final simulations of radial invasion profiles and numerically simulated well logs for rock types 1 to 3 after 1.0 - 1.5 days of WBM invasion. Table 5.8 describes the final capillary pressure and relative permeability curves for the selected rock types using Brooks-Corey's parametric model and plotted in Fig. 5.20.

### 5.6.5 Saturation-Height Modeling After Invasion Simulation

Using the capillary pressure curves calibrated from invasion simulation, we derived saturation-height relations for rock types 1 to 3 (described in Table 5.9). To that

end, we fit 14 core MICP measurements with Brooks-Corey's parametric model and found that the parameters included in Brooks-Corey's function were closely correlated to Leverett's reservoir quality index. Better rock quality indicates higher $P_c^0$ and $e_p$ together with lower $S_{wirr}$ and $P_e$ (Fig. 5.21), which enables a consistent petrophysical interpretation between well-log-derived saturation height and core MICP data.

Figure 5.22 shows the radial profiles of water saturation, salt concentration, and resistivity for each rock type after WBM invasion. In general, good-quality sands exhibit low irreducible water saturation but not necessarily more residual oil saturation due to wettability variations. The best quality sands exhibit the largest separation between deepest and shallowest apparent resistivity. Salt dispersivity plays an important role in the near-borehole process of salt exchange between mud filtrate and connate water. Low porosity-permeability rocks typically exhibit large salt dispersivity, which yields a smoother radial salt concentration front (Fig. 5.22, center panel).

## 5.7 SUMMARY AND CONCLUSIONS

Hydraulic rock typing must be based on pore geometry because it relates all petrophysical properties of reservoir rocks. Although it is relatively simple to infer or quantify pore geometry from routine and special core analysis, it remains challenging to quantify it solely with conventional well logs. E-facies diagnosed from apparent well logs are not satisfactory because the latter are simultaneously sensitive to mineralogy and pore fluids. Buckle's number relates to pore geometry in a direct manner but is only applicable to reservoir zones that are at irreducible water saturation conditions. We constructed a synthetic case with pre-defined rock types to illustrate how E-facies and Buckle's number are biased toward capillary transition zones. New methods are necessary to perform hydraulic rock typing in thick oil reservoirs that exhibit long capillary transition zones.

We studied and appraised three conventional core-based hydraulic rock typing methods and performed numerical correlation testing to confirm their petrophysical similarity. Consequently, the three methods should perform equally well in detecting petrophysical rock types with different pore-throat radii. The key to reliable rock typing for reservoir characterization is to construct well-log-derived attributes that directly link rock types diagnosed from core measurements to well logs.

This chapter introduced a new method for hydraulic rock typing in multiple wells penetrating a capillary transition zone that integrates vertical distributions of initial water saturation with reservoir capillary pressure. Conventional Leverett's *J*-function and Thomeer's *G* factor were invoked to quantify reservoir quality in terms of pore geometry. The new method honors both vertical saturation-height behavior and mud-filtrate invasion, both of which bear different expressions of hydraulic rock types. We successfully verified the new method with measurements acquired in two thick turbidite oil reservoirs from the Central North Sea and the deepwater Gulf of Mexico. In both cases, a good agreement was reached between core-derived and well-log-derived rock types, which were also validated with the estimation of permeability.

The petrophysical quality of young deepwater turbidite reservoirs is chiefly controlled by sedimentary grain sizes. Therefore, a link exists between petrofacies and depositional facies that can be effectively applied in reservoir development efforts. Reservoir capillary transition enables the estimation of grain sizes from saturation-height data. In the Central North Sea case examined in this chapter, we showed how to implement saturation-height-derived rock types to quantify lateral variability of reservoir petrophysical quality and to guide well placement and steering with minimum LWD data in a submarine fan. In the deepwater Gulf of Mexico case, we showed that multi-well rock typing can assist in stratigraphic and sedimentary studies, which are often used for

exploration in frontier basins or in deepwater environments, where subsalt or pre-salt reservoirs cannot be clearly imaged with seismic data and well drilling is limited due to high rig cost. It was also found the two field cases could be approached with the same rock-type scheme when using the ratio of permeability between neighboring sandy rock types. This observation is not coincidental, and it has geological and petrophysical significance. Rock types associated with young-age turbidite reservoirs can still be differentiated by their median grain sizes, whereas neighboring rock types exhibit a grain size ratio close to 1.5 or $\sqrt{2}$. Well-log-derived rock types capture this property, which suggests that rock typing in similar cases may generally follow the same principle.

We suggest that rock typing should not only separate rocks into different groups. The more important task is to calculate static and dynamic petrophysical properties associated with each rock type based on core-log integration. The new interpretation method introduced in this chapter provides a good initial estimation of rock-type-averaged capillary pressure and relative permeability. Both properties are further calibrated for each rock type by numerically simulating well logs based on the physics of mud-filtrate invasion. It was emphasized that each rock type is associated with a specific radial invasion profile due to differences in pore geometry. Therefore, it is possible to use invasion behavior to define dynamic petrophysical facies (or invasion facies) for reservoir simulation.

The method introduced in this chapter assumes that the reservoir under analysis is hydraulically connected and underwent hydrocarbon migration similar to a primary drainage process. Complex hydrocarbon migration may give rise to saturation hysteresis which could deviate from the saturation-height relation defined by core MICP measurements. Reservoir pressure measurements should be used to confirm reservoir connectivity, whereas core-derived capillary pressure curves should be used to verify the

well-log-derived saturation-height relation. One limitation of the method introduced in this chapter is that it is only applicable to reservoir zones above oil-water or gas-water contacts. Moreover, the resolution of rock types is limited by the vertical resolution of the deep apparent resistivity log.

**Table 5.1:** Coefficients of mathematical expressions associated with three core-based properties.

| | ***x*** | ***y*** | ***z*** |
|---|---|---|---|
| Leverett's RQI | 0.5 | -0.5 | 0.0 |
| Winland $R_{35}$ | 0.588 | -0.864 | 0.732 |
| Amaefule's FZI | 0.5 | -0.5 | variable with porosity |

**Table 5.2:** Statistical distributions of porosity, permeability, and RQI for each hydraulic rock type and associated mean grain-size (MGS) interpretation in the North Sea field case.

| Rock Type | Porosity (p.u.) | Permeability (md) | RQI (µm) | MGS |
|---|---|---|---|---|
| RRT0 | 24.0 ± 1.86 | 1058 ± 232 | 66.3 ± 8.5 | LC |
| RRT1 | 24.1 ± 2.26 | 541 ± 184 | 46.9 ± 6.7 | UM |
| RRT2 | 24.2 ± 1.95 | 255 ± 63 | 32.2 ± 3.6 | LM |
| RRT3 | 22.7 ± 2.40 | 98.0 ± 34 | 20.3 ± 3.4 | UF |
| RRT4 | 18.8 ± 2.91 | 16.0 ± 9.0 | 8.8 ± 2.3 | LF |
| RRT5 | 14.2 ± 4.08 | 1.30 ± 0.9 | 2.8 ± 0.8 | VF |
| RRT6 | 11.1 ± 2.45 | 0.20 ± 0.1 | 0.9 ± 0.3 | ST |

**Table 5.3:** Summary of mudcake, fluid, and formation properties assumed in the simulation of the process of mud-filtrate invasion.

| Variable | Units | Value |
|---|---|---|
| Wellbore radius | inch | 6.15 |
| Maximum invasion time | days | 2 |
| Formation outer boundary | ft | 2000 |
| Reservoir temperature | $^{o}F$ | 213 |
| Initial reservoir pressure | psi | 3800 |
| Gas viscosity (reservoir conditions) | cP | 0.02 |
| Oil viscosity (reservoir conditions) | cP | 0.5 |
| Water viscosity (reservoir conditions) | cP | 0.3 |
| Overbalance pressure | psi | 1400 |
| Mud-filtrate density (at STP) | $g/cm^3$ | 0.9 |
| Mud-filtrate viscosity (at STP) | cP | 5 |
| Mud-filtrate compressibility (at STP) | $psi^{-1}$ | $3.6x10^{-6}$ |
| Formation compressibility | $psi^{-1}$ | $4 \times 10^{-7}$ |
| Mudcake reference permeability | md | 0.03 |
| Mudcake reference porosity | frac. | 0.35 |
| Mud solid fraction | frac. | 0.06 |
| Mudcake maximum thickness | inch | 0.4 |
| Mudcake compressibility exponent | frac. | 0.40 |
| Mudcake exponent multiplier | frac. | 0.10 |

**Table 5.4:** Rock-fluid properties calibrated and optimized with the simulation of mud-filtrate invasion for rock types 1 to 3 using Brooks-Corey's model.

| RT | RQI | $S_{wirr}$ | $S_{or}$ | $k^0_{rnw}$ | $e_{nw}$ | $k^0_{rw}$ | $e_w$ | $P_c^0$ | $e_p$ |
|---|---|---|---|---|---|---|---|---|---|
| 1 | 46.9 | 0.03 | 0.2 | 0.9 | 3.2 | 0.36 | 4.6 | 168 | 21.4 |
| 2 | 32.2 | 0.05 | 0.22 | 0.88 | 3.0 | 0.34 | 3.8 | 128 | 16.1 |
| 3 | 20.3 | 0.07 | 0.25 | 0.86 | 2.6 | 0.3 | 3.2 | 96 | 11.2 |

**Table 5.5:** Saturation height relations for rock types 1 to 3.

| | |
|---|---|
| **RT1:** | $S_w(H) = 0.03 + 0.97[1 - (0.0015H)^{0.047}]$ |
| **RT2:** | $S_w(H) = 0.05 + 0.95[1 - (0.0014H)^{0.062}]$ |
| **RT3:** | $S_w(H) = 0.07 + 0.93[1 - (0.0012H)^{0.091}]$ |

**Table 5.6:** Statistical distributions of porosity, permeability, and RQI for each hydraulic rock type in the Gulf of Mexico field case.

| Rock Type | Porosity (p.u.) | Permeability (mD) | RQI (μm) |
|---|---|---|---|
| RRT1 | 33.6 ± 1.8 | 1099 ± 291 | 56.8 ± 7.2 |
| RRT2 | 33.3 ± 2.1 | 549 ± 130 | 40.4 ± 4.9 |
| RRT3 | 31.5 ± 4.4 | 179 ± 63.7 | 23.4 ± 3.4 |
| RRT4 | 24.1 ± 6.1 | 42.9 ± 19.1 | 13.1 ± 2.1 |
| RRT5 | 19.7 ± 3.9 | 11.3 ± 3.9 | 7.50 ± 1.1 |
| RRT6 | 19.6 ± 3.7 | 4.00 ± 1.5 | 4.40 ± 0.9 |

**Table 5.7:** Summary of mudcake, fluid, and formation properties assumed in the simulation of the process of mud-filtrate invasion.

| Variable | Units | Value |
|---|---|---|
| Wellbore radius | inch | 6.0 |
| Maximum invasion time | days | 1.0 - 1.5 |
| Formation outer boundary | ft | 2000 |
| Reservoir temperature | $^{o}F$ | 120 |
| Initial reservoir pressure | psi | 7800 |
| Water viscosity (reservoir conditions) | cP | 0.92 |
| Oil viscosity | cP | 0.8 |
| Overbalance pressure | psi | 500 |
| Salt dispersivity | ft | 0.1 - 0.5 |
| Mud-filtrate density (at STP) | $g/cm^3$ | 1.02 |
| Mud-filtrate viscosity (at STP) | cP | 0.92 |
| Mud-filtrate compressibility (at STP) | $psi^{-1}$ | $3.6 \times 10^{-6}$ |
| Formation compressibility | $psi^{-1}$ | $4 \times 10^{-7}$ |
| Mudcake reference permeability | md | 0.01 |
| Mudcake reference porosity | frac. | 0.35 |
| Mud solid fraction | frac. | 0.06 |
| Mudcake maximum thickness | inch | 0.4 |
| Mudcake compressibility exponent | frac. | 0.40 |
| Mudcake exponent multiplier | frac. | 0.10 |

**Table 5.8:** Rock-fluid properties calibrated with the simulation of mud-filtrate invasion for rock types 1 to 3 using Brooks-Corey's model.

| RT | RQI | $S_{wirr}$ | $S_{or}$ | $k^0_{rnw}$ | $e_{nw}$ | $k^0_{rw}$ | $e_w$ | $P_c^0$ | $e_p$ |
|---|---|---|---|---|---|---|---|---|---|
| 1 | 60.3 | 0.05 | 0.22 | 0.85 | 3.2 | 0.3 | 5.0 | 270 | 26 |
| 2 | 38.9 | 0.08 | 0.23 | 0.87 | 3.0 | 0.25 | 4.5 | 185 | 18.6 |
| 3 | 24.6 | 0.12 | 0.18 | 0.9 | 3.0 | 0.3 | 4 | 121 | 12.4 |

**Table 5.9:** Saturation-height relations for rock types 1 to 3.

| | |
|---|---|
| **RT1:** | $S_w(H) = 0.05 + 0.95[1 - (0.0011H)^{0.039}]$ |
| **RT2:** | $S_w(H) = 0.08 + 0.92[1 - (0.0010H)^{0.054}]$ |
| **RT3:** | $S_w(H) = 0.12 + 0.88[1 - (0.0010H)^{0.081}]$ |

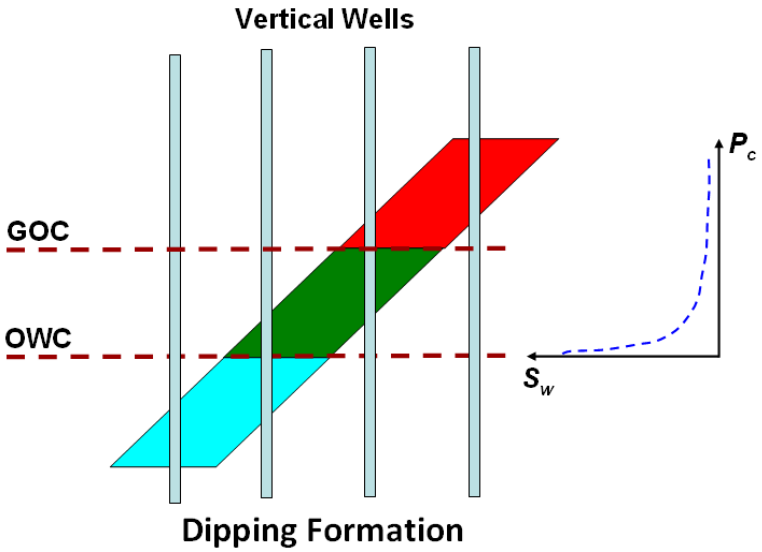


**Figure 5.1:** Schematic of the effect of capillary transition on rock typing with multi-well well logs (Peters, 2012).

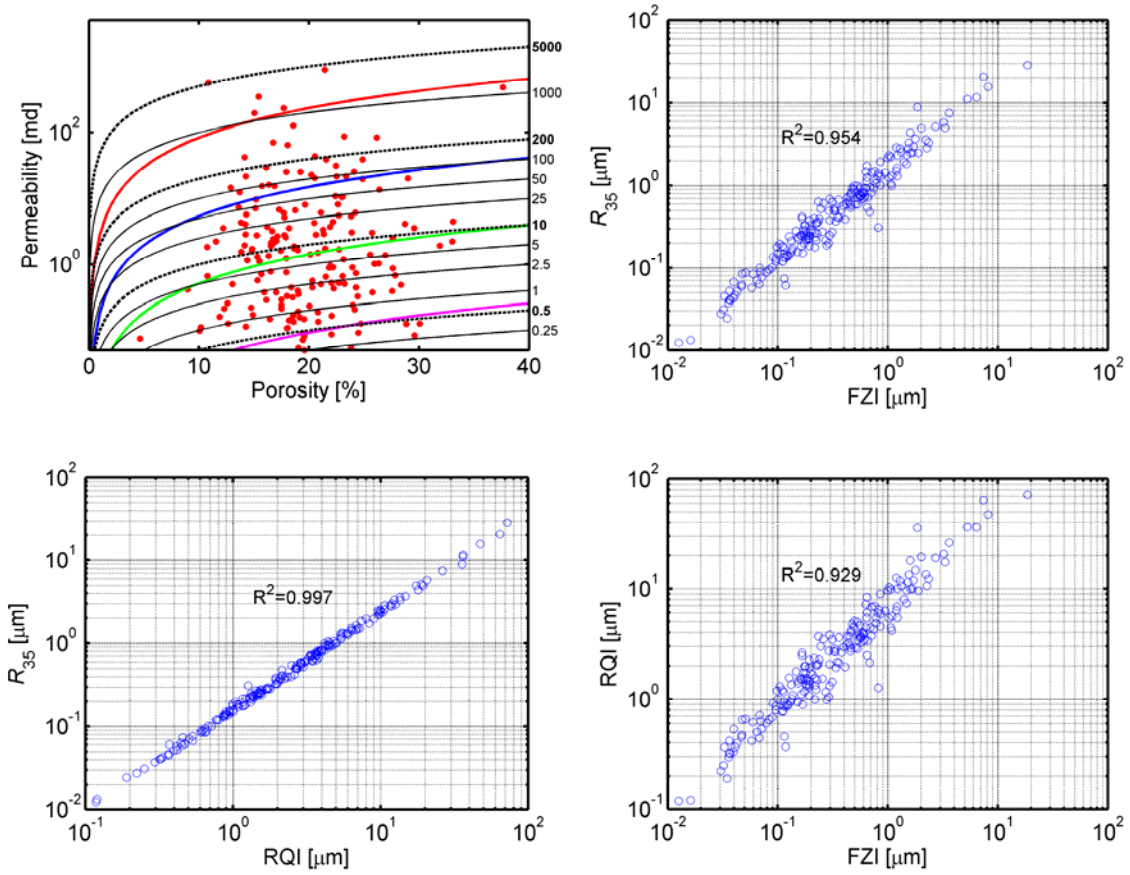


**Figure 5.2:** Numerical testing of the correlation between Leverett's RQI, Winland $R_{35}$, and FZI using randomly generated porosity-permeability values.

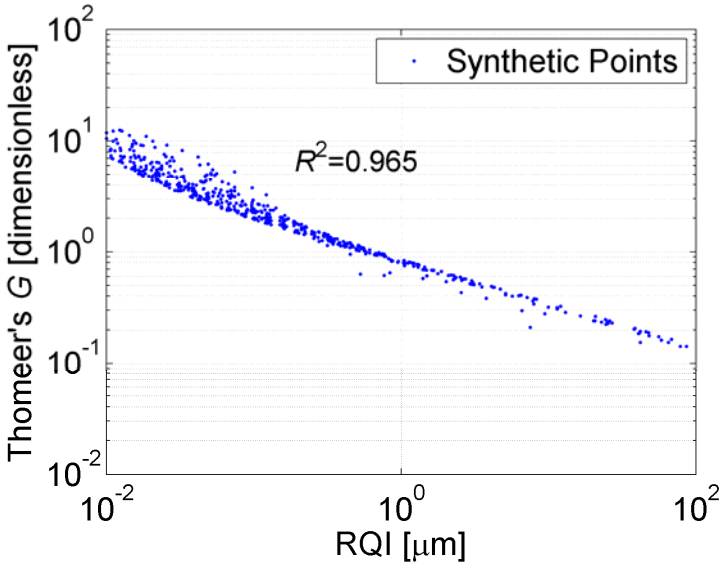


**Figure 5.3:** Numerical testing of the correlation between log-derived Leverett's RQI and Thomeer's *G* factor.

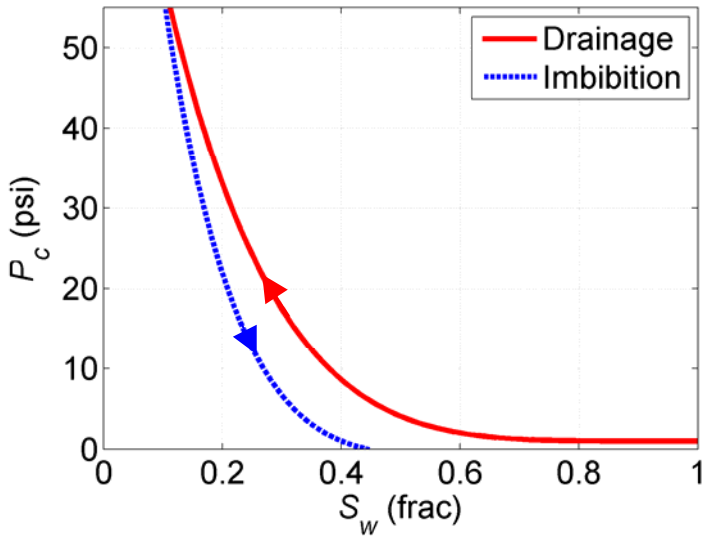


**Figure 5.4:** Example of saturation-dependent drainage and imbibition capillary pressure curves for the same rock.

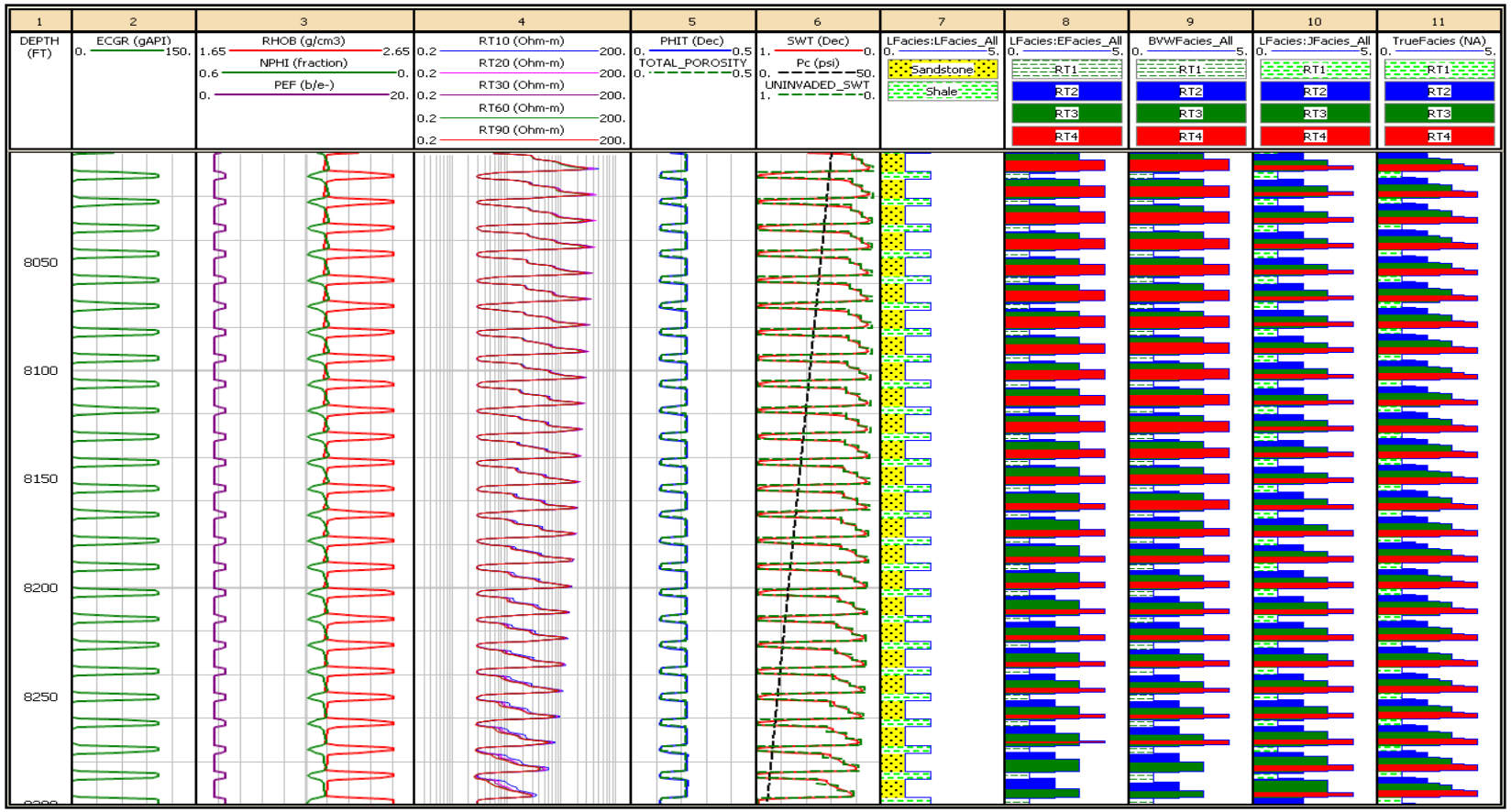


**Figure 5.5:** Rock typing in a synthetic reservoir model. Track 1: Depth; Track 2: Gamma ray; Track 3: Bulk density, neutron porosity, and photoelectric factor; Track 4: Resistivity; Track 5: Total porosity from both well logs and model; Track 6: Total water saturation from both well logs and model, and reservoir capillary pressure; Track 7: Lithofacies; Track 8: Electrofacies; Track 9: BVW rock typing; Track 10: Rock typing from log-derived J-function; Track 11: pre-defined rock type model.

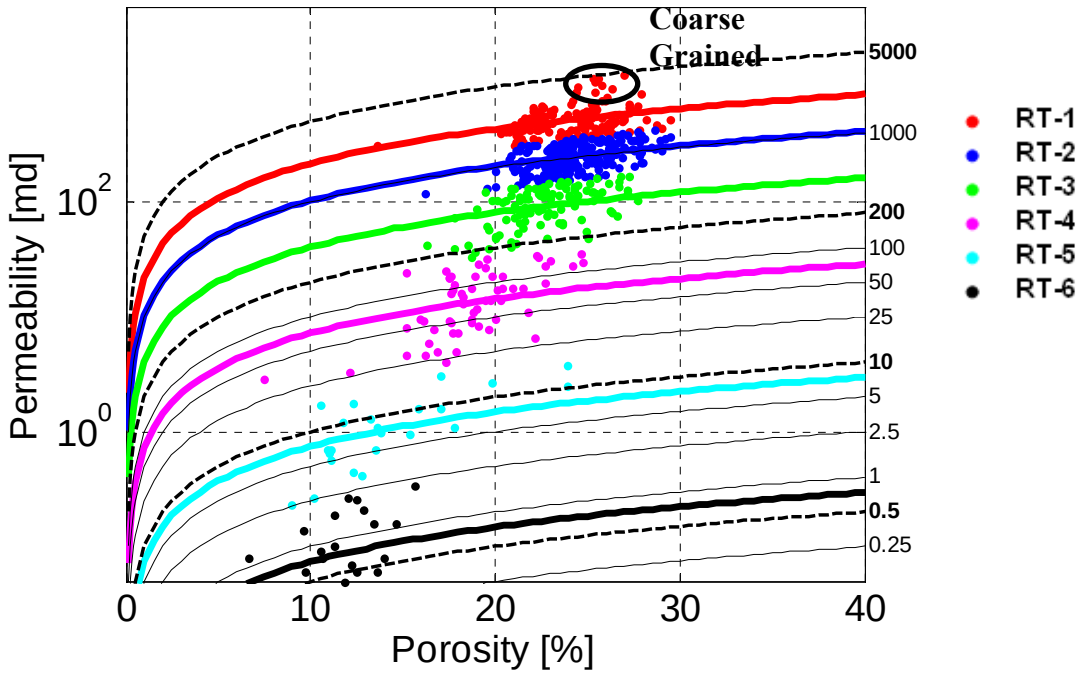


**Figure 5.6:** Core-based hydraulic rock typing with Leverett's RQI in the North Sea field case.

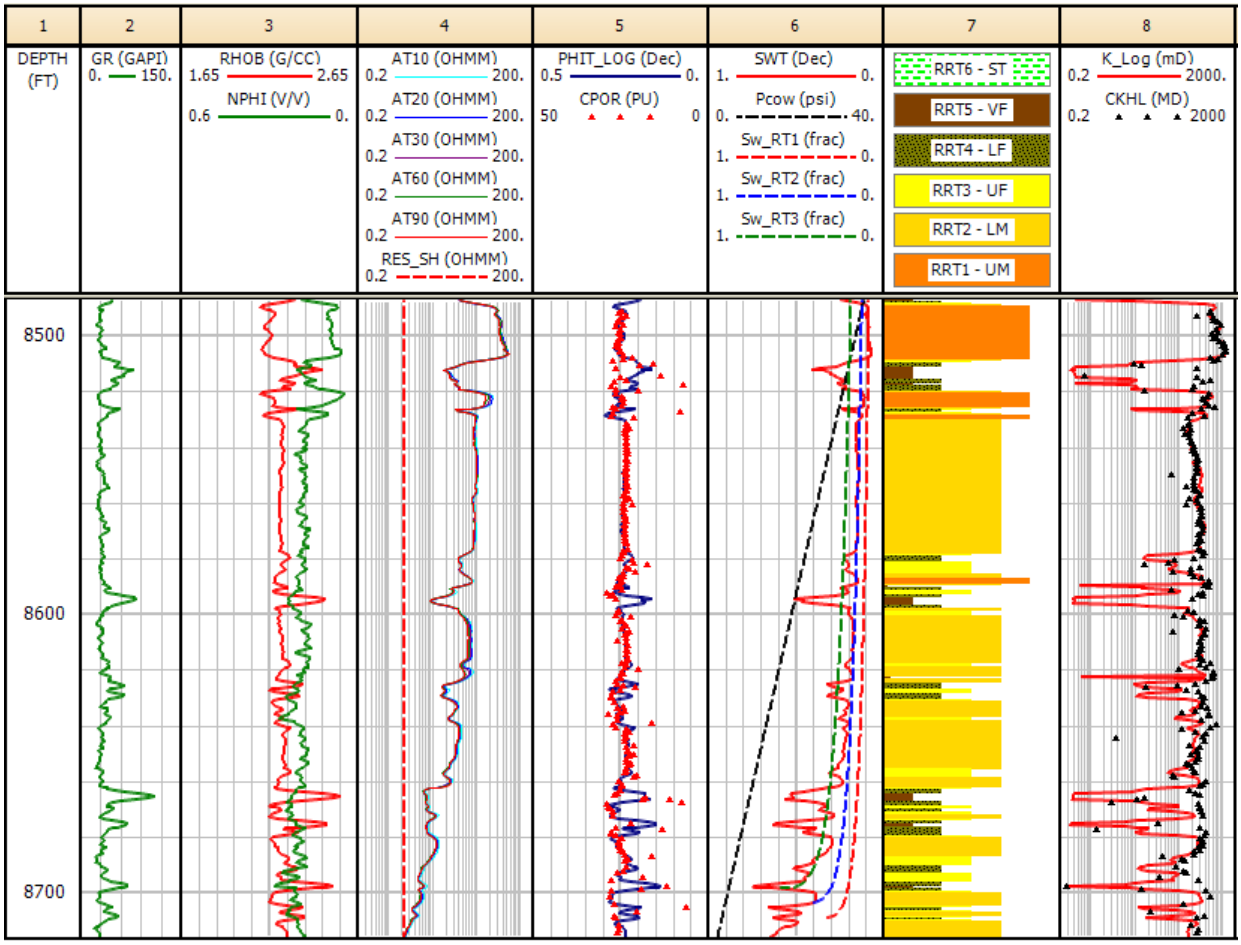


**Figure 5.7:** Rock typing results in the key well of the Central North Sea case. Tracks 1-4: basic well logs; Tracks 5-6: standard well-log analysis, saturation-height for rock type 1 to 3; Tracks 7: distribution of rock types in M40-50 sands; Track 8: permeability prediction based on rock types and comparison to core permeability.

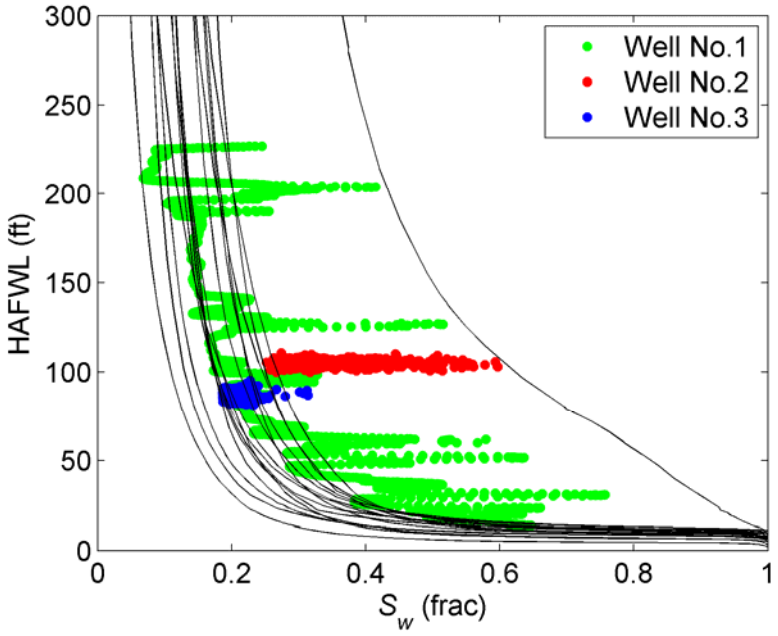


**Figure 5.8:** Reconciliation between core-measured MICP and log-derived saturation-height relation.

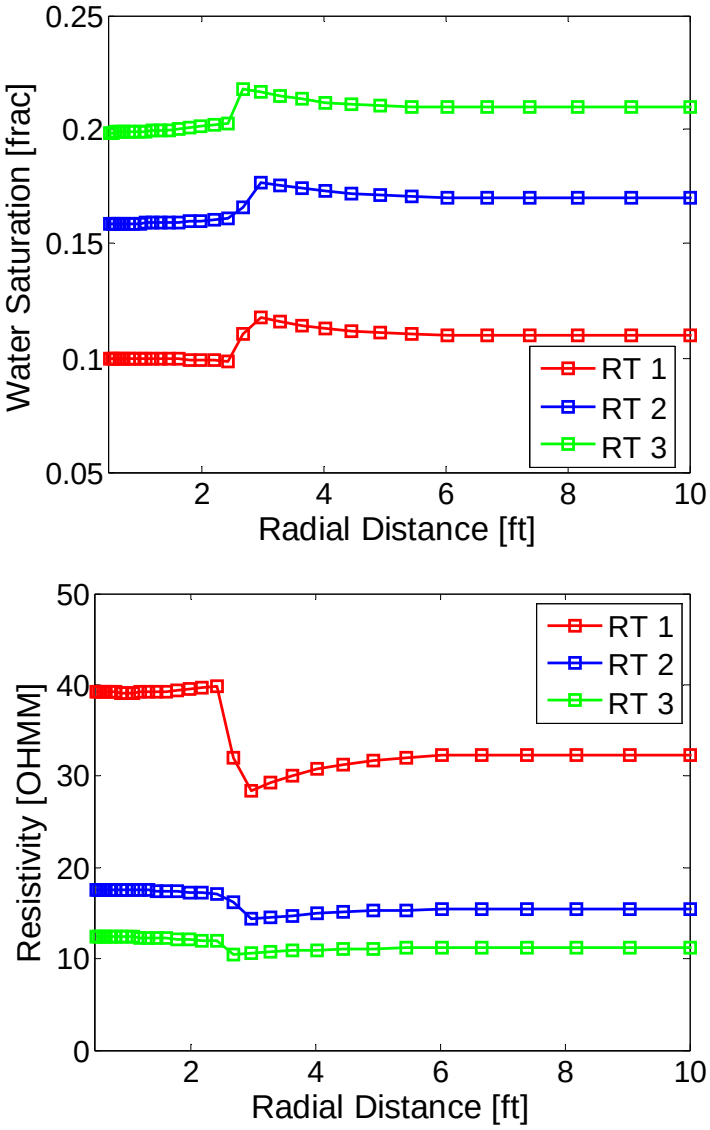


**Figure 5.9:** Radial distributions of water saturation (upper panel) and resistivity (lower panel) of rock types 1 to 3 after invasion with OBM for 2 days. The best rock type exhibits the largest resistivity, the lowest water saturation, and the shallowest invasion.

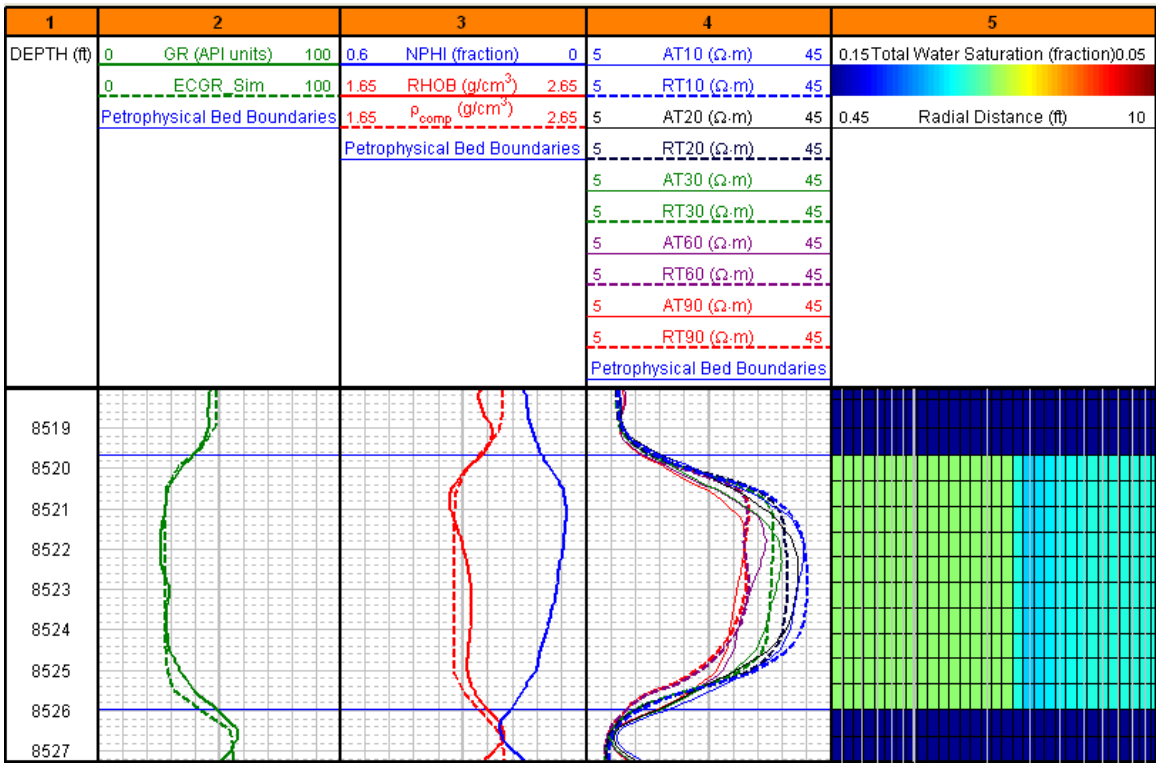
1
2
3
4
5
DEPTH (ft)
0 GR (API units) 100
0 ECGR_Sim 100
Petrophysical Bed Boundaries
0.6 NPHI (fraction) 0
1.65 RHOB (g/cm3) 2.65
1.65 ρcomp (g/cm3) 2.65
Petrophysical Bed Boundaries
5 AT10 (Ω·m) 45
5 RT10 (Ω·m) 45
5 AT20 (Ω·m) 45
5 RT20 (Ω·m) 45
5 AT30 (Ω·m) 45
5 RT30 (Ω·m) 45
5 AT60 (Ω·m) 45
5 RT60 (Ω·m) 45
5 AT90 (Ω·m) 45
5 RT90 (Ω·m) 45
Petrophysical Bed Boundaries
0.15 Total Water Saturation (fraction) 0.05
0.45 Radial Distance (ft) 10
8519
8520
8521
8522
8523
8524
8525
8526
8527

**(a)**

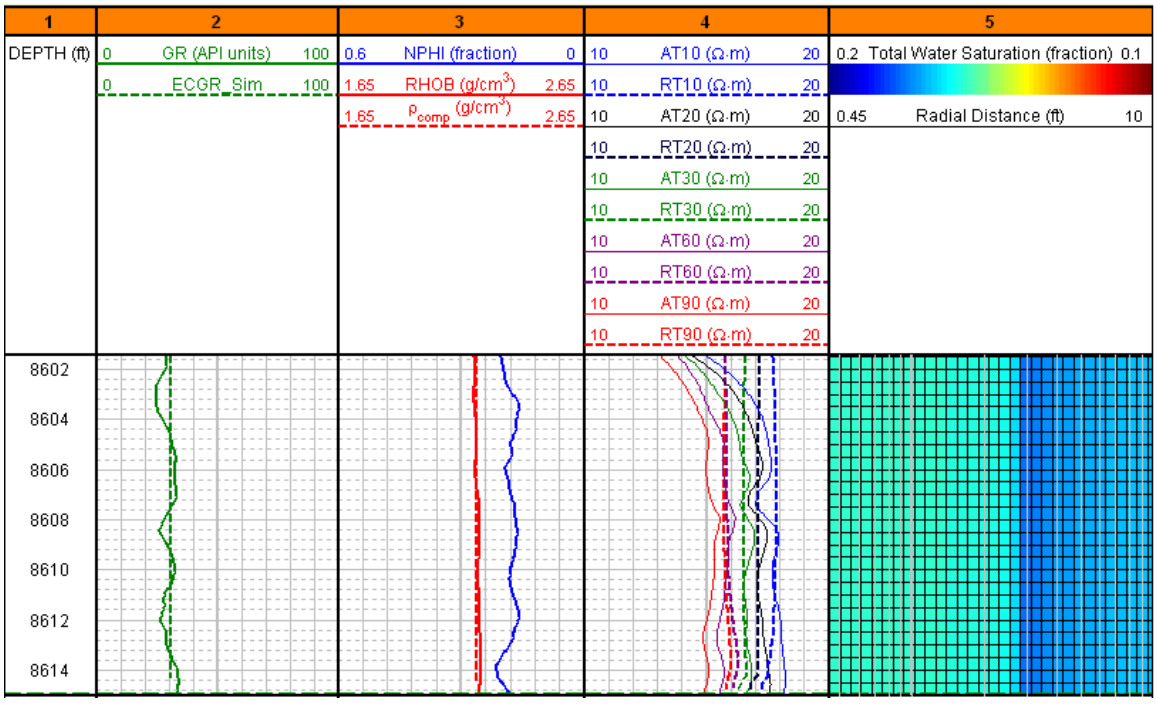
1
2
3
4
5
DEPTH (ft)
0 GR (API units) 100
0 ECGR_Sim 100
0.6 NPHI (fraction) 0
1.65 RHOB (g/cm3) 2.65
1.65 ρcomp (g/cm3) 2.65
10 AT10 (Ω·m) 20
10 RT10 (Ω·m) 20
10 AT20 (Ω·m) 20
10 RT20 (Ω·m) 20
10 AT30 (Ω·m) 20
10 RT30 (Ω·m) 20
10 AT60 (Ω·m) 20
10 RT60 (Ω·m) 20
10 AT90 (Ω·m) 20
10 RT90 (Ω·m) 20
0.2 Total Water Saturation (fraction) 0.1
0.45 Radial Distance (ft) 10
8602
8604
8606
8608
8610
8612
8614

**(b)**

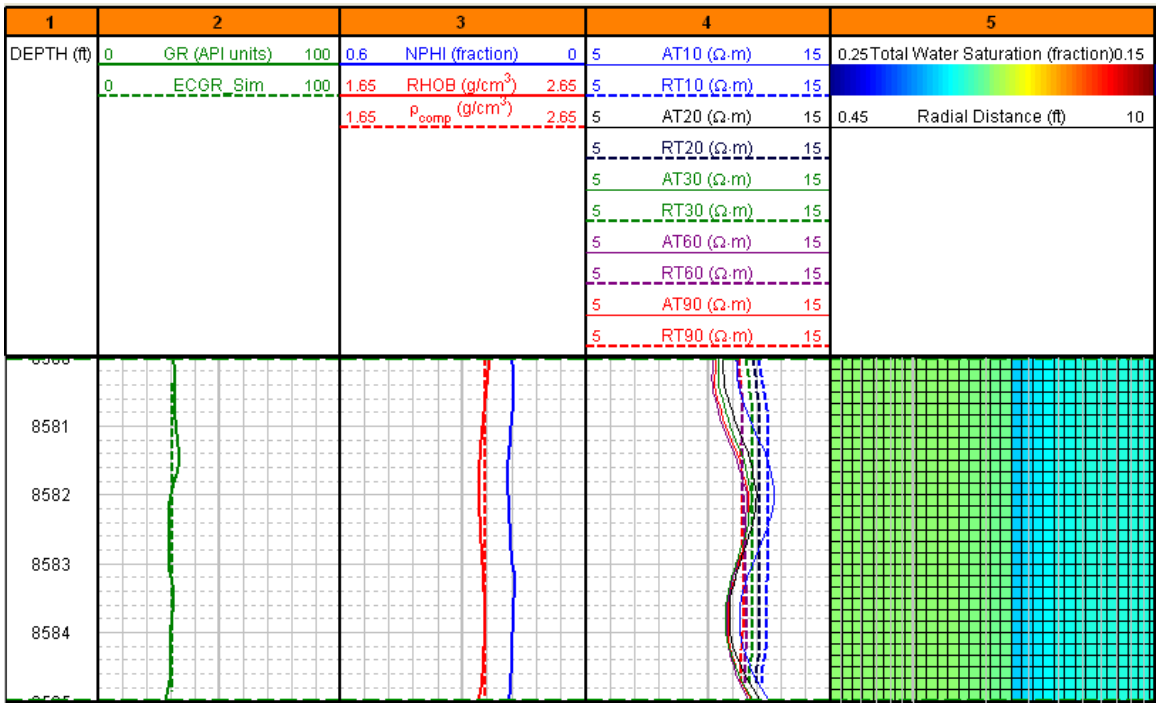


**(c)**

**Figure 5.10:** Invasion simulation for rock types 1 to 3 (a - c) and the corresponding numerical log simulation compared to field logs. Track 1: depth; Track 2: GR log; Track 3: bulk density and neutron porosity logs; Track 4: induction (AIT) resistivity logs; Track 5: cross-section (vertical and radial directions) of water saturation.

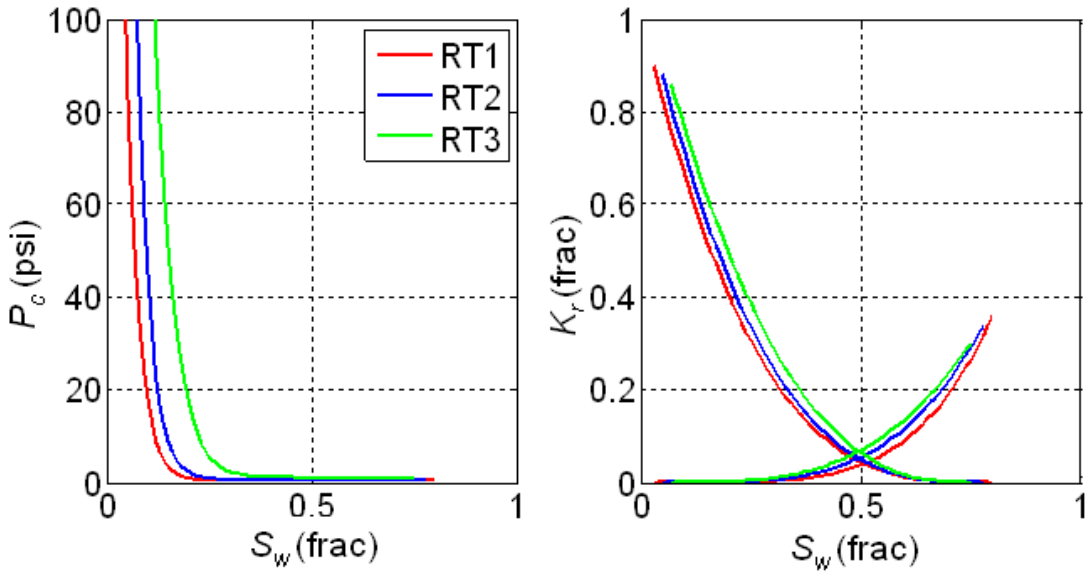


**Figure 5.11:** Invasion-calibrated, saturation-dependent capillary pressure (left) and relative permeability (right) for each rock type.

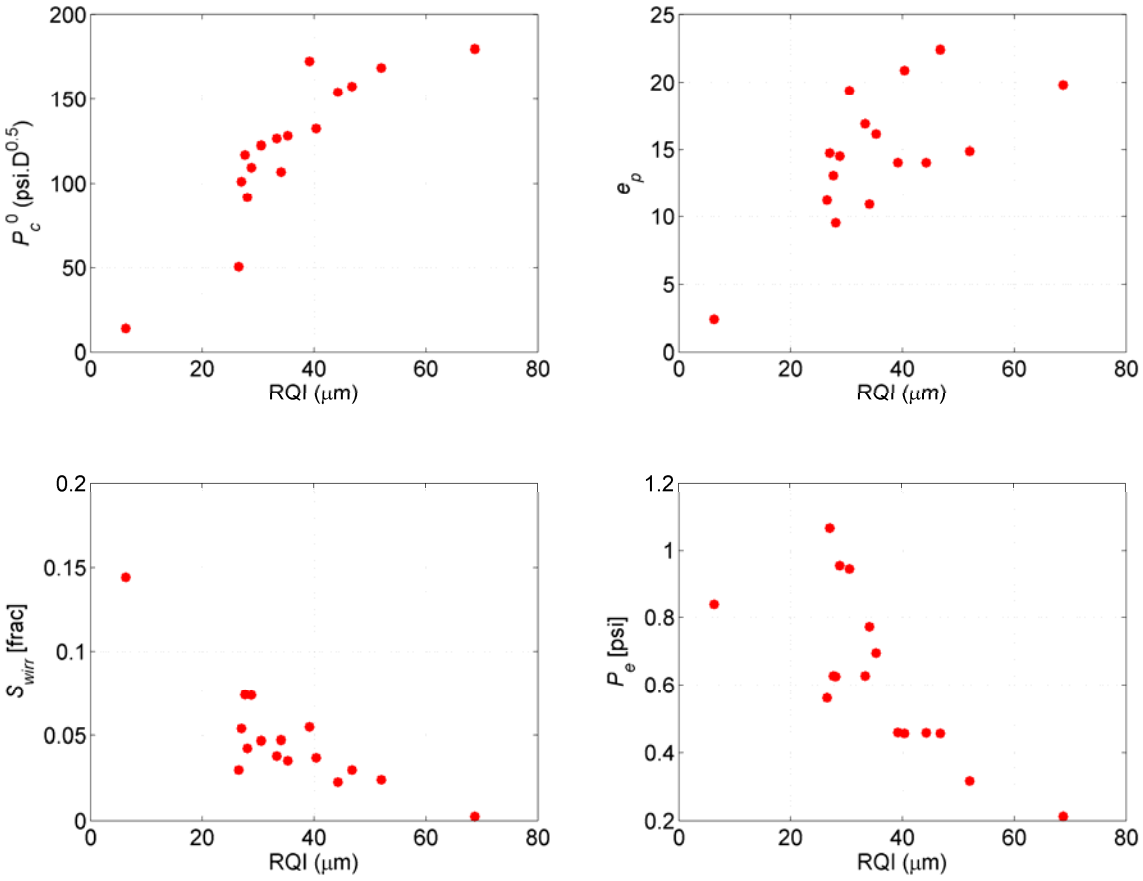


**Figure 5.12:** Correlation between Leverett's rock quality index and capillary pressure properties: $P_c^0$, $e_p$, $S_{wirr}$, and $P_e$ from 16 core MICP data in the North Sea field case.


**Figure 5.13:** Description of the possible drilling scenarios interpreted from rock typing in horizontal wells.

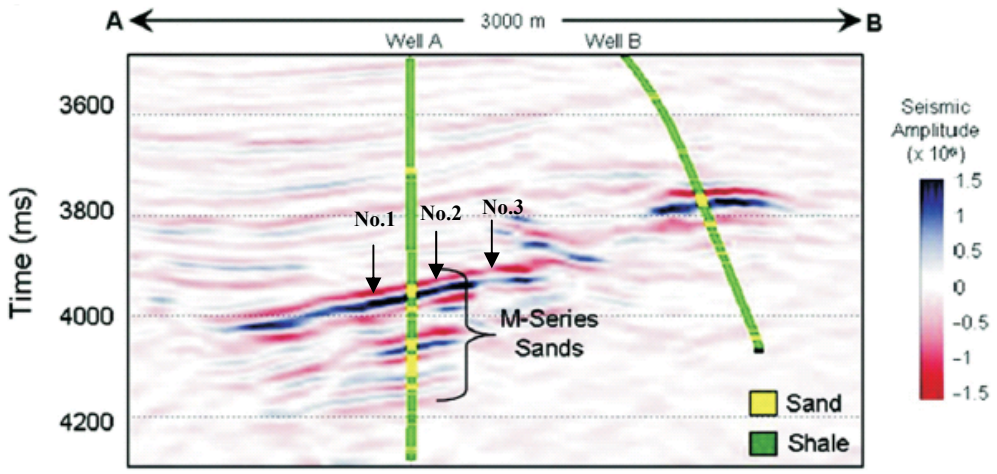


**Figure 5.14:** Three well locations displayed on a seismic cross-section with litho-type well logs indicating the vertical interval of the Miocene M-series sands (Contreras et al., 2006).

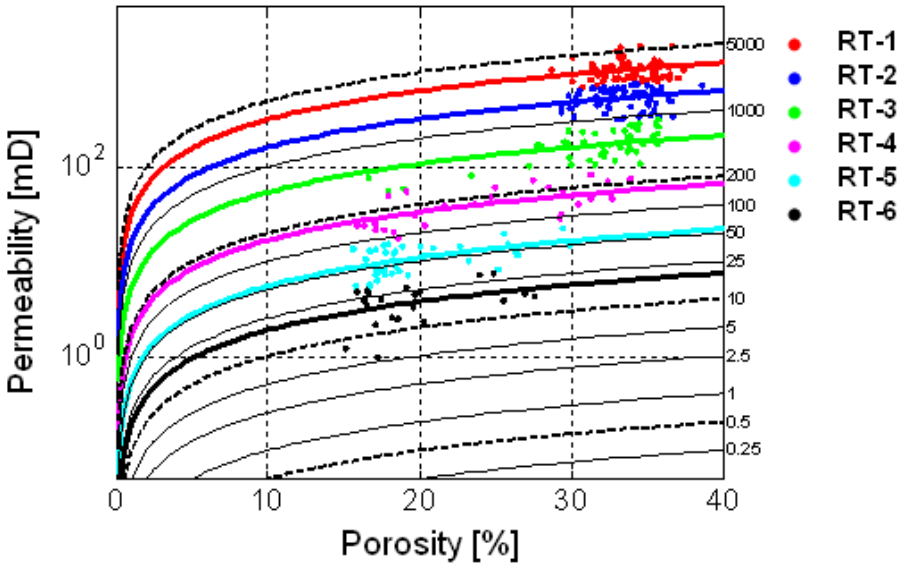


**Figure 5.15:** Core-based hydraulic rock typing from Leverett's RQI in the deepwater Gulf of Mexico field case.

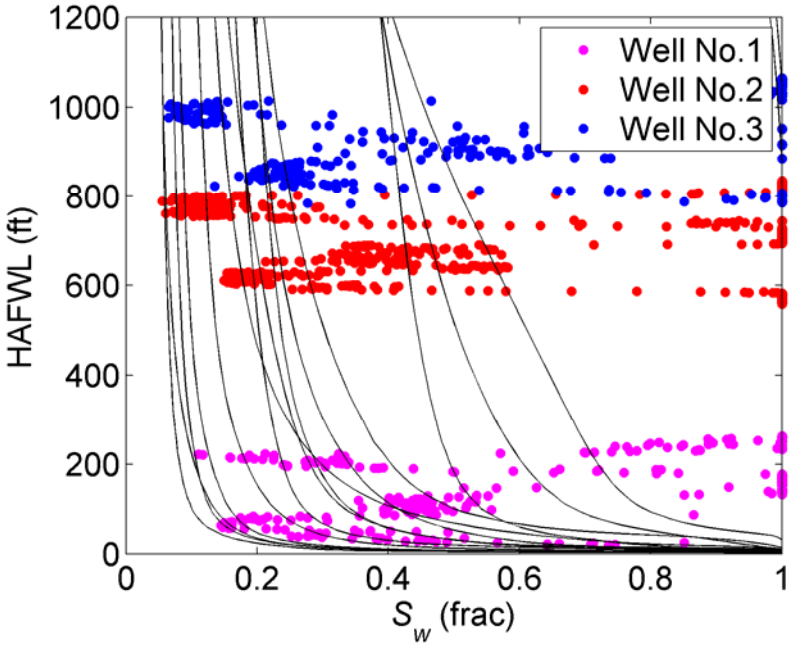


**Figure 5.16:** Reconciliation between core-measured MICP and log-derived saturation-height relations in multiple wells.

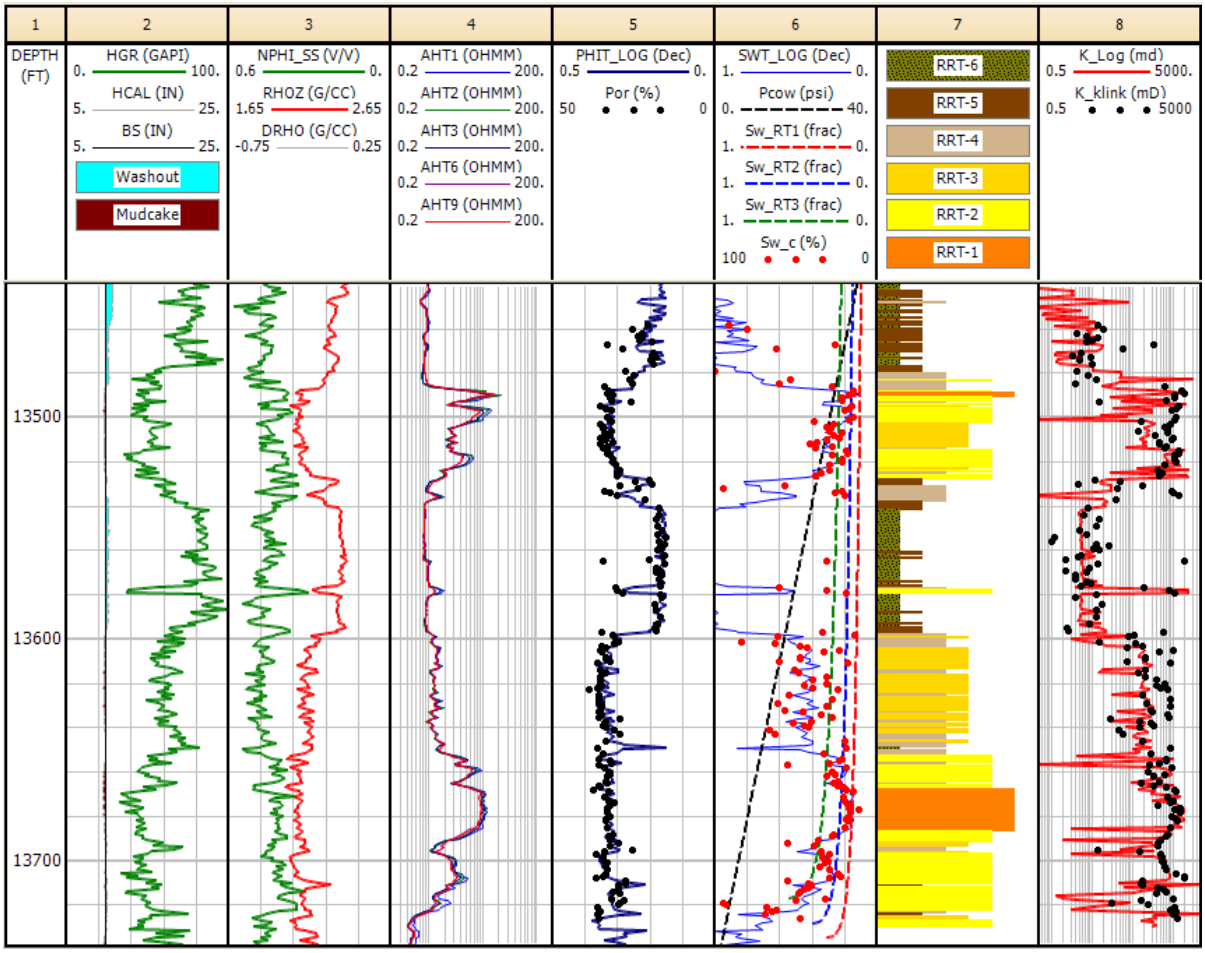


**Figure 5.17:** Rock typing results in the key well of the Gulf of Mexico case. Tracks 1-4: basic well logs; Tracks 5-6: standard well-log analysis, saturation-height for rock types 1 to 3; Tracks 7: distributions of rock types in M40-50 sands; Track 8: permeability prediction based on rock types and comparison to core permeability. Permeability is underestimated only in thin-bed zones.

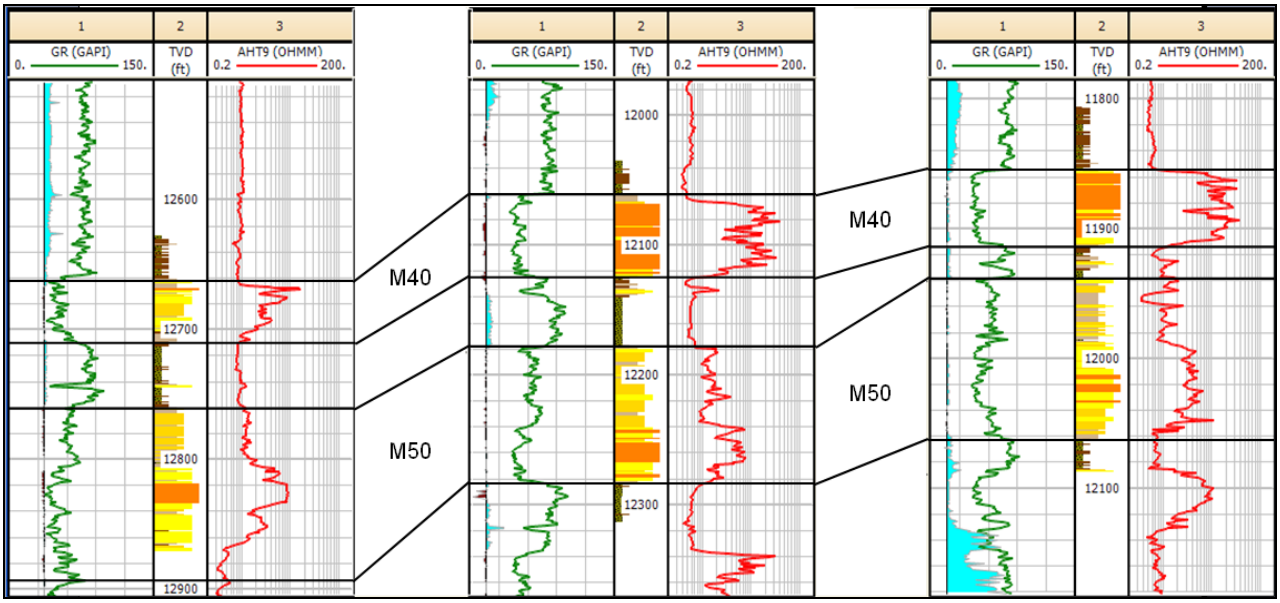


**Figure 5.18:** Use of rock-type distributions in multiple wells to assist sedimentological and stratigraphic interpretation in the Gulf of Mexico field case.

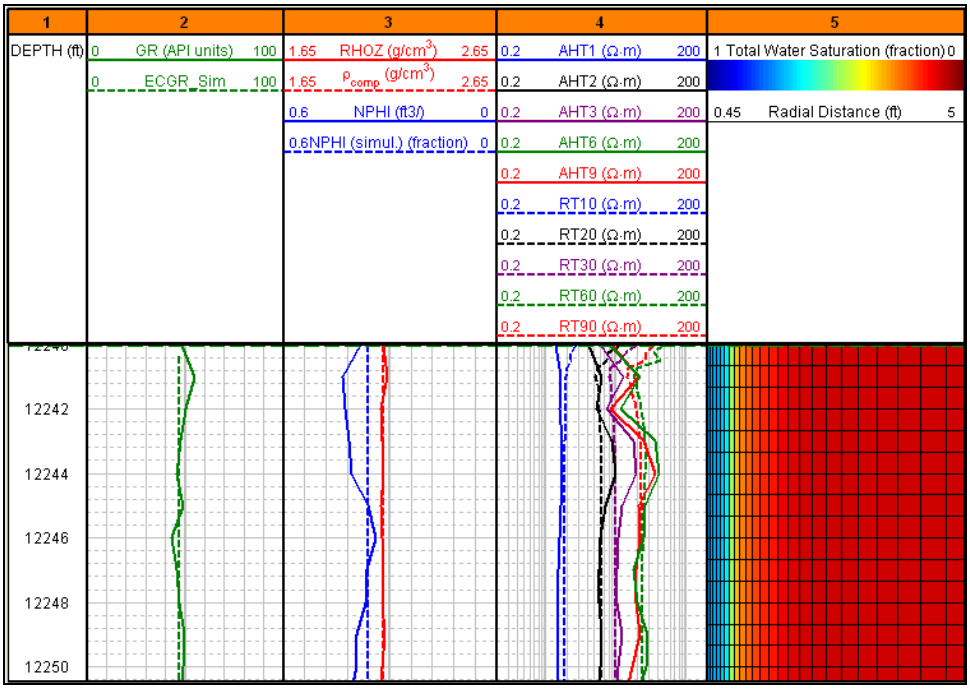
1
2
3
4
5
DEPTH (ft)
0 GR (API units) 100
0 ECGR_Sim 100
1.65 RHOZ (g/cm3) 2.65
1.65 ρcomp (g/cm3) 2.65
0.6 NPHI (ft3/) 0
0.6NPHI (simul.) (fraction) 0
0.2 AHT1 (Ω.m) 200
0.2 AHT2 (Ω.m) 200
0.2 AHT3 (Ω.m) 200
0.2 AHT6 (Ω.m) 200
0.2 AHT9 (Ω.m) 200
0.2 RT10 (Ω.m) 200
0.2 RT20 (Ω.m) 200
0.2 RT30 (Ω.m) 200
0.2 RT60 (Ω.m) 200
0.2 RT90 (Ω.m) 200
1 Total Water Saturation (fraction) 0
0.45 Radial Distance (ft) 5
12242
12244
12246
12248
12250

**(a)**

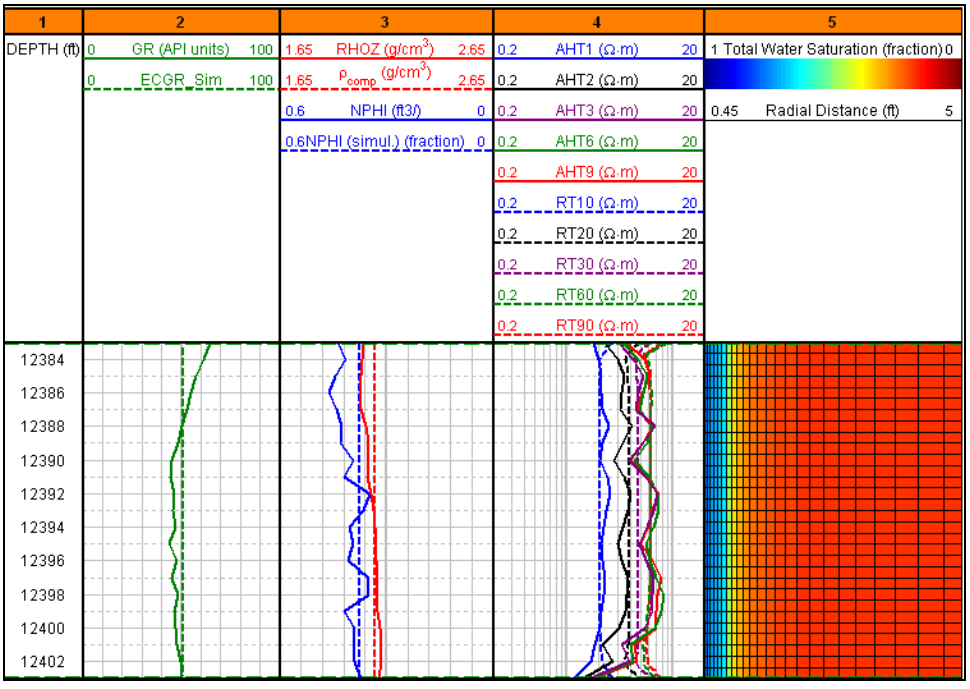
1
2
3
4
5
DEPTH (ft)
0 GR (API units) 100
0 ECGR_Sim 100
1.65 RHOZ (g/cm3) 2.65
1.65 ρcomp (g/cm3) 2.65
0.6 NPHI (ft3/) 0
0.6NPHI (simul.) (fraction) 0
0.2 AHT1 (Ω.m) 20
0.2 AHT2 (Ω.m) 20
0.2 AHT3 (Ω.m) 20
0.2 AHT6 (Ω.m) 20
0.2 AHT9 (Ω.m) 20
0.2 RT10 (Ω.m) 20
0.2 RT20 (Ω.m) 20
0.2 RT30 (Ω.m) 20
0.2 RT60 (Ω.m) 20
0.2 RT90 (Ω.m) 20
1 Total Water Saturation (fraction) 0
0.45 Radial Distance (ft) 5
12384
12386
12388
12390
12392
12394
12396
12398
12400
12402

**(b)**

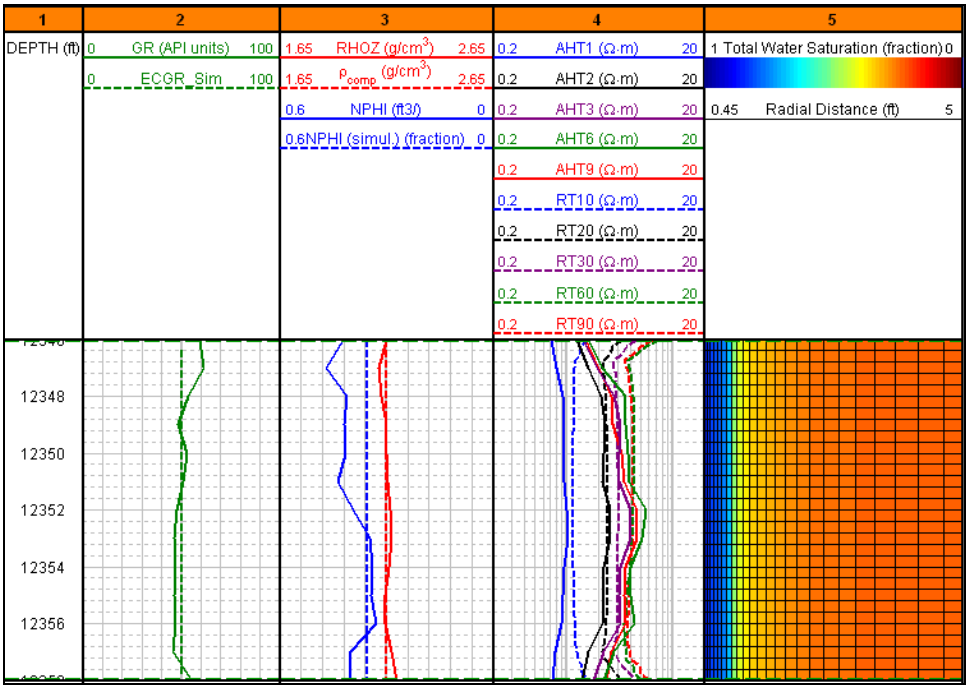


**(c)**

**Figure 5.19:** Invasion simulation for rock types 1 to 3 (a-c) and corresponding numerical well-log simulation compared to field logs. Track 1: Depth; Track 2: GR log; Track 3: Bulk density and neutron logs; Track 4: Induction (AIT) resistivity logs; Track 5: Cross-section (vertical and radial directions) of water saturation. Three different rock types exhibit the same nuclear-log responses. Only resistivity logs can be used to differentiate rock types.

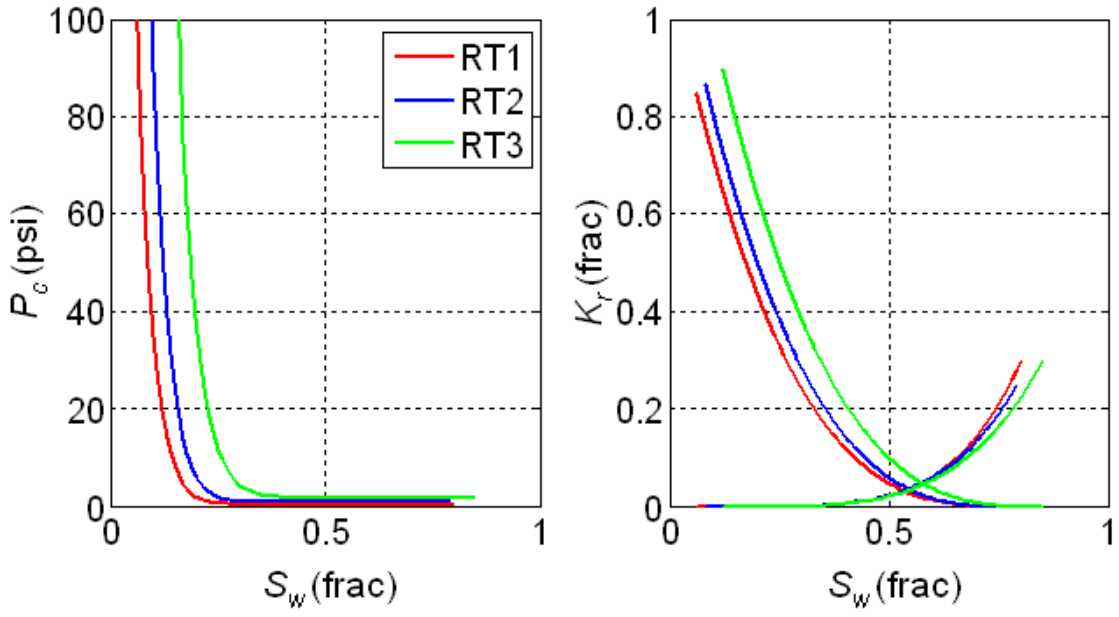


**Figure 5.20:** Invasion-calibrated, saturation-dependent capillary pressure (left) and relative permeability (right) for each rock type.

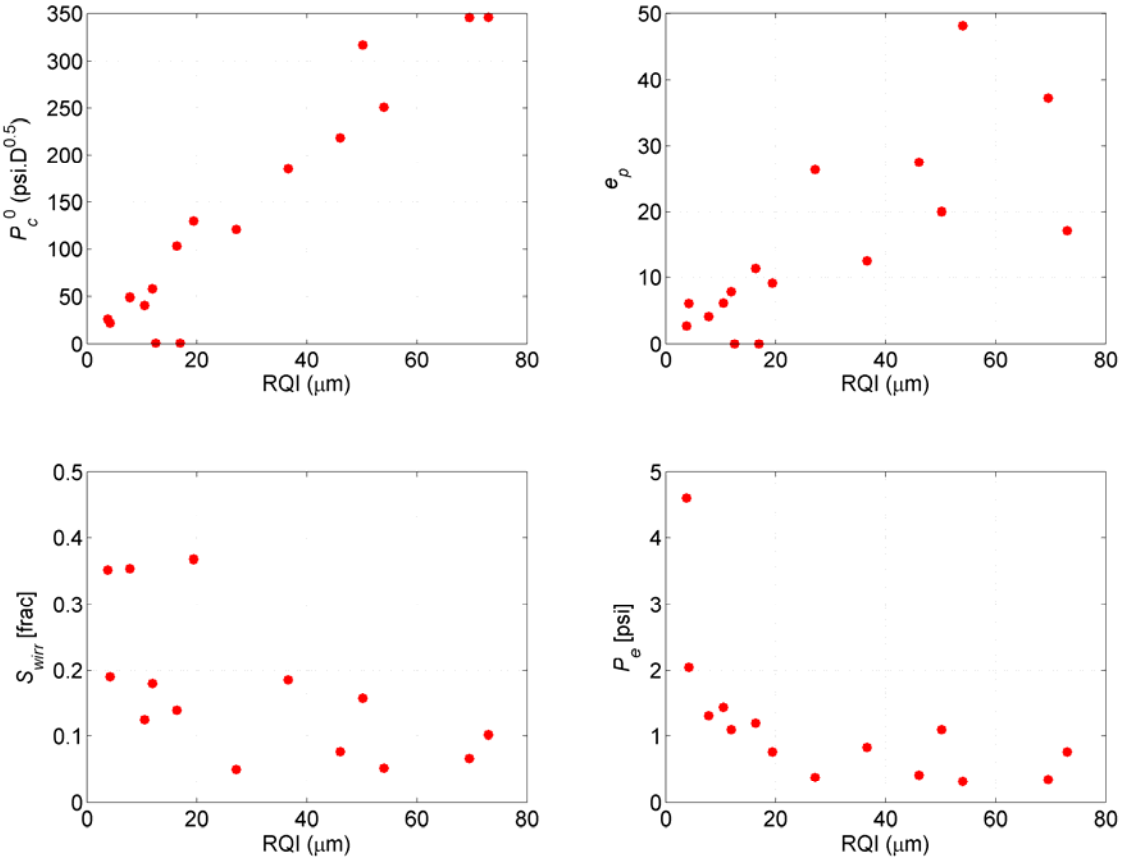


**Figure 5.21:** Correlation between Leverett's rock quality index and capillary pressure properties: $P_c^0$, $e_p$, $S_{wirr}$, and $P_e$ from 14 core MICP data in the Gulf of Mexico field case.

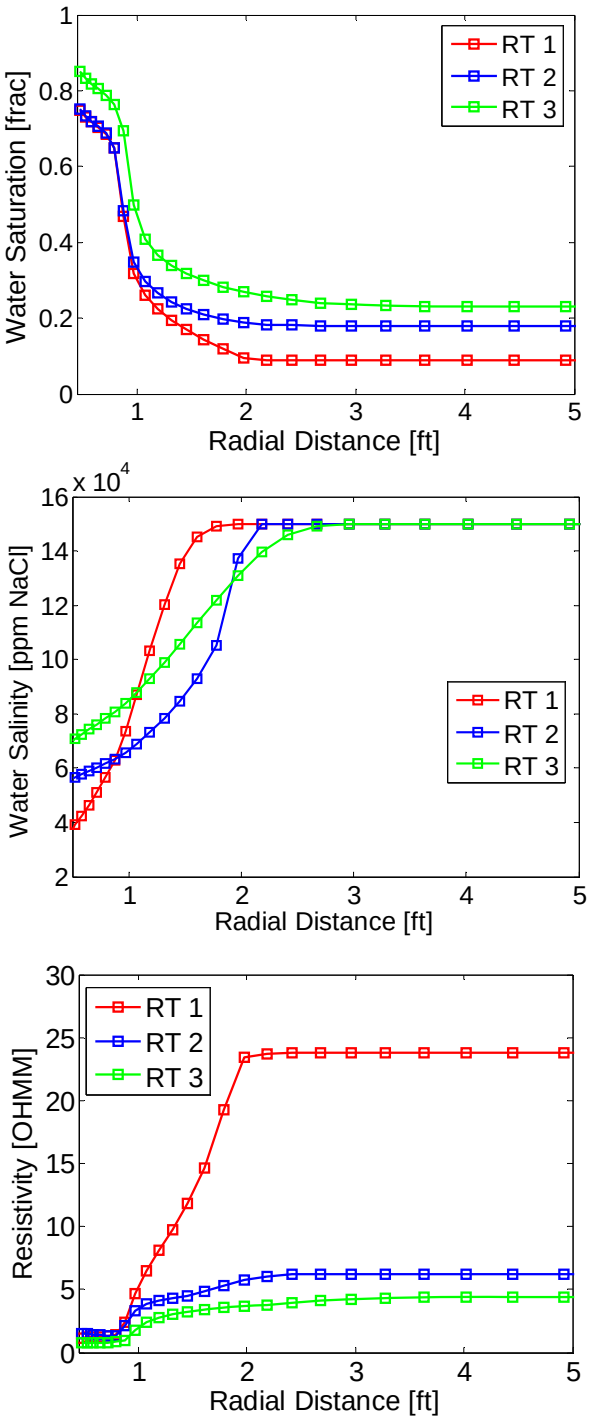


**Figure 5.22:** Radial distributions of water saturation (upper panel), salt concentration (center panel), and resistivity (lower panel) for rock types 1 to 3 after invasion with WBM for 1 - 1.5 days.

# Chapter 6: Rock Classification Connecting Static and Dynamic Petrophysical Properties with Core Measurements and Conventional Logs in a Mixed Clastic-Carbonate Reservoir

Petrophysical rock classification in carbonate reservoirs is challenging due to high spatial heterogeneity and complex pore structure. In extreme cases, conventional rock typing methods such as Leverett's reservoir quality index, Winland $R_{35}$, and flow zone indicator are inadequate to capture the heterogeneity and complexity of carbonate petrofacies. Furthermore, these methods are based on core measurements, and hence are not applicable to uncored reservoir zones.

This chapter introduces a new method for petrophysical rock classification in carbonate reservoirs that honors multiple well logs and emphasizes the connection between static and dynamic petrophysical properties signified by mud-filtrate invasion. An inversion-based algorithm is implemented to simultaneously estimate mineralogy, porosity, and water saturation from well logs. We numerically simulate the process of mud-filtrate invasion in each core-calibrated rock type and quantify the corresponding effects on nuclear and resistivity measurements to derive invasion-induced well-log attributes, which are subsequently integrated into the rock classification. Under favorable conditions, the interpretation method advanced in this work can distinguish bimodal from unimodal behavior in saturation-dependent capillary pressure, a result that is otherwise only possible with special core analysis.

We successfully apply the new method to a mixed clastic-carbonate sequence in the Hugoton gas field, Kansas. Rock types derived with the new method are in good agreement with lithofacies described from core samples. The distribution of permeability and saturation estimated from well-log-derived rock types agrees with routine core

measurements, with the corresponding uncertainty significantly reduced when compared to results obtained with conventional porosity-permeability correlations.

## 6.1 INTRODUCTION

Rock typing is critical for decision-making in mature fields for optimizing production. Conventional rock typing methods such as Leverett's (1941) reservoir quality index (RQI), Winland $R_{35}$ (Pittman, 1992), flow zone indicator (FZI) (Amaefule, 1993), and rock fabric number (RFN) (Lucia, 1999) are highly dependent on core data. New techniques adopt intelligent systems such as artificial neural networks to classify rock types using well logs, but require significant amounts of data, including both core measurements and well logs, for supervised training (Dubois et al., 2006; Doveton, 2012). Conventional log-based rock typing techniques, however, often overlook dynamic petrophysical properties of rocks (e.g., absolute permeability, saturation-dependent capillary pressure and relative permeability) in the absence of special core measurements. For instance, assessment of permeability based on well logs has been only possible with empirical formulae, which correlate permeability to static petrophysical properties such as porosity and irreducible water saturation (Tixier, 1949; Timur, 1968). The latter methods often yield large uncertainty in permeability assessments of carbonate formations. Recently developed methods take into account the physics of mud-filtrate invasion and its effect on well logs to estimate permeability (Salazar et al., 2006) and saturation-dependent capillary pressure and relative permeability (Heidari and Torres-Verdín, 2010) using well logs. Similar work was also reported in carbonate formations (George et al., 2003; Miranda et al., 2009). Recent publications implemented such simulation-based techniques for reliable well-log-based rock typing in siliciclastic

sedimentary sequences (Gandhi et al., 2010; Heidari et al., 2011). Log-based rock typing in carbonate reservoirs, however, remains a challenging topic among petrophysicists.

In carbonate formations, various attributes can be used to distinguish rock types, such as lithology, porosity types (Choquette and Pray, 1970), and pore-size distribution (Archie, 1950). In addition to petrophysical evaluation, lithology assessment is also difficult in carbonate formations due to the complex mineral composition. Correlations between porosity and permeability are commonly low in carbonates, which renders conventional well-log interpretation techniques unsatisfactory for permeability estimation. It has been shown that dynamic petrophysical properties such as saturation-dependent capillary pressure and relative permeability should also be considered in carbonate rock typing (Al-Farisi et al., 2009), which has been impossible thus far in the absence of significant amounts of special core measurements as exemplified in Chapters 2 and 3. All these technical challenges have made rock typing in carbonate formations extremely dependent on core measurements. The rapid variation of compositional and petrophysical properties in carbonate formations, however, makes it impossible for core measurements to capture all the rock types exhibited by spatially heterogeneous carbonates.

The proposed rock typing method for carbonate formations honors the geology of the reservoirs as well as static and dynamic petrophysical properties estimated from logs. The first step after pre-processing of the data is to apply a depth-by-depth nonlinear inversion of well logs to estimate porosity, water saturation, volumetric concentration of shale, and volumetric concentrations of mineral constituents (Heidari et al., 2012). We then use Leverett's RQI method to classify hydraulic rock types based on core measurements. The identified hydraulic rock types are then used to rank dynamic rock-fluid properties (i.e., saturation-dependent capillary pressure and relative permeability).

In the next step, we investigate the effects of dynamic petrophysical properties (saturation-dependent capillary pressure and relative permeability) for different rock types on well logs, by invoking the physics of mud-filtrate invasion followed by numerical simulation of well logs. The characterization of invasion-induced log signatures can be integrated into rock classification based on conventional well logs. Permeability is then estimated via porosity-permeability correlations specific for each rock type. We apply the proposed method to data acquired in the Hugoton gas field (Kansas), which comprises mixed clastic-carbonate gas-bearing sequences, to classify petrophysical rock types.

The method introduced in this chapter provides reliable rock classification of carbonate reservoirs, by taking into account both static and dynamic petrophysical properties; it integrates core measurements for assessment of basic formation properties such as Archie's constants and rock type calibration. This process takes into account both pore structure and fluid-flow mechanisms in rock typing to reduce uncertainty in petrophysical assessments. Reliable permeability assessments are also possible by assimilating rock types in type-dependent porosity-permeability correlations.

## 6.2 METHODS AND WORKFLOW

### 6.2.1 Petrophysical Analysis Using Nonlinear Joint Inversion of Well Logs

Heidari et al. (2012) introduced depth-by-depth and bed-by-bed nonlinear joint inversion methods for assessment of petrophysical and compositional formation properties. The main advantage of these methods over conventional multi-mineral solvers is their ability to take into account the nonlinear correlation between the volumetric concentration of mineral/fluid constituents and well logs, which becomes important in the presence of both gas and complex lithology. Furthermore, the bed-by-bed inversion

technique enables corrections of shoulder-bed effects on low-resolution logs while performing the estimation of mineral/fluid concentrations.

In this chapter, we estimate compositional and petrophysical properties using depth-by-depth nonlinear joint inversion of well logs. The reason for this choice over conventional multi-mineral solvers is the presence of gas and complex mineral composition in the studied field example, where conventional multi-mineral solvers are not accurate. In the field example studied here, the effect of shoulder beds on well logs is not significant in the pay zones. Accordingly, we implement a depth-by-depth joint inversion of well logs instead of bed-by-bed interpretation in order to reduce CPU time.

The depth-by-depth nonlinear joint inversion of well logs takes conventional well logs as input. It then applies an inversion of physical properties of the formation (i.e., electrical conductivity, photoelectric factor, density, neutron migration length, and U, Th, and K volumetric concentrations) to estimate petrophysical and compositional properties (i.e., porosity, water saturation, volumetric concentration of shale, and volumetric concentrations of mineral constituents) at each well-log sampling point. In doing so, we use Schlumberger's software, SNUPAR[4], to estimate photoelectric factor and neutron migration length based on volumetric concentrations of mineral and fluid components of the formation and their chemical composition.

Well logs input to the inversion include gamma ray (GR), apparent electrical resistivity, density, neutron porosity, and photo-electric factor (PEF). We assume that the dominant non-clay minerals in this formation include quartz, calcite, and dolomite. Based on GR-spectroscopy data in addition to PEF and density logs in other wells penetrating this formation, the clay type is verified to be mainly illite. Inversion products are

[4] Mark of Schlumberger

porosity, fluid saturations, and volumetric concentrations of clay, quartz, calcite, and dolomite.

### 6.2.2 Core-Based Hydraulic Rock Typing

Hydraulic rock typing considers both storage and flow capacity of reservoir rocks and should be based on both pore size distribution and connectivity (Archie, 1950; Rushing et al., 2008). Three core-based hydraulic rock typing methods are widely used by the industry, including Leverett's RQI (1941), Winland $R_{35}$ (Pittman, 1992), and flow zone index (FZI) (Amaefule et al., 1993). Chapter 5 presents the mathematical and petrophysical similarity of these methods using random porosity-permeability data, and indicates that the three estimators should work equally well as long as they can be connected to certain petrophysical attributes in the well-log data domain. For core-based hydraulic rock typing, in this chapter Leverett's RQI is consistently used to classify hydraulic rock types based on routine core measurements. Furthermore, hydraulic rock types are used to rank dynamic rock-fluid properties including saturation-dependent capillary pressure and relative permeability.

### 6.2.3 Invasion Facies Modeling (IFM)

Invasion-induced well-log signatures bear rich petrophysical information connecting to dynamic flow behavior in the near-borehole region. After core-based rock typing, porosity-permeability trends, saturation-height relations, capillary pressure and relative permeability curves can be obtained for all rock types. We proceed to simulate the process of mud-filtrate invasion at reservoir conditions for each rock type. Inputs to this simulation include (a) petrophysical properties such as porosity, permeability, fluid saturations, and saturation-dependent capillary pressure and relative permeability, (b) drilling parameters such as mud type, invasion time, and overbalance pressure, (c) fluid

properties such as density, viscosity, composition, and salt concentration (NaCl equivalent), and (d) formation properties such as temperature and pressure. With relatively stable drilling conditions and constant fluid properties, rock petrophysical properties determine the radial distributions of water saturation which affect the radial distributions of various physical properties such as electrical resistivity, density, and migration length. The simulated radial distributions of physical properties are then input into numerical simulations of apparent resistivity, density, and neutron logs (Gandhi et al., 2010). By matching all available well logs after mud-filtrate invasion, we obtain a set of estimated rock-fluid dynamic petrophysical properties, including saturation-dependent capillary pressure and relative permeability. We adopt Voss et al.'s (2009) procedures to iteratively estimate petrophysical properties using UTAPWeLS. Environmentally-corrected well logs are used to compare against numerical simulations in the described process.

### 6.2.4 Log-Based Rock Classification

In log-based rock classification, assessment of static petrophysical properties using well-log interpretation techniques is as critical as the assessment of dynamic petrophysical properties. Static petrophysical properties that we use in rock classification include volumetric concentration of clay ($C_{cl}$), total porosity ($\phi_t$), and initial total water saturation ($S_{wi}$). All these petrophysical properties bear a closer relationship to hydraulic rock types than do apparent logs. Therefore, we suggest a rock typing technique based on estimated petrophysical properties whenever possible. Furthermore, there exist log-derived attributes that are indirectly related to reservoir quality, such as neutron-density separation (due to residual gas after invasion), spontaneous potential (SP) deflection, and ratio between shallow and deep resistivity logs, which are valuable in the estimation

process. This method classifies rock types via cluster analysis on all relevant petrophysical attributes including estimated petrophysical properties using well logs, saturation-height relation (only applicable above the hydrocarbon-water contact), and invasion-induced log signatures such as separation between resistivity logs with different radial lengths of investigation.

### 6.2.5 Permeability Prediction and Saturation-Height Modeling

After log-based rock typing, we implement rock-type based porosity-permeability correlations to estimate permeability based on porosity estimates from well logs. In addition, the vertical distribution of water saturation can be calculated using rock-type-based saturation-height relations derived from core MICP data. Estimates of permeability and water saturation are then verified using core measurements.

## 6.3 FIELD CASE: CHASE GROUP, HUGOTON GAS FIELD, ANADARKO BASIN, KANSAS

### 6.3.1 Reservoir Background

The Hugoton field in Kansas is one of the largest conventional gas fields in North America. Cumulatively it has produced more than 23 TCF of gas during the past 70 years (Olson et al., 1997). Gas production originates mainly from the Lower Permian Chase and Council Grove Groups. The whole reservoir is divided into 13 stratigraphic intervals that have complex lithofacies spreading from continental and marine siltstones to sandstones, mudstone to grainstone limestones, fine- to medium-crystalline dolomites, and phylloid algal bafflestones (Dubois et al., 2006). Reservoir quality is controlled by depositional texture with significant diagenetic overprints such as dolomotization, chemical compaction, leaching, and cementation (Olson et al., 1997). The Kansa Geological Survey (KGS) conducted a comprehensive core study and classified rocks into 11 lithofacies based on depositional sequences (siliciclastic or carbonate), rock

texture, and principal pore size (Dubois et al., 2006). A standard single-hidden-layer neural network was then applied to predict lithofacies based on wireline well logs in 1,600 node wells throughout the Hugoton and Panoma fields (Dubois et al., 2006). However, the link between static and dynamic petrophysical properties and their imprint on well logs through mud-filtrate invasion remains an interesting topic to be investigated. This study examined two key wells in the Hugoton field. Both wells include routine and special core measurements. Wireline log data are limited to a conventional logging suite that includes gamma ray, neutron porosity, density, photo-electric factor, and dual-induction apparent resistivity logs. A technical challenge in this field is relatively deep invasion due to low reservoir pressure (Torres-Verdín et al., 2006). Deep mud-filtrate invasion affects even the deep apparent resistivity logs, leading to unreliable estimates of water saturation. Thus, it is necessary to invoke rock typing to model both vertical and radial distributions of water saturation. Furthermore, the permeability range for a given value of porosity straddles several orders of magnitude. It follows that petrophysical rock typing is necessary to reduce the uncertainty associated with permeability estimation from well logs.

### 6.3.2 Inversion-Based Petrophysical Analysis

This analysis applied depth-by-depth nonlinear joint inversion of GR, PEF, neutron porosity, density, and apparent electrical resistivity logs and estimated porosity, water saturation, and volumetric concentrations of clay, quartz, calcite, and dolomite. Table 6.1 lists Archie's parameters and rock and fluid properties assumed for petrophysical analysis. Figure 6.1 shows the inversion results compared to core data. A single porosity-permeability correlation was used to estimate permeability using porosity estimated from nonlinear joint inversion. Not surprisingly, the estimated permeability

distribution does not match core data very well due to both the averaging effect of well logs and lack of attention to specific rock classes (Figure 6.1, Track 10). In addition, water saturation calculated in the interval of 2680 – 2760 ft is significantly lower than that of core measurements (Figure 6.1, Track 9). The first explanation for this behavior is that water saturation in core samples increases due to quick spurt loss invasion that can be very deep when (a) reservoir pressure is very low, and (b) porosity is low. A second explanation is that the Archie's constants may change with rock types due to the presence of secondary porosity. In this case, the poor estimation of both water saturation and permeability calls for petrophysical rock typing as an improved alternative for petrophysical estimation.

### 6.3.3 Core-Based Hydraulic Rock Typing

Before performing rock classification with well logs, it is necessary to study rock types and their petrophysical variabilities from ground-truthing core data carefully. Then, well-log signatures due to these rock types at specific reservoir conditions (e.g., temperature, pressure, and connate-water salt concentration) should be modeled and understood to guide log-based rock classification. This is a reliable way to reconcile core data and multi-physics borehole measurements for improved reservoir characterization.

In this study, hydraulic rock types are first established using routine core porosity-permeability measurements. Five hydraulic rock types were identified from the histogram distribution of Leverett's reservoir quality index (Figure 6.2). Table 6.2 summarizes the statistical variability of petrophysical properties associated with each rock type. Due to the absence of core plugs in non-reservoir facies (shale or mudstone), there is one rock type (RT6) missing from the core-based classification. For completeness, RT6 will also

be classified from well logs. In our naming convention, RT1 designates the highest reservoir quality and RT6 designates the lowest.

Figure 6.2 indicates clear trends of porosity-permeability correlations for each rock type. If well logs can indicate the rock type in the core domain, permeability estimation becomes less uncertain. Noteworthy is that petrophysical rock type only considers pores instead of grains. Thus, marine sandstone may be classified as the same rock type as grainstone when rock typing is only based on pore geometry. To distinguish lithofacies, it is necessary to integrate nuclear logs such as PEF and neutron porosity in the analysis.

Next, we use the identified rock types to classify dynamic petrophysical properties including saturation-dependent capillary pressure and relative permeability (Figure 6.3). Defined rock types reflect dominant pore throat sizes (plateau of saturation-dependent capillary pressure curves). The saturation-dependent relative permeability of the gas phase is similar in all rock types, whereas the water-phase relative permeability varies significantly across different rock types. This behavior can be explained from wettability properties. Because gas is the non-wetting phase occupying the largest pores, a given pore volume in the large pore-size end entails a similar gas phase relative permeability. On the other hand, water is the wetting phase filling the smallest pores, which exhibit more variability, as evidenced by the core MICP data.

### 6.3.4 Invasion Facies Modeling (IFM)

If log-based rock typing links static and dynamic petrophysical properties, the vertical distribution of water saturation can be accurately estimated based on rock types and the height above the gas-water contact. Likewise, the saturation-dependent relative permeability of each layer can be upscaled to reservoir grids for accurate flow simulation.

After core-based rock typing, we estimate an average saturation-dependent capillary pressure and relative permeability for each rock type. We then select thick zones of each rock type at different reservoir heights, simulate the process of mud-filtrate invasion under observed drilling and reservoir conditions, calculate radial distributions of fluid saturations, and numerically simulate gamma-ray, bulk density, neutron porosity, photo-electric factor, and dual-induction apparent resistivity logs, taking into account the effect of mud-filtrate invasion. Table 6.3 lists the assumed simulation parameters; these properties simultaneously honor routine core measurements, the well-log-derived saturation-height relation, and mud-filtrate invasion. Therefore, they are suitable for upscaling in reservoir simulation grids. One key advantage of invasion-calibrated dynamic petrophysical properties is that these properties have been calculated at reservoir conditions. The best rock type gives rise to the highest resistivity due to the lowest connate water saturation. Additionally, permeable rocks allow deeper mud-filtrate invasion, which gives rise to separation of apparent resistivity logs with different lengths of investigation.

The following sections describe each invasion facies (IF) in detail. In this ranking convention, IF-1 and IF-5 identify the best and poorest reservoir quality, respectively. Table 6.4 summarizes the properties of each invasion facies and their associated lithofacies interpretation. For improved understanding of invasion, we introduce them from the least (IF-5) to the most invaded facies (IF-1).

#### *6.3.4.1 Invasion Facies No. 5 (IF-5)*

Rock type IF-5 is a shale/mudstone facies located in a gas-bearing zone. The corresponding depth interval is almost not invaded by mud filtrate due to its extremely low permeability. One of the most prominent features of IF-5 is that there is no separation

between electrical resistivity logs with different radial lengths of investigation, thereby indicating negligible invasion or no invasion. Permeability of IF-5 can be considered as an invasion threshold, below which mud filtrate cannot penetrate deep enough during the drilling time scale to exchange salt with connate water. Therefore, invasion has negligible impact even on the shallowest apparent resistivity log. At the same time, there are some other log attributes available to distinguish this facies. For example, the GR log is relatively high, and the neutron-density separation is prominent. PEF reads approximately 2.8 b/e, which is consistent with the major clay type – illite. Figure 6.4 describes numerical simulations of nuclear and resistivity logs as well as radial distributions of total water saturation, salt concentration, and electrical resistivity, obtained from the numerical simulation of the process of mud-filtrate invasion.

#### *6.3.4.2 Invasion Facies No. 4 (IF-4)*

Rock type IF-4 is a wackestone facies located in a gas-bearing zone. The corresponding depth interval is only slightly invaded (or skin invasion) due to its low permeability. IF-4 is different from IF-5 in that it does exhibit separation between shallow and medium/deep apparent resistivity logs, which is attributed to very shallow mud-filtrate invasion. The key petrophysical parameter to differentiate from IF-5 is its permeability range, which is above the invasion threshold defined in IF-5. However, due to the low permeability involved in this rock type, mud-filtrate invasion in the drilling time scale can only impact the shallow resistivity. Water saturation and salt concentration in the deep radial zone are nearly constant. Salt exchange between connate water and mud filtrate in the shallow radial zone gives rises to resistivity enhancement (i.e., shallow resistivity > deep/medium resistivity). Additionally, neutron-density logs show a significant separation due to substantial clay concentration. PEF is larger than 3.0 b/e,

thereby suggesting a carbonate mineral base. Figure 6.5 shows the corresponding numerical simulations of nuclear and resistivity logs as well as radial distributions of total water saturation, salt concentration, and electrical resistivity obtained from simulations of mud-filtrate invasion.

#### *6.3.4.3 Invasion Facies No. 3 (IF-3)*

Rock type IF-3 is a packstone facies located in a fully water-saturated zone. The corresponding depth interval is deeply invaded due to a combination of low porosity and medium permeability. Both water saturation and salt concentration exhibit prominent radial variations. The separation between shallow and deep/medium resistivity is much larger than in the cases of IF-4 and IF-5. Deep and medium apparent resistivity logs are also slightly separated, which indicates invasion beyond the depth of investigation (DOI) of medium resistivity (i.e., about 3 ft in this case). Low gamma ray and very high PEF (~ 5.0 b/$e^-$) indicate major limestone composition. Figure 6.6 shows the corresponding numerical simulations of nuclear and resistivity logs as well as radial distributions of total water saturation, salt concentration, and electrical resistivity, obtained from the simulation of mud-filtrate invasion.

#### *6.3.4.4 Invasion Facies No. 2 (IF-2)*

Rock type IF-2 is a dolomitized grainstone facies located in a gas-bearing zone. The whole interval is deeply invaded. IF-2 is similar to IF-3 in terms of separation between shallow and deep/medium resistivity. However, there is no separation between deep and medium resistivity, indicating an invasion depth shallower than the DOI of the medium resistivity log. The underlying petrophysics that explains shallower invasion than in the case of IF-3 is larger porosity due to dolomitization. Resistivity values in IF-2 are relatively larger than those of IF-3 due to a saturation-height relation governed by the

pore-throat size distribution. Meanwhile, low gamma ray and a PEF reading close to 3.0 b/e indicate major concentration of dolomite instead of limestone. Figure 6.7 shows the corresponding numerical simulations of nuclear and resistivity logs as well as radial distributions of total water saturation, salt concentration, and electrical resistivity, calculated from the process of mud-filtrate invasion.

#### *6.3.4.5 Invasion Facies No. 1 (IF-1)*

Rock type IF-1 is a marine sandstone facies located in a gas-bearing zone. IF-1 is very similar to IF-2 in terms of both resistivity values and resistivity separation patterns. Larger porosity results in even shallower invasion that is not distinguishable from that of IF-2 using resistivity logs of only 3 different radial lengths of investigation. A more prominent difference is the PEF reading which is lower than 3.0 b/e, thereby indicating a major mineral composition of quartz/clay other than dolomite/limestone. In fact, IF-1 has the best reservoir quality, including both high porosity (storage capacity) and high permeability (flow capacity). Figure 6.8 shows the corresponding numerical simulations of nuclear and resistivity logs as well as radial distributions of total water saturation, salt concentration, and electrical resistivity, calculated from the process of mud-filtrate invasion.

### 6.3.5 Sensitivity Analysis of Radial Invasion Profiles to Rock Facies

Figure 6.9 shows radial distributions of water saturation, salt concentration, and electrical resistivity obtained from the numerical simulation of mud-filtrate invasion in each rock type. Rock types IF-4 and IF-5 do not exhibit significant radial variations of water saturation, salt concentration, and electrical resistivity due to shallow or negligible invasion. IF-1, IF-2, and IF-3 all exhibit substantial radial variations of water saturation, salt concentration, and electrical resistivity, which are an indication of good permeability.

Based on the radial distribution of water saturation in Figure 6.9a, the rock with the highest porosity exhibits the shallowest invasion, whereas the rock with the lowest porosity exhibits the deepest invasion. Radial distributions of salt concentration in the three facies are very similar due to their close dispersivity. However, small differences still exist in the radial distributions of salt concentration in the different rock facies. IF-3 exhibits a smooth radial profile of salt concentration compared to those of IF-1 and IF-2, due to its larger salt dispersivity (Figure 6.9b). With the presence of mobile gas, all facies exhibit an annulus resistivity profile, which is a consequence of radially dephased water saturation and salt concentration fronts (Torres-Verdín et al., 2004).

### 6.3.6 Sensitivity Analysis of Radial Invasion Profiles to Initial Water Saturation

Initial water saturation plays an important role in determining the invasion-induced radial resistivity profile. The underlying petrophysics is governed by saturation-dependent relative permeability. Mud-filtrate invasion was simulated in a packstone with three different initial water saturations: 1.0, 0.6, and 0.35, corresponding to different heights above the gas-water contact (GWC). Initial water saturation ($S_{wi}$) of 1.0 is representative of a fully water-saturated zone; initial water saturation ($S_{wi}$) of 0.65 is representative of gas-bearing zone in transition zone; initial water saturation ($S_{wi}$) of 0.35 is representative of gas-bearing zone at irreducible water saturation. Figure 6.10 shows the radial distribution of electrical resistivity for these three cases. An annulus effect is only observed in the presence of gas ($S_{wi}$ = 0.35 and 0.6), but not in the case of the fully water-saturated zone. This experiment confirms that the annulus profile is a consequence of high gas mobility coupled with salt dispersion (Torres-Verdín et al., 2004).

### 6.3.7 Invasion Facies: Bimodal vs. Unimodal Pore-Size Distributions

Carbonate rocks sometimes exhibit bimodal pore-size distributions due to presence of vugs, fractures, and moldic pores. This special type of rock is often associated with unique capillary pressure and relative permeability when compared to that of unimodal pore-size distributions. Consequently, the invasion behavior is also different for two reasons: (1) different $S_{wi}$ due to saturation-height behavior, (2) different saturation-dependent relative permeability. Figure 6.11 shows an example of two rocks of essentially the same porosity and permeability but different pore-size distribution. At a given height above the GWC (i.e., 100 ft), the bimodal rock type exhibits much higher initial connate water saturation. Meanwhile, at the same water saturation, lower water relative permeability inhibits quick displacement of gas by mud filtrate. As a result, the separation between shallow and deep electrical resistivity logs decreases (Figure 6.12b). Also, there is no annulus observed in this type of rock. In the field case, two depth intervals included such rock types, one in the gas-bearing zone at the depth of 2796 ft and the other in the water-bearing zone at the depth of 2880 ft.

### 6.3.8 Well-Log Based Rock Typing, Permeability Estimation, and Saturation-Height Modeling

After quantifying invasion-induced log signatures, invasion properties can be integrated into rock classification. Several log-derived attributes are used to classify and rank reservoir rock types. Table 6.5 summarizes the correlation between log attributes and rock types. The goal is to consistently interpret those log attributes and rank their reservoir quality by connecting physics, petrophysics, and geology. Figure 6.13 shows rock classification results (Track 8) and corresponding estimations of water saturation (Track 9) and permeability (Track 10); they show a good agreement between estimated permeability and core measurements. Here, because water saturation derived from rock

types and reservoir height is independent of Archie's equation, it is only marginally affected by factors such as variable $R_w$, $a$, $m$, and $n$. The introduced rock classification honors both static and dynamic petrophysical properties and assimilates their corresponding effects on well logs. Therefore, it provides distributions of rock type that are suitable for flow simulation and production optimization.

## 6.4 CONCLUSIONS

We successfully applied a new rock classification method to describe a challenging gas reservoir comprising mixed clastic-carbonate sequences. The new method is based on conventional well logs and reconciles both static and dynamic petrophysical properties by integrating inversion-based petrophysical analysis and dynamic mud-filtrate invasion modeling. It was found that mud-filtrate invasion, which is affected by both dynamic and static petrophysical properties of the invaded formation, gives rise to unique and specific well-log signatures on different rock types. Such signatures can be used for rock classification. A new concept, referred to as invasion facies, was developed to describe rock types with their dynamic flow behavior in the near-borehole region. Well-log attributes connecting both static and dynamic petrophysical properties were invoked to classify rock types. The resulting distribution of rock types can be used to improve the estimation of permeability and saturation, hence their agreement with core measurements. The field application of the new method in the Hugoton gas field verifies the reliability and accuracy of the new interpretation method.

**Table 6.1:** Summary of core-calibrated Archie's parameters, rock and fluid properties for petrophysical analysis in the Hugoton gas field.

| Variable | Unit | Value |
|---|---|---|
| Archie's factor, *a* | - | 1.0 |
| Archie's porosity exponent, *m* | - | 1.96 |
| Archie's saturation exponent, *n* | - | 1.83 |
| Connate water resistivity @ 96 $^{o}$F | ohm.m | 0.04 |
| Connate water salt concentration | ppm NaCl | 170,000 |
| Mud-filtrate water resistivity @ 96 $^{o}$F | ohm.m | 0.84 |
| Mud-filtrate salt concentration | ppm NaCl | 5147 |
| Connate water density | g/cm$^3$ | 1.06 |
| In-situ gas density | g/cm$^3$ | 0.02 |
| Shale porosity | p.u. | 10.0 |
| Mudstone porosity | p.u. | 3.0 |

**Table 6.2:** Statistical distributions of porosity, permeability, and RQI for each rock type.

| Rock Type | Total Porosity (p.u.) | Permeability (mD) | RQI (µm) | Lithofacies Interpretation |
|---|---|---|---|---|
| RT1 | 16.9 ± 6.3 | 28.2 ± 12 | 14.3 ± 7.0 | Marine sandstone or grainstone |
| RT2 | 15.6 ± 5.0 | 9.30 ± 5.2 | 7.50 ± 1.4 | Grain-dominated packstone |
| RT3 | 12.5 ± 4.3 | 1.60 ± 1.0 | 3.50 ± 0.7 | Packstone or very fine crystalline sucrosic dolomite |
| RT4 | 11.0 ± 3.0 | 0.47 ± 0.19 | 2.05 ± 0.27 | Mud-dominataed packstone |
| RT5 | 6.60 ± 3.2 | 0.052 ± 0.045 | 0.85 ± 0.27 | Wackestone |
| RT6 | [0 – 12] | < 0.001 | < 0.1 | Marine siltstone/shale or mudstone |

**Table 6.3:** Summary of mudcake, fluid, and formation properties assumed in the simulation of mud-filtrate invasion.

| Variable | Value | Unit |
|---|---|---|
| Wellbore radius | 4.0 | inch |
| Maximum invasion time | 2 | days |
| Formation outer boundary | 2000 | ft |
| Reservoir temperature | 96 | $^{o}F$ |
| Initial reservoir pressure | 200 | psi |
| Water viscosity (at reservoir condition) | 0.9 | cP |
| Gas viscosity | 0.0149 | cP |
| Overbalance pressure | 1000 | psi |
| Salt dispersivity | 0.4 - 1.0 | ft |
| Mud-filtrate density (at STP) | 1.04 | $g/cm^3$ |
| Mud-filtrate viscosity (at STP) | 0.9 | cP |
| Mud-filtrate compressibility (at STP) | $3.6 \times 10^{-6}$ | $psi^{-1}$ |
| Formation compressibility | $4 \times 10^{-7}$ | $psi^{-1}$ |
| Mudcake reference permeability | 0.01 | mD |
| Mudcake reference porosity | 0.35 | frac. |
| Mud solid fraction | 0.06 | frac. |
| Mudcake maximum thickness | 0.4 | inch |
| Mudcake compressibility exponent | 0.40 | frac. |
| Mudcake exponent multiplier | 0.10 | frac. |

**Table 6.4:** Summary of petrophysical properties of each invasion facies and corresponding lithofacies interpretation.

| Invasion Facies | Average Porosity (p.u.) | Average In Situ Permeability (mD) | Invasion Depth | Lithofacies Interpretation |
|---|---|---|---|---|
| IF-5 | 12 | < 0.0001 | Negligible | Shale/Mudstone |
| IF-4 | 6 | 0.1 | Skin invasion | Wackestone |
| IF-3 | 13 | 1 | Deep invasion | Packstone or very fine crystalline sucrosic dolomite |
| IF-2 | 18 | 10 | Medium invasion | Grain-dominated packstone |
| IF-1 | 24 | 50 | Medium invasion | Grainstone or marine sandstone |

**Table 6.5:** Summary of the petrophysical interpretation of log attributes and their correlations with reservoir quality.

| Log Attribute | Petrophysical Interpretation | Reservoir Quality Correlation |
|---|---|---|
| Clay volume | Larger clay volume, smaller average pore throat size | Negative |
| Total porosity | Larger porosity, likely high pore connectivity | Positive |
| Water saturation (at a given height above GWC) | At the same height, lower water saturation, and larger average pore-throat size | Negative |
| Radial resistivity separation | Larger separation, deeper filtrate invasion | Positive |
| Neutron-density separation | Larger separation, higher clay and water volumes | Negative |
| Neutron-density crossover | Larger crossover, low clay volume and more in-situ gas | Positive |
| SP log deflection | Deflection relates to irreducible water saturation | Positive |
| PEF | Good indicator of major mineral components | NA |

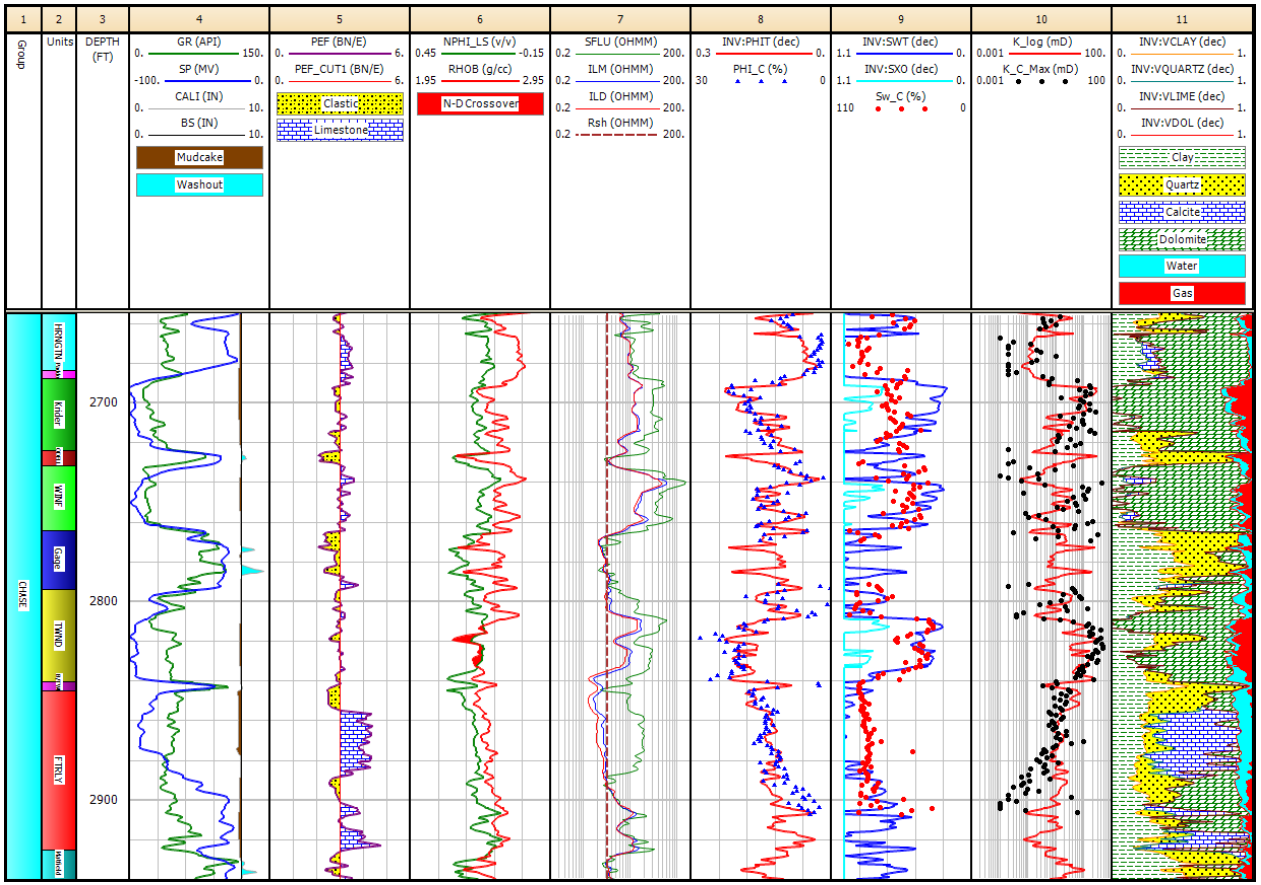


**Figure 6.1:** Hugoton gas field: Conventional well logs and corresponding estimates of petrophysical and compositional properties. Tracks from left to right include, Tracks 1-2: Stratigraphic units of Chase Group; Track 3: Depth, Tracks 4 – 7: Conventional well logs. Tracks 8 – 9: Comparison of estimated porosity and water saturation from well logs against core measurements; Track 10: Comparison of permeability estimates against core measurements; Track 11: Mineralogy estimates obtained via nonlinear joint inversion of well logs.

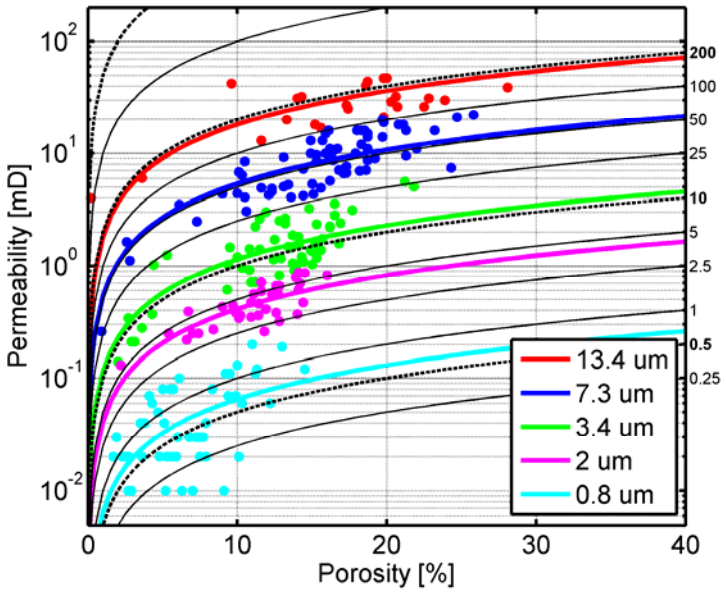


**Figure 6.2:** Core-based hydraulic rock typing using Leverett's RQI. Five rock types (RT1 – RT5) are defined with corresponding porosity-permeability correlations. RT6 is bypassed in core plugging.

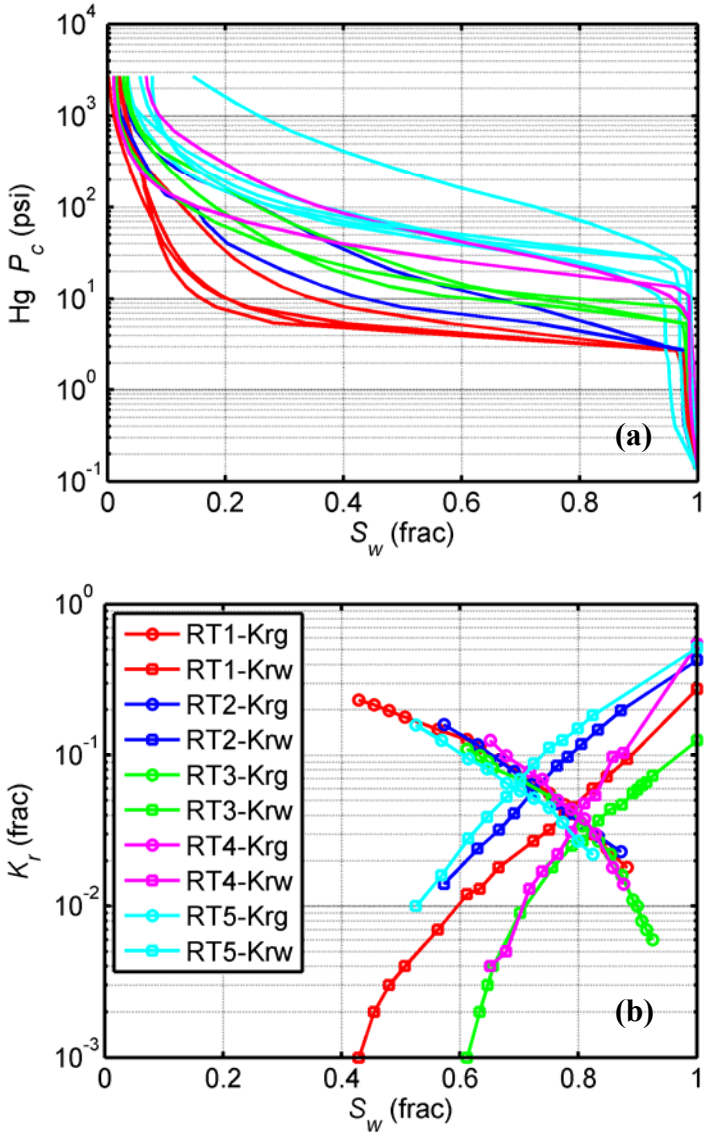


**Figure 6.3:** Comparison of saturation-dependent **(a)** MICP, and **(b)** drainage relative permeability for different rock types.

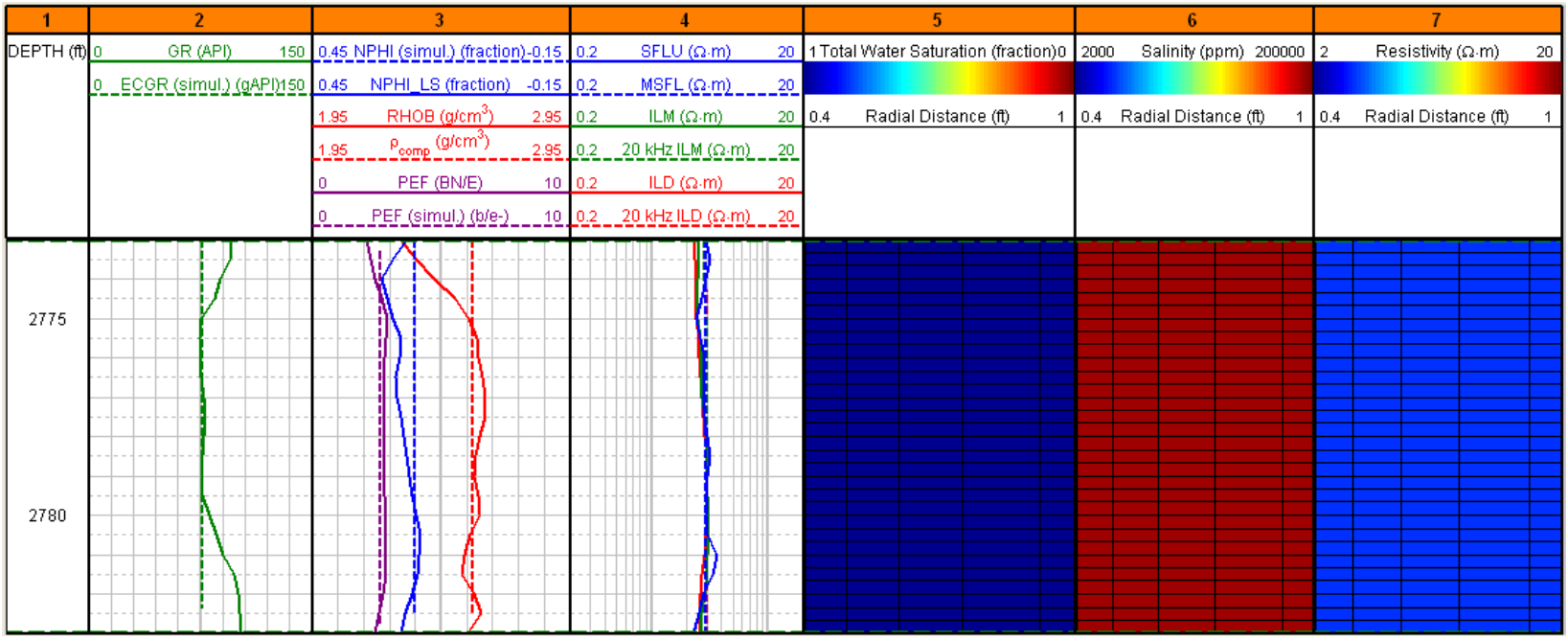


**Figure 6.4:** Rock type IF-5: Numerical simulations of nuclear and resistivity logs (Tracks 2 to 4) and radial distributions of total water saturation, salt concentration, and electrical resistivity (Tracks 5 to 7). This model corresponds to a gas-bearing shale/mudstone facies exhibiting negligible mud-filtrate invasion, average porosity of 12 p.u., and absolute permeability lower than 0.0001 mD.

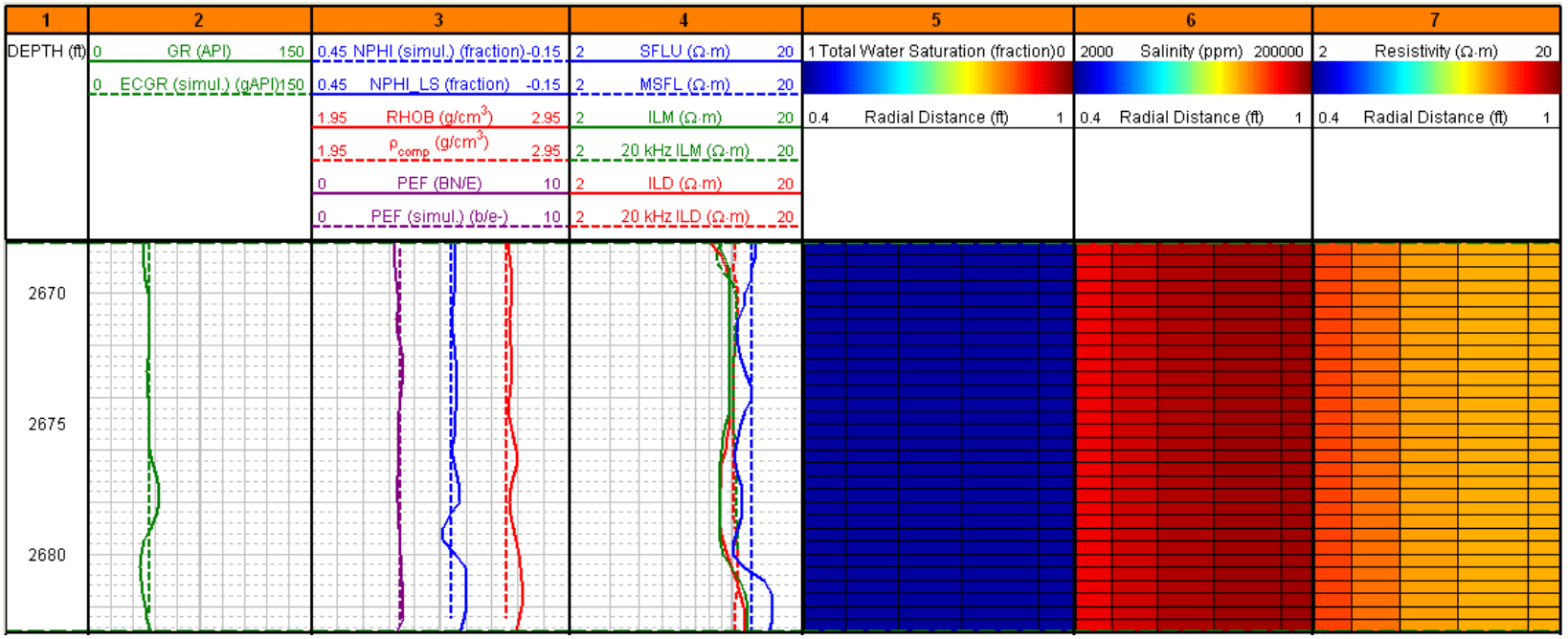


**Figure 6.5:** Rock type IF-4: Numerical simulations of nuclear and resistivity logs (Tracks 2 to 4) and radial distributions of total water saturation, salt concentration, and electrical resistivity (Tracks 5 to 7). This model corresponds to a gas-bearing wackestone facies with skin mud-filtrate invasion, average porosity of 5 p.u., and absolute permeability in the range of [0.001 – 0.01] mD.

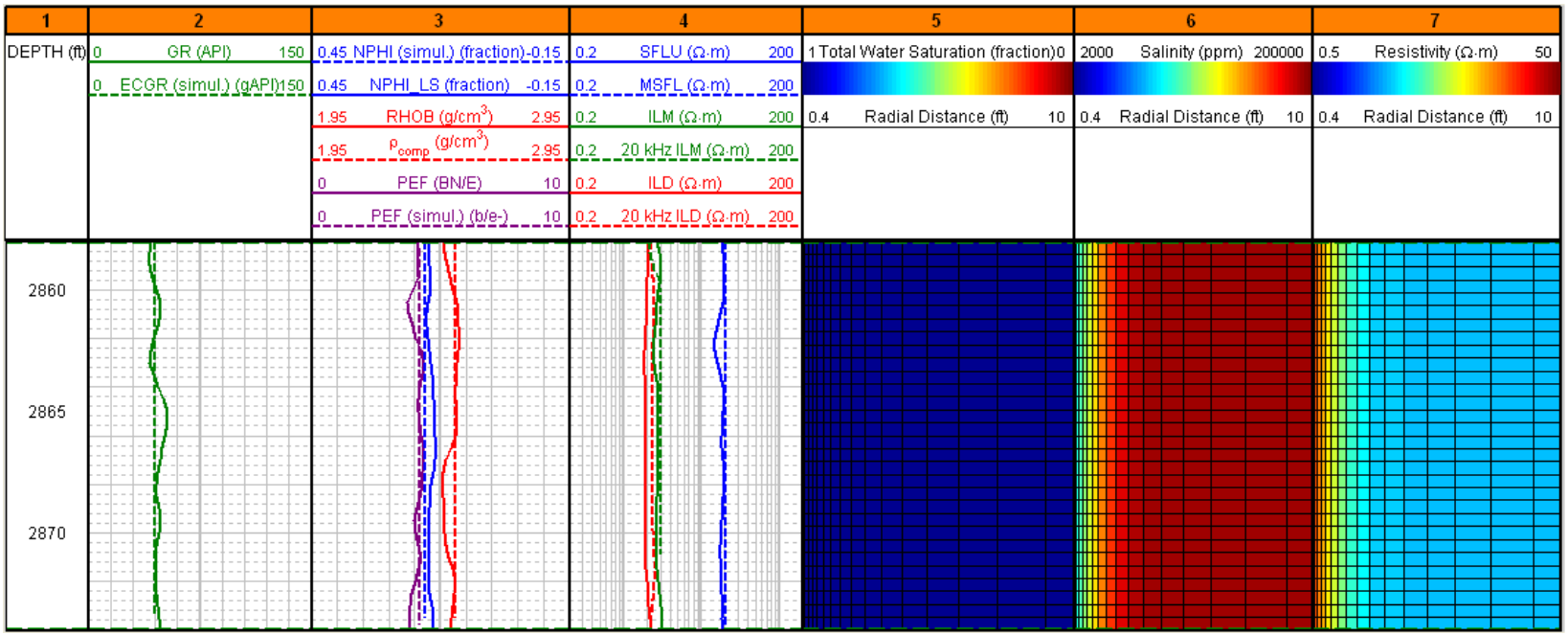


**Figure 6.6:** Rock type IF-3: Numerical simulations of nuclear and resistivity logs (Tracks 2 to 4) and radial distributions of total water saturation, salt concentration, and electrical resistivity (Tracks 5 to 7). This model corresponds to a water-saturated packstone facies with deep mud-filtrate invasion, average porosity of 13 p.u., and absolute permeability in the range of [0.5 ~ 5] mD.

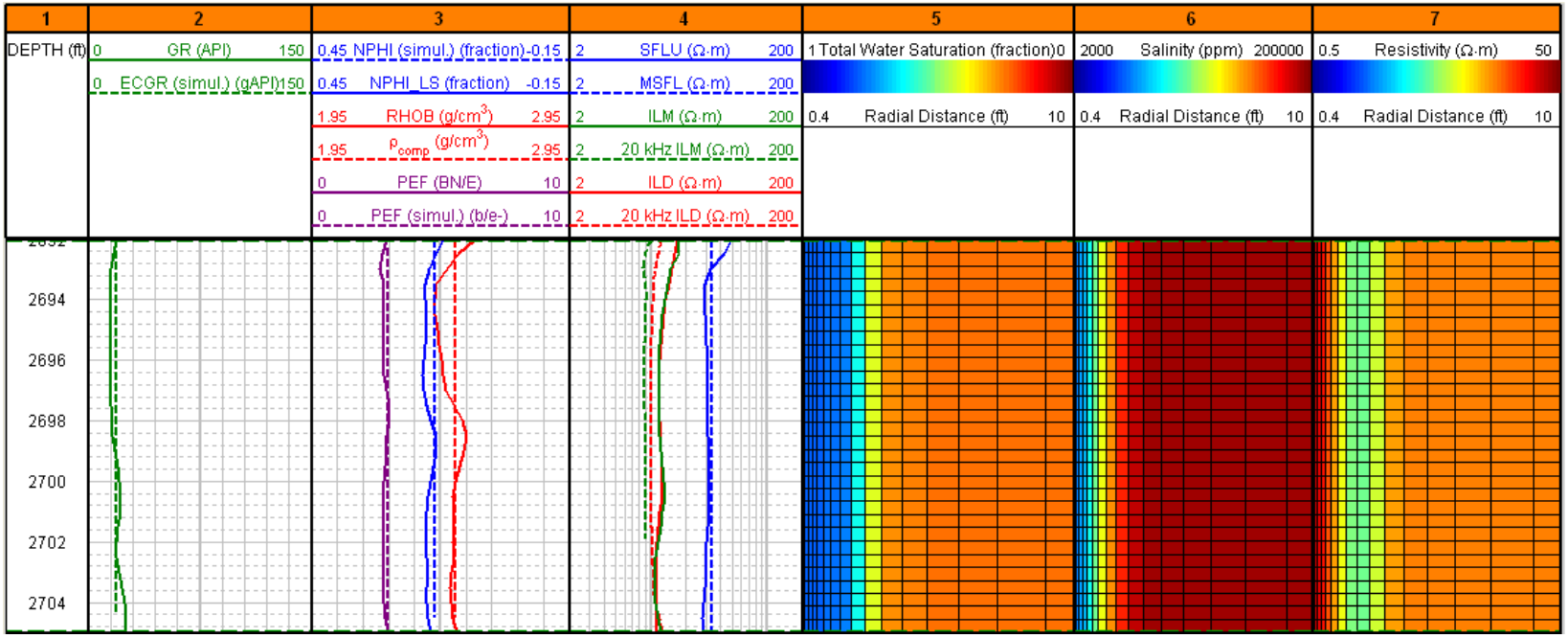


**Figure 6.7:** Rock type IF-2: Numerical simulations of nuclear and resistivity logs (Tracks 2 to 4) and radial distributions of total water saturation, salt concentration, and electrical resistivity (Tracks 5 to 7). This model corresponds to a gas-bearing grainstone facies with medium mud-filtrate invasion, average porosity of 18 p.u., and absolute permeability of about 10 mD.

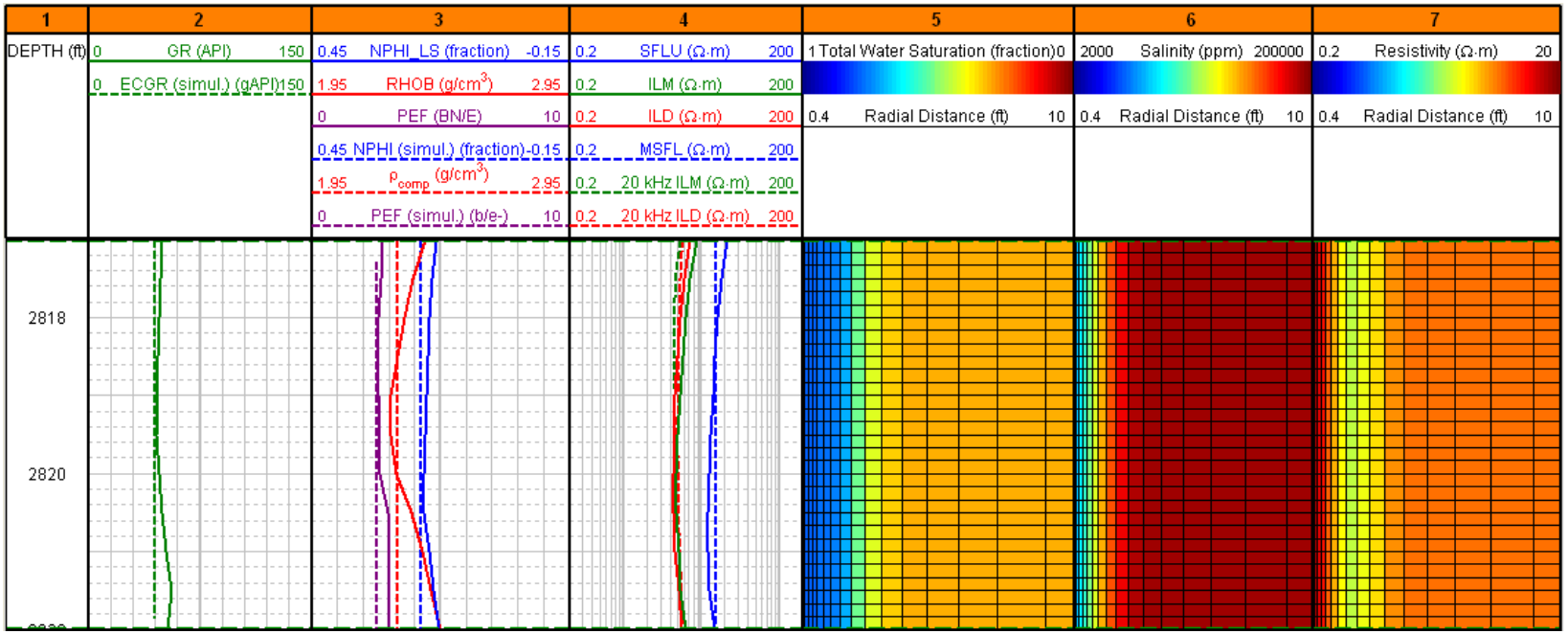


**Figure 6.8:** Rock type IF-1: Numerical simulations of nuclear and resistivity logs (Tracks 2 to 4, respectively) and radial distributions of total water saturation, salt concentration, and electrical resistivity (Tracks 5 to 7, respectively). This model corresponds to a gas-bearing marine sandstone facies with relatively shallow mud-filtrate invasion, average porosity of 22 p.u., and absolute permeability of 50 mD.

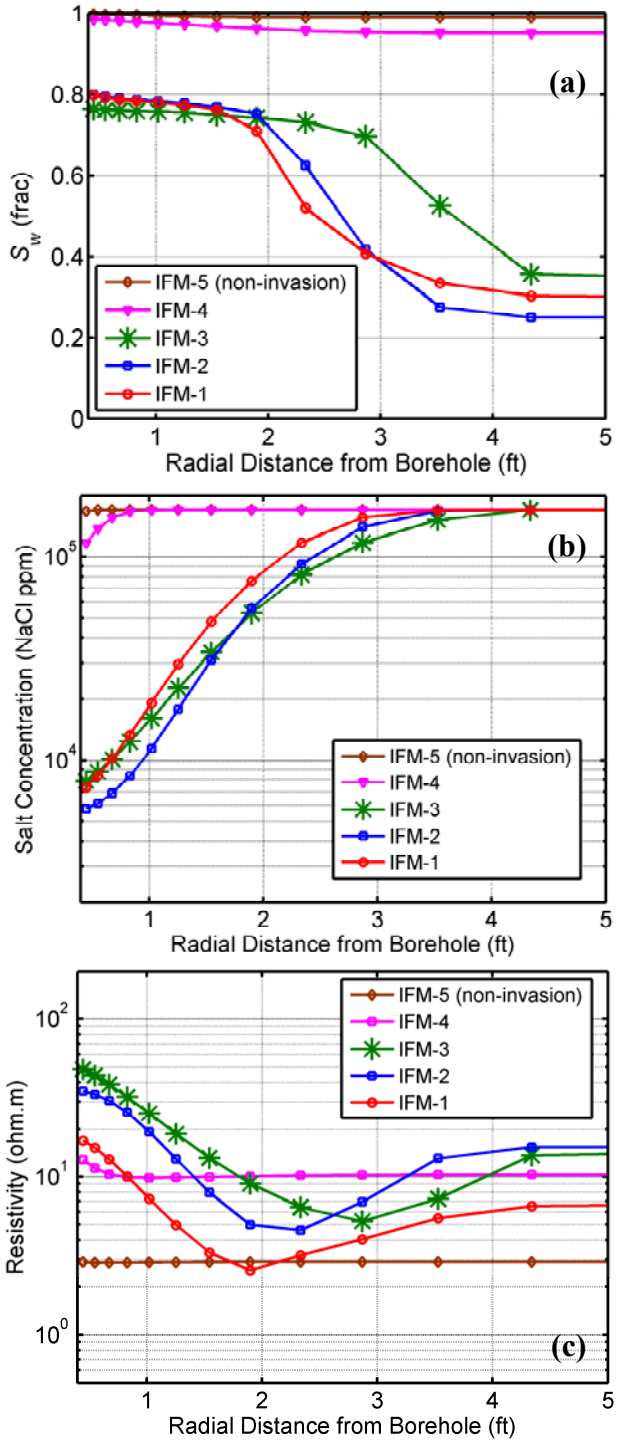


**Figure 6.9:** Radial distribution of **(a)** total water saturation, **(b)** salt concentration, and **(c)** electrical resistivity for the identified invasion facies.

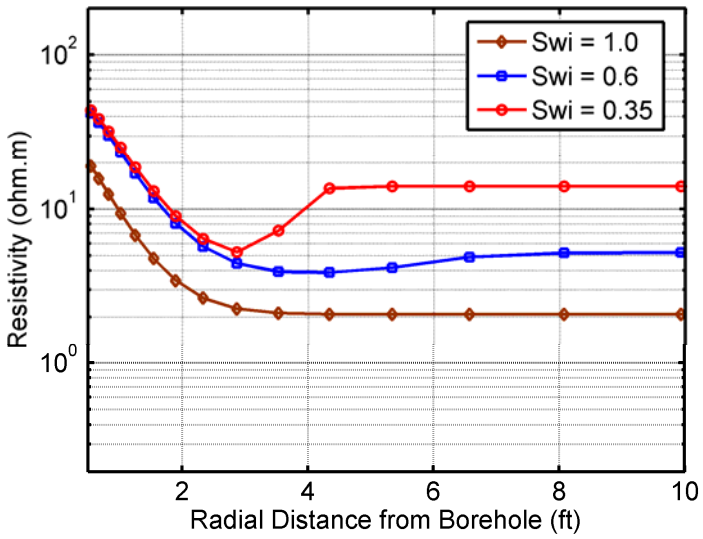


**Figure 6.10:** Radial distribution of electrical resistivity for three examples with equal rock properties but different initial water saturation. Values of initial water saturation correspond to different depths above the free-water level (FWL).

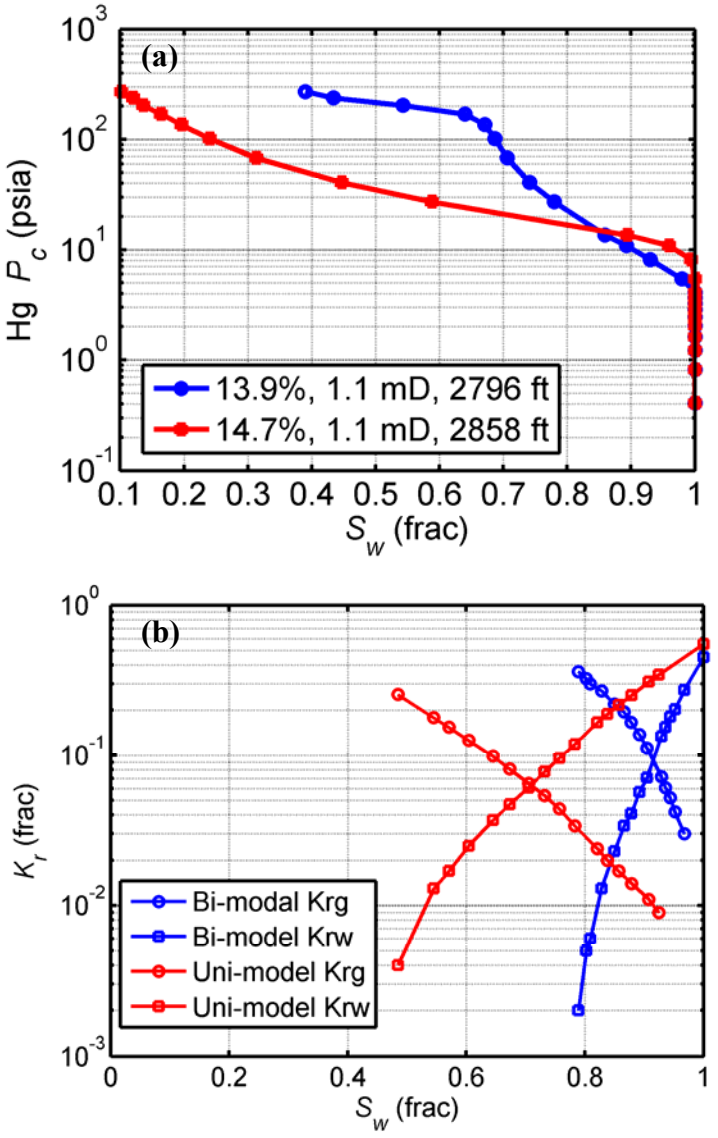


**Figure 6.11** Comparison of saturation-dependent **(a)** MICP, and **(b)** relative permeability for rocks with unimodal (red) and bimodal (blue) pore-size distributions.

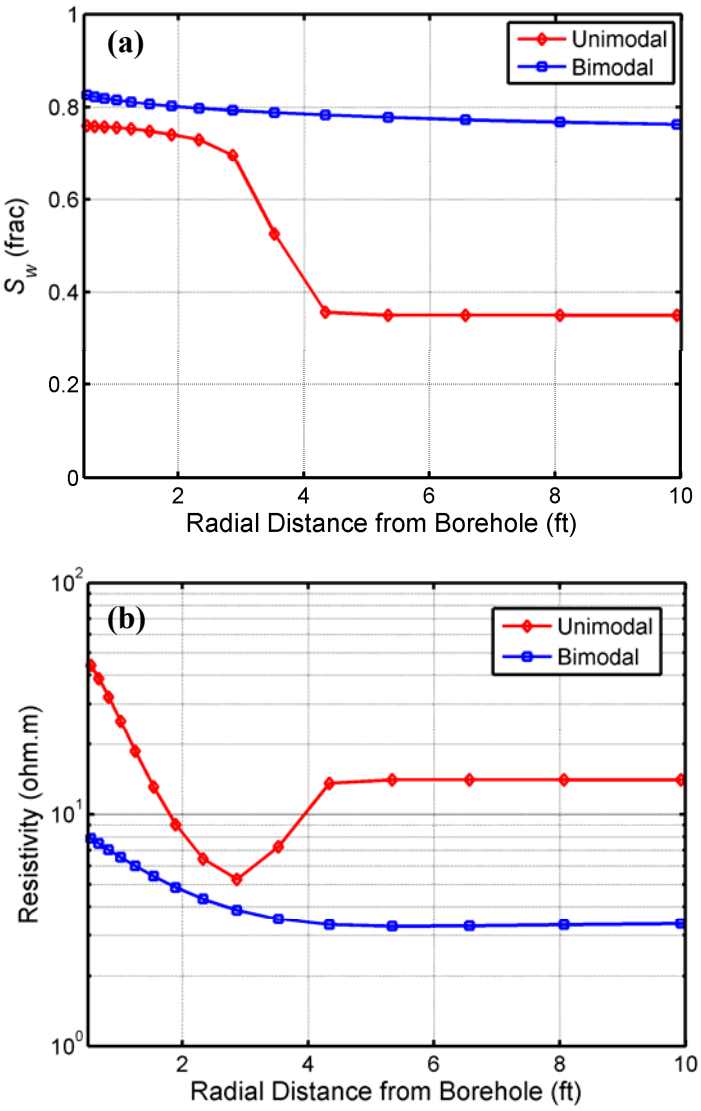


**Figure 6.12:** Radial distribution of **(a)** water saturation and **(b)** electrical resistivity after 2 days of mud-filtrate invasion in two rock types with unimodal and bimodal, saturation-dependent capillary pressure.

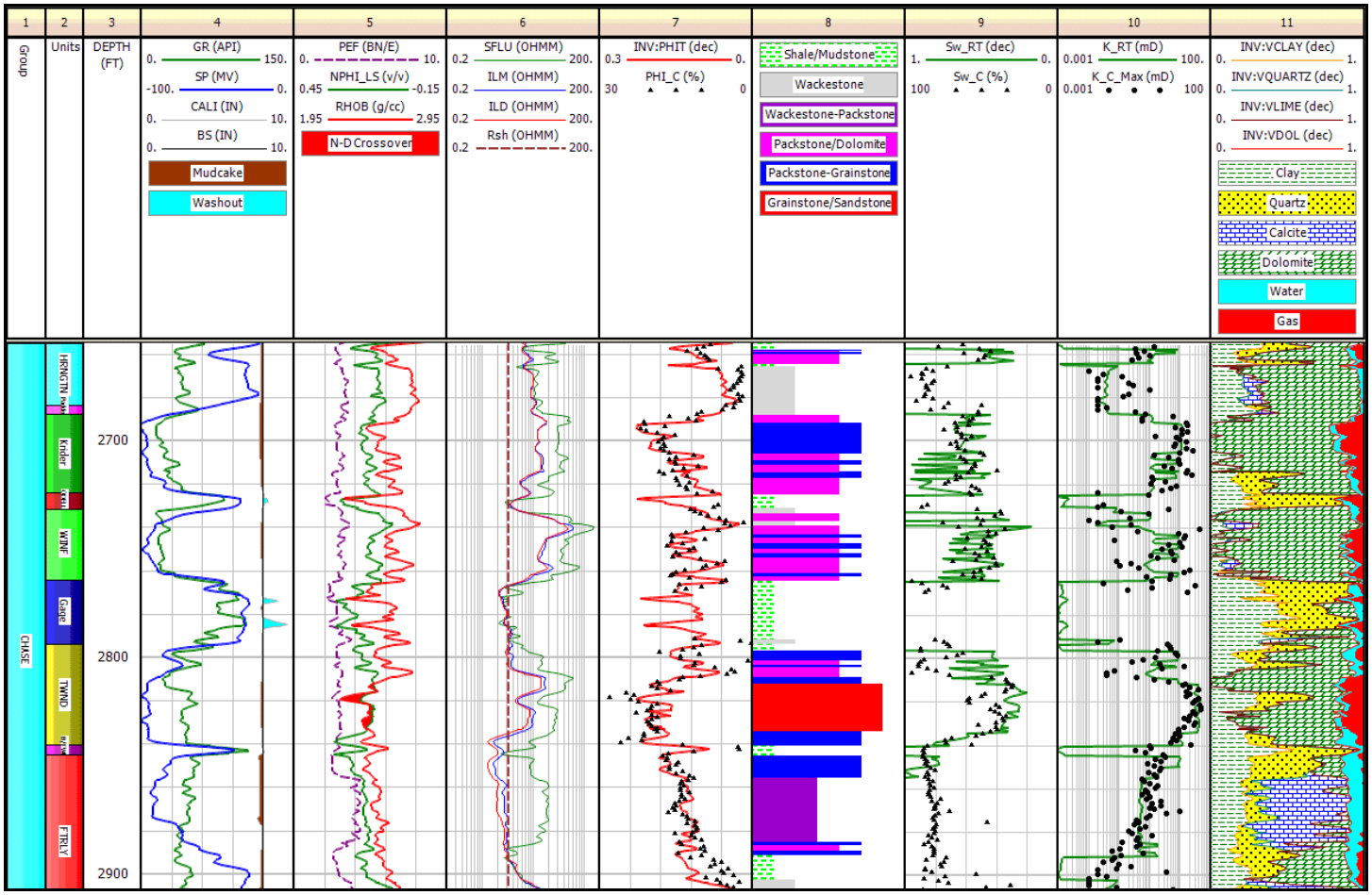


**Figure 6.13:** Rock typing with multiple log-attributes, including invasion facies. Tracks 1-2: stratigraphic units; Tracks 3-6: conventional well logs; Track 7: total porosity from inversion; Track 8: rock type; Track 9: saturation; Track 10: permeability; Track 11: mineralogy estimates from nonlinear depth-by-depth joint inversion of well logs.

# Chapter 7: Bayesian Hypothesis Testing with Fast Well-Log Forward Modeling to Validate Petrophysical Rock Typing and to Quantify Uncertainty in a Deltaic Gas Reservoir

Rock typing is critical in deepwater reservoir characterization to construct stratigraphic models populated with static and dynamic petrophysical properties. However, rock typing based on multiple well logs is challenging because different logging-tool physics exhibit different volumes of investigation. Consequently, large uncertainty is typically associated with rock typing in thinly bedded or laminated reservoirs because true physical properties cannot be resolved due to shoulder-bed effects. To circumvent this problem, we introduce a new Bayesian approach that inherently adopts the scientific method of iterative hypothesis testing to perform rock typing by simultaneously honoring different logging-tool physics in a multi-layered earth model. In addition to estimating the vertical distribution of rock types with maximum likelihood, the Bayesian method quantifies the uncertainty of rock types and associated petrophysical properties layer-by-layer.

Bayesian rock classification is performed with a fast sampling technique based on the Markov-Chain Monte Carlo method, thereby enabling an efficient search of rock types to obtain final results. We use a fast linear iterative refinement method to simulate nuclear logs and a 2D forward modeling code to simulate array-induction resistivity logs. A rock-type distribution hypothesis is considered acceptable only when all observed well logs are reproduced with forward modeling.

Both synthetic and field cases are used to verify the effectiveness of the new rock typing method. In a field case of deltaic gas reservoirs from offshore Trinidad, the Bayesian method differentiates rock types that exhibit subtle petrophysical variations due to grain size change. We show that the new method provides more than 77% agreement

between log-derived and core-derived rock types, whereas conventional deterministic methods achieve only 60% agreement due to the presence of thin beds and laminations. Rock types are verified with independent data sources such as laser particle size measurements and MICP.

Although large uncertainty is observed in thinly bedded and laminated zones, the Bayesian rock-typing method still yields rock types and petrophysical properties that agree well with core-plug measurements acquired in these layers. As a result, the overall correlation between log-derived permeability and core-measured permeability is improved by approximately 16% when compared to conventional deterministic methods. More importantly, the quantified petrophysical uncertainty provides critical information for estimating the uncertainty of reservoir storage and productivity to guide decision-making for later phases of reservoir development.

## 7.1 INTRODUCTION

Conventional petrophysical rock typing heavily relies on representative laboratory core measurements, including mineral concentrations, grain-size and pore-size distribution, fluid saturation and distribution (Archie, 1950 and 1952; Buckles, 1965; Pittman, 1992). Significant effort was devoted to deriving rock types from well logs with minimum core calibration or supervision (as in Chapters 5 and 6). A common issue faced in log-based rock typing is that log-derived rock types do not match core-derived rock types to a satisfactory level in thinly bedded or laminated reservoirs. Furthermore, when rock typing is based on well logs, which are physical measurements indirectly sensing geological or petrophysical attributes, large uncertainty is commonly associated with rock typing due to overlapping of log responses, even for the same geological or petrophysical rock type.

Forward physical modeling can predict unique well-log responses given a vertical distribution of rock types and their associated petrophysical properties. However, petrophysical interpretation, which aims to estimate rock petrophysical properties from well logs, is often subject to non-uniqueness (i.e., the concern of multiple working hypotheses in geosciences). This is particularly true when petrophysical thin beds are present. Unfortunately, such a simple fact has been routinely ignored in existing, deterministic apparent-log-based rock typing methods which generate only definite rock type distributions based on the philosophy of "*what I see is what I have*." Therefore, such deterministic methods often fail to deliver accurate rock type distributions and lack the ability to quantify the uncertainty of rock types and their associated petrophysical properties.

This chapter integrates a-priori core measurements and fast well-log forward modeling to test hypothetical rock type distributions based on quantitative comparisons between well logs and their numerical simulations. Efficient Bayesian sampling techniques (Yang and Torres-Verdín, 2011) are employed to narrow down the space of possible rock types in each petrophysical layer. The new method is capable of assimilating a-priori rock type information from core measurements. Furthermore, the bottom-up approach of building a hypothetical earth model allows closing the gap between log-scale and core-scale measurements. Uncertainty of rock types and petrophysical properties are also obtained after accumulating sufficient realizations of rock type distributions. The new method becomes a good example of integration of multiple disciplines, including numerical modeling, logging-tool physics and petrophysics, together with an explicit connection to a geological framework for enhanced reservoir description.

The following sections introduce the method and workflow of Bayesian rock typing, followed by a simple synthetic case that aims to illustrate the procedure of Bayesian rock typing. A field case of a Deltaic gas reservoir from offshore Trinidad, is then used to verify the performance of Bayesian rock typing in reservoir description.

## 7.2 METHOD AND WORKFLOW

Figure 7.1 shows the petrophysical workflow of log-based Bayesian rock typing. It begins with a hypothetical rock type distribution or earth model. Each rock type is associated with Gaussian distributions of various petrophysical properties. Well logs are then simulated numerically based on petrophysical properties at reservoir conditions. Available well logs are next compared to the numerically simulated logs to reject or accept the hypothetical rock type distribution. This procedure is iterated until a sufficient number of rock type realizations are obtained for further statistical analysis.

### 7.2.1 Fast Numerical Log Simulation in a Common Stratigraphic Framework

A multi-layered earth model, referred to as common stratigraphic framework (CSF) (Voss et al., 2009), is used to simulate well logs. We use a fast linear iterative refinement method to simulate nuclear logs (Mendoza et al., 2010; Ijasan et al., 2010) and a 2D forward modeling code to simulate array-induction resistivity logs (Wang et al., 2009).

The relationship between the earth model (**m**) and well logs (**d**) is referred to as the forward problem, given by:

$$\mathbf{G}(\mathbf{m}) = \mathbf{d}, \tag{7.1}$$

where **G** is the forward function, **m** is a vector of rock type distribution, and $\mathbf{d} = [\sigma_t, \rho_b, \phi_N, \gamma]^T$ is the vector of observed well logs based on the rock type distribution and their petrophysical properties. In this study, volumetric concentration of shale, water

saturation, total porosity, apparent electrical conductivity, bulk density, neutron porosity, and gamma ray are denoted by $C_{sh}$, $S_w$, $\phi$, $\sigma_t$, $\rho_b$, $\phi_N$, and $\gamma$, respectively. To perform rock typing and quantify uncertainty, one needs to estimate vector **m** from the available well logs.

### 7.2.2 Statistical Description of Basis Rock Types

Rock type defines a set of rock samples that exhibit similar geological attributes, and/or petrophysical properties, and/or physical log responses. Therefore, a rock type normally represents distributions of these properties instead of single-value properties. In this work, Gaussian (or log-normal) distributions are employed to describe rock properties. A statistical partitioning method is used to separate different rock types that exhibit significant overlapping rock properties (Vrubel, 2007; John et al., 2008). Figure 7.2 shows an example of the distributions of gamma ray values for four different rock types in a field case. The statistical description of each rock property should be obtained from thorough core study and used as a-priori information for Bayesian rock typing.

### 7.2.3 Bayesian Sampling of Rock Types

The Bayesian inversion process is essentially a stochastic search of earth models for which the simulated measurements agree with observations to a certain level. For an earth model of $L$ layers and 5 rock types, there are $5^L$ hypothetical vertical rock type distributions to be tested during inference. An efficient and adaptive sampling technique is used to infer the most likely rock type distributions that honor the available well logs (Yang and Torres-Verdín, 2011).

Bayesian rock classification is performed with a fast sampling technique based on the Markov-Chain Monte Carlo method to enable efficient search of rock types. The idea of Markov-Chain Monte Carlo method is to generate random samples from the rock

type posterior distribution by constructing a Markov chain. Yang and Torres-Verdín (2013) introduced an adaptive solution to generate the Markov chain. The solution is a set of rock types along the well trajectory that define the posterior distribution.

This work used four well logs: bulk density, neutron porosity, resistivity, and gamma ray. The a-priori distribution of formation properties is $p(\mathbf{m})$; the likelihood function is $p(\mathbf{d}|\mathbf{m})$, and the posterior probability distribution for properties is $q(\mathbf{m}|\mathbf{d})$. The prior distribution of properties is determined from prior field knowledge or other external information about the properties, such as core data. Tables 7.1 and 7.2 show examples of a-priori distributions of formation properties used in synthetic and field examples, respectively. The likelihood function measures the probability of observing the well logs, **d**, when the rock type distribution is **m**. On the other hand, the posterior distribution quantifies how well a rock type distribution agrees with available information and measurements. Bayes' theorem relates a-priori and posterior distributions in a way that makes the computations of $q(\mathbf{m}|\mathbf{d})$ tractable (Aster et al., 2005). It can be written as:

$$q(\mathbf{m} \mid \mathbf{d}) \propto p(\mathbf{d} \mid \mathbf{m})\, p(\mathbf{m}). \tag{7.2}$$

### 7.2.4 Iterative Hypothesis Testing Against Well Logs

Once a vertical rock type distribution with associated petrophysical properties is sampled and populated into the predefined CSF, numerically simulated well logs are compared to field logs to test the hypothesis. A hypothesis of rock type distribution is only acceptable when all available well logs are reproduced with fast well-log forward modeling given the hypothetical rock type distribution.

Yang and Torres-Verdín (2011) introduced a method to determine the number of steps needed to converge to the stationary distribution within an acceptable error. The

procedure comes to a halt if any of the following two convergence criteria are met in the iteration process:

1) The actual iteration number reaches the maximal iteration number, $I_{max}$, and,
2) The accepted sample sequence is tested by a modified z-test and results reach the Geweke z-score requirement (Geweke, 1991).

### 7.2.5 Probabilistic Interpretation of Hybrid Rock Classes

Petrophysical zones segmented by well logs normally have a thickness ranging from 1 to 5 ft. In heterogeneous reservoirs, those intervals typically include hybrid rock classes composed of different basis rock types defined at the core scale. Two different approaches are used to describe hybrid rock classes: volumetric basis (will be introduced in Chapter 8) and probabilistic basis (this Chapter). Figure 7.3 describes hybrid rock classes based on the probability of occurrence of each basis rock type.

### 7.2.6 Uncertainty Quantification

After a certain number of hypothetical rock type distributions have been accepted after testing, the uncertainty of rock types in each layer can be analyzed in a statistical manner. A distribution of possible rock types in each layer can be visualized with a histogram that describes the rock type with the maximum likelihood and the associated standard deviation. The uncertainty of a given rock type thence propagates to the estimation of uncertainty of permeability, for instance.

### 7.2.7 Rock Type Validation

Contingency tables (Bishop et al., 1975) are used to in this chapter to quantify the agreement between core-derived and log-derived rock types. In a contingency table, the

contingency coefficient, $C$, is defined as the ratio of diagonal elements to the total number of samples, and quantifies rock typing accuracy as

$$C = \sqrt{\frac{\chi^2}{N + \chi^2}}, \tag{7.3}$$

whereas Cramer's $V$ quantifies the strength of the dependence between two variables as

$$V = \sqrt{\frac{\chi^2}{N(K-1)}}, \tag{7.4}$$

where $N$ is the total number of rock samples, $\chi^2$ is the Pearson's chi-squared test, and $K$ is the number of rock types under comparison.

## 7.3 SYNTHETIC CASE: INTERBEDDED SAND-SHALE SEQUENCE

A synthetic earth model of interbedded sand-shale sequences was constructed to illustrate the standard workflow of Bayesian rock typing. Five different rock types are assumed to be present in the reservoir: sands A, B, C, shaly sand D (with dispersed clay), and pure shale (SH). Sands A, B, and C were deposited with different flow energy; therefore they exhibit different grain sizes and reservoir quality. Shaly sand D has poor reservoir quality due to cementation of dispersed clay. Pure shales are non-reservoir facies. Table 7.1 lists the statistical descriptions of properties for each rock type.

Figure 7.4 shows the synthetic earth model and the corresponding well logs (contaminated with 10%, zero-mean additive Gaussian noise), which are here regarded as field measurements. Uncertainty mainly originates from measurement noise and shoulder-bed effects. To test the Bayesian rock typing method, we assume that the earth model is unknown and we use well logs to test various hypothetical rock type distributions and quantify how closely available well logs agree with their numerical simulations. The method starts with a prior earth model of all shales.

Tracks 5 and 6 in Fig. 7.4 compare the synthetic earth model and the inferred earth model to results obtained with the Bayesian rock typing method. For each layer, the rock type with maximum likelihood agrees with the synthetic model, where the corresponding uncertainty is narrowly distributed in thick beds. This synthetic example confirms that the Bayesian method is capable of both inferring rock type distributions accurately and quantifying the uncertainty of a given rock type in each layer.

Figure 7.5 shows a hypothetical rock type distribution which significantly differs from the true earth model. Consequently, numerically simulated well logs also significantly differ from field measurements. This hypothetical rock type distribution should be rejected during the iterations leading to final estimation results. Such a procedure is in principle equivalent to the scientific method of iterative hypothesis testing. Figure 7.6 shows the probabilistic descriptions of two shale layers. The thin bed exhibits relatively larger uncertainty than the thick bed due to shoulder-bed effects on well logs.

## 7.4 FIELD CASE: DELTAIC GAS RESERVOIR, OFFSHORE TRINIDAD

The formation under consideration is a sandstone unit deposited in a deltaic sedimentary system in the Columbus Basin, offshore Trinidad (Liu et al., 2007). Different facies exhibit distinct grain-size distributions and clay volumetric concentrations, which result in different pore-size distributions. Therefore, a cause-effect relationship exists between depositional facies and hydraulic rock types. The reservoir is saturated with gas and was penetrated with a vertical key-study well drilled with synthetic oil-base mud (SOBM). Approximately 80 ft of whole core were acquired in the upper deltaic sequence for both geological and petrophysical studies. The cored zone was estimated to be at a height above free water level (HAFWL) between 400 and 500 ft. High in-situ capillary

pressure between gas and water phases ensures that water saturation be close to irreducible saturation. Fluorescence analysis on sliced whole core confirmed that the invasion of SOBM during coring was negligible. Helium porosity, gas permeability (with Klinkenberg effect correction), and Dean-Stark water saturation were measured on 104 preserved core plugs, among which 11 core plugs were further subject to MICP measurement and 24 core plugs were studied with a laser particle size analyzer (LPSA). The effects of mud-filtrate invasion on well logs are negligible due to very shallow radial length of invasion and absence of free water.

### 7.4.1 Basis Rock Classes from Core Measurements

Rock typing was performed with Leverett's (1941) reservoir quality index calculated from routine porosity-permeability data (Fig. 7.7a) and the core-measured water saturation of each rock type (Fig. 7.7b) was studied. It was found that BVW measured with Dean-Stark's method was consistently ranked with rock types, i.e., better rock types were associated with lower BVW, and poorer rock types were associated with higher BVW (Fig. 7.7b). Figure 7.8 shows the Buckles' plot constructed with core porosity and Dean-Stark water saturation, indicating a good correlation between rock types and BVW. The LPSA data from 24 core samples verify that grain size distribution and clay volumetric concentration are also closely related to hydraulic rock types (Fig. 7.9). In general, smaller median grain size indicates higher clay volumetric concentration and poorer hydraulic rock types. Figure 7.10 shows that MICP data are also ranked consistently with the defined rock types. Better rock types generally exhibit larger major pore throat sizes. Table 7.2 summarizes the statistical variability of total porosity, absolute permeability, and Dean-Stark water saturation together with BVW for each rock type.

### 7.4.2 Petrophysical Zonation

The reservoir unit under analysis comprises a total depth interval of 260 ft, a scale that can be visually identified from seismic amplitude data. We use gamma-ray, bulk density, and resistivity logs to segment the reservoir unit into 80 petrophysical zones with an average thickness of approximately 2.9 ft. Figure 7.11 shows the histogram of zone thickness. Most zones exhibit thicknesses ranging from 1.0 to 4 ft, and the zones are mostly a mixture of more than one rock type.

### 7.4.3 Bayesian Rock Typing from Logs

After defining rock types and their associated petrophysical properties, Bayesian rock typing is invoked to infer the rock type distribution by iteratively testing hypothetical rock types. Figure 7.12, track 5, shows the final rock typing results: the vertical distribution of rock types with maximum likelihood and their associated uncertainty. Visual comparison indicates good agreement with core-derived rock types. It is also observed that, in general, rock typing in thicker beds has lower uncertainty.

### 7.4.4 Rock Types: Core vs. Well Logs

Table 7.3 shows a contingency table that compares rock types estimated via clustering of well logs to core-derived rock types; it indicates a low rate of agreement in terms of the contingency coefficient (Bishop et al., 1975), roughly equal to 60%. Table 7.4 shows a similar contingency table comparing rock types estimated with the Bayesian method to core-derived rock types. In this case, the rate of agreement increases to 78%.

### 7.4.5 Uncertainty Analysis of Rock Types

Two sand layers of different thickness are selected to compare their associated rock-type uncertainties. Both layers are classified as rock type 1. Figure 7.13 shows that

their uncertainties are quite different because of bed thickness; the rock typing in thicker bed centered at 12,502 ft exhibits relatively lower uncertainty.

Table 7.4 also shows that, in general, good rock types are less prone to misclassification. This behavior is due partly to the large population of good rock types, and partly to their larger bed thickness because there is correlation between reservoir quality and bed thickness.

### 7.4.6 Permeability Estimation and Uncertainty Analysis

Each inferred distribution of rock types generates a corresponding permeability distribution obtained by calculating the permeability with rock-type specific porosity-permeability relations established with core data. A statistical analysis of all permeability distributions quantifies the uncertainty of permeability in each layer. Track 6 in Fig. 7.12 shows the distribution of maximum-likelihood permeability and its associated uncertainty. Low rock-type uncertainty gives rise to low permeability uncertainty. Figure 7.14 shows the correlations between log-estimated permeability and core permeability. The correlation coefficient is improved from 0.62 with conventional rock typing method to 0.78 with the Bayesian estimation method (which explicitly corrects for shoulder-bed effects on well logs).

### 7.4.7 Applications to Geological Interpretation

It is important to associate petrophysical rock types to depositional facies in reservoir description. Bed thickness and grain size are two important geological attributes that connect petrophysical rock types with depositional facies. In the field case, a clear correlation was established between petrophysical rock types and grain sizes. Therefore, a stack of vertical rock types provides useful information to geologists for interpretation

of geological facies and to reduce uncertainty when constructing a stratigraphic reservoir model based on well logs.

Figure 7.15 compares the vertical distribution of rock types inferred in this chapter against the sedimentological description performed with its outcrop analogue from the onshore Mayaro Formation of the same deltaic succession (Bowman, 2004). The distribution of rock types is consistent with the geological framework and indicates an aggradational delta front with three facies in a coarsening-upward trend: distal delta front interbedded with channelized slope turbidites and slump sheets, mouthbar facies interbedded with wave/storm- dominated proximal delta front facies, and proximal delta front facies (Bowman, 2004). In addition, the distributions of petrophysical rock types and the estimated permeability values provide additional details to construct a stratigraphic reservoir model for fluid flow simulation.

### 7.4.8 Computational Performance Analysis

A common disadvantage of stochastic estimation methods is the need to perform a multitude of forward calculations to sample the posterior probability function in model space. Yang and Torres-Verdín (2013) introduced two strategies to enhance the efficiency of the stochastic method, which reduce the CPU time to approximately 4 hours to obtain 100 realizations of hypothetical distributions of rock types (100 ft interval) using a desktop PC (3.4 GHz CPU) and Matlab platform. The computer time required by the calculations can be further reduced by using parallel-computing techniques.

## 7.5 CONCLUSIONS

We developed a new core-calibrated and log-based Bayesian rock typing method that employs fast numerical simulation of well logs for iterative hypothesis testing. The new method effectively reduces shoulder-bed effects on well logs, which give rise to

significant uncertainty in rock typing across thinly bedded formations. A probabilistic method was introduced and successfully verified for describing hybrid rock classes.

The application of the new method to a field case indicated more than 77% agreement between log- and core-derived rock types. Overall, the correlation between predicted permeability and core-measured permeability was improved by approximately 16% compared to conventional deterministic methods. In addition, the method quantified the uncertainty associated with rock-type identification and permeability estimation. The final distribution of maximum-likelihood rock types was consistent with the geological framework and provided useful information for stratigraphic reservoir construction and modeling.

Computational performance can be a limitation when implementing the Bayesian rock typing method in field studies because of the requirement of heavy data processing. However, the method remains accurate and reliable for detailed reservoir description in deepwater field developments where only a few wells are available.

**Table 7.1:** Statistical distributions of clay volume concentration, porosity, water saturation, and permeability for synthetic rock types.

| Rock Type | $C_{cl}$ (frac) | $\phi_t$ (frac) | $S_w$ (frac) |
|---|---|---|---|
| **A** | 0.02 ± 0.01 | 0.25 ± 0.03 | 0.15 ± 0.05 |
| **B** | 0.02 ± 0.01 | 0.22 ± 0.04 | 0.25 ± 0.08 |
| **C** | 0.02 ± 0.01 | 0.20 ± 0.04 | 0.35 ± 0.10 |
| **D** | 0.05 ± 0.02 | 0.15 ± 0.04 | 0.55 ± 0.15 |
| **SH** | 1.0 | 0.12 ± 0.01 | 1.0 |

**Table 7.2:** Statistical distributions of total porosity, absolute permeability, Dean-Stark water saturation and BVW, and volumetric clay concentration for each rock type in the offshore Trinidad field case.

| Rock Type | $\phi_t$ (frac) | $k$ (mD) | Dean-Stark $S_w$ (frac) | Dean-Stark BVW (frac) | $C_{cl}$ (frac) |
|---|---|---|---|---|---|
| **RT-1** | 0.231 ± 0.019 | 1255 ± 455 | 0.064 ± 0.036 | 0.014 ± 0.006 | 0.006 ± 0.003 |
| **RT-2** | 0.215 ± 0.014 | 358 ± 125 | 0.092 ± 0.019 | 0.020 ± 0.004 | 0.018 ± 0.005 |
| **RT-3** | 0.140 ± 0.023 | 52.5 ± 27.9 | 0.337 ± 0.105 | 0.045 ± 0.007 | 0.051 ± 0.018 |
| **RT-4** | 0.065 ± 0.016 | 3.2 ± 2 | 0.70 ± 0.22 | 0.056 ± 0.005 | 0.119 ± 0.027 |

**Table 7.3:** Contingency table of rock types determined with the conventional rock typing method in the offshore Trinidad field case. (Crammer's $V = 0.44$; Contingency Coefficient $C = 60.7\%$).

| Rock Type | 1 | 2 | 3 | 4 | Total |
|---|---|---|---|---|---|
| **1** | 21 | 3 | - | - | 24 |
| **2** | 6 | 17 | 1 | 1 | 25 |
| **3** | 3 | 7 | 1 | 2 | 13 |
| **4** | 1 | 2 | 2 | 2 | 7 |
| **Total** | 31 | 29 | 4 | 5 | 69 |

**Table 7.4:** Contingency table of rock types determined with the Bayesian rock typing method in the offshore Trinidad field case. (Crammer's V = 0.71; Contingency Coefficient C = 77.7%).

| Rock Type | 1 | 2 | 3 | 4 | Total |
|---|---|---|---|---|---|
| **1** | 28 | 2 | - | - | 30 |
| **2** | 3 | 26 | 1 | - | 30 |
| **3** | - | 1 | 2 | 2 | 5 |
| **4** | - | - | 1 | 3 | 4 |
| **Total** | 31 | 29 | 4 | 5 | 69 |

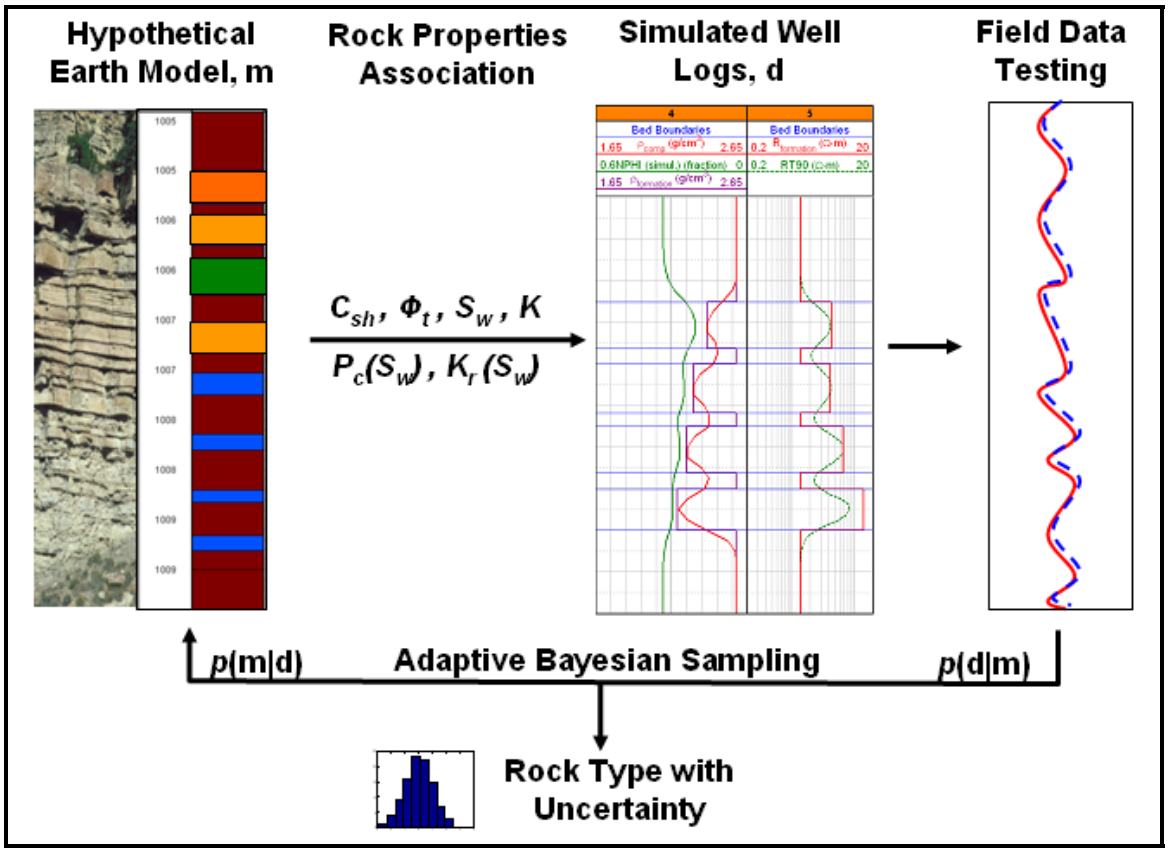


**Figure 7.1:** Petrophysical workflow of well-log based and core-calibrated Bayesian rock typing.

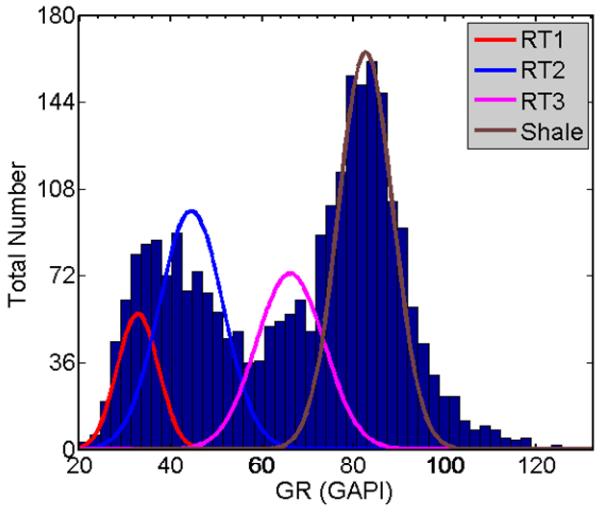


**Figure 7.2:** Example of statistical distribution of gamma-ray values for four different rock types in a field case. Significant overlapping is observed between neighboring rock types.

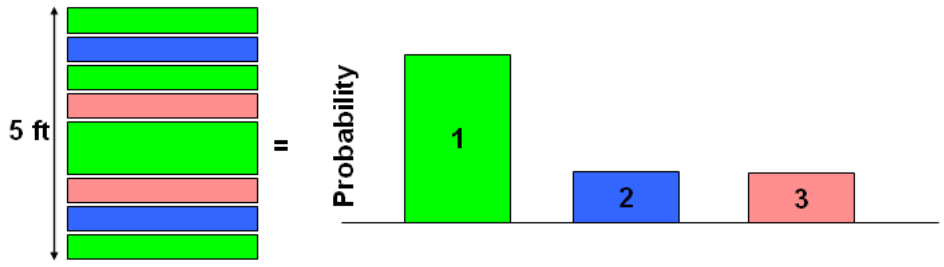


**Figure 7.3:** Description of hybrid rock classes using a probabilistic approach. Rock type 1 exhibits the maximum likelihood in this example.

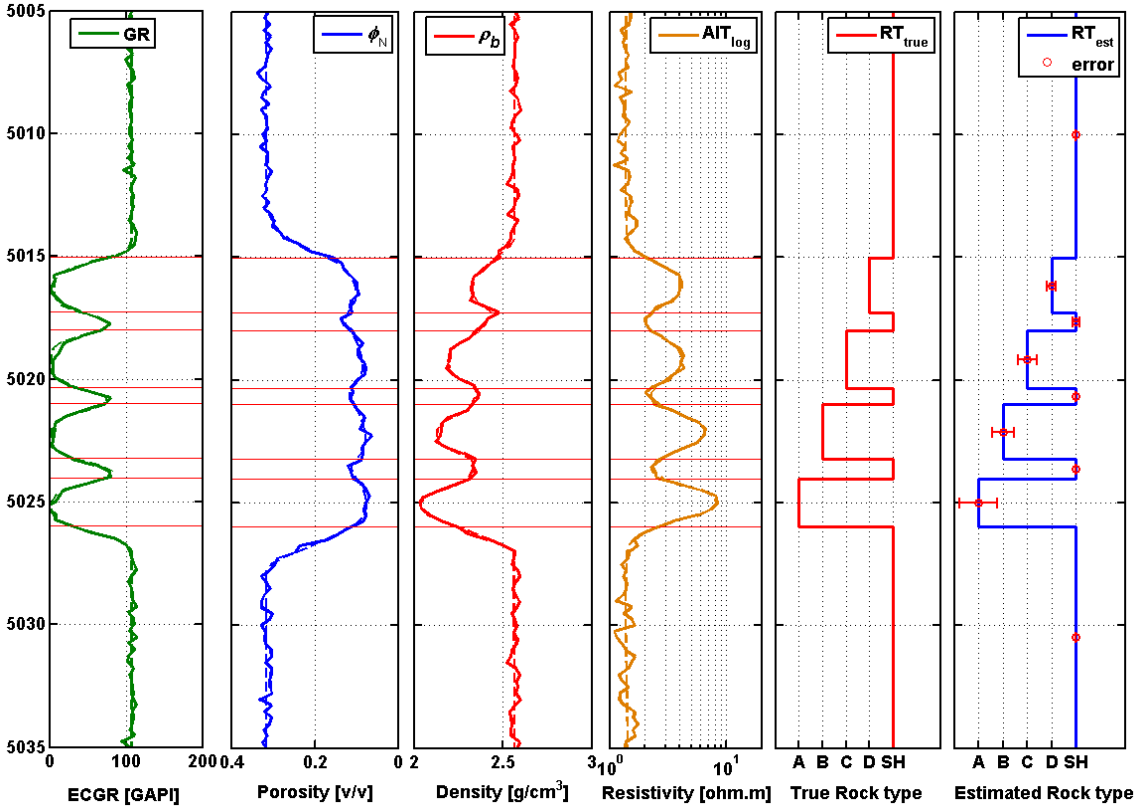


**Figure 7.4:** Bayesian rock typing in a synthetic interbedded sand-shale sequence based on the corresponding simulated well logs. Solid lines: well logs with 10% additive, zero-mean Gaussian noise considered as field measurements in this synthetic case; Dashed lines: reproduced logs based on the rock type distribution with maximum likelihood.

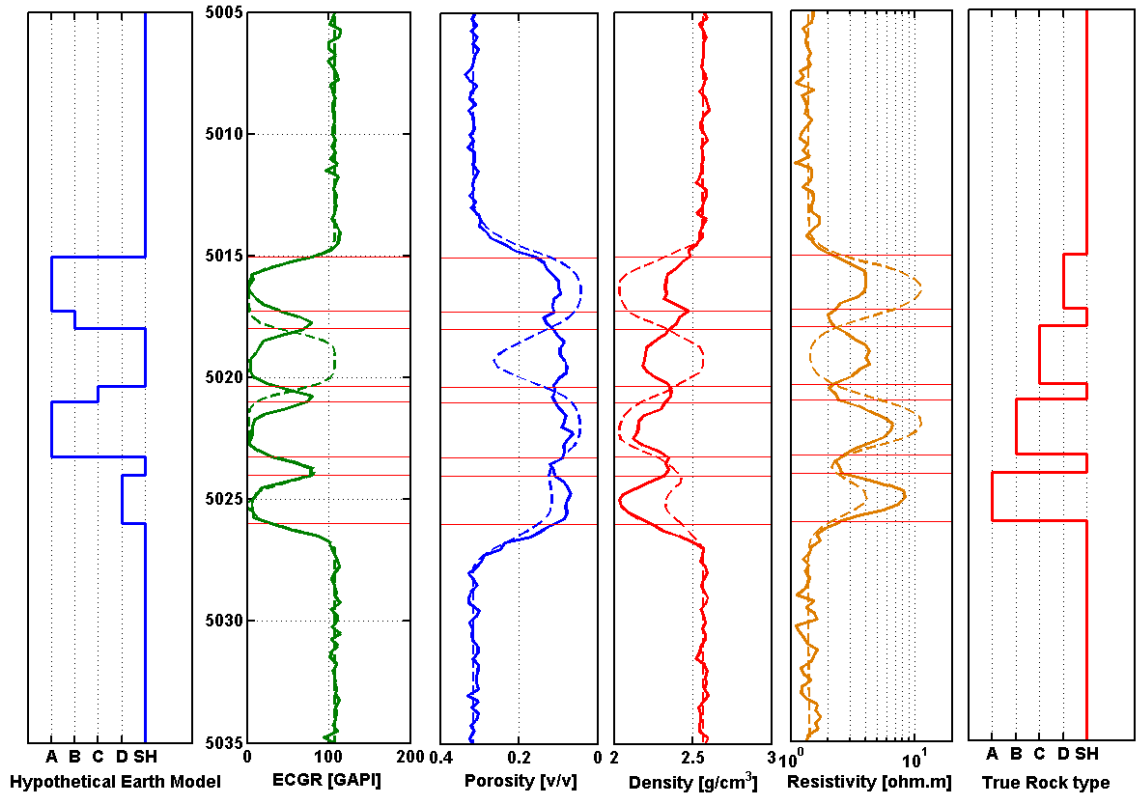


**Figure 7.5:** Example of a rejected hypothetical rock type distribution. Simulated well logs significantly differ from those of the actual model.

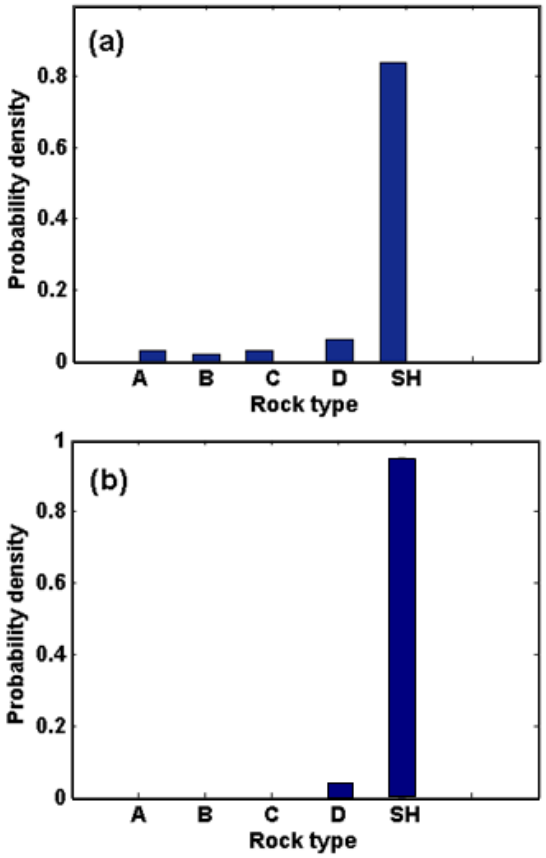


**Figure 7.6:** Rock type uncertainty quantified in two petrophysical zones of the synthetic case. (a) Thin bed at 5018 ft, and (b) thick bed at 5010 ft.

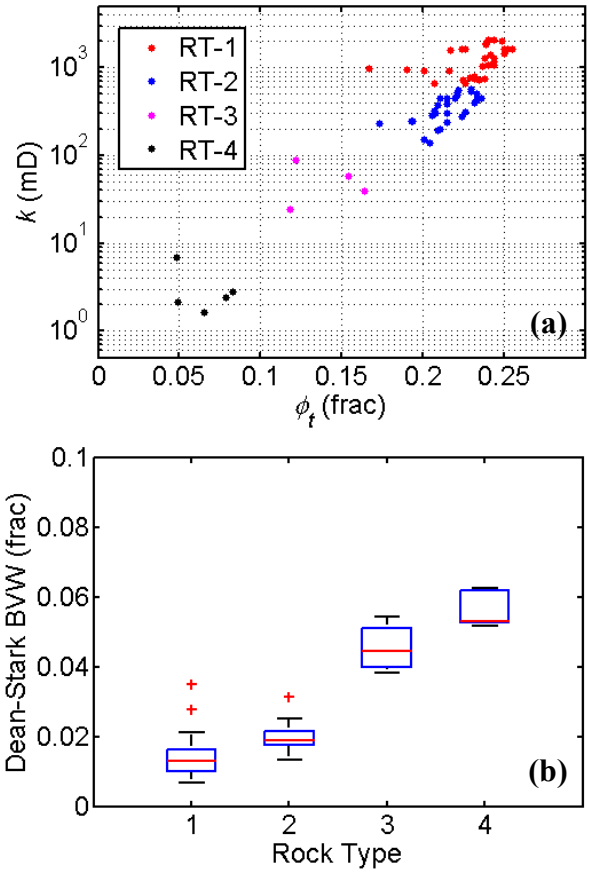


**Figure 7.7:** **(a)** Porosity-permeability crossplot grouped according to rock types, and **(b)** box-plot of core-measured BVW grouped with rock types in the offshore Trinidad field case.

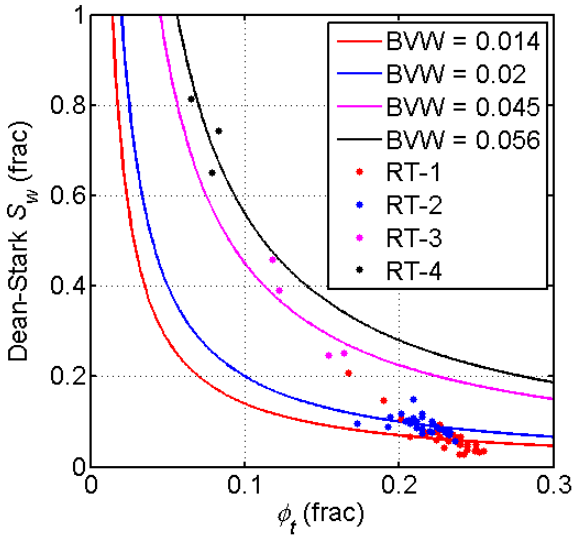


**Figure 7.8:** Buckle's plot constructed with core porosity and Dean-Stark water saturation in the offshore Trinidad field case.

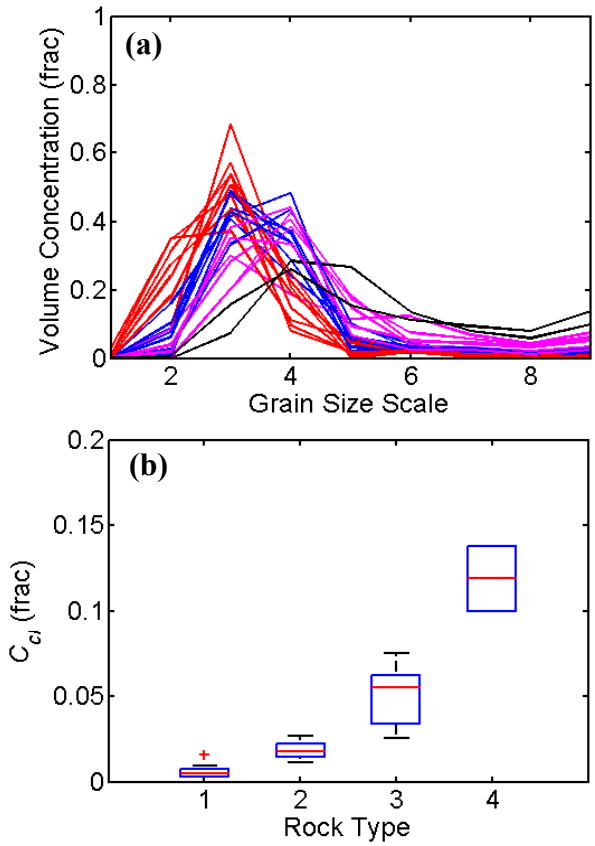


**Figure 7.9: (a)** Grain size distribution data grouped according to rock types, and **(b)** box plot of clay volumetric concentration grouped according to rock types in the offshore Trinidad field case.

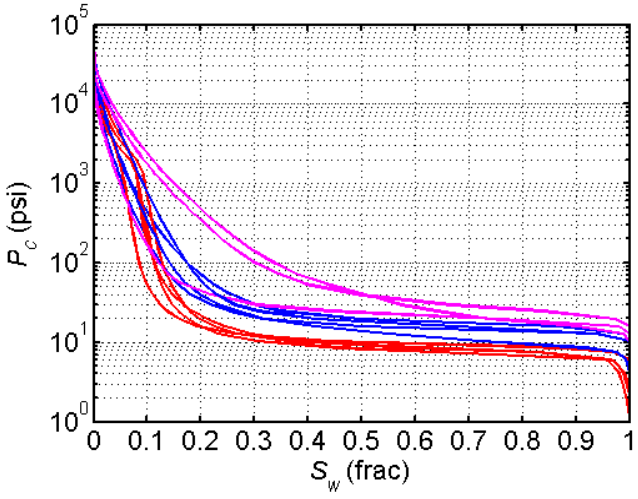


**Figure 7.10:** MICP data color-coded with classified rock types in the offshore Trinidad field case. RT-4 was not studied with MICP.

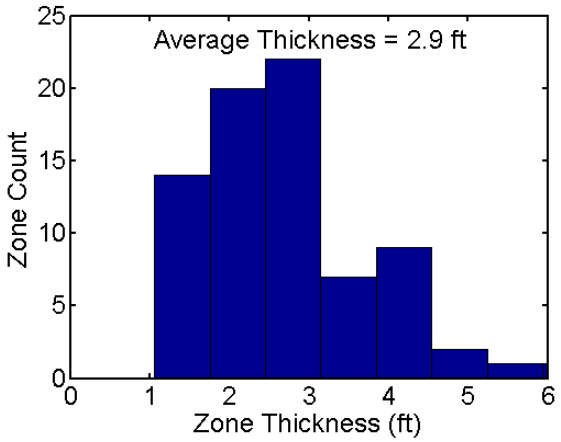


**Figure 7.11:** Statistical distribution of petrophysical zone thickness in the Trinidad deltaic gas sand reservoir.

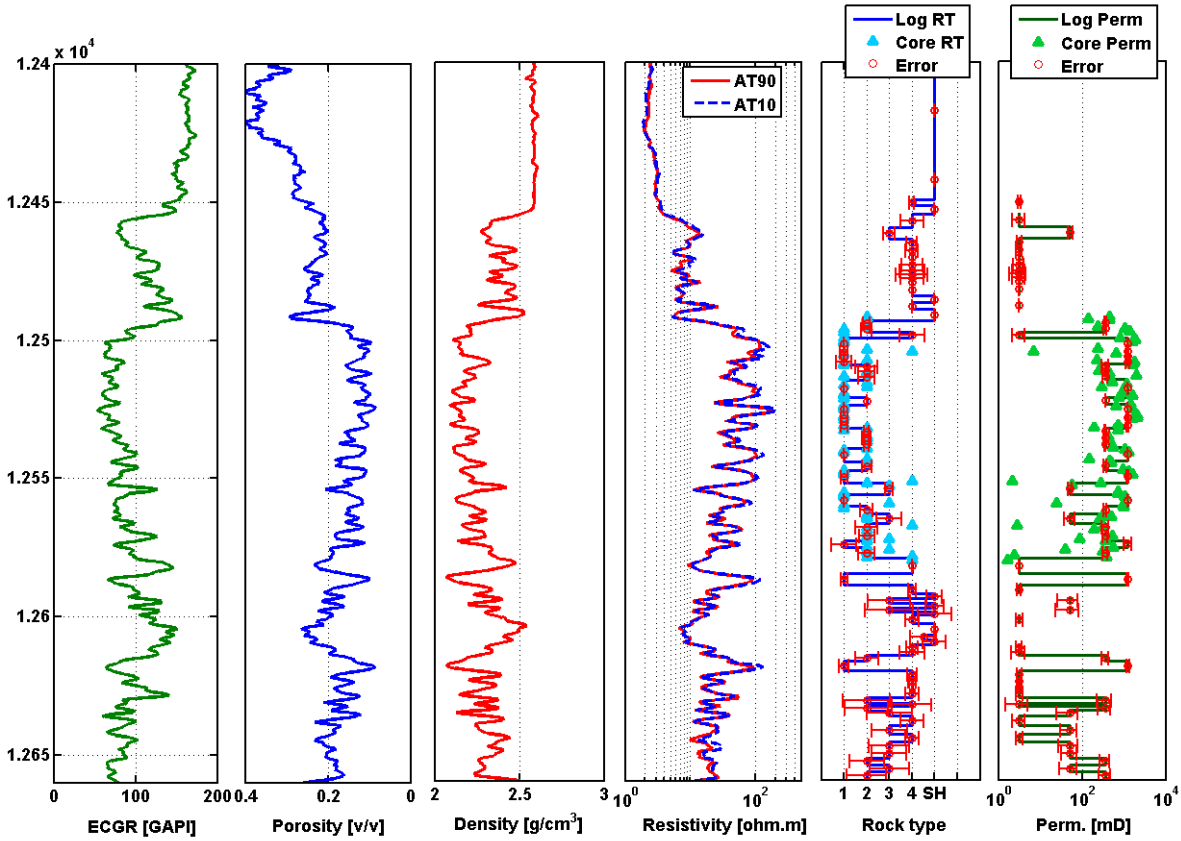


**Figure 7.12:** Field case of Bayesian rock typing and uncertainty quantification. From left to right, Track 1: Gamma Ray; Track 2: Porosity; Track 3: Density; Track 4: Resistivity; Track 5: Rock type and uncertainty; Track 6: Permeability and uncertainty. Triangles in Tracks 5 and 7 identify core measurements.

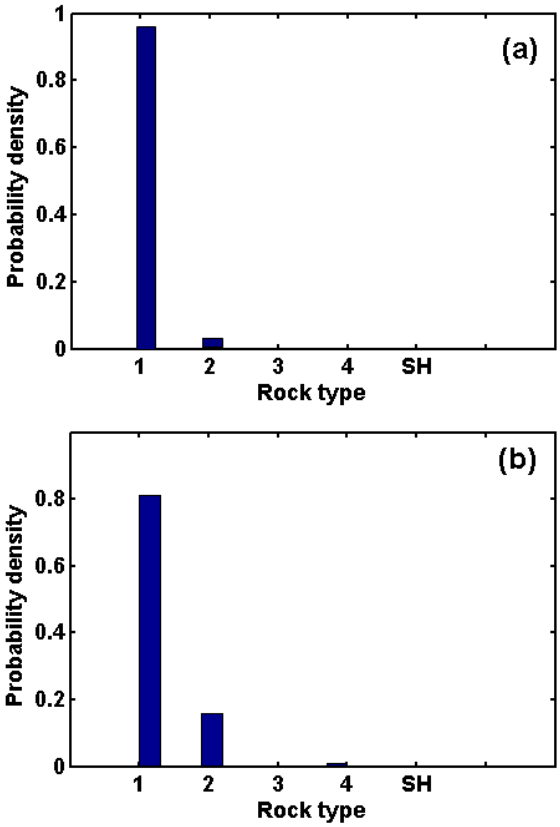


**Figure 7.13:** Uncertainty of rock types quantified in two petrophysical zones in the offshore Trinidad field case. (a) thick bed at 12,502 ft, and (b) thin bed at 12,508 ft.

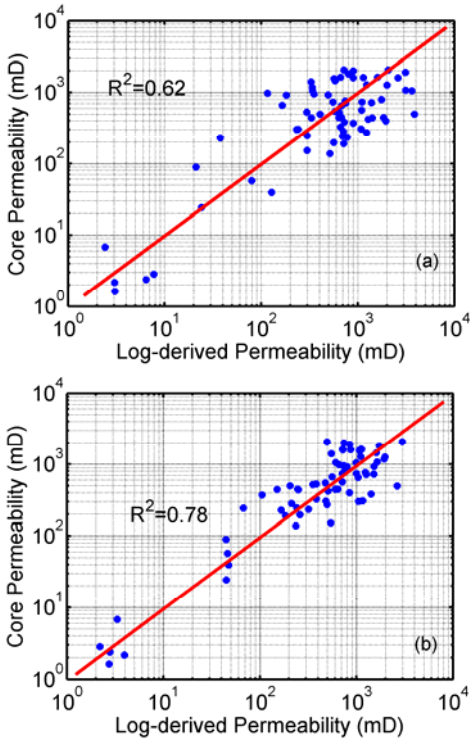


**Figure 7.14:** Comparison of permeability estimation with (a) conventional rock typing method, and (b) Bayesian rock typing method in the offshore Trinidad field case.

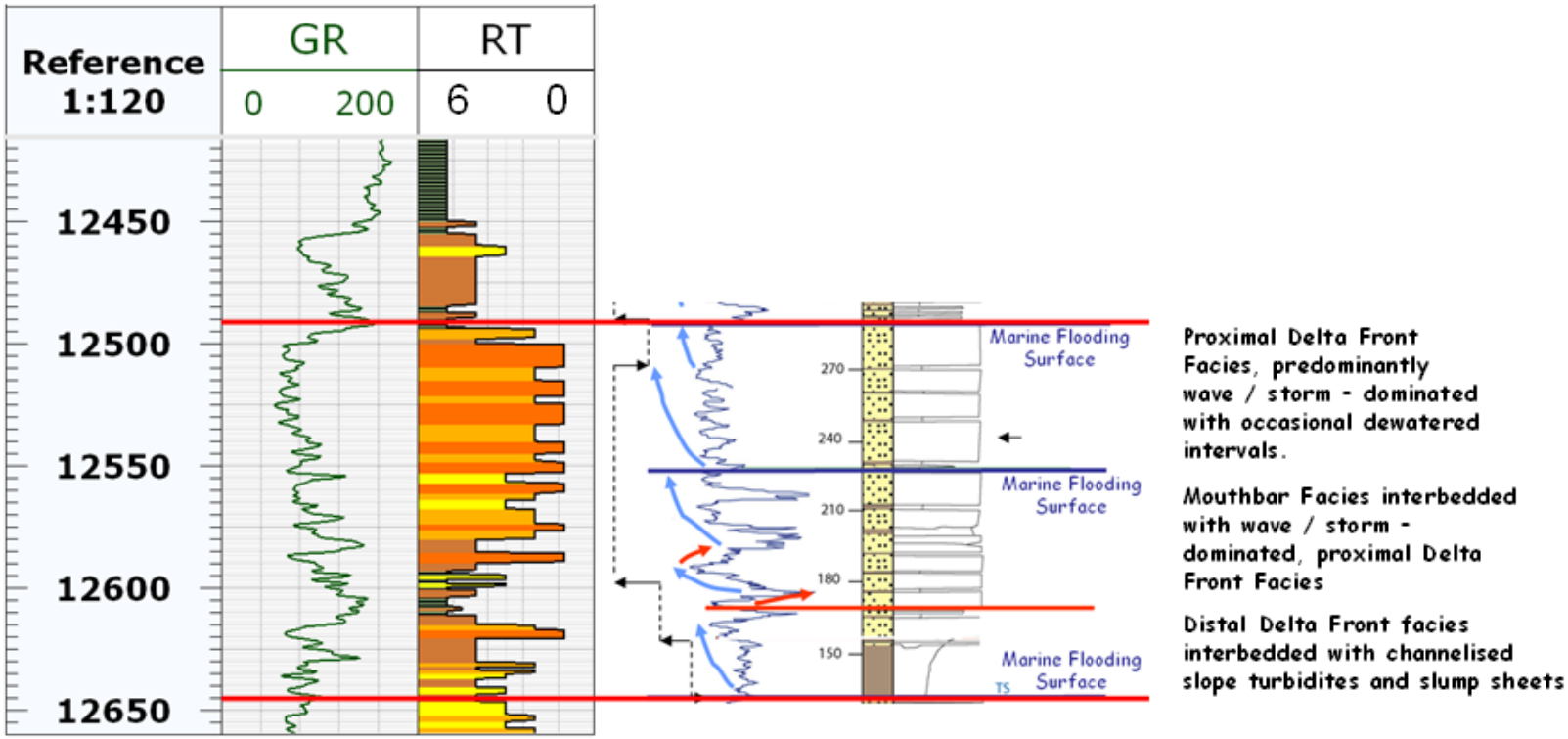


**Figure 7.15:** Comparison between estimated rock types and the facies description based on the outcrop analogue (Mayaro Formation). Left panel: rock types inferred with the Bayesian method; Right panel: facies description (Bowman, 2004).

# Chapter 8: Multi-Scale Orthogonal Rock Class Decomposition: Top-Down Reservoir Characterization Integrating Logs and Core in Tight-Gas Sands

Reservoirs are described and quantified at multiple scales with multiple physical measurements, including seismic surveys, well logs, core data, and pore-scale imaging. As an important reservoir description tool, rock typing also needs to follow a multi-scale approach to best describe the intrinsic mixture of rock properties. This chapter introduces a new top-down petrophysical workflow, referred to as multi-scale orthogonal rock class decomposition, which integrates well logs and core data to quantify heterogeneous tight-gas sand reservoirs of the Bonner and York Members, Bossier Formation, Upper Jurassic Cotton Valley Group in the East Texas Basin. We document rock-class decomposition techniques bridging four different scales: (1) from seismic scale to log scale; (2) from log scale to core scale; and (3) from core scale to pore scale.

Rock class decomposition from seismic scale to log scale is accomplished by detecting, matching, optimizing, and testing bed boundaries with a suite of conventional well logs; it partitions a reservoir unit (seismic scale) into a set of petrophysical zones (log scale) by capturing the maximum combined variability of all available well logs. Each petrophysical zone is regarded as a mixture of basis rock types (core scale), which originate from distinct depositional and diagenetic processes.

Rock class decomposition from log scale to core scale is performed by calculating the proportion of each basis rock type assuming a parallel-stacking model in each petrophysical zone. Gaussian distributions are used to represent the variability of log responses and petrophysical properties of each elemental rock type. Different physical mixing laws are simultaneously honored by applying exact logging measurement physics

models to a stack of elemental rock classes in a common stratigraphic framework. Each basis rock class is further considered as a mixture of pore types (pore scale).

Rock class decomposition from core scale to pore scale is performed by integrating MICP, core NMR measurements, and NMR logs. We use a bimodal log-normal density function to describe complex pore systems and quantify petrophysical orthogonality (or dissimilarity) between different rock classes based on the "bundle of tubes" model. The definition of orthogonality is extrapolated to routine and special core measurements, and the sensitivity of each well log to orthogonality between rock classes is investigated in detail to derive the most relevant attributes for log-based rock typing.

## 8.1 INTRODUCTION

The concept of rock type straddles multiple scales and links multiple disciplines (Gunter et al., 1997a; Rushing et al., 2008). Petrophysical rock typing (also known as hydraulic rock typing) has been recognized as one of the most reliable and effective approaches to facilitate large-scale reservoir modeling and simulation. This task often requires full integration of multi-disciplinary data such as core measurements, well logs, and seismic surveys to propagate petrophysical properties into reservoir grids. On one hand, core samples are regarded as "ground truth" when inferring subsurface geological and petrophysical information, but they have limited spatial coverage due to high operational risk and prohibitive laboratory measurement costs. On the other hand, abundant well logs are readily available in each drilled well but are still not fully utilized for interpretation. Therefore, it is imperative to develop new log-based and core-calibrated rock typing methods that bridge the gap between measurement scales, reconcile multiple physics (or petrophysics), and connect to the geological framework.

Practical log-based rock typing needs to be core-calibrated. Yet, it remains challenging to map core-derived rock types to the well-log domain for several reasons: (1) a scale-crossing problem arising from plug scale (~ 1 inch) to log scale (~ 1 ft); (2) indirect and non-unique links that occur between physical properties and geological or petrophysical attributes; (3) apparent logs that do not always reflect true physical properties due to shoulder-bed and mud-filtrate invasion effects.

Thick (> 3 ft) homogeneous beds of a single rock class are rare in heterogeneous reservoirs (Campbell, 1967). Instead, most heterogeneous reservoirs are composed of different rock types that mix at the decimeter or even centimeter scale. Thinly bedded deltaic facies, laminated turbidite facies, and high-frequency cycle carbonate facies are typical geological occurrences of such Hybrid Rock Classes (HRC) resulting from deposition. Even for initially homogeneous facies, complex diagenesis effects give rise to significant internal heterogeneity, which is typical in tight-gas sand reservoirs. Therefore, a valid log-based rock typing solution needs to honor different physical mixing laws associated with different well logs by implementing exact physical modeling on a mixture of rock types. Further, physical mixing laws need to be translated into petrophysical mixing laws in an upscaled reservoir model.

Most well logs are more sensitive to fluids residing in the pores than to the pore structure itself. Fortunately, fluid saturation and its spatial distribution are petrophysical consequences of pore structure in many cases. Therefore, it is critical to understand how pore structures control vertical fluid distribution in the contexts of reservoir saturation-height and radial fluid distribution under mud-filtrate invasion for more reliable rock typing (as in Chapters 5 and 6).

This chapter introduces a new rock typing workflow, referred to as multi-scale orthogonal rock class (ORC) decomposition, which closely integrates core data and multi-physical well logs to describe heterogeneous reservoirs in a top-down approach. Figure 8.1 shows a detailed petrophysical workflow connecting four different measurement scales with the application of three decomposition techniques.

A seismic-scale reservoir unit is segmented into multiple petrophysical zones by capturing the maximum variability of all available well logs. A petrophysical zone is described as a mixture of basis rock types (BRT) by honoring the physical or petrophysical mixing laws. Furthermore, BRTs are established from pore structure (pore-size distribution), as evidenced by MICP and laboratory NMR measurements. The effects of mud-filtration invasion on well logs are studied in detail to derive the most diagnostic log-attributes for estimating volumetric concentrations of different BRTs in a petrophysical zone.

The above-mentioned workflow is applied to tight-gas sand units in the Bonner and York members of the Bossier Formation, Upper Jurassic Cotton Valley Group in the East Texas Basin. Estimated storage and flow capacities are compared to core using an up-scaled model implemented with cumulative storage and flow profiles (Gunter et al., 1997b). Even though the documented field cases are from tight-gas sands, the workflow is generally applicable to other conventional reservoir types, including turbidites and carbonates. The reversed workflow implies a bottom-up or upscaling approach to construct a quantitative reservoir model for reserve estimation and production forecasting.

## 8.2 METHODS AND WORKFLOW

### 8.2.1 Partitioning a Reservoir Unit into Petrophysical Zones: Seismic Scale to Well-Log Scale

This research implemented a new computerized workflow for detecting, matching, and testing bed boundaries with a common suite of raw well logs that have not been depth-matched. Possible bed boundaries are first detected on each well log by locating inflection points and are then juxtaposed and referenced for depth matching between different logs. Similarly to stratigraphic correlation between wells, a series of control lines are depicted across different logs to match both bed boundaries and log peaks. These control lines are then flattened based on a selected reference log to which all other logs are depth-matched. After that, principal components of the depth-matched logs after resampling are extracted for variance analysis with a sliding window. Based on the variance, an initial set of boundaries is selected for subsequent optimization and testing with fast numerical simulations of nuclear and resistivity logs. Final outputs from the workflow include: (1) a set of petrophysical zones that capture the maximum variability of all well logs segmented by an optimal number of bed boundaries; and (2) squared logs that represent log values in each zone which can reconstruct continuous log traces via numerical modeling. The advantage of the new workflow is that it implicitly integrates depth shifting and numerical well-log simulation into formation evaluation and verifies the squared logs for further processing.

Figure 8.2 shows an example of nuclear and resistivity logs acquired in different logging runs. Bed boundaries detected with nuclear logs do not match those detected with resistivity logs due to several possible technical problems, including depth shifting, stick-and-slip, and unequal measurement resolutions. Bed boundaries detected with nuclear logs served as reference and resistivity logs were shifted accordingly. Inversion was then

performed on each log to estimate true physical bed properties. Figure 8.3 shows shifted logs together with inverted results for both bulk density and resistivity. Comparison between log and inverted values indicates that true bed properties cannot be resolved in many thin beds. This exercise confirms that petrophysical estimation or rock typing based on apparent well logs can be prone to errors.

### 8.2.2 Estimation of Pore-Size Distributions from MICP: Core Scale to Pore Scale

Chapter 2 has formulated an inverse problem to fit MICP curves based on a bimodal log-normal pore-size distribution model, which is expressed as

$$p(\log R; w_1, \log \mu_1, \log \sigma_1; w_2, \log \mu_2, \log \sigma_2)$$
$$= w_1 \frac{1}{\sqrt{2\pi}\log \sigma_1} e^{-\frac{(\log R - \log \mu_1)^2}{2(\log \sigma_1)^2}} + w_2 \frac{1}{\sqrt{2\pi}\log \sigma_2} e^{-\frac{(\log R - \log \mu_2)^2}{2(\log \sigma_2)^2}}, \quad (8.1)$$

where $R$ is pore-throat radius in $\mu$m, $w_1$ and $w_2$ are weighting coefficients for each Gaussian mode, $\log\mu_1$ and $\log\mu_2$ are the mean values of logarithmic pore-throat radius, and $\log\sigma_1$ and $\log\sigma_2$ are the corresponding standard deviations of logarithmic pore-throat radius.

Figure 8.4 shows results obtained from the application of the inversion method to an example of MICP data from the tight-gas sand reservoir under study.

### 8.2.3 Modeling Petrophysical Properties from Pore-Size Distributions.

As indicated by Eq. (8.1), a bimodal log-normal density function includes six attributes to describe a pore-size distribution. Each attribute has petrophysical implications interpreted as follows:

$w_1$: fraction of pore volume connected by large pore-throat sizes where most of the residual non-wetting phase resides during imbibition. Flow capacity or permeability

of reservoir rocks is dominantly controlled by this fraction of pore volume and the associated pore-throat radius ($\mu_1$).

$w_2$: fraction of pore volume connected by small pore-throat sizes where most irreducible wetting-phase saturation resides during drainage; therefore, its contribution to fluid flow is minor.

$\mu_1$ and $\mu_2$: mean values of large and small logarithmic pore-throat radius modes, respectively; larger values indicate higher permeability; $\mu_1$ is correlated with hydraulic radius.

$\sigma_1$ and $\sigma_2$: standard deviation of large and small pore-throat radius modes, respectively, which represent the uniformity of "capillary tube sizes" (Childs and Collis-George, 1950); larger values indicate lower sorting of tube sizes and higher tortuosity of the pore network, hence lower permeability given the same mean value of pore-throat radius and pore volume.

The above Gaussian attributes provide useful information for modeling dynamic petrophysical properties including saturation-dependent capillary pressure and relative permeability during both drainage and imbibition cycles (Huang et al., 1997).

### 8.2.4 Rock Classification with Pore-System Orthogonality

The orthogonality between two pore systems is quantified as

$$ORT_{1,2} = \log(\frac{\phi_1}{\phi_2}) + 2\log(\frac{\mu_1}{\mu_2}) - 0.5\log(\frac{\sigma_1}{\sigma_2}), \tag{8.2}$$

where $ORT_{1,2}$ represents orthogonality between two single-mode Gaussian pore-size distributions. A positive value indicates better reservoir quality, whereas a negative value indicates poorer reservoir quality. Under this definition, orthogonality has the following properties:

(i) the orthogonality between two identical pore systems (if they do exist) is zero;

(ii) $$ORT_{1,3} = ORT_{1,2} + ORT_{2,3}, \quad (8.3)$$

where subscripts 1, 2, and 3 represent three pore systems.

After fitting all MICP curves (total number = *N*), we quantify the petrophysical orthogonality between each core sample pair using Eq. (8.2) for both large and small pore-size modes, which are described in the form of *N*x*N* matrices. Diagonal elements of orthogonality matrices are all zero. The matrices rank all core samples in terms of reservoir quality, whereby they become suitable for petrophysical rock classification. We apply the dissimilarity matrix clustering technique (Hahsler and Hornik, 2011) to orthogonality matrices and classify MICP core samples into BRTs with descending order of reservoir quality.

### 8.2.5 Rock-Type-Based Forward Modeling of Well Logs

After core-based rock classification, we obtain the statistical descriptions of rock properties including porosity, permeability, bulk volume water (BVW), capillary pressure, relative permeability, and pore-size distribution for each rock type. Together with a simplified mineralogy model (shaly-sand model in this chapter), these petrophysical properties can predict well log responses at downhole conditions. To better understand the sensitivity of various log attributes to rock type, we simulate log responses of each rock type both before and after mud-filtrate invasion.

#### *8.2.5.1 Pre-Invasion Modeling*

Log simulations for pre-invaded formations are relatively straightforward. Mineral volumetric concentrations, total porosity, and total water saturation are the necessary inputs to calculate spontaneous radioactivity, bulk density, migration length, and electrical resistivity. Apparent nuclear and resistivity logs are then simulated with UTAPWeLS (Voss et al., 2009) using a common stratigraphic framework (CSF).

#### *8.2.5.2 Post-Invasion Modeling*

The effects of mud-filtrate invasion on well logs contain rich dynamic petrophysical information that is suitable for rock typing. Mud-filtrate invasion in each rock type was simulated at reservoir conditions. This simulation involves rock petrophysical properties such as porosity, permeability, capillary pressure, and relative permeability. It also considers drilling engineering parameters such as mud type, invasion duration, and overbalance pressure (Pour, 2011). Fluid properties such as density, viscosity, salt concentration, and temperature are also taken into consideration. With stable drilling conditions and constant fluid properties, rock petrophysical properties determine the radial distributions of water saturation, which are used to calculate radial distributions of physical properties such as electrical resistivity, density, and migration length, to numerically simulate the corresponding apparent resistivity, density, and neutron logs (Voss et al., 2009).

### 8.2.6 Decomposing a Petro-Zone into Basis Rock Types: Log Scale to Core Scale

Petrophysical zones segmented by well logs normally have thicknesses ranging from 1 to 5 ft. In heterogeneous reservoirs, those intervals are typically hybrid rock classes composed of different basis rock types defined at the core scale. Two different approaches are used to describe hybrid rock classes: volumetric basis or probabilistic basis (Chapter 7). Figure 8.5 illustrates the description of a hybrid rock class based on volumetric concentrations of each basis rock type. Under this assumption, many physical properties abide by a linear mixing law on a volumetric basis, such as bulk density and electrical conductivity. A linear system of equations similar to multi-mineral models is constructed as follows:

$$M = \sum_{i=1}^{n} v_i M_i \ , \tag{8.4}$$

with $v_i$ subject to

$$0 \le v_i \le 1, \tag{8.5}$$

and

$$\sum_{i=1}^{n} v_i = 1.0, \tag{8.6}$$

where $i$ is rock type index, $n$ is total number of rock types, $M$ represents any physical property abiding by a linear mixing law, and $M_i$ is average property value for each rock type. An inversion-based solver was developed to estimate volumetric concentrations of each basis rock type when selecting log attributes that are sensitive to rock types.

## 8.3 FIELD CASE: BOSSIER TIGHT-GAS SANDSTONE RESERVOIR, THE EAST TEXAS BASIN

The tight-gas sandstone units considered in this chapter are the Bonner and York members of the Bossier Formation, Upper Jurassic Cotton Valley Group in the East Texas Basin. Porosity ranges from 2 to 10 p.u. and permeability ranges from 0.001 to 1 mD. The reservoir is gas saturated and abnormally pressured, and it lacks a down-dip water contact (Salazar, 2004; Rushing et al., 2008).

Detailed sedimentological interpretation based on sliced whole core indicates the presence of different depositional facies including distal delta front, distributary mouth bar, transgressive open shelf, and deep open shelf (Rushing et al., 2008). Petrographic studies show that rock textures are siltstones, silty sandstones, and fine-grained to very-fine grained silty sandstones and sandstones. Shales and silty shales interbedded with sands and siltstones are commonly observed in core samples. Framework grains are dominantly composed of quartz with small amounts of plagioclases, clays, carbonates, and pyrite. Diagenesis effects such as mechanical compaction, quartz overgrowth, and

grain coating/pore lining clay development significantly reduce both storage and flow capacities (Newsham et al., 2002).

Comprehensive core data from a key-study well (WBM drilled) was acquired to enable high-resolution petrophysical reservoir description (Rushing et al., 2008). Routine core porosity and permeability measurements were acquired from more than 100 core plugs. In addition, both high-pressure MICP (0 – 60, 000 psi) and NMR measurements were acquired on 20 preserved core plugs covering a range of depositional facies from a continuous full-diameter whole core.

### 8.3.1 Establishing Basis Rock Types

We applied the inversion method to derive bimodal log-normal pore-size distributions from 20 MICP curves and calculated the petrophysical orthogonality between each core sample pair using Eq. (8.4) for both large and small pore-size modes. Two 20x20 orthogonality matrices with zero diagonal elements were obtained from this step. We applied a dissimilarity matrix clustering technique (Hahsler and Hornik, 2011) to the orthogonality matrices and classified the 20 core samples into 4 rock types, denoted as RT1, RT2, RT3, and RT4 in descending order of reservoir quality.

Figure 8.6a shows the ranked MICP data in the form of $P_c$ vs. $S_w$ crossplots and Fig. 8.6b shows the MICP-derived pore-size distributions ranked with rock types classified with the clustering orthogonality matrices. All rock types exhibit a major pore-size distribution and a tail of small pore-size distribution. We use the classification results obtained with clustering orthogonality matrices to color-code the porosity-permeability crossplot (Fig. 8.7). Clear porosity-permeability trends emerge for all rock types. The MICP-derived rock types are further extended to routine porosity-permeability crossplots by correlating petrophysical orthogonality with porosity and permeability (Fig. 8.8).

Table 8.1 summarizes the statistical distributions of porosity, permeability, and major pore-throat radius for each rock type.

### 8.3.2 Rock-Type-Based Buckles' Plot Analysis

Bulk volume water (BVW) is an important petrophysical quantity to characterize reservoir rock quality in terms of hydraulic capacity (Buckles, 1965; Asquith and Gibson, 1982). Figure 8.9 shows the Buckles plot constructed with core porosity and Dean-Stark water saturation, exhibiting a good correlation between rock types and BVW. This study confirms that the BVW attribute is still diagnostic of hydraulic rock typing at reservoir conditions for clastic reservoirs with negligible free water saturation (Asquith and Gibson, 1982).

### 8.3.3 Rock-Type-Based Core NMR Analysis

NMR measurements have been widely used to quantify tight-gas sands (Liu et al., 2011; Xiao et al., 2012). In this case, laboratory NMR experiments were performed on the same 20 core samples (100% brine saturated) using a MARAN Ultra Magnetic Resonance Core Analyzer (operating frequency ~ 2 MHz) with inter-echo spacing of 300 and 600 μs, respectively. Transverse relaxation time ($T_2$) distributions were obtained by inverting multi-exponential echo data with 51 preset decay times logarithmically spaced between 0.1 ms and 10,000 ms. In water-filled and water-wet rocks, diffusion effects on proton relaxation are negligible. Therefore, relaxation times are mainly determined by pore-body size (Winkler et al., 2006). Under the assumption that pore-body size is well correlated to pore-throat size, it is possible to derive synthetic capillary pressure curves from NMR $T_2$ spectra (Altunbay et al., 2001). Therefore, rock types derived from MICP data should also consistently rank NMR $T_2$ spectra. Figure 8.10 shows the core NMR $T_2$ spectra grouped by rock types, and Fig. 8.11 shows the crossplot of permeability and

T2LM color-coded by rock type. Generally, $T_2$ peak locations move to the left (lower $T_2$) as rock type number increases (overall reservoir quality decreases). Table 8.1 summarizes the statistical distributions of NMR T2LM for each rock type.

### 8.3.4 Rock-Type-Based Dynamic Petrophysical Modeling

Dynamic petrophysical properties such as saturation-dependent capillary pressure and relative permeability play important roles in controlling fluid flow at all time and length scales. Relative permeability measurements of tight-gas sandstone samples require extremely long times for their acquisition. Therefore, it is useful to model relative permeability curves from MICP data for different rock types.

Because WBM invading gas reservoirs is an imbibition process, we derived imbibition capillary pressure and relative permeability curves from the bimodal Gaussian pore-size distribution using the modified Corey-Burdine's model (Brooks and Corey, 1966; Corey, 1994; Burdine, 1953; Huang et al., 1997). Critical water saturation ($S_{wcrit}$) is calculated from its correlation with Gaussian parameter $w_2$, whereas the end point of gas relative permeability is predicted by its correlation with Gaussian parameter $\mu_1$. Table 8.2 summarizes the gas relative permeability properties of each rock type. Figure 8.12 shows the corresponding modeled results for each rock type.

### 8.3.5 Numerical Modeling of Conventional Well Logs (Pre-Invasion)

Based on the statistical rock properties, we construct an ideal rock type model with average porosity and BVW values to simulate conventional logs in uninvaded rock types. Figure 8.13 shows the simulation results. The best reservoir rock type exhibits the largest neutron-density crossover and the highest resistivity, which is a direct consequence of the highest initial gas saturation.

### 8.3.6 Numerical Modeling of Conventional Well Logs (Post-Invasion)

We proceed to simulate mud-filtrate invasion for the ideal rock type model with the previously modeled dynamic petrophysical properties and assumed drilling conditions. After invasion, the neutron-density crossover decreases for all rock types due to the increase of water saturation in the shallow radial region. Deep and medium apparent resistivity logs decrease significantly for RT1 and RT2 due to relatively deep invasion, while they remain almost unchanged for other rock types due to very shallow invasion. Simulations indicate that apparent deep resistivity is unreliable for calculating initial water saturation in RT1 and RT2.

### 8.3.7 NMR Log Modeling: Pre-Invasion vs. Post-Invasion

The NMR log is shallow reading, whereby it is extremely sensitive to mud-filtrate invasion. The presence of residual gas in the shallow region renders the NMR $T_2$ log unreliable for direct correlation with pore-size distribution. We simulated NMR $T_2$ distributions in RT1 and RT2 based on original pore-size distributions before and after invasion (Fig. 8.15). Neither distribution can reliably reproduce a PSD-like $T_2$ distribution due to invasion and artifacts introduced during the inversion of raw-echoes.

We found that capillary bound water (CBW) derived from NMR $T_2$ distributions by enforcing the same cutoff for both pre-invasion and post-invasion models were very close, i.e., NMR-derived CBW was not appreciably affected by WBM invasion in this gas-reservoir. Therefore, it is possible to use NMR-derived CBW for calculating volumetric concentrations of BRTs because it approximately abides by a linear mixing law on a volumetric basis (Cao Minh and Sundararaman, 2011).

### 8.3.8 Log Attributes vs. Rock Types

Well-log forward modeling indicates that there are three log attributes that remain sensitive to rock types in the presence of mud-filtrate invasion and approximately abide by linear mixing laws on a volumetric basis. Table 8.3 describes these attributes, namely N-D crossover, deep resistivity, and NMR-derived CBW, and their correlations with petrophysical reservoir quality. Each attribute individually provides a statistically good ranking criterion for petrophysical reservoir quality. Table 8.4 summarizes the statistical distributions of these log-attributes for each rock type in the Bossier tight-gas sands. Rock types of better reservoir quality normally exhibit larger N-D crossover, higher resistivity, and lower NMR-derived CBW.

The separation between medium and deep resistivity logs can effectively differentiate RT 1-2 from RT 3-4 and shale. This attribute, however, contains some redundant information with resistivity in reservoir zones and does not abide by linear mixing laws on a volumetric basis. Therefore, it was unsuitable for solving volumetric concentrations of basis rock types in this chapter. The potential use of this attribute for rock typing has been reported elsewhere (Gandhi et al., 2010; Heidari et al., 2011).

### 8.3.9 Orthogonal Rock Classes Decomposition in Bossier Tight-Gas Sandstones

The following sections apply the synthesized multi-scale ORC decomposition workflow to the Bonner and York members.

#### *8.3.9.1 Zone No. 1: Bonner Member (13, 010 – 13, 070 ft)*

The reservoir unit of the Bonner sand member has a total depth interval of 60 ft - a scale that can be visually identified from seismic surveys. Gamma-ray, bulk density, and resistivity logs to segment the reservoir unit into 22 petrophysical zones with an average thickness of approximately 2.7 ft. Figure 8.16 shows the histogram of zone

thickness in the Bonner sand member. Most zones exhibit thicknesses between 1.5 and 4 ft.

Tracks 1-6 in Fig. 8.17 show the well logs and core data acquired in the Bonner sand member. Some petrophysical zones contain more than one core plug exhibiting significant variability in permeability. This behavior is good evidence that a petrophysical zone is indeed a mixture of basis rock types. We construct a linear system of equations as previously described and substitute the average log-attribute values listed in Table 8.4 to estimate volumetric concentrations of pre-defined basis rock types. Track 7 in Fig. 8.17 shows the calculated volumetric concentrations of pre-defined basis rock types. Because RT1 and RT2 are the dominant contributors to gas flow, a zone with high volumetric concentrations of RT1 and RT2 is a good flow unit. On the other hand, a zone with a high concentration of RT4 may act as a baffle to fluid flow. The description of hybrid rock classes provides a new visual aid to interpret flow units, which is useful for guiding perforations and completions in later development phases. In heterogeneous reservoirs, point-by-point comparisons of core permeability and log-derived permeability are not useful. Storage and flow capacities estimated from core and well logs were compared in cumulative storage and flow profiles to validate an upscaled petrophysical model. Figure 8.18 shows that both storage and flow capacity agree well with core- and log-derived models.

#### *8.3.9.2 Zone No. 2: York Member (13, 128 – 13, 270 ft)*

The reservoir unit of the York sand member has a total thickness of 140 ft. The same petrophysical zonation workflow was used to segment the reservoir unit into 40 petrophysical zones with an average thickness of 3.25 ft. Figure 8.19 shows a histogram

of zone thickness in the York sand member. The thickness of most units varies between 1.5 and 4.5 ft.

A similar estimation procedure was applied to the York sand member to solve the volumetric proportions of different BRTs in each petrophysical zone. Track 7 in Fig. 8.20 shows the calculated volumetric concentrations of pre-defined basis rock types. Figure 8.21 compares the storage and flow capacities estimated with core and well logs in the form of cumulative storage and flow profiles. Higher discrepancy between core- and log-derived storage and flow profiles is observed due to the higher spatial heterogeneity in the York sand member.

From the calculated volumetric proportions of RT1 and RT2, we observe that the overall reservoir quality of the York sand member is lower than that of the Bonner sand member, a conclusion that is also validated by the cumulative storage and flow profiles constructed from the two intervals.

## 8.4 CONCLUSIONS

We developed a new petrophysical rock typing workflow to describe heterogeneous reservoirs. The workflow synthesizes rock class decomposition techniques at multiple measurements scales and follows a top-down approach to describe the intrinsic mixture of rock properties.

Petrophysical zonation based on bed boundary detection and optimization ensures minimum shoulder-bed effects on well logs. This study proposed a volumetric-based hybrid rock class description method that simultaneously honors physical mixing laws in a parallel-stacking of basis rock types.

A bimodal log-normal density function was invoked to characterize complex pore systems and quantify petrophysical orthogonality (or dissimilarity) between different

rock classes via the "bundle of tubes" model. The definition of orthogonality was extrapolated to routine and special core measurements. Pre-invasion and post-invasion log modeling suggests that the most relevant attributes for log-based rock typing are neutron-density crossover, deep resistivity, and NMR-derived capillary bound water in the field example considered in this chapter. Similar modeling work should be performed on a case-by-case basis to better understand the sensitivity of well logs to rock types.

The integrative petrophysical workflow was applied to tight-gas sand units in the Bonner and York members of Bossier Formation, Upper Jurassic Cotton Valley Group in the East Texas Basin. Estimated storage and flow capacities agreed with routine core data when compared to up-scaled cumulative storage and flow profiles.

The new method is fundamentally different from conventional approaches that perform depth-by-depth deterministic rock classification based on apparent well logs. Furthermore, the new interpretation workflow is generally applicable to other conventional reservoir types, including turbidites and carbonates. The reversed workflow implies a bottom-up or upscaling approach to construct a quantitative reservoir model for reserves estimation and production forecasting.

**Table 8.1:** Statistical distributions of petrophysical properties for the basis rock types.

| Rock Type | Porosity (frac) | BVW (frac) | Permeability (mD) | Major Pore Radius (μm) | Core T2LM (ms) |
|---|---|---|---|---|---|
| **RT-1** | 0.087 ± 0.008 | 0.0056 ± 0.0014 | 0.152 ± 0.051 | 0.264 ± 0.042 | 46.4 ± 10.5 |
| **RT-2** | 0.082 ± 0.011 | 0.011 ± 0.004 | 0.053 ± 0.021 | 0.170 ± 0.009 | 25.3 ± 3.2 |
| **RT-3** | 0.075 ± 0.008 | 0.018 ± 0.006 | 0.020 ± 0.006 | 0.116 ± 0.017 | 11.9 ± 4.3 |
| **RT-4** | 0.070 ± 0.001 | 0.030 ± 0.009 | 0.0065 ± 0.0007 | 0.052 ± 0.011 | 7.1 ± 2.0 |

**Table 8.2:** Initial gas saturation, critical gas saturation, and critical water saturation assumed to model capillary pressure and relative permeability.

| Rock Type | $S_{gi}$ (frac) | $S_{gc}$ (frac) | $S_{wcrit}$ (frac) |
|---|---|---|---|
| RT-1 | 0.92 | 0.32 | 0.08 |
| RT-2 | 0.84 | 0.40 | 0.16 |
| RT-3 | 0.72 | 0.48 | 0.28 |
| RT-4 | 0.40 | 0.05 | 0.60 |

**Table 8.3:** Log-attributes sensitive to rock types and their corresponding correlations with reservoir quality.

| Log Attribute | Petrophysics | Reservoir Quality Correlation |
|---|---|---|
| **N-D Crossover** | Bulk volume of residual gas after invasion | Positive correlation |
| **Deep Resistivity** | In-situ bulk volume water | Positive correlation |
| **NMR Derived CBW** | Irreducible bulk volume water | Negative correlation |

**Table 8.4:** Summary of statistical distributions of log attributes for each rock type.

| Log Attribute | N-D Crossover (frac) | Deep Resistivity (ohm-m) | NMR-Derived CBW (frac) |
|---|---|---|---|
| **RT1** | 0.06 ± 0.02 | 101 ± 22 | 0.006 ± 0.002 |
| **RT2** | 0.03 ± 0.012 | 45 ± 18 | 0.012 ± 0.005 |
| **RT3** | 0.01 ± 0.006 | 22 ± 8 | 0.020 ± 0.008 |
| **RT4** | -0.002 ± 0.004 | 10 ± 3 | 0.032 ± 0.010 |

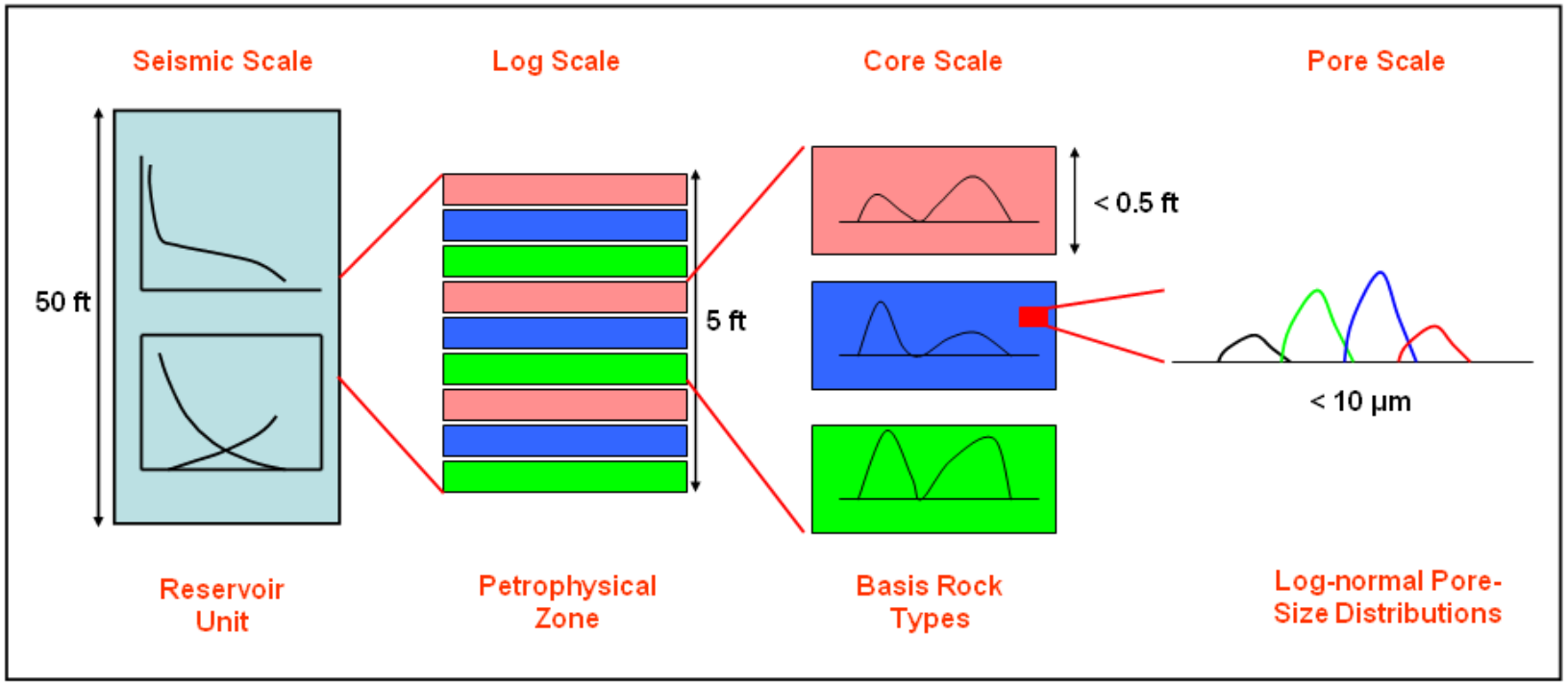


**Figure 8.1:** Top-down reservoir characterization workflow using multi-scale orthogonal rock class decomposition.

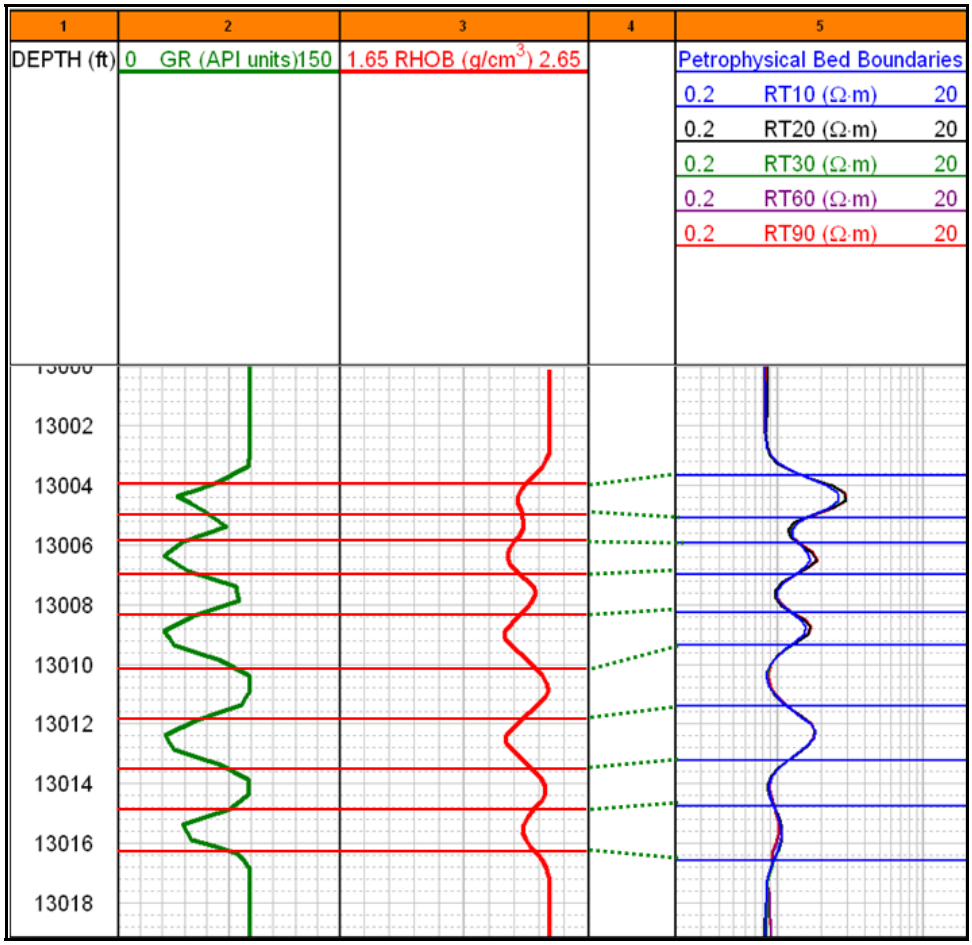


**Figure 8.2:** Example of detecting different bed boundaries with resistivity and nuclear logs due to depth shifting and stick-and-slip in different acquisition runs.

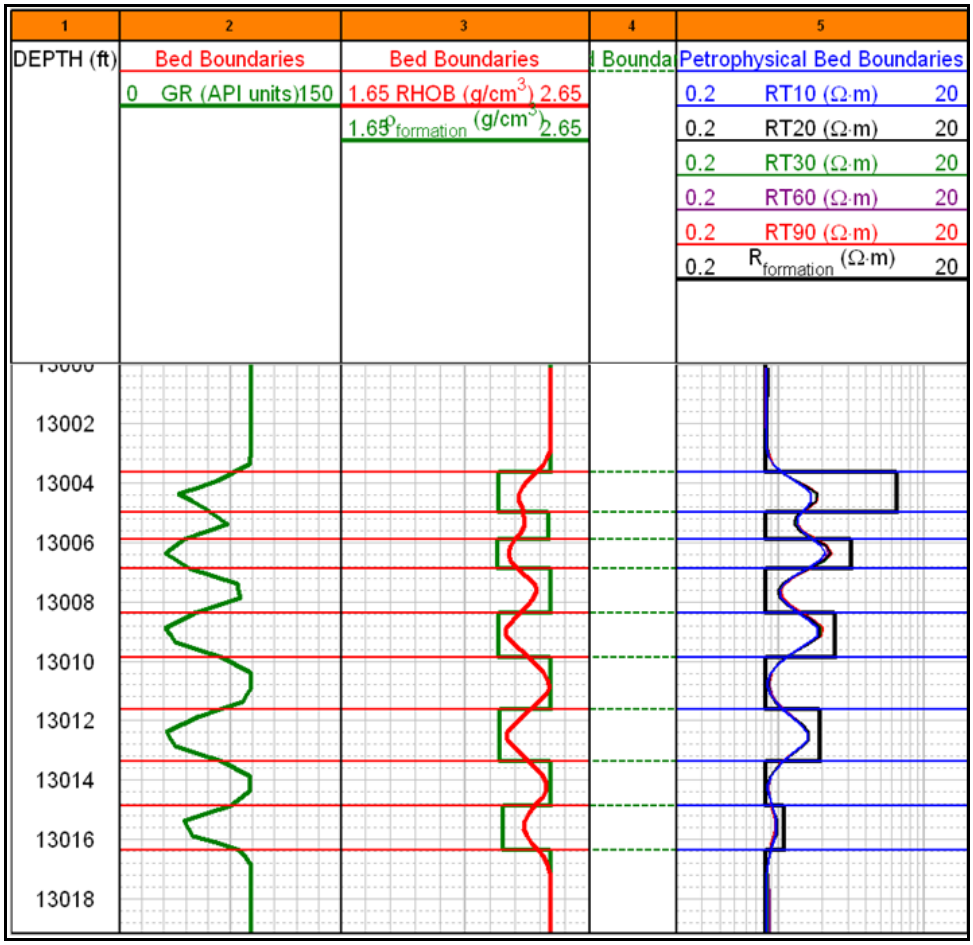


**Figure 8.3:** Example of applying the workflow of detecting, matching, and testing bed boundaries with gamma-ray, density, and resistivity logs to segment a reservoir unit into petrophysical zones. Inverted results are displayed as squared logs.

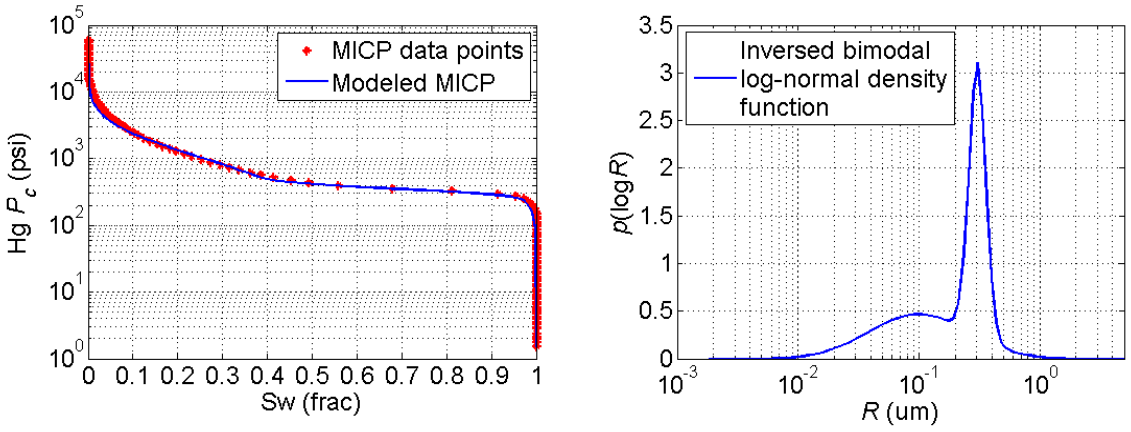


**Figure 8.4:** Example of derivation of a bimodal log-normal pore-size distribution from MICP using the inversion method introduced in Chapter 2.

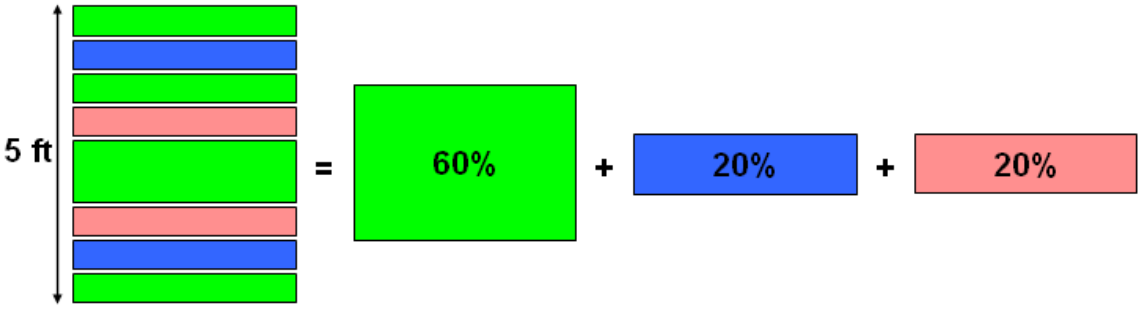


**Figure 8.5:** Description of hybrid rock classes using a parallel-stacking model. Volumetric concentrations of basis rock types determine up-scaled petrophysical properties.

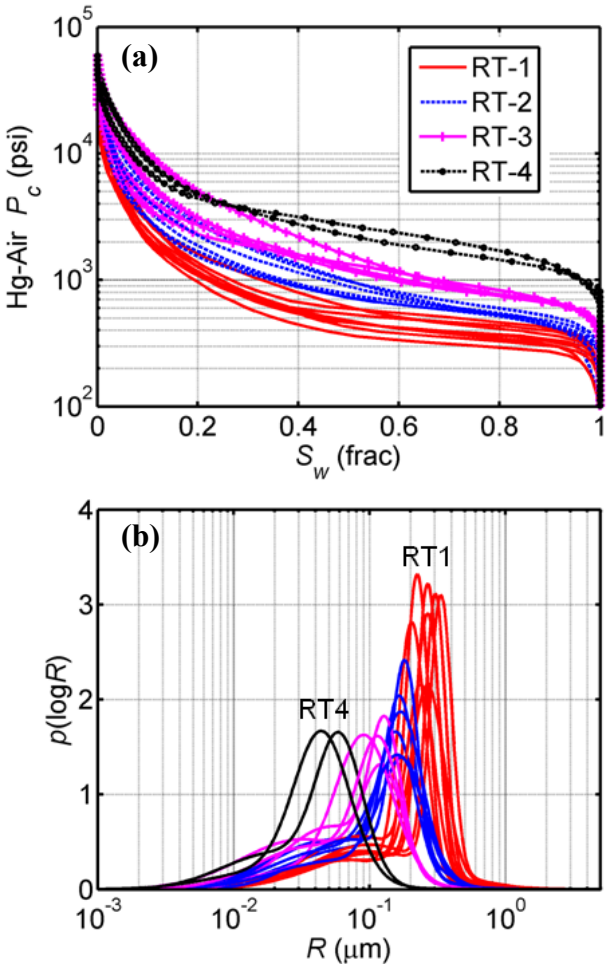


**Figure 8.6:** **(a)** MICP data in the form of $P_c$ vs. $S_w$, and **(b)** MICP-derived pore-size distributions grouped with rock types classified from clustering orthogonality matrices.

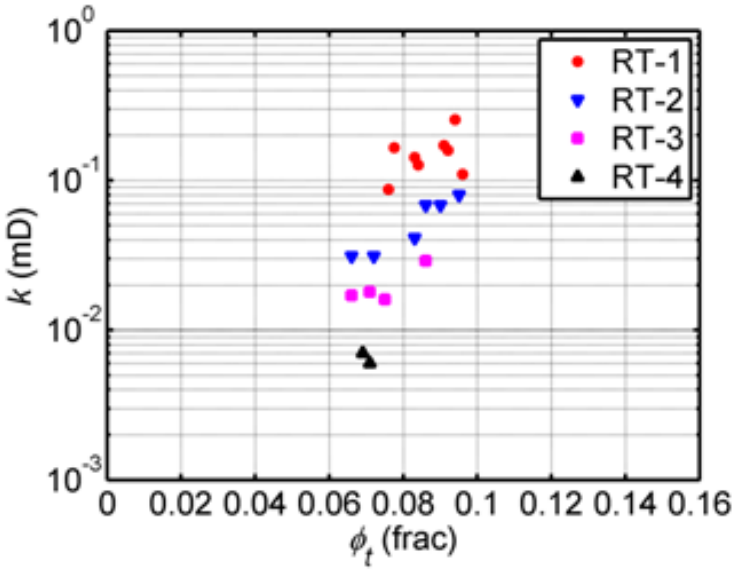


**Figure 8.7:** Porosity-permeability crossplot grouped with rock types classified from clustering orthogonality matrices.

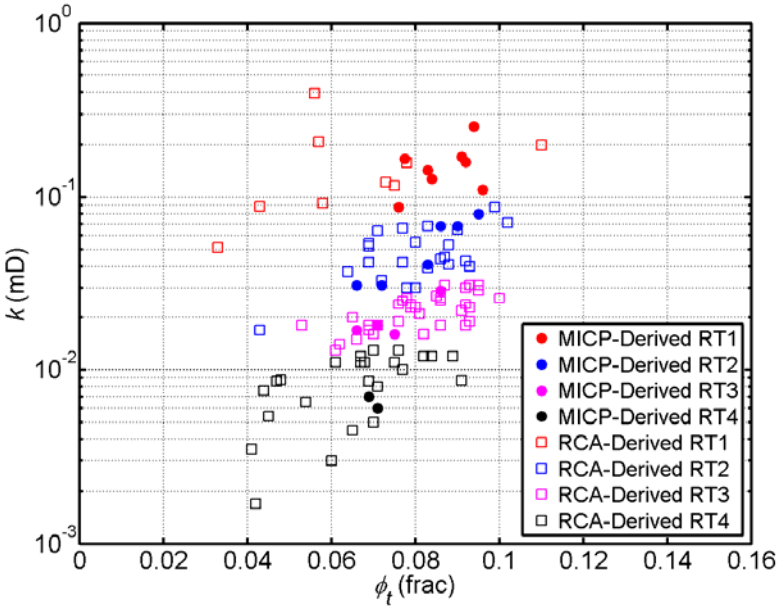


**Figure 8.8:** Comparison of MICP-derived and RCA-derived rock types.

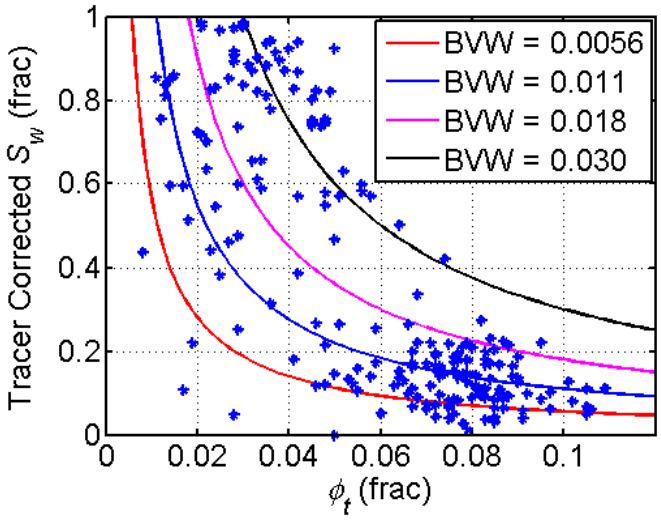


**Figure 8.9:** Buckles plot constructed with core porosity and tracer-corrected Dean-Stark water saturation.

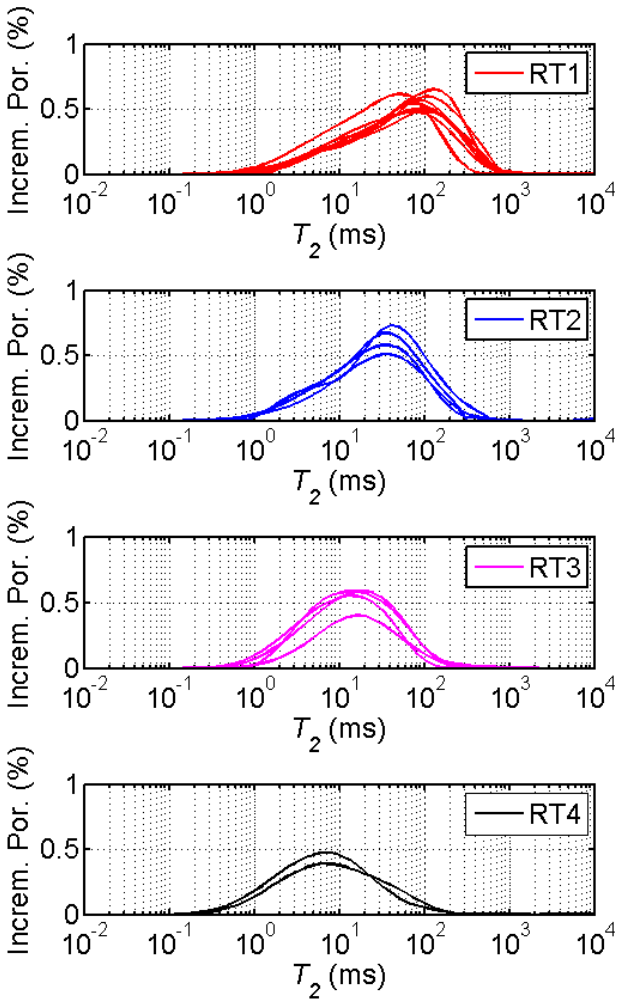


**Figure 8.10:** Core NMR on 100% brine-saturated samples grouped according to rock type.

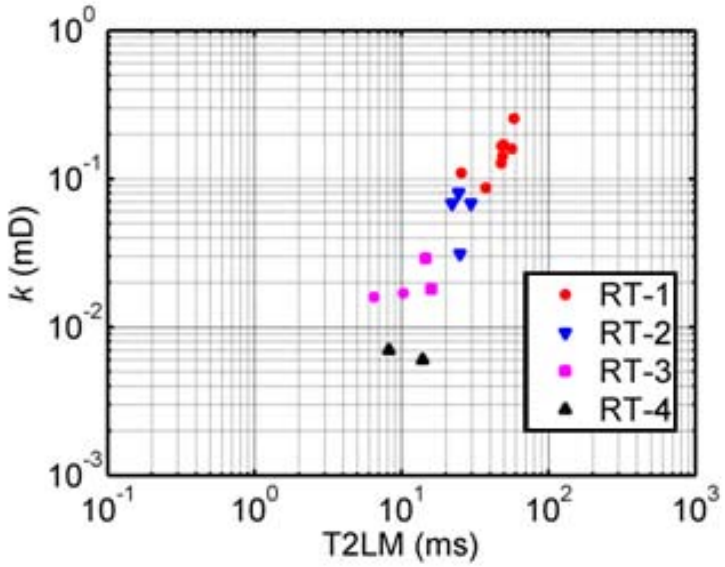


**Figure 8.11:** Crossplot of permeability and T2LM color- coded according to rock type.

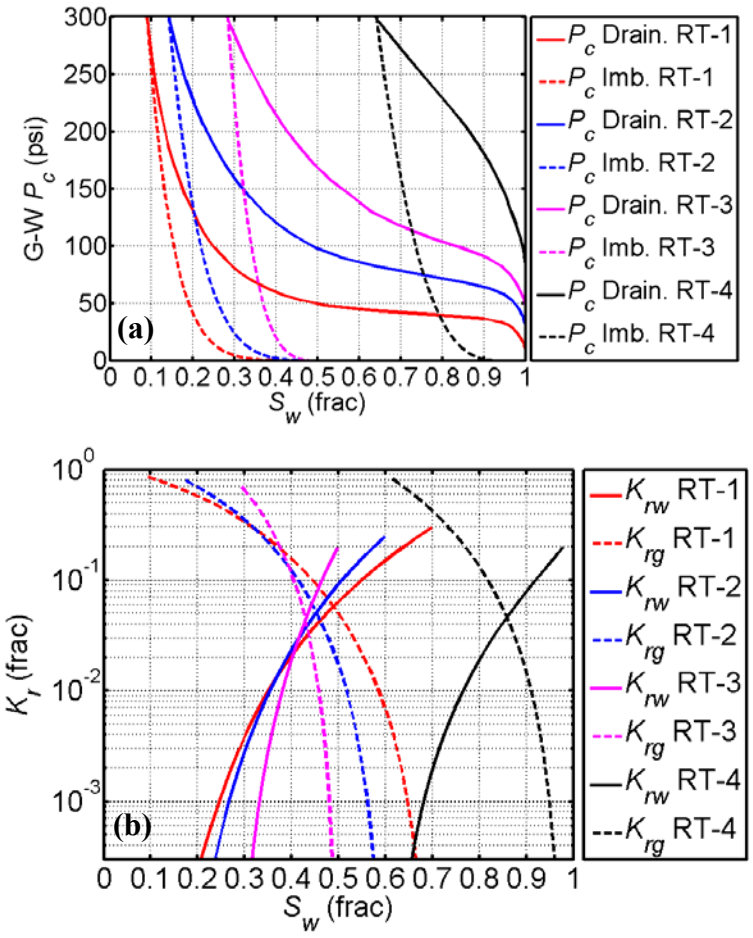


**Figure 8.12: (a)** Modeled drainage and imbibition capillary pressure curves for each rock type. **(b)** Modeled imbibition relative permeability curves for each rock type.

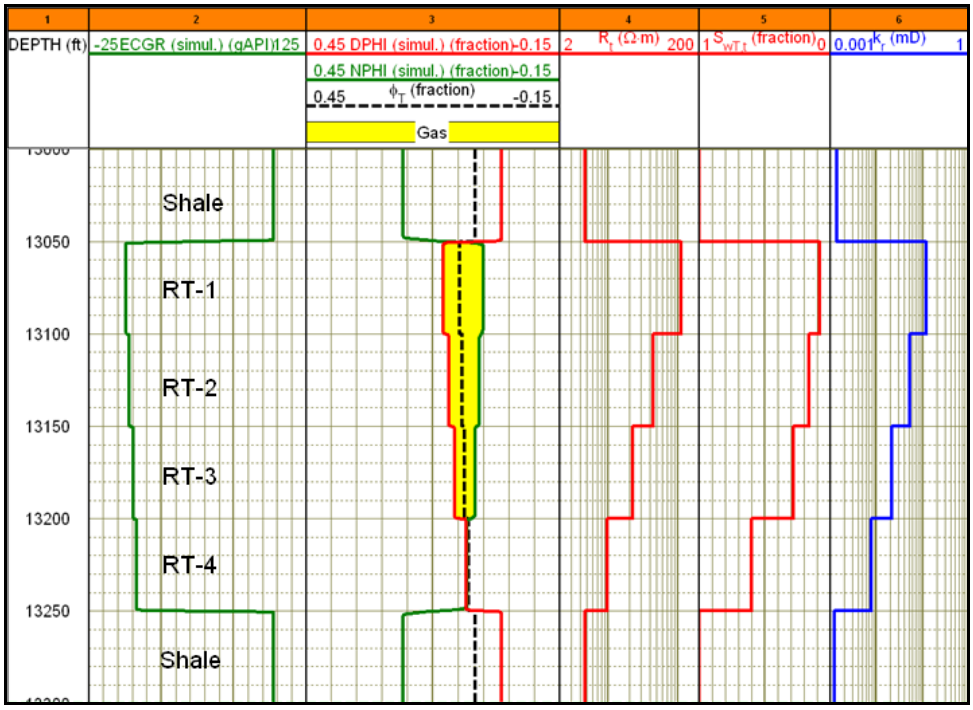


**Figure 8.13:** Numerical modeling of conventional well logs before invasion across basis rock types.

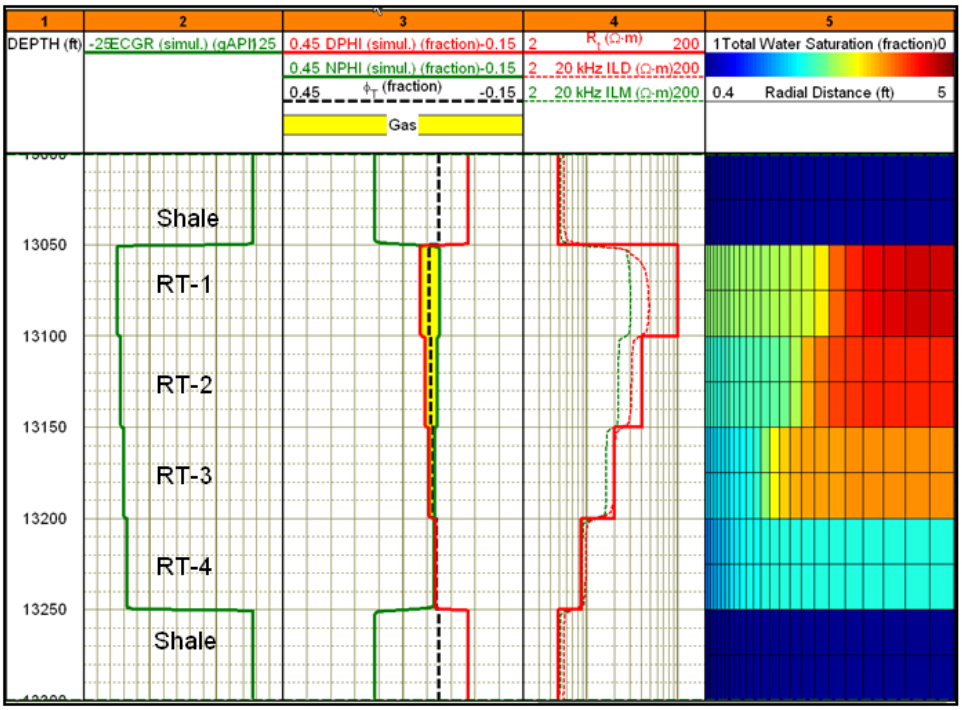


**Figure 8.14:** Numerical modeling of conventional well logs after invasion across basis rock types.

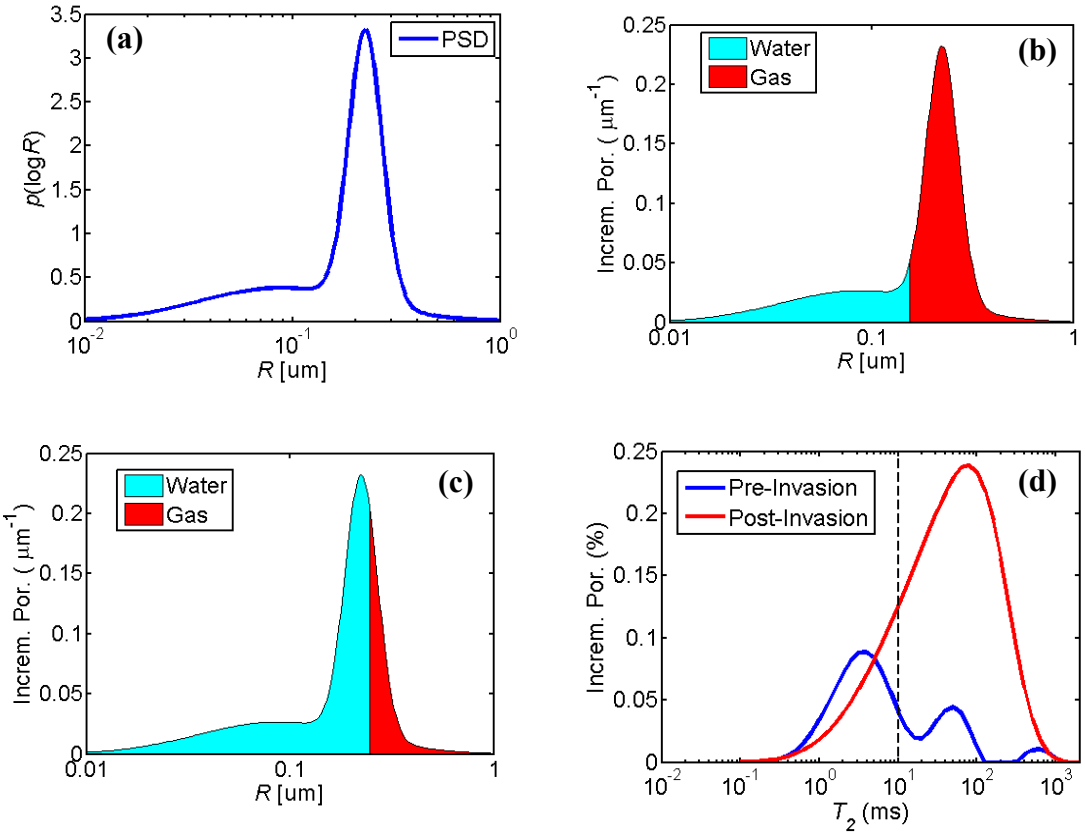


**Figure 8.15:** Fluid and NMR $T_2$ distributions in RT1 based on the original pore-size distribution before and after invasion. **(a)** pore-size distribution; **(b)** pre-invasion fluid distribution; **(c)** post-invasion fluid distribution, and **(d)** NMR $T_2$ modeling.

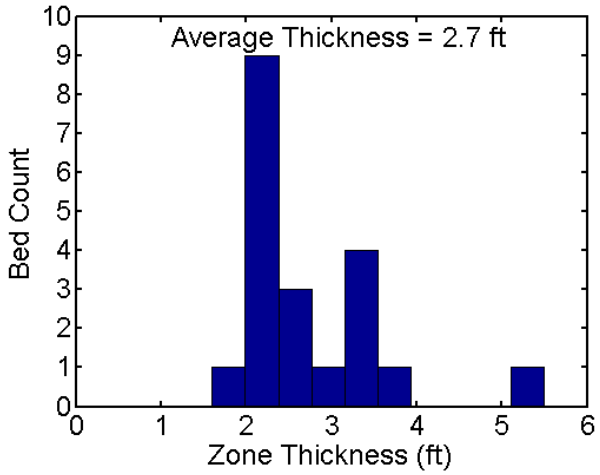


**Figure 8.16:** Statistical distribution of petrophysical zone thickness in the Bonner sand member.

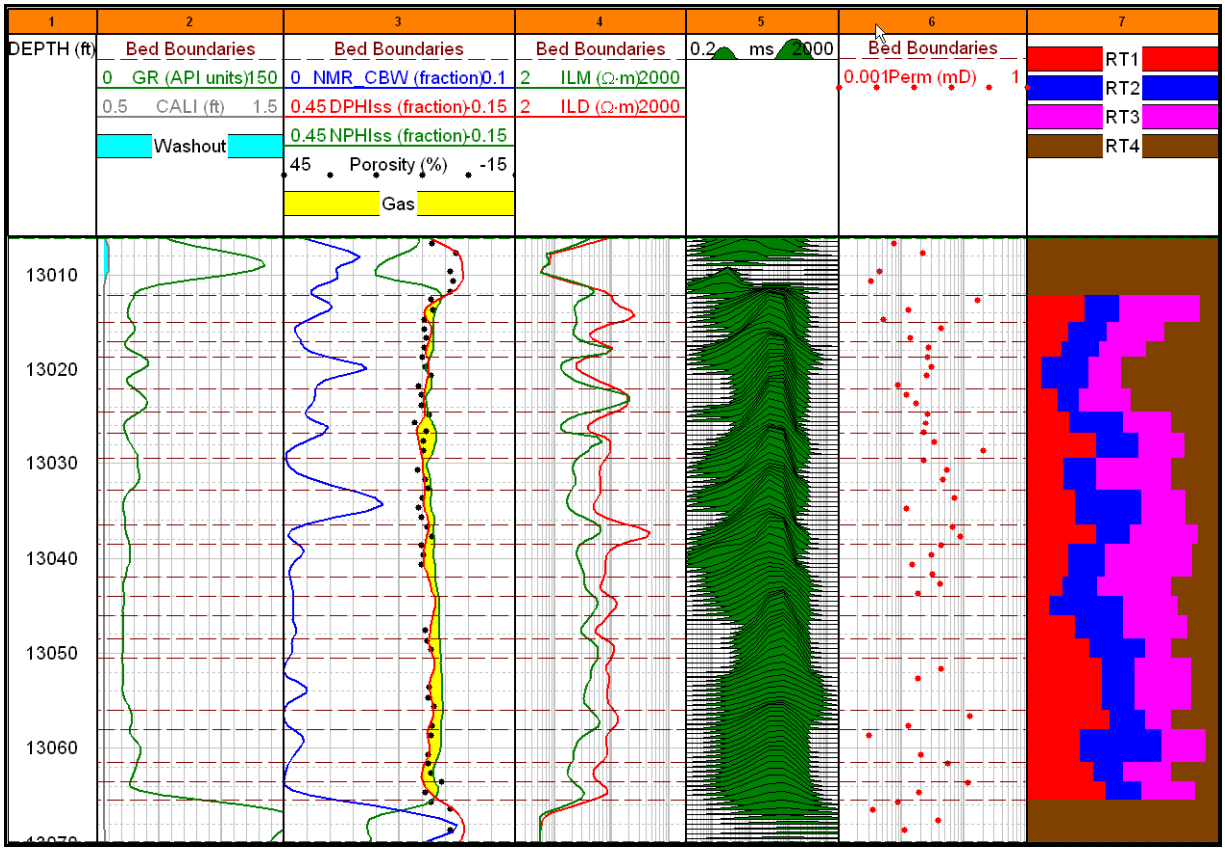


**Figure 8.17:** Application of the multi-scale ORC decomposition workflow to the Bonner sand member. Track 1: depth; Track 2: Gamma ray; Track 3: Neutron and density porosity in sandstone units, bulk density, NMR-derived CBW, and core porosity; Track 4: Apparent resistivity logs; Track 5: NMR $T_2$ Distribution; Track 6: Core permeability; Track 7: Volumetric concentrations of four pre-defined basis rock types.

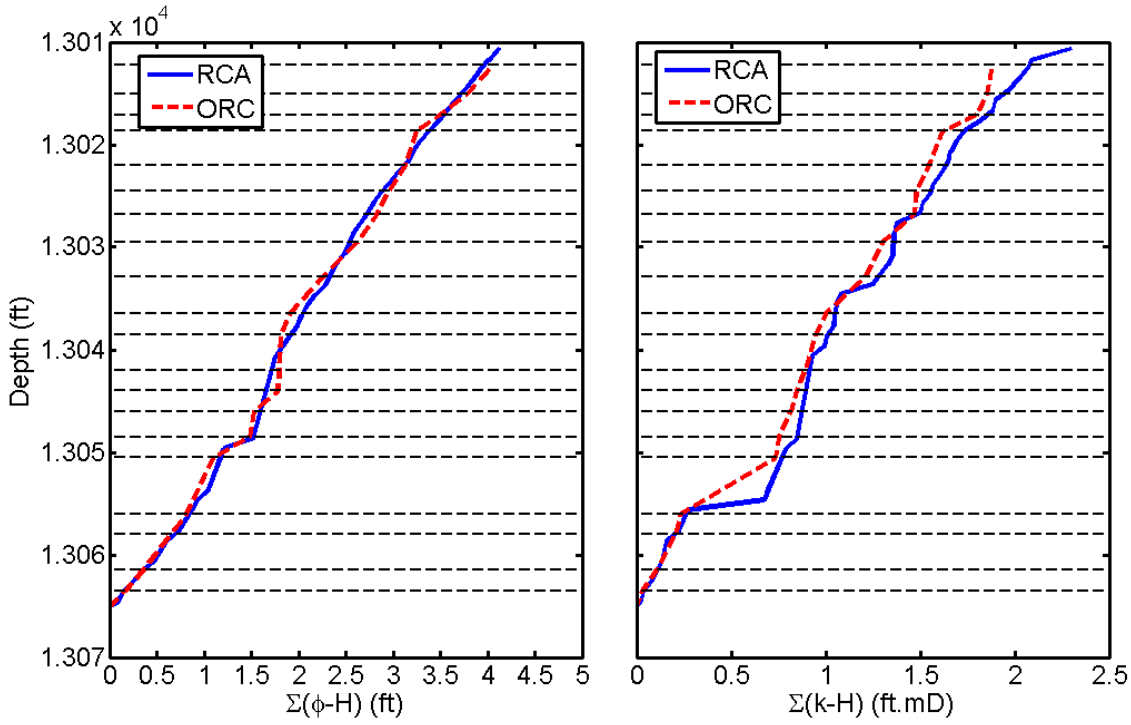


**Figure 8.18:** Comparison of storage capacity (left panel) and flow capacity (right panel) using cumulative storage and flow profiles constructed with core data and log-derived rock types in the Bonner sand member.

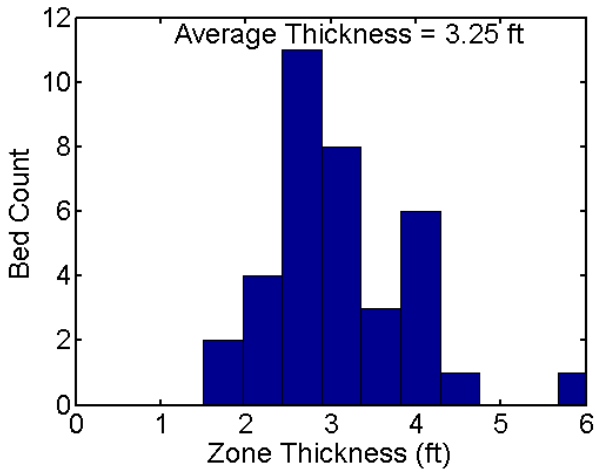


**Figure 8.19:** Statistical distribution of petrophysical zone thickness in the York sand member.

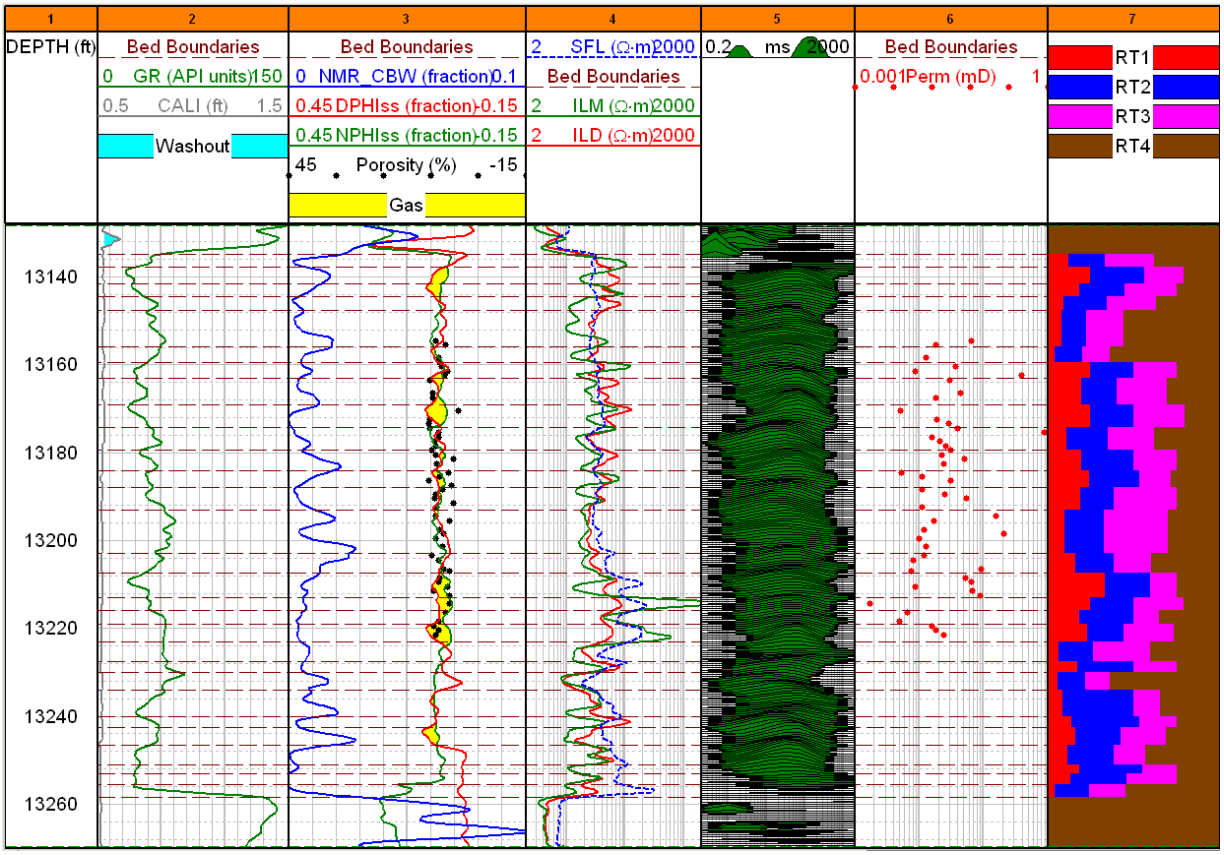


**Figure 8.20:** Application of the multi-scale ORC decomposition workflow to the York sand member. Track 1: depth; Track 2: Gamma ray; Track 3: Neutron and density porosity in sandstone units, NMR-derived CBW, and core porosity; Track 4: Apparent resistivity logs; Track 5: NMR $T_2$ Distribution; Track 6: Core permeability; Track 7: Volumetric concentrations of four pre-defined basis rock types.

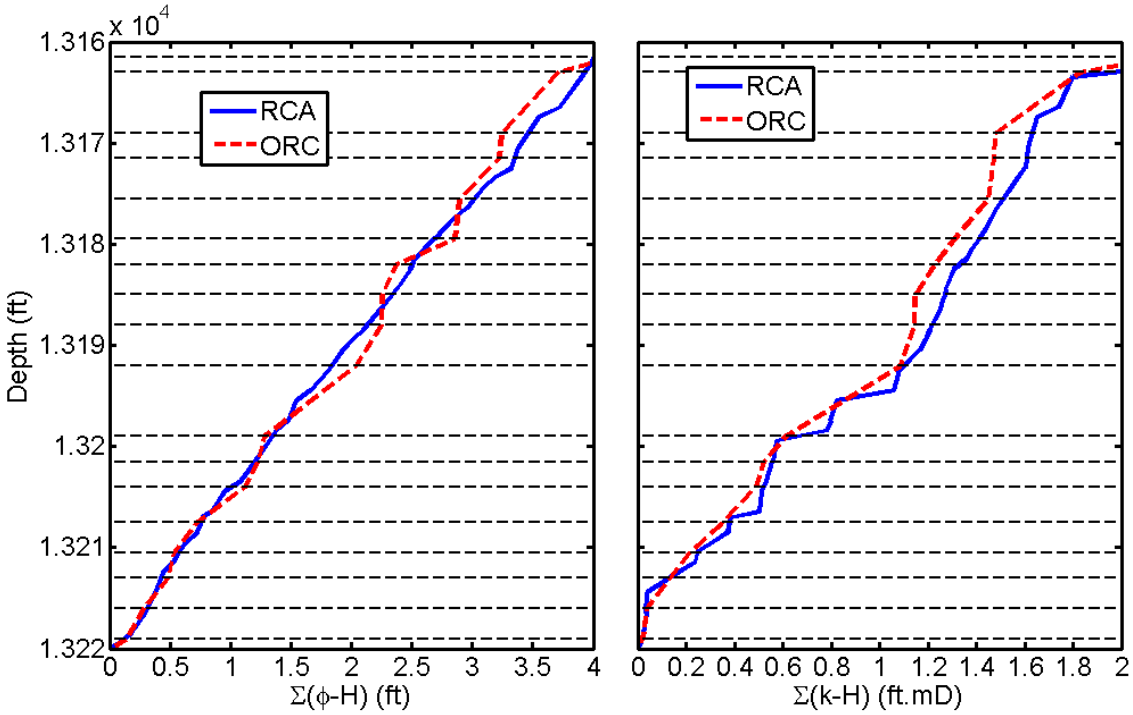


**Figure 8.21:** Comparison of storage (left panel) and flow capacities (right panel) using cumulative storage and flow profiles constructed with core data and log-derived rock types in the York sand member.

# Chapter 9: Summary, Conclusions, and Recommendations

The final chapter summarizes important technical observations and learnings stemming from this dissertation research. Main conclusions are reiterated, and recommendations regarding future research are also provided.

## 9.1 SUMMARY

This dissertation develops a series of topics on integrating core and well logs to enhance reservoir description by solving the compounded "geometrical problems" noted by Archie (1950). New rock classification schemes, methods, and workflows are developed to simultaneously honor scientific laws of geology, petrophysics, and tool physics. This dissertation is firmly anchored on pore geometry for petrophysical rock classification. Furthermore, petrophysical rock types are connected to a geological framework by investigating the cause-and-effect chain linking geological processes and the pore geometry at different measurement scales. A new element developed in this work is to invoke fast numerical well log simulation techniques to quantify physical log responses of different rock types established with core data. The dissertation research consists of three stages.

The first stage (Chapters 2, 3, and 4) quantifies pore-size distribution, pore network, and fluid distribution using routine and special core data, particularly MICP and NMR. A bimodal log-normal density function is employed to analytically model pore-size distribution as evidenced from MICP data, which generates six attributes for subsequent petrophysical modeling and rock typing. The attributes of the Gaussian density function relate directly and intuitively to pore-system characteristics including pore volume, major pore-throat radius, and pore-throat size uniformity. Testing of the method in the Hugoton gas field verifies its effectiveness in describing complex pore

systems in carbonate reservoir rocks that have undergone significant diagenesis. A new petrophysical quantity conceptualized as orthogonality, which combines all six Gaussian attributes, is defined to rank petrophysical rock types and enforce petrophysical consistency between static and dynamic rock properties. The method was applied to a challenging field case of tight-gas sandstone in the East Texas Basin and greatly improved the petrophysical ranking of low-porosity and low-permeability rocks. Further, we developed a simple 3D cubic pore network model that was constrained by both NMR and MICP data to study microscopic fluid distribution and phase connectivity during two-phase fluid displacement. Relative permeability was then quantified based on the quasi-static fluid distribution and phase connectivity, and results showed agreement between core data and model-predicted values.

The second stage (Chapters 5 and 6) extended the understanding of fluid distribution from microscopic scale to macroscopic scales: a vertical reservoir column scale (tens to hundreds of feet scale) and a radial near-borehole scale (feet scale). Vertical fluid distribution resulting from hydrocarbon migration, which is assumed to be a primary drainage process, gives rise to observable signatures on resistivity logs. A trend between saturation and reservoir column height was captured for quantitative use of resistivity logs for hydraulic rock typing. In two deepwater turbidite reservoirs where hydraulic rock types were mainly controlled by grain size, the classified petrophysical rock types are correlated to geological facies as defined by sedimentary energy. Radial fluid distribution induced by mud-filtrate invasion also contains rich petrophysical information that can be used for rock typing and associated with dynamic properties of rocks. A new concept referred to as invasion facies was developed to link the invasion-induced log signatures to petrophysical rock types that exhibit similar static and dynamic

rock-fluid properties. The application of this method to data acquired from WBM-drilled wells in a carbonate field verified its practicality.

The last stage (Chapters 7 and 8) introduced two integrated petrophysical workflows to characterize heterogeneous reservoirs. A bottom-up Bayesian approach was implemented to test multiple rock type distribution hypotheses against field-observed well logs and quantify the uncertainty associated with rock types and their petrophysical properties. In a deltaic gas reservoir where thin beds are dominant, this method enhances the permeability prediction by 16% compared to conventional rock typing methods. On the other hand, a top-down rock class decomposition technique was developed to characterize reservoir from the flow unit or seismic scale down to the core scale by integrating previously developed core-based rock typing methods and numerical well log simulation techniques. In a tight-gas sandstone reservoir, this method generated cumulative storage and flow profiles that were close to those inferred from core data.

## 9.2 CONCLUSIONS

This section reiterates important conclusions from each individual chapter and then presents some general conclusions of the overall dissertation.

### 9.2.1 Pore-System Characterization and Petrophysical Rock Classification Using a Bimodal Gaussian Density Function

i. Bimodal Gaussian density function is a useful analytical tool to describe complex pore systems. Gaussian attributes included in this model have interpretable petrophysical meaning, which can be quantitatively used for petrophysical modeling and rock typing.
ii. Verification studies in the Hugoton gas field yielded the following petrophysical interpretations:

(1) Absolute permeability is mainly controlled by the large pore-throat size mode. It is positively correlated with mean pore-throat radius and the associated pore volume and negatively correlated with standard deviation.

(2) Irreducible or critical water saturation is mainly controlled by the small pore-throat size mode. Both are correlated with the mean value of small pore-throat size mode and the associated pore volume fraction.

(3) The end point value for gas relative permeability at critical water saturation is mainly controlled by the large pore-throat size mode, especially the mean value.

iii. Moderate to high correlations were observed between Gaussian attributes and various petrophysical properties. Therefore, it is possible to model several static and dynamic petrophysical properties (irreducible and critical water saturation, absolute permeability, drainage relative permeability) based on a bimodal Gaussian density function.

iv. Given sufficient core calibration, pore systems in reservoir rocks can be fully characterized by a set of six Gaussian attributes that predict consistent petrophysical properties for subsequent reservoir characterization studies. Petrophysical rock typing based on Gaussian attributes provides reliable ranking of reservoir quality and simplifies reservoir modeling by enforcing a consistent petrophysical description based on pore geometry.

### 9.2.2 Petrophysical Rock Classification in the Cotton Valley Tight-Gas Sand Reservoir with a Clustering Pore-System Orthogonality Matrix

i. Conventional rock typing methods dominantly emphasize hydraulic radius and tend to neglect the impact of effective pore volume and pore-size uniformity on overall petrophysical quality. Consequently, they are prone to misclassifications in tight-gas sandstones that exhibit poor correlation between hydraulic radius and other pore-system attributes.
ii. Rock classification via clustering orthogonality matrices enables consistent reservoir quality ranking in all petrophysical data domains, including porosity-permeability trends, pore-size distribution, MICP, and core NMR $T_2$ spectra.
iii. The analytical bimodal Gaussian pore-size distribution model lends itself to the prediction of saturation-dependent relative permeability with Corey-Burdine's model.

### 9.2.3 Quantifying Fluid Distribution and Phase Connectivity with a Simple 3D Cubic Pore Network Model Constrained by NMR and MICP

i. The integration of NMR and MICP data significantly reduces the uncertainty of the pore network model. It quantifies pore-throat radius distribution and quasi-static fluid distribution during a two-phase drainage displacement.
ii. Fluid distribution in rocks is a wide distribution rather than a clear cutoff separation. It is still true that the non-wetting phase preferentially invades large pore bodies first when a body-throat correlation exists.
iii. The modeled fluid distribution and phase connectivity at partially saturated rocks are useful in quantifying relative permeability in tight rocks.

### 9.2.4 Saturation-Height and Invasion Consistent Hydraulic Rock Typing Using Multi-Well Conventional Logs

i. Hydraulic rock typing must be based on pore geometry because it relates all petrophysical properties of reservoir rocks.

ii. Electrofacies diagnosed from apparent well logs are not satisfactory because the latter are simultaneously sensitive to mineralogy and pore fluids.

iii. Buckle's number relates to pore geometry in a direct manner, but it is only applicable to reservoir zones that are at irreducible water saturation conditions.

iv. The three conventional rock typing methods should perform equally well in detecting petrophysical rock types with different pore-throat radii. The key to reliable rock typing for reservoir characterization is to construct well-log-derived attributes that directly link rock types diagnosed from core measurements to well logs.

v. The petrophysical quality of young deepwater turbidite reservoirs is chiefly controlled by sedimentary grain sizes. Therefore, a link exists between petrofacies and depositional facies that can be effectively applied in reservoir development efforts.

vi. Reservoir capillary transition enables the estimation of grain sizes from saturation-height data. Rock types associated with young turbidite reservoirs can still be differentiated by their median grain sizes, whereas neighboring rock types exhibit a grain size ratio close to 1.5 or $\sqrt{2}$ .

### 9.2.5 Rock Classification Connecting Static and Dynamic Petrophysical Properties with Core Measurements and Conventional Logs in a Mixed Clastic-Carbonate Reservoir

i. The conventional method of estimating permeability from linear correlation of total porosity is subject to large uncertainty due to the complex pore geometry encountered in carbonate reservoirs.
ii. Mud-filtrate invasion, which is affected by both dynamic and static petrophysical properties of the invaded formation, gives rise to unique and specific well-log signatures on different rock types. Such signatures, when incorporated into rock classification, can significantly reduce the uncertainty of permeability estimation.
iii. The resulting distribution of rock types can be used to improve the estimation of permeability and saturation, hence their agreement with core measurements. The field application of the new method in the Hugoton gas field verifies the reliability and accuracy of the new interpretation method.

### 9.2.6 Bayesian Hypothesis Testing: Integrating Fast Well-Log Forward Modeling to Validate Petrophysical Rock Typing and to Quantify Uncertainty in Deepwater Reservoirs

i. The Bayesian rock typing method effectively reduces shoulder-bed effects on well logs, thereby mitigating the uncertainty in rock typing across thinly bedded formations. A probabilistic method was introduced and successfully verified for describing hybrid rock classes.
ii. The application of the Bayesian rock typing method to a field case indicated more than 77% agreement between log- and core-derived rock types. Overall, the correlation between predicted permeability and core-measured permeability

was improved by approximately 16% compared to conventional deterministic methods.

iii. The Bayesian rock typing method quantified the uncertainty associated with rock-type identification and permeability estimation. The final distribution of maximum-likelihood rock types was consistent with the geological framework, and it provided useful information for stratigraphic reservoir construction and modeling.

iv. Computational performance can be a limitation when implementing the Bayesian rock typing method in field studies because heavy data processing is required. However, the method remains accurate and reliable for detailed reservoir description in deepwater field developments where only a few wells are available.

### 9.2.7 Multi-Scale Orthogonal Rock Class Decomposition: Top-Down Reservoir Characterization Integrating Logs and Core in Tight Gas Sands

i. A new petrophysical rock typing workflow has been developed to describe heterogeneous reservoirs. The workflow synthesizes rock class decomposition techniques at multiple measurements scales and follows a top-down approach to describe the intrinsic mixture of rock properties.

ii. Petrophysical zonation based on bed-boundary detection and optimization ensures minimum shoulder-bed effects on well logs. We proposed a volumetric-based hybrid rock class description method that simultaneously honors physical mixing laws in a parallel-stacking of basis rock types.

iii. Pre-invasion and post-invasion log modeling suggests that the most relevant attributes for log-based rock typing are neutron-density crossover, deep resistivity, and NMR-derived capillary bound water in the field example.

iv. The integrative petrophysical workflow was applied to tight-gas sand units in the Bonner and York members of the Bossier Formation, Upper Jurassic Cotton Valley Group in the East Texas Basin. Estimated storage and flow capacities agreed with routine core data when compared to up-scaled cumulative storage and flow profiles.

v. The new method is fundamentally different from conventional approaches that perform depth-by-depth deterministic rock classification based on apparent well logs. Furthermore, the new interpretation workflow is generally applicable to other conventional reservoir types, including turbidites and carbonates. The reversed workflow implies a bottom-up or upscaling approach to construct a quantitative reservoir model for reserves estimation and production forecasting.

### 9.2.8 General Conclusions

In this section, we answer the three questions raised at the beginning of this dissertation.

- **How can petrophysical rock classification improve reservoir description?**

  When petrophysical rock type is firmly anchored on pore geometry resulting from depositional and diagenetic processes, it relates all static and dynamic petrophysical properties and connects to the geological framework. A scientific petrophysical rock classification incorporating core and log data enhances reservoir description in many aspects, including (relative) permeability modeling, saturation-height analysis, facies interpretation, dynamic petrophysical modeling, uncertainty quantification, petrophysical upscaling, and production forecasting.

- **Why should core and log data be integrated to achieve this goal?**

Core and logs complement each other in their measurement scale, accuracy, and coverage. Core data focus on inch-scale and highly-accurate measurements, but they have limited reservoir coverage. Log data have more reservoir coverage, but they are acquired on foot-scale and subjected to many operational issues. In addition, log data mostly measure rock physical properties instead of petrophysical properties. A thorough understanding of log responses for each core-established rock type is critical in classifying rock types from well logs. In heterogeneous reservoirs where rock types intermix at sub-foot scale, core data are particularly important to guide log-based rock typing following different physical mixing laws. Therefore, log-based and core-calibrated rock classification is highly recommended.

- **What type of problem rock classification is in essence: a geological hypothesis, a petrophysical interpretation, a physical model, or a mathematical description?**

The answer is all of them, and I adhere to the order mentioned above. Rock classification should be first treated as a geological hypothesis because nothing is more important than understanding the genesis of rock types. Also, study of rocks from incomplete subsurface data is always a hypothesis-testing procedure. In this regard, sufficient attention should be devoted to the core petrographic descriptions and sedimentary analysis from geologists before undertaking any quantitative work.

Secondly, petrophysical interpretation plays an important role in both core and log analysis. Different petrophysical quantities should be used to describe "pore geometry", which itself is a loosely defined term. For example, this

dissertation investigates many attributes, including pore size, pore throat size, pore morphology, pore volume, pore connectivity, fluid saturation and distribution from core data, and then transfers the physical understanding of these attributes to well logs by numerical pore-level modeling and well-log simulations.

Thirdly, physical modeling is indispensible in bridging the understandings of rock types on core scale and log scale. Well logs measure physical properties of rocks, whereas core data focus more directly on petrophysical properties. It is therefore necessary to predict the physical log responses to those petrophysical properties before performing log-based rock typing.

Finally, it is a mathematical description when it comes to using classification or clustering algorithms to optimally separate entire rock populations into different groups based on single or multiple rock attributes. This is also an important step, but it should never be done before the previous steps.

## 9.3 RECOMMENDATIONS

This dissertation investigated a list of fundamental issues in petrophysical rock classification and developed scientific approaches for integrating core data and well logs to describe reservoir rock-fluid systems. It by no means intends to approach all rock-classification-related challenges raised by the industry because new resource types continue to emerge and advanced tool measurements become available. Here below, I tentatively suggest a list of possible research projects that could expand the technical topics investigated in this dissertation:

i. Development of new rock classification schemes for unconventional reservoirs, particularly gas-bearing shale and coalbed methane, which have different storage and flow mechanisms from those of conventional reservoir types discussed in this dissertation. Of particular interest is the understanding of core and log measurements of rock geochemical and geomechanical properties to assess maturity and fracturability of these source rocks.

ii. Rock typing based on a combination of LWD logs to enable real-time reservoir quality analysis, facies interpretation, and well placement and geo-steering to facilitate early interactions between geoscientists and drilling engineers.

iii. Quantitative incorporation of high-resolution image logs to provide high-fidelity rock type distributions comparable to core description.

iv. Incorporation of NMR logs to probe pore geometry in more detail with consideration of thin-bed mixing and invasion-induced fluid effects.

v. Inclusion of sonic waveform data for characterizing secondary porosity, fractures, and geomechanical properties, which are not considered in this dissertation.

vi. Calibration and validation of rock typing at the flow-unit scale using production surveillance and well testing data. This work could provide reservoir model conditioning before running reservoir simulation.

vii. Challenges posed by horizontal/deviated wells or dipping layers in well-log interpretation are also confronted in log-based rock typing. Advanced log-modeling techniques dealing with 3D earth models and anisotropy are indispensible for rock typing in these types of formations.

viii. Use of a variable number of Gaussian modes to model pore-size distributions. Rocks of trimodal pore-size distribution are commonly observed in carbonate reservoirs. In some extreme cases, rocks of unimodal, bimodal, and trimodal pore-size distributions may coexist in the same reservoir.

ix. Use of different pore-scale models to define petrophysical orthogonality.

x. Consideration of wettability in pore network modeling. Oil-bearing carbonate reservoirs are often found to be preferentially oil-wet or mixed-wet.

xi. Modeling fluid distributions in pore networks during imbibition cycles to assess residual hydrocarbon saturation in different rock types.

xii. Rock typing in challenging field cases that exhibit combined complexities including thin beds, invasion, and capillary transitions.

xiii. Application of rock typing in integrated multi-disciplinary field studies. Of particular interest is the potential use of rock types in geostatistical reservoir modeling.

xiv. Interpretation of diagenetic facies based on petrophysical rock classification.

xv. Investigation of correlation between petrophysical rock types and seismic facies to enable propagation of petrophysical properties in 3D reservoir models constrained by seismic amplitude data.

xvi. Consideration of anisotropy for rock classification.

xvii. Comparison of different classification and clustering methods in their accuracy and reliability for classifying rock types after complete understanding of the geology, petrophysics, and physics associated with core and log data.

# Appendix A: Formulation of the Inverse Problem to Estimate a Bimodal Gaussian Pore-Size Distribution from MICP Data

The evaluation of a bimodal Gaussian pore-size distribution from MICP data is performed by minimizing the quadratic cost function:

$$Q(X) = \left\| W_s \bullet [S_w(X) - S_{w,m}] \right\|_2^2 + \alpha^2 \left\| X \right\|_2^2, \tag{A.1}$$

where $S_w(X)$ is the modeled wetting-phase saturation that is equivalent to the CDF described in Eq. (2.2), $S_{w,m}$ is the measured wetting-phase saturation from MICP data, $W_s$ is a data-weighting matrix, α is a regulation (stabilization) parameter, and vector $X$ contains the six Gaussian attributes, expressed as:

$$X = [w_1, \log \mu_1, \log \sigma_1, w_2, \log \mu_2, \log \sigma_2]^T, \tag{A.2}$$

subject to

$$w_1 + w_2 = 1.0, \tag{A.3}$$

and

$$w_i > 0. \tag{A.4}$$

The superscript $T$ in Eq. (A.2) indicates transpose.

# Appendix B: Inverted Gaussian Attributes for 33 Core Samples with MICP in the Hugoton Gas Field

The inversion method was implemented to estimate bimodal Gaussian pore-size distributions from 33 MICP curves. Table B.1 lists all Gaussian attributes together with total porosity, permeability, and irreducible water saturation (at $P_c$ = 1000 psi) for each core sample.

**Table B.1:** Gaussian attributes, total porosity, permeability, and irreducible water saturation for 33 core samples with MICP from the Hugoton gas field, Kansas.

| Sample No. | $w_1$ (frac) | $w_2$ (frac) | $\mu_1$ (μm) | $\mu_2$ (μm) | $\log\sigma_1$ | $\log\sigma_2$ | $\Phi_t$ (frac) | $k$ (mD) | $S_{wirr}$ (frac) |
|---|---|---|---|---|---|---|---|---|---|
| 1 | 0.680 | 0.320 | 2.230 | 0.209 | 0.098 | 0.713 | 0.187 | 15.681 | 0.112 |
| 2 | 0.554 | 0.446 | 1.079 | 0.092 | 0.019 | 0.682 | 0.098 | 0.376 | 0.233 |
| 3 | 0.372 | 0.628 | 3.304 | 0.303 | 0.206 | 0.626 | 0.156 | 5.728 | 0.154 |
| 4 | 0.562 | 0.439 | 8.025 | 0.545 | 0.173 | 0.954 | 0.125 | 29.712 | 0.116 |
| 5 | 0.657 | 0.343 | 0.495 | 0.077 | 0.299 | 0.792 | 0.076 | 0.110 | 0.201 |
| 6 | 0.360 | 0.640 | 1.500 | 0.080 | 0.500 | 0.050 | 0.134 | 0.774 | 0.671 |
| 7 | 0.650 | 0.350 | 2.993 | 0.651 | 0.175 | 0.551 | 0.237 | 28.284 | 0.044 |
| 8 | 0.538 | 0.462 | 0.677 | 0.134 | 0.213 | 0.486 | 0.142 | 0.774 | 0.196 |
| 9 | 0.652 | 0.348 | 0.182 | 0.055 | 0.137 | 1.307 | 0.111 | 0.246 | 0.275 |
| 10 | 0.585 | 0.415 | 2.933 | 0.402 | 0.158 | 0.856 | 0.188 | 19.771 | 0.109 |
| 11 | 0.308 | 0.692 | 2.016 | 0.292 | 0.247 | 0.797 | 0.189 | 13.885 | 0.217 |
| 12 | 0.710 | 0.290 | 3.184 | 0.694 | 0.101 | 0.885 | 0.194 | 30.500 | 0.056 |
| 13 | 0.722 | 0.278 | 3.243 | 0.512 | 0.078 | 1.048 | 0.224 | 65.302 | 0.070 |
| 14 | 0.794 | 0.207 | 3.244 | 0.353 | 0.071 | 1.199 | 0.261 | 102.711 | 0.066 |
| 15 | 0.998 | 0.002 | 0.052 | 0.024 | 0.767 | 0.011 | 0.131 | 0.010 | 0.648 |
| 16 | 0.629 | 0.371 | 0.310 | 0.094 | 0.199 | 0.724 | 0.095 | 0.031 | 0.217 |
| 17 | 0.868 | 0.132 | 0.220 | 0.069 | 0.498 | 3.397 | 0.048 | 0.002 | 0.300 |
| 18 | 0.565 | 0.435 | 2.416 | 0.343 | 0.194 | 0.753 | 0.160 | 5.850 | 0.099 |
| 19 | 0.483 | 0.518 | 1.261 | 0.300 | 0.112 | 0.549 | 0.157 | 1.951 | 0.109 |
| 20 | 0.353 | 0.648 | 1.479 | 0.216 | 0.158 | 0.750 | 0.093 | 0.428 | 0.220 |
| 21 | 0.513 | 0.487 | 1.589 | 0.230 | 0.133 | 0.757 | 0.123 | 1.537 | 0.155 |
| 22 | 0.758 | 0.242 | 0.366 | 0.027 | 0.297 | 0.889 | 0.089 | 0.048 | 0.228 |
| 23 | 0.568 | 0.433 | 0.410 | 0.059 | 0.351 | 0.801 | 0.129 | 0.357 | 0.308 |
| 24 | 0.683 | 0.317 | 0.295 | 0.045 | 0.207 | 0.703 | 0.123 | 0.065 | 0.254 |
| 25 | 0.497 | 0.503 | 0.667 | 0.223 | 0.154 | 0.428 | 0.161 | 0.496 | 0.109 |
| 26 | 0.372 | 0.628 | 0.441 | 0.055 | 0.144 | 0.612 | 0.122 | 0.061 | 0.426 |
| 27 | 0.947 | 0.053 | 0.029 | 0.011 | 0.139 | 0.016 | 0.096 | 0.002 | 1.000 |
| 28 | 0.533 | 0.467 | 0.614 | 0.011 | 0.170 | 1.113 | 0.103 | 0.136 | 0.371 |
| 29 | 0.574 | 0.426 | 0.779 | 0.061 | 0.213 | 0.519 | 0.127 | 0.553 | 0.287 |
| 30 | 0.123 | 0.877 | 0.022 | 0.011 | 0.165 | 0.029 | 0.035 | 0.001 | 1.000 |
| 31 | 0.550 | 0.450 | 0.059 | 0.048 | 0.622 | 0.213 | 0.072 | 0.009 | 0.843 |
| 32 | 0.710 | 0.291 | 0.102 | 0.028 | 0.163 | 0.724 | 0.076 | 0.014 | 0.690 |
| 33 | 0.430 | 0.570 | 0.406 | 0.125 | 0.046 | 0.490 | 0.061 | 0.023 | 0.266 |

# Appendix C: Interfacial Tension and Contact Angle for Different Fluid Systems

The conversion between capillary pressure and pore-throat size is by using Laplace's equation (Peters, 2012):

$$P_c = \frac{2\Gamma|\cos\theta|}{R}, \tag{C.1}$$

where $R$ is pore-throat radius, $\Gamma$ is interfacial tension, and $\theta$ is contact angle. The values of term $\Gamma|\cos\theta|$ used for different fluid systems at both laboratory and reservoir conditions in this dissertation are given in Table C.1.

**Table C.1:** Values of interfacial tensions and contact angles for mercury-air, oil-brine, and gas-brine fluid systems at both laboratory and reservoir conditions (Archer and Wall, 1986).

| **Condition** | **Fluid System** | $\Gamma$ **(dyne/cm)** | $\theta$ ($^0$) | $\Gamma\lvert\cos\theta\rvert$ **(dyne/cm)** |
|---|---|---|---|---|
| **Laboratory** | Mercury-Air | 480 | 140 | 372 |
| | Oil-Brine | 48 | 30 | 42 |
| | Gas-Brine | 72 | 0 | 72 |
| **Reservoir** | Mercury-Air | -- | -- | -- |
| | Oil-Brine | 30 | 30 | 26 |
| | Gas-Brine | 50 | 0 | 50 |

# Appendix D: NMR Echo Decay Signal Simulation with a Cubic Pore-Work Model

For a simple cubic pore-network model with quantified fluid distribution, the NMR echo decay signal $A(t)$ can be simulated by adding the magnetization decay originating from each individual pore body:

$$A(t) = \sum_{i}^{n} A_i e^{-t/T_{2i}}, \tag{D.1}$$

where $A_i$ is the initial signal amplitude for each single pore which is determined by the pore volume and the hydrogen index of fluids, $T_{2i}$ is the transverse relaxation time of each single pore which is quantified as (Coates et al., 1999)

$$\frac{1}{T_{2i}} = \frac{1}{T_{2iS}} + \frac{1}{T_{2iB}} + \frac{1}{T_{2iD}}, \tag{D.2}$$

where $T_{2iS}$ is surface relaxation time, $T_{2iB}$ is bulk relaxation time, and $T_{2iD}$ is diffusion relaxation time. For pores occupied by water, surface and bulk relaxations dominate while diffusion relaxation is negligible, i.e.,

$$\frac{1}{T_{2i}} \approx \frac{1}{T_{2iS}} + \frac{1}{T_{2iB}}, \tag{D.3}$$

For pores occupied by gas, diffusion relaxation needs to be considered as well.

# Acronyms, Nomenclature, and Greek Symbols

**ACRONYMS**

| | | |
|---|---|---|
| 2D | : | Two-Dimensional |
| 3D | : | Three-Dimensional |
| AIT | : | Array Induction Tool |
| API | : | American Petroleum Institute |
| BRT | : | Basis Rock Type |
| BVW | : | Bulk Volume of Water |
| CBW | : | Capillary Bound Water |
| CDF | : | Cumulative Distribution Function |
| CPU | : | Computer Processing Unit |
| CSF | : | Common Stratigraphic Framework |
| DIT | : | Dual-Induction Tool |
| DOI | : | Depth of Investigation |
| ERF | : | Gaussian Error Function |
| FWL | : | Free Water Level |
| FZI | : | Flow Zone Index |
| G-W | : | Gas-Water |
| GWC | : | Gas-Water Contact |
| HAFWL | : | Height Above Free Water Level |
| HRC | : | Hybrid Rock Class |
| IF | : | Invasion Facies |
| IFM | : | Invasion Facies Modeling |
| K | : | Potassium |
| KGS | : | Kansas Geological Survey |
| LPSA | : | Laser Particle Size Analyzer |
| LWD | : | Logging While Drilling |
| MGS | : | Mean Grain Size |

| | | |
|---|---|---|
| MICP | : | Mercury Injection Capillary Pressure |
| NaCl | : | Sodium Chloride |
| N-D | : | Neutron-Density |
| NMR | : | Nuclear Magnetic Resonance |
| OBM | : | Oil-Base Mud |
| ORC | : | Orthogonal Rock Class |
| OWC | : | Oil-Water Contact |
| ppm | : | Parts Per Million |
| PSD | : | Pore-Size Distribution |
| p.u. | : | Porosity Unit |
| RBLM | : | Log-Mean Pore-Body Size |
| RCA | : | Routine Core Analysis |
| RFN | : | Rock Fabric Number |
| RQ | : | Reservoir Quality |
| RQI | : | Leverett's Reservoir Quality Index |
| RRT | : | Reservoir Rock Type |
| RT | : | Rock Type |
| SNUPAR | : | Schlumberger Nuclear Parameter Code |
| SOBM | : | Synthetic Oil-Base Mud |
| SP | : | Spontaneous Potential |
| STP | : | Standard Temperature and Pressure |
| T2LM | : | Log-Mean Transverse Relaxation Time |
| TCF | : | Trillion Cubic Feet |
| Th | : | Thorium |
| TVD | : | True Vertical Depth |
| U | : | Uranium |
| UTAPWeLS | : | University of Texas at Austin's Petrophysical and Well-Log Simulator |
| WBM | : | Water-Base Mud |

**NOMENCLATURE**

| | | |
|---|---|---|
| $a$ | : | Linear coefficient in empirical $J$ function, [] |
| $A$ | : | NMR echo decay signal amplitude, [mV] |
| $b$ | : | Exponent in empirical J function, [] |
| $C$ | : | Contingency coefficient, [] |
| $C_{cl}$ | : | Volumetric concentration of clay, [frac] |
| $C_i$ | : | Volumetric concentration of mineral $i$, [frac] |
| $C_{sh}$ | : | Volumetric concentration of shale, [] |
| $\mathbf{d}$ | : | Vector of observed well logs, [] |
| $e_{nw}$ | : | Experimental exponent for $k_{rnw}$ equation, [] |
| $e_p$ | : | Pore-size distribution exponent, [] |
| $e_w$ | : | Experimental exponent for $k_{rw}$ equation, [] |
| $G$ | : | Thomeer's pore geometrical factor, [] |
| $\mathbf{G}(\bullet)$ | : | Forward function, [] |
| GR | : | Gamma Ray Log, [gAPI] |
| $H$ | : | Height above the free-water level, [ft] |
| $I_{max}$ | : | Maximal iteration number, [] |
| $J$ | : | Leverett's $J$ function, [] |
| $k$ | : | Absolute permeability, [mD] |
| $k_{air}$ | : | Air permeability, [mD] |
| $k_r$ | : | Relative permeability, [] |
| $k_{rg}$ | : | Gas relative permeability, [frac] |
| $k_{rnw}$ | : | Non-wetting phase relative permeability, [] |
| $k_{rw}$ | : | Water relative permeability, [frac] |
| $K$ | : | Number of rock types, [] |
| $L$ | : | Number of rock layers, [] |
| $\mathbf{m}$ | : | Vector of rock type distribution, [] |

| | | |
|---|---|---|
| $m$ | : | Archie's porosity exponent, [] |
| $n$ | : | Archie's saturation exponent, [] |
| $N$ | : | Number of rock samples, [] |
| $NRT$ | : | Number of rock types, [] |
| ORT | : | Orthogonality, [] |
| $p$ | : | Density function of logarithmic pore-throat radius, [] |
| $P$ | : | Cumulative distribution function of logarithmic pore-throat radius, [] |
| PEF | : | Photoelectric Factor Log, [] |
| $P_c$ | : | Capillary pressure, [psi] |
| $P_c^0$ | : | Coefficient for Pc equation, [psi.darcy$^{1/2}$] |
| $P_e$ | : | Entry capillary pressure, [PSI] |
| $p(\mathbf{m})$ | : | A-priori distribution of model parameters, [] |
| $p(\mathbf{d}\|\mathbf{m})$ | : | Conditional probability distribution, [] |
| $q(\mathbf{m}\|\mathbf{d})$ | : | Posterior probability distribution for model parameters, [] |
| $Q$ | : | Quadratic cost function, [] |
| $R$ | : | Pore-throat radius, [μm] |
| $R^2$ | : | Correlation coefficient, [] |
| $R_{35}$ | : | Pore throat radius at 35% non-wetting phase saturation, [μm] |
| $R_b$ | : | Pore-body radius, [μm] |
| $R_{th}$ | : | Pore-throat radius, [μm] |
| $R_w$ | : | Connate water resistivity, [ohm.m] |
| $S$ | : | Pore surface area, [] |
| $S_{gr}$ | : | Residual gas saturation, [frac] |
| $S_g^*$ | : | Gas saturation corrected for hydration water, [frac] |
| $S_{hg}$ | : | Mercury saturation, [frac] |
| $S_{hw}$ | : | Hydrated water saturation, [frac] |
| $S_{or}$ | : | Residual oil saturation, [frac] |
| $S_w$ | : | Wetting Phase or Water saturation, [frac] |

| | | |
|---|---|---|
| $S_{wcrit}$ | : | Critical water saturation, [frac] |
| $S_{wi}$ | : | Initial water saturation, [] |
| $S_{wirr}$ | : | Irreducible water saturation, [frac] |
| $S_w^*$ | : | Normalized water saturation, [frac] |
| $T$ | : | Transpose of a matrix, [] |
| $T_2$ | : | NMR transverse relaxation time, [ms] |
| $T_{2B}$ | : | Bulk relation time, [ms] |
| $T_{2D}$ | : | Diffusion relaxation time, [ms] |
| $T_{2S}$ | : | Surface relaxation time, [ms] |
| T2LM | : | Logarithmic mean of NMR transverse relaxation time, [ms] |
| $V$ | : | Cramer's V, [] |
| $V_i$ | : | Volumetric concentration of rock type I, [] |
| $V_p$ | : | Pore volume, [frac] |
| $w_1$ | : | Fraction of pore volume connected by large pore-throat size, [frac] |
| $w_2$ | : | Fraction of pore volume connected by small pore-throat size, [frac] |
| $W_s$ | : | Weighting matrix, [] |
| $X$ | : | Gaussian attributes vector, [] |
| $x$ | : | Coefficient of permeability in rock quality, [] |
| $y$ | : | Coefficient of porosity in rock quality, [] |
| $z$ | : | Constant term in rock quality, [] |

**GREEK SYMBOLS**

| | | |
|---|---|---|
| $\alpha$ | : | Scaling factor in saturation-height modeling, [] |
| $\gamma$ | : | Gamma ray, [gAPI) |
| $\Delta\rho$ | : | Density difference between water and oil, [g/ $cm^3$] |
| $\theta$ | : | Contact angle between wetting and non-wetting phase, [degree] |
| $\lambda$ | : | Regularization parameter, [] |
| $\log \mu_1$ | : | Mean value of the large pore-throat radius Gaussian mode, [μm] |
| $\log \mu_2$ | : | Mean value of the small pore-throat radius Gaussian mode, [μm] |
| $\Gamma$ | : | Interfacial tension between wetting and non-wetting phase, [dyne/cm] |
| $\rho$ | : | Surface relaxivity, [μm/s] |
| $\rho_b$ | : | Bulk density, [g/$cm^3$] |
| $\log \sigma_1$ | : | Standard deviation of the large pore-throat radius Gaussian mode, [μm] |
| $\log \sigma_2$ | : | Standard deviation of the small pore-throat radius Gaussian mode, [μm] |
| $\sigma_t$ | : | Apparent conductivity, [mS/m] |
| $\tau$ | : | Pore network tortuosity, [] |
| $\phi_D$ | : | Density porosity, [frac] |
| $\phi_N$ | : | Neutron porosity, [frac] |
| $\phi_t$ | : | Total porosity, [frac] |
| $\chi^2$ | : | Pearson's chi-squared test, [] |
| $\otimes$ | : | A symbol for quantifying pore-throat size, [μm] |

# References


Ahmadi, M., Sawyers, M., Kenyon-Roberts, S., Stanworth, B., Kugler, K., Kristensen, J., and Fugelli, E., 2003, The Millennium Atlas: Petroleum Geology of the Central and Northern North Sea, Chapter 14, The Geological Society of London.

Akbar, N., Mavko, G., Nur, A., and Dvorkin, J., 1994, Seismic signatures of reservoir transport properties and pore fluid distribution, Geophysics, 59(8): 1222-1236.

Al-Farisi, O., Elhami, M., Al-Felasi, A., and Yammahi, F., 2009, Revelation of carbonate rock typing – the resolved gap, paper SPE 125576 presented at SPE/EAGE Reservoir Characterization and Simulation Conference, Abu Dhabi, UAE, October 19 – 21.

Al-Kharusi, A., and Blunt, M.J., 2007, Network extract from sandstone and carbonate pore space images, Journal of Petroleum Science and Engineering, 56: 219-231.

Al-Tarawneh, K.K., Buzzi, O., Krabbenhoft, K., Lyamin, A.V., and Sloan, S.W., 2009, An indirect approach for correlation of permeability and diffusion coefficients, Defect and Diffusion Forum, (283-286): 504-514.

Altunbay, M., Martain, R., and Robinson, M., 2001, Capillary pressure data from NMR logs and its implications on field economics, paper SPE 71703 presented at the SPE Annual Technical Conference and Exhibition, New Orleans, Louisiana, September 30 – October 3.

Amaefule, J.O., Altunbay, M., Tiab, D., Kersey, D.G., and Keelan, D.K., 1993, Enhanced reservoir description: using core and log data to identify hydraulic (flow) units and predict permeability in uncored intervals/wells, paper SPE 26436 presented at SPE Annual Technical Conference and Exhibition, Houston, Texas, October 3-6.

Archer, J.S., and Wall, C.G., 1986, Petroleum Engineering, Graham & Trotman, London, England.

Archie, G.E., 1950, Introduction to petrophysics of reservoir rocks, AAPG Bulletin, 34 (5): 943 - 961.

Archie, G.E., 1952, Classification of carbonate reservoir rocks and petrophysical considerations, AAPG Bulletin, 36(2): 278-298.

Asquith, G.B., and Gibson, C.R., 1982, Basic Well Log Analysis for Geologists, 1st edition, American Association of Petroleum Geologists Publication.

Aster, R.C., Borchers, B., and Thurber, C.H., 2005, Parameter Estimation and Inverse Problems, Elsevier Academic.

Balhoff, M.T., Thompson, K.E., and Hjortso, M., 2007, Coupling pore-scale networks to continuum-scale models of porous media, Computers & Geosciences, 33(3): 393-410.

Basan, P.B., Lowden, B.D., Whattler, P.R., and Attard, J., 1997, Pore-size data in petrophysics: a perspective on the measurement of pore geometry, Geological Society, London, Special Publications 122: 47-67.

Benson, S.M., and Cole, D.R., 2008, $CO_2$ sequestration in deep sedimentary formations, Elements, 4(5): 325-331.

Bishop, Y.M.M., Fienberg, S.E., and Holland, P.W., 1975, Discrete Multivariate Analysis: Theory and Practice, MIT Press.

Blunt, M.J., 2001, Flow in porous media – pore-network models and multiphase flow, Colloid & Interface Science, 6:197-207.

Blunt, M.J., Jackson, M.D., Piri, M., and Valvatne, P.H., 2002, Detailed physics, predictive capabilities and macroscopic consequences for pore-network models of multiphase flow, Advances in Water Resources, 25:1069-1089.

Bowman, A.P., 2004, Sequence Stratigraphy and Reservoir Characterization in the Columbus Basin, Trinidad, Ph.D. Dissertation, Imperial College London.

BP, 2003, The UK Upstream Asset Portfolio, BP Exploration, Farburn Industrial Estate, Dyce, Aberdeen, U.K.

Brooks, R.H., and Corey, A.T., 1966, Properties of porous media affecting fluid flow, Journal of Irrigation and Drainage Division, 92(2): 61-90.

Bryant S.L., Mellor D.W., and Cade C.A., 1993, Physically representative network models of transport in porous media, American Institute of Chemical Engineers Journal, 39(3): 387-396.

Buckles, R.S., 1965, Correlating and averaging connate water saturation data, Journal of Canadian Petroleum Technology, 9(1): 42-52.

Buiting, J.J.M., 2011, Upscaling saturation-height technology for Arab carbonates for improved transition-zone characterization, SPE Reservoir Evaluation & Engineering, 14(1): 11-24.

Burdine, N.T., 1953, Relative permeability calculations from pore-size distribution data, Journal of Petroleum Technology, 51(3): 71-78.

Byrnes, A.P., 2008, Issues with gas relative permeability in low-permeability sandstones, in S. P. Cumella, K. W. Shanley, and W. K. Camp, eds., Understanding, Exploring, and Developing Tight-Gas Sands — 2005 Vail Hedberg Conference: AAPG Hedberg Series, No. 3, p. 63– 76.

Campbell, C.V., 1967, Lamiae, laminaset, bed and bedset, Sedimentology, 8: 7-26.

Cao Minh, C., and Sundararaman, P., 2011, Nuclear magnetic resonance petrophysics in thin sand/shale laminations, SPE Journal, 16(2): 223-238.

Chang, D., Ioannidis, M.A., and Chatzis, I., 2000, Relationships between non-wetting phase invasion and magnetization evolution connected pore systems as revealed

by network simulation, International Symposium of the Society of Core Analysts, Abu Dhabi, UAE, October 18-20.

Chen, S., Liaw, H.K., and Watson, A.T., 1994, Measurement and analysis of fluid saturation-dependent NMR relaxation and line broadening in porous media, Magnetic Resonance Imaging, 12(2): 201-202.

Chen, S., Qin, F., and Watson, A.T., 2004, Determining fluid saturations during multiphase flow experiments by NMR imaging techniques, American Institute of Chemical Engineers Journal, 40(7), 1238 – 1245.

Childs, E.C., and Collis-George, N., 1950, The permeability of porous materials, Proceedings of the Royal Society A, 201(1066): 392–405.

Choquette, P.W., and Pray, L.C., 1970, Geologic nomenclature and classification of porosity in sedimentary carbonates, AAPG Bulletin, 54 (2): 207-244.

Clerke, E.A., 2009, Permeability, relative permeability, microscopic displacement efficiency, and pore geometry of M_1 Bimodal pore systems in Arab D limestone, SPE Journal, 14(3):524-531.

Clerke, E.A., Mueller, H.W., Phillips, E.C., Eyvazzadeh, R.Y., Jones, D.H., Ramamoorthy, R., and Srivastava, A., 2008, Application of Thomeer hyperbolas to decode the pore systems, facies, and reservoir properties of the Upper Jurassic Arab D limestone, Ghawar field, Saudi Arabia: a "Rosetta Stone" approach, GeoArabia, 13(4): 113-160.

Coates, G.R., Xiao, L., and Prammer, M.G., 1999, NMR Logging Principles and Application, Halliburton Energy Services, Gulf Publishing Company, Houston, Texas.

Comisky, J.T., Newsham, K.E., Rushing, J.A., and Blasingame, T.A., 2007, A comparative study of capillary-pressure-based empirical models for estimating absolute permeability in tight gas sands, paper SPE 110050 presented at SPE Annual Technical Conference and Exhibition, Anaheim, California, November 11-14.

Contreras, A., Torres-Verdín, C., Chesters, W., Kvien, K., and Fasnacht T., 2006, Extrapolation of flow units away from wells with 3D pre-stack seismic amplitude data: field example, Petrophysics, 47(3): 223-238.

Corey, A.T., 1994, Mechanics of Immiscible Fluids in Porous Media, Water Resources Publications, Highland Ranch, Colorado.

Darling, T., 2005, Well Logging and Formation Evaluation, Gulf Professional Publishing.

Diniz-Ferreira, E.L., and Torres-Verdín, C., 2012, Improved estimation of pore connectivity and permeability in deepwater carbonates with construction of multi-layer static and dynamic petrophysical models, SPWLA 53rd Annual Logging Symposium, Cartagena, Colombia, June 16-20.

Diaz, C.E., Chatzis, I., and Dullien, F.A.L., 1986, Simulation of capillary pressure curves using bond correlated site percolation on a simple cubic network, Transport in Porous Media, 2(3): 215-240.

Doveton, J.H., 2012, Mathematical Petrophysics. Personal communication.

Dubois, M.K., Byrnes, A.P., Bhattacharya, S., Bohling, G.C., Doveton J.H., and Barba, R.E., 2006, Hugoton Asset Management Project (HAMP): Hugoton Geomodel Final Report. Kansas Geologic Survey Open File Report.

Dullien, F.A.L., 1979, Porous Media, Fluid Transport and Pore Structure. New York: AP Press.

Dunham, R. J., 1962, Classification of Carbonate Rocks According to Depositional Texture, in Ham, W. E. ed., Classification of Carbonate Rocks, American Association of Petroleum Geologists, Memoir 1, 108-121.

Endres, A.L., and Knight, R., 1991, The effects of pore-scale fluid distribution on the physical properties of partially saturated tight sandstones, Journal of Applied Physics, 69(2): 1091-1098.

Fisher, W.L., 1982, Depositional systems and environments, in Encyclopedia of Science and Technology: New York, McGraw-Hill, 5th ed., 104-108.

Freedman, R., and Heaton, N., 2004, Fluid characterization using nuclear magnetic resonance logging, Petrophysics, 45(3): 241-250.

Gandhi, A., Torres-Verdín, C., Voss, B., Gabulle, J., and Seminario F., 2010, Construction of reliable static and dynamic multi-layer petrophysical models in Camisea gas reservoirs, Peru, SPWLA 51st Annual Logging Symposium, Perth, Australia, June 19 - 23.

Gao, B., Wu, J., Chen, S., Kwak, H., and Funk, J., 2011, New method for predicting capillary pressure curves from NMR data in carbonate rocks, SPWLA 52nd Annual Logging Symposium, Colorado Springs, Colorado, May 14 - 18.

Garrouch, A.A., and Sharma, M.M., 1995, Dielectric properties of partially saturated rocks, Energy & Fuels, 9(3): 413-419.

Genty, C., Jensen, J.L., and Ahr, W.M., 2007, Distinguishing carbonate reservoir pore facies with nuclear magnetic resonance measurements, Natural Resources Research, 16(1): 45-54.

George, B.K., Torres-Verdín, C., Delshad, M., Sigal, R., Zouioueche, F., and Anderson, B., 2003, A case study integrating the physics of mud-filtrate invasion with the physics of induction logging: assessment of in-situ hydrocarbon saturation in the presence of deep invasion and highly saline connate water, SPWLA 44th Annual Logging Symposium, Galveston, Texas, June 22 – 25.

Geweke, J., 1991, Evaluating the accuracy of sampling-based approaches to the calculation of posterior moments: Federal Reserve Bank of Minneapolis, Research Department Staff Report 148.

Glover, P.W.J., Zadjali, I.I., and Frew, A., 2006, Permeability prediction from MICP and NMR data using an electrokinetic approach, Geophysics, 71(4): F49-F60.

Gunter, G.W., Pinch, J.J., Finneran, J.M., and Bryant, W.T., 1997a, Overview of an integrated process model to develop petrophysical based reservoir descriptions, paper SPE 38748 presented at the SPE Annual Technical Conference and Exhibition, San Antonio, Texas, October 5-8.

Gunter, G.W., Finneran, J.M., Hartmann, D.J., and Miller, J.D., 1997b, Early determination of reservoir flow units using an integrated petrophysical method, paper SPE 38679 presented at the SPE Annual Technical Conference and Exhibition, San Antonio, Texas, October 5-8.

Hahsler, M., and Hornik, K., 2011, Dissimilarity plots: a visual exploration tool for partitional clustering, Journal of Computational and Graphical Statistics, 20(2): 335-354.

Handy, L.L., and Datta, P., 1966, Fluid distributions during immiscible displacements in porous media, SPE Journal, 6(3): 261-266.

Heidari, Z., Hamman, J., Day, P., Gorney, D., and Alfred, D., 2011, Assessment of movable gas saturation and rock typing based on the combined simulation of petrophysical borehole measurements, SPWLA 52nd Annual Logging Symposium, Colorado Springs, Colorado, May 14 – 18.

Heidari, Z., and Torres-Verdín, C., 2010, Estimation of dynamic petrophysical properties of water-bearing sands invaded with oil-base mud from multi-physics borehole geophysical measurements, Presented at Society of Exploration Geophysicists 80th Annual International Meeting, Denver, Colorado, October 17 - 22.

Heidari, Z., Torres-Verdín, C., Mendoza, A., and Wang, G.L. 2011, Assessment of residual hydrocarbon saturation with the combined quantitative interpretation of resistivity and nuclear logs, Petrophysics, 52 (3): 217 - 237.

Heidari, Z., Torres-Verdín, C., and Preeg, W.E., 2012, Improved estimation of mineral and fluid volumetric concentrations in thinly bedded and invaded formations, Geophysics, 77 (3): WA79 – WA98.

Hidajat, I., Mohanty, K.K., Flaum, M., and Hirasaki, G., 2004, Study of vuggy carbonates using X-ray CT scanner and NMR, SPE Reservoir Evaluation & Engineering, 7(5): 365-377

Hill, H.J., Shirley, O.J., and Klein, G.E., 1979, Edited by Waxman, M.H., and Thomas E.C., Bound water in shaly sands – its relation to $Q_v$ and other formation parameters, The Log Analyst May-June: 3 -19.

Hirasaki, G.J., 2009, Flow and transport in porous media I: geology, chemistry and physics of fluid transports, Unpublished Rice University Lecture Notes.

Hou, J., Mallan, R. K., and Torres-Verdín, C., 2006, Finite-difference simulation of borehole EM measurements in 3D anisotropic media using coupled scalar-vector potentials, Geophysics, 71(5): 225-233.

Huang, D.D., Honarpour, M.M., and Al-Hussainy, R., 1997, An improved model for relative permeability and capillary pressure incorporating wettability, International Symposium of Society of Core Analysts, Calgary, Canada, September 7-10.

Ijasan, O., Torres-Verdín, C., Preeg, W., and Mendoza, A., 2010, Rapid modeling of LWD nuclear measurements acquired in high-angle and horizontal wells for improved petrophysical and geometrical interpretation, SPWLA 52nd Annual Logging Symposium, Colorado Springs, Colorado, May 14 - 18.

Jin, G., Torres-Verdín, C., Radaelli, F., and Rossi, E., 2007, Experimental validation of pore-level calculations of static and dynamic petrophysical properties of clastic rocks, paper SPE 109547 presented at SPE Annual Technical Conference and Exhibition, Anaheim, California, November 11-14.

John, A.K., Lake, L.W., Torres-Verdín, C., and Srinivasan, S., 2008, Seismic facies identification and classification using simple statistics, SPE Reservoir Evaluation & Engineering, 11(6):984-990.

Jorand, R., Klitzsch, N., Mohnke, O., Clauser, C., Schleifer, N., and de Wijn, B., 2011. Deducing relative permeability of tight gas rocks from NMR measurements. American Geophysical Union, Fall Meeting 2011, abstract #H31D-1193.

Kerans, C., and Tinker, S., 1999, Sequence stratigraphy and characterization of carbonate reservoirs, SEPM Short Course no. 40.

Kharrat, R., Mahdavi, R., Bagherpour, H., and Hejri, S., 2009, Rock type and permeability prediction of a heterogeneous carbonate reservoir using artificial neural networks based on flow zone index approach, paper 120166 presented at SPE Middle East Oil and Gas Show and Conference, Bahrain, March 15-18.

Kirkpatrick, S., 1971, Classical transport in disordered media: scaling and effective medium theories, Physical Review Letters, 27: 1722-1725.

Knight, R., 1991, Hysteresis in the electrical resistivity of partially saturated sandstone, Geophysics, 56(12): 2139-2147.

Knight, R., and Nolen-Hoeksema R., 1990, A laboratory study of the dependence of elastic wave velocities on pore scale fluid distribution, Geophysical Research Letters, 17(10): 1529-1532.

Kumar, M., Senden, T., Knackstedt, M.A., Latham, S.J., Pinczewski, V., Sok, R.M., Sheppard, A.P., and Turner, M.L., 2009, Imaging of pore scale distribution of fluids and wettability, Petrophysics, 50(4): 311-321.

Lake, L.W., 1996, Enhanced Oil Recovery, 1st Edition, Prentice Hall.

La Vigne, J., Barber, T., and Bratton, T., 1997, Strange invasion profiles : what multiarray induction logs can tell us about how oil-based mud affects the invasion process and wellbore stability, SPWLA 38th Annual Logging Symposium, Houston, Texas, June 15-18.

Leverett, M.C., 1941, Capillary behavior in porous solids, Transactions of the AIME, 142: 159–172.

Li, P., 1997, Nuclear Magnetic Resonance Imaging of Fluid Displacements in Porous Media, Ph.D. dissertation, The University of Texas at Austin.

Liaw, H.K., Kulkarni, R., Chen, S., and Watson, A.T., 1996, Characterization of fluid distributions in porous media by NMR techniques, American Institute of Chemical Engineers Journal, 42(2): 538-546.

Liu, S., Spain, D.R., Devier, C., Buller, D., and Murphy, E., 2011, Integrated petrophysical study in North American Cotton Valley tight gas sand: Cotton Valley formation, East Texas, SPWLA 52nd Annual Logging Symposium, Springs, Colorado, May 14 - 18.

Liu, S., Spain, D.R., and Dacy, J.J.M., 2012, Beyond volumetrics: petrophysical characterization using rock types to predict dynamic flow behavior in tight gas sands, SPWLA 53rd Annual Logging Symposium, Cartagena, Colombia, June 16 – 20.

Liu, Z., Torres-Verdín, C., Wang, G. L., Mendoza, A., Zhu, P., and Terry, R., 2007, Joint inversion of density and resistivity logs for the improved petrophysical assessment of thinly-bedded clastic rock formations, SPWLA 48th Annual Logging Symposium, Austin, Texas, June 3-6.

Lucia, F.J., 1995, Rock-fabric/petrophysical classification of carbonate pore space for reservoir characterization, AAPG Bulletin, 79(9): 1275– 1300.

Lucia, F.J., 1999, Carbonate Reservoir Characterization, Springer-Verlag, Berlin.

Marschall, D., Gardner, J.S., Mardon, D., and Coates, G.R., 1995, Method for correlating NMR relaxometry and mercury injection data, International Symposium of Society of Core Analysts, San Francisco, California, September 7-10.

Martin, A.J., Robertson, D., Wreford, J., and Lindsay, A., 2005, High-accuracy oriented perforating extends the sand-free production life of Andrew field, paper SPE 93639 presented at Offshore Europe Conference, Aberdeen, United Kingdom, September 6 - 9.

Mendoza, A., Torres-Verdín, C., and Preeg, W. E., 2007, Rapid simulation of borehole nuclear measurements with approximate spatial flux-scattering functions, SPWLA 48th Annual Logging Symposium, Austin, Texas, June 3-6.

Mendoza, A., Torres-Verdín, C., and Preeg, W. E., 2010, Linear iterative refinement method for the rapid simulation of borehole nuclear measurements, Part I: vertical wells, Geophysics, 75(1): E9-E29.

Miranda, L.J., Torres-Verdín, C., and Lucia, J., 2009, Modeling mud-filtrate invasion effects on resistivity logs to estimate permeability of vuggy and fractured carbonate formations, paper SPE 121136 presented at SPE 2008 EUROPEC Conference, Amsterdam, The Netherlands, June 8 – 11.

Mohanty, K.K., 1981, Fluids in Porous Media: Two-Phase Distribution and Flow, Ph.D. dissertation, University of Minnesota.

Mohanty, K.K., and Salter, S.J., 1982, Multiphase flow in porous media: II. pore-level modeling, paper SPE 11018 presented at SPE Annual Technical Conference and Exhibition, New Orleans, Louisiana, September 26-29.

Muto, T., Steel, R., and Swenson, J., 2007, Autostratigraphy: a framework norm for genetic stratigraphy, Journal of Sedimentary Research, 77: 2-12.

Neasham, J.W., 1977, The morphology of dispersed clay in sandstone reservoirs and its effect on sandstone shaliness, pore space and fluid flow properties, paper SPE 6858 presented at the SPE Annual Fall Technical Conference and Exhibition, Denver, Colorado, October 9-12.

Newsham, K.E., Rushing, J.A., Chaouche, A., and Bennion, D.B., 2002, Laboratory and field observations of an apparent sub capillary-equilibrium water saturation distribution in a tight gas sand reservoir, paper SPE 75710 presented at the SPE Gas Technology Symposium, Calgary, Alberta, Canada, April 30 – May 2.

Nimmo, J.R., 2004, Porosity and pore size distribution, in Encyclopedia of Soils in the Environment, London, Elsevier 3: 295-303.

Olson, T.M., Babcock, J.A., Prasad, K.V.K., Boughton, S.D., Wagner, P.D., Franklin, M.K., and Thompson, K.A., 1997. Reservoir characterization of the giant Hugoton gas field, Kansas, AAPG Bulletin, 81(11):1785-1803.

Oren, P.E., Bakke, S., and Arntzen, O.J., 1998, Extending predictive capabilities to network models, SPE Journal, 3(4): 324-336.

Parnell, J., and Schwab, A., 2003, Seismic evidence for the distribution and migration of fluids in sedimentary basins, Geofluids, 3(4): 213-217.

Patzek, T.W., 2001, Verification of a complete pore network simulator of drainage and imbibition, SPE Journal, 6(2): 144-156.

Peters, E.J., 2012, Advanced Petrophysics – Volumes 1 and 2, Greenleaf Book Group, Austin, Texas.

Peters, E.J., and Hardham, W.D., 1990, Visualization of fluid displacements in porous media using computed tomography imaging, Journal of Petroleum Science and Engineering, 4(2): 155-168.

Pirson, J.S., 1983, Geologic Well Log Analysis. Third Edition, Gulf Professional Publishing.

Pittman, E.D., 1992, Relationship of porosity and permeability to various parameters derived from mercury injection-capillary pressure curves for sandstone, AAPG Bulletin, 76 (2): 191 -198.

Pour, R.A., 2011, Development and Application of a 3D Equation-of-State Compositional Fluid-Flow Simulator in Cylindrical Coordinates for Near-Wellbore Phenomena, Ph.D. Dissertation, The University of Texas at Austin.

Pour, R.A., Torres-Verdín, C., and Sepehrnoori, K., 2011, Quantifying wettability alteration during oil-base mud-filtrate invasion and corresponding effects on resistivity logs, SPWLA 52nd Annual Logging Symposium, Colorado Springs, May 14 - 18.

Press, W.H., Teukolsky S.A., Vetterling, W.T., and Flannery, B.P., 2007, Section 16.1: Gaussian mixture models and k-Means clustering, Numerical Recipes, The Art of Scientific Computing, 3rd Ed., New York: Cambridge University Press.

Prodanovic, M., and Bryant, S.L., 2006, A level set method for determining critical curvatures for drainage and imbibition, Journal of Colloid and Interface Science, 304(2): 171-184.

Purcell, W.R., 1949, Capillary pressures - their measurement using mercury and the calculation of permeability, Trans. AIME, 186 (1949), 39-48.

Rushing, J.A., Newsham, K.E., and Blasingame, T.A., 2008, Rock typing – keys to understanding productivity in tight gas sands, paper SPE 114164 presented at SPE Unconventional Reservoirs Conference, Keystone, Colorado, February 10-12.

Salazar, J.M., 2004, Assessment of Permeability from Well Logs on Core Calibration and Simulation of Mud-Filtrate Invasion, Master's thesis, The University of Texas at Austin.

Salazar, J.M., Malik, M., Torres-Verdín, C., Wang, G.L., and Duan, H.Y., 2007, Fluid density and viscosity effects on borehole resistivity measurements acquired in the presence of oil-based mud and emulsified surfactants, paper SPE 109946 presented at SPE Annual Technical Conference and Exhibition, Anaheim, California, November 11 - 14.

Salazar, J.M., Torres-Verdín, C., Alpak, F.O., Habashy, T.M., and Klein, J.D., 2006, Estimation of permeability from borehole array induction measurements:

application to the petrophysical appraisal of tight-gas sands, Petrophysics, 47(6): 527-544.

Serra, O., and Abbott, H.T., 1980, The contribution of logging data to sedimentology and stratigraphy, paper 9270 presented at 55th SPE Annual Fall Technical Conference and Exhibition, Dallas, Texas.

Serra, O., and Serra, L., 2003, Well Logging and Geology. Technip.

Serra, O., and Sulpice, L., 1975, Sedimentological analysis of shale-sand series from well logs, SPWLA 16th Annual Logging Symposium, Jun 4-7.

Sigal, R., 2002, Coates and SDR permeability: two variations on the same theme, Petrophysics, 43(1): 38-46.

Silin, D., Tomutsa., L., Benson, S.M., and Patzek, T.W., Microtomography and pore-scale modeling of two-phase fluid distribution, Transport in Porous Media, 86(2): 495-515.

Slatt, R.M., 2007, Stratigraphic Reservoir Characterization for Petroleum Geologists, Geophysicists, and Engineers, Elsevier Publication.

Spain, D.R., Liu, S., and Devier, C., 2011, Petrophysical rock typing in tight gas sands: beyond porosity and saturation – an example from the Cotton Valley formation, East Texas, paper SPE 142808 presented at SPE Middle East Unconventional Gas Conference and Exhibition, Muscat, Oman, January 31– February 2.

Spencer, D.W., 1963, The interpretation of grain size distribution curves of clastic sediments, Journal of Sedimentary Petrology, 33(1): 180 – 190.

Theys, P.P., 1999, Log Data Acquisition and Quality Control. 2nd Edition, Technip.

Thomeer, J.H.M., 1960, Introduction of a pore geometrical factor defined by the capillary pressure curve, Journal of Petroleum Technology, 12(3):73-77.

Timur, A., 1968, An investigation of permeability, porosity, and residual water saturation relationships for sandstone reservoirs, The Log Analyst, 9(4): 8–17.

Tixier, M.P., 1949, Evaluation of permeability from electric-log resistivity gradients. Oil and Gas Journal, June 16.

Tomutsa, L., Mahmood, S.M., Brinkmeyer, A., and Honarpour, M., 1990, Application of integrated pore-to-core image analysis to study fluid distribution in reservoir rocks, paper 20478 presented at SPE Annual Technical Conference and Exhibition, New Orleans, LA, September 23 - 26.

Torres-Verdín, C., 2012, Integrated Geological-Petrophysical Interpretation of Well Logs, Lecture Notes for Fundamentals of Well Logging, The University of Texas at Austin, Unpublished.

Torres-Verdín, C., Alpak, F. O., and Habashy, T. M., 2006, Petrophysical inversion of borehole array-induction log: Part II - field data examples, Geophysics, 71 (5): G261 - G268.

Torres-Verdín, C., George, B. K., Delshad, M., Sigal, R., Zouioueche, F., and Anderson, B., 2004, Assessment of in-situ hydrocarbon saturation in the presence of deep invasion and highly saline connate water, Petrophysics, 45 (2): 141-156.

Van Wagoner, J.C., Mitchum, R.M., Campion, K.M., and Rahmanian, V.D., 1990, Siliciclastic Sequence Stratigraphy in Well Logs, Cores, and Outcrops. AAPG methods in exploration series, No. 7, Tulsa.

Voss, B., Torres-Verdín, C., Gandhi, A., Alabi, G., and Lemkecher, M., 2009, Common stratigraphic framework to simulate well logs and to cross-validate static and dynamic petrophysical interpretations, SPWLA 50th Annual Logging Symposium, The Woodlands, Texas, June 21 – 24.

Vrubel, N.K., 2007, Statistical Partitioning of Well Logs and Core Measurements to Detect and Quantify Petrophysical Properties, M.S. Thesis, The University of Texas at Austin.

Wang, G.L., Torres-Verdín, C., Salazar, J. M., and Voss, B., 2009, Fast 2D inversion of large borehole EM induction data sets with an efficient Fréchet-derivative approximation, Geophysics, 74(1): E75-E91.

Webb, P.A., 2001, An introduction to the physical characterization of materials by mercury intrusion porosimetry with emphasis on reduction and presentation of experimental data. Micromeritics Instrument Corporation Report.

Wentworth, C.K., 1922, A scale of grade and class terms for clastic sediments, Journal of Geology, 30: 377–392.

Wescott, W.A., 1984, Diagenesis of Cotton Valley sandstone (Upper Jurassic), East Texas: implications for tight gas formation pay recognition, AAPG Bulletin, 67(6):1002-1013.

Winkler, M., Freeman, J.J., Quint, E., and Caputi, M., 2006, Evaluating tight gas reservoirs with NMR – the perception, the reality and how to make it work, SPWLA 47th Annual Logging Symposium, Veracruz, Mexico, June 4-7.

Xiao, L., Mao, Z.Q., Wang, Z.N., and Jin, Y., 2012, Application of NMR logs in tight gas reservoirs for formation evaluation: a case study of Sichuan Basin in China, Journal of Petroleum Science and Engineering, 81: 182-195.

Xu, C., Heidari, Z., and Torres-Verdín, C., 2012, Rock classification in carbonate reservoirs based on static and dynamic petrophysical properties estimated from conventional well logs, paper SPE 159991 presented at SPE Annual Technical Conference and Exhibition, San Antonio, Texas, October 5-9.

Xu, C., and Torres-Verdín, C., 2012, Saturation-height and invasion consistent hydraulic rock typing using multi-well conventional logs, SPWLA 53rd Annual Logging Symposium, Cartagena, Colombia, June 16-20.

Xu, C., and Torres-Verdín, C., 2013, Pore system characterization and petrophysical rock classification using a bimodal Gaussian density function, Mathematical Geosciences, 45(6): 753-771 (DOI: 10.1007/s11004-013-9473-2).

Xu, C., and Torres-Verdín, C., 2013, Quantifying fluid distribution and phase connectivity with a simple 3D cubic pore network model constrained by NMR and MICP data: in press, Computers & Geosciences.

Xu, C., and Torres-Verdín, C., 2013, Petrophysical rock classification in the Cotton Valley tight gas sand reservoir with a clustering pore-system orthogonality matrix, SEG Interpretation Journal (submitted for review).

Xu, C., Torres-Verdín, C., Ma, J., and Li, W., 2012, Fluid substitution analysis to correct borehole geophysical measurements acquired in gas-bearing formations invaded by oil-base mud, Society of Exploration Geophysicists 83rd Annual Meeting, Las Vegas, Nevada, Nov 4-9.

Xu, C., Torres-Verdín, C., and Steel, R.J., 2012, Facies interpretation based on quantitative analysis of grain size and bed thickness from well logs in deepwater turbidite reservoirs, AAPG Annual Convention and Exhibition, Long Beach, California, April 22 - 25.

Xu, C., and Torres-Verdín, C., 2013. Rock-type based analysis of hydration water effect on capillary pressure in shaly sand formations: a case study in a deltaic gas reservoir, offshore Trinidad, Journal of Petroleum Science and Engineering (submitted for review).

Xu, C., and Torres-Verdín, C., 2013, Multi-scale orthogonal rock class decomposition: top-down reservoir characterization integrating logs and core in tight-gas sands. SPWLA 54th Annual Logging Symposium, New Orleans, Louisiana, June 22-26.

Xu, C., Yang, Q., and Torres-Verdín, C., 2013, Bayesian hypothesis testing: integrating fast well-log forward modeling to validate petrophysical rock typing and to quantify uncertainty in deepwater reservoirs, SPWLA 54th Annual Logging Symposium, New Orleans, Louisiana, June 22-26.

Xu, C., Torres-Verdín, C., Yang, Q., and Diniz-Ferreira, E., 2013. Water saturation – irreducible or not: the key to reliable hydraulic rock typing in reservoirs straddling multiple capillary windows. Paper 166082 presented at SPE Annual Technical Conference and Exhibition, New Orleans, Louisiana, September 30-October 2.

Xu, C., Torres-Verdín, C., and Steel, R.J., 2013. Geological attributes from well logs: relating rock types to depositional facies in deepwater turbidite reservoirs. Paper 166178 presented at SPE Annual Technical Conference and Exhibition, New Orleans, Louisiana, September 30-October 2.

Xu, C., and Torres-Verdín, C., 2013. Core-based petrophysical rock classification by quantifying pore-system orthogonality with a bimodal Gaussian density function. Paper SCA2013-079 presented at International Symposium of Society of Core Analysts. Napa Valley, California, September 16 – 19.

Xu, C., Torres-Verdín, C., and Gao, S., 2013. Electrical vs. hydraulic rock types in clastic reservoirs: pore-scale understanding verified with field observations in the Gulf of Mexico, U.S. 84th SEG Annual Meeting, Houston, Texas, September 22-27.

Yang, Q., and Torres-Verdín, C., 2011, Efficient 2D Bayesian inversion of borehole resistivity measurements, Society of Exploration Geophysicists 82nd Annual Meeting, San Antonio, Texas, September 18-23.

Yang, Q., and Torres-Verdín, C., 2013, Joint stochastic interpretation of conventional well logs acquired in hydrocarbon-bearing shale, SPWLA 54th Annual Logging Symposium, New Orleans, Louisiana, June 22-26.

Youssef, S., Bauer, D., Bekri, S., Rosenberg, E., and Vizika, O., 2010, 3D in-situ fluid distribution imaging at the pore scale as a new tool for multiphase flow studies, paper 135194 presented at SPE Annual Technical Conference and Exhibition, Florence, Italy, September 19 - 22.

Zhou, M., Lu, D., Dunsmuir, J., and Thomann, H., 2000, Irreducible water distribution in sandstone rock: two phase flow simulations in CT-based pore network, Physics and Chemistry of the Earth, Part A: Solid Earth and Geodesy, 25(2): 169-174.

# Vita

Chicheng Xu, the son of Mr. Changshui Xu and Mrs. Meiqin Hu, was born in Wuhu City, Anhui Province, China, in 1983. He received his B.Sc. degree in Physics from the University of Science and Technology of China in 2002 and his MPHIL degree in Physics from The Chinese University of Hong Kong in 2004. He worked for Schlumberger Beijing Geoscience Center as a project engineer between November 2004 and January 2009. After that, he started Ph.D. study in the Formation Evaluation Research Consortium Group in the Department of Petroleum and Geosystems Engineering at The University of Texas at Austin. In the summers of 2010 through 2012, he worked as an intern petrophysicist with BP America Inc., characterizing various reservoir types including coalbed methane (Colorado, US), Paleogene deepwater turbidite (Gulf of Mexico, US), and deepwater carbonate (Offshore Brazil). Chicheng is a member of AAPG, SEG, SPE, and SPWLA/SCA and he has published more than 10 technical papers.

Permanent address: Feng Shu Tang, Sanli, Nanling
Wuhu, Anhui, 242410, CHINA

Email: xuchicheng@gmail.com

This dissertation was typed by the author.